universität
wien

DISSERTATION

Titel der Dissertation

The eventful life of galaxies in low density environments

or

Evolution of galaxy groups

angestrebter akademischer Grad
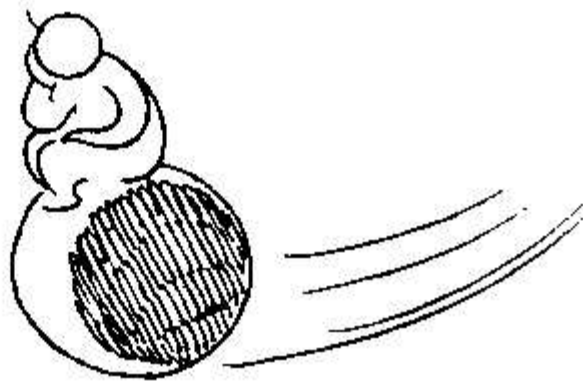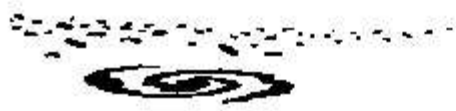
Doktorin der Naturwissenschaften (Dr. rer. nat.)

Verfasserin:	Ruth Grützbauch
Matrikel-Nummer:	a9605967
Dissertationsgebiet (lt. Studienblatt):	Astronomie
Betreuer:	Ao. Univ.-Prof. Dr. Werner W. Zeilinger

Wien, am 31. Oktober 2007

"Why waste time learning, when ignorance is instantaneous?"

— Hobbes (The Tiger) —

Zusammenfassung

Ziel dieser Arbeit ist die Untersuchung der Entwicklung von Galaxiengruppen durch die Eigenschaften ihrer Röntgenemission und ihrer Zwerggalaxienpopulation.

Die meisten Galaxien im lokalen Universum befinden sich in Galaxiengruppen. Der Großteil der Entwicklungprozesse wie Interaktionen zwischen Gruppenmitgliedern, Akkretion von Begleitern und Merging von Galaxien findet in Galaxiengruppen statt. Diese Prozesse beeinflussen nicht nur die Eigenschaften der individuellen Galaxien, sondern können auch zur Transformation der gesamten Gruppe in eine einzige riesige elliptische Galaxie führen.

Dieser Entwicklungsweg kann auf verschiedene Weise verfolgt werden:

- durch die Eigenschaften der dominanten elliptischen Galaxie, die ja vermutlich das Endprodukt der Merging-prozesse in der Gruppe ist

- durch die Zwerggalaxienpopulation der Gruppe, die das Merging wegen der längeren Mergingzeitskala von masseärmeren Galaxien überlebt haben sollte

- durch die diffuse Röntgenemission des Intra-Gruppen Mediums, die auf Grund der langen Kühlzeitskala des Röntgenhalos noch beobachtbar sein sollte.

Das Endprodukt der Entwicklung einer Galaxiengruppe wäre dann eine riesige ellitpische Galaxie mit einem ausgedehnten leuchtkräftigen Röntgenhalo und einer signifikanten Population an Zwerggalaxien, die sogenannten "fossilen Gruppen".

Um dieses Szenario zu überprüfen, wurde in dieser Arbeit die Umgebung von 4 Galaxienpaaren, die sich aus einer riesigen elliptischen Galaxie und einer Spiralgalaxie zusammensetzen, untersucht. Die Galaxienpaare zeigen ähnliche optische Eigenschaften, unterscheiden sich aber entscheidend in ihrer Röntgenemission. Zwei Paare verfügen über ausgedehnte, diffuse Röntgenemission einer heißen Gaskomponente, während die anderen beiden einen Mangel an heißem Gas aufweisen.

Die Beobachtungen der Zwerggalaxienkandidaten rund um die Galaxienpaare zeigen, dass die diffuse Röntgenemission nicht unbedingt mit einer zahlreichen Zwerggalaxienpopulation verbunden ist. Eine mögliche Erklärung dafür ist, dass die Röntgenemission nicht von der Gruppenumgebung sondern vom dynamischen Alter der

zentralen elliptischen Galaxie abhängt. Dafür spricht auch, dass die dynamischen Eigenschaften der Gruppen nicht mit der Röntgenleuchtkraft der Gruppe korreliert sind, sondern mit deren großräumiger Umgebung.

Die Leuchtkraftfunktionen deuten an, dass sich die röntgen-leuchtkräftigen Paare in einer späteren Entwicklungsphase befinden als ein Sample von Galaxiengruppen mit vergleichbarer Röntgenleuchtkraft aus der Literatur. Die röntgen-schwachen Paare hingegen könnten eine frühere Phase in der Entwicklung dieser röntgen-leuchtkräftigen Galaxiengruppen darstellen, in der Galaxienwechselwirkungen den früher vorhandenen Röntgenhalo zerstört haben könnten.

Abstract

The aim of this thesis is studying the evolution of poor groups of galaxies via the properties of their diffuse X-ray emitting gas component and their faint galaxy population.

It is believed that galaxy groups, the most common environment for galaxies in the local universe, are the preferential sites for galaxy evolution via galaxy interactions, accretion and merging. This does not only affect the properties of the group galaxies but may also lead to the transformation of the whole group into a single giant elliptical galaxy, the supposed final point of group evolution in Low Density Environments (LDE).

This evolutionary path can be traced via

- the properties of the dominant group elliptical, which is supposed to be the outcome of past or recent galaxy merging

- the group's faint galaxy population, which should survive the merging because of the longer merging timescale of fainter group member galaxies and

- the diffuse X-ray emission from a hot Intra-Group Medium (IGM), that may still be observed due to the X-ray halo's long cooling time.

The final product of a merged group would then be a luminous isolated elliptical with an extended X-ray halo and a significant population of faint companions, the so-called "fossil groups". However, recent X-ray observations of merger remnants show that their hot diffuse gas components are under-luminous in X-ray compared with typical mature elliptical galaxies into which these merger remnants are expected to evolve. The picture is thus far from being completely understood.

Physical pairs of galaxies dominated by an elliptical, located in very low density environments and possibly showing extended X-ray emission represent very promising objects to test the above evolutionary scenario.

We investigated the environment of 4 mixed morphology (elliptical and spiral) galaxy pairs, 2 of which show extended "group-like" X-ray emission. The results of new X-ray observations of the IGM around these 2 pairs with `XMM-Newton` are presented.

IV

The pair was also observed with the Wide Field Imager (WFI) at the European Southern Observatory (ESO) and investigated for signatures of interaction. The ellipticals of the X-ray luminous pairs were found to be dynamically evolved, unperturbed objects, whereas the X-ray faint pairs show clear signs of recent interaction. A faint candidate member galaxy population in the $0.5° \times 0.5°$ WFI field around each of the pairs was detected. We investigated the photometric and structural properties of the candidates to determine the likelihood of their association to the pair. The candidates were then observed with the VIsible Multi Object Spectrograph (VIMOS) at the ESO Very Large Telescope (VLT).

We found that only few candidates are associated to their respective pair. However, since the observing program was not completed, there might be a significant fraction of additional members, especially in 1 pair. From the available data we found that the presence of extended diffuse X-ray emission from an IGM is not necessarily connected to the presence of a numerous faint galaxy population. A possible explanation for this is that the X-ray emission is not dependent on the group environment but on the dynamical age of the central elliptical. This is also supported by the finding that the dynamical quantities of the newly defined groups are not correlated with the group X-ray luminosity, but with the large-scale environment of the pairs.

The study of Luminosity Functions (LFs) indicate that our X-ray luminous pairs are more dynamically evolved than a sample of poor groups with comparable X-ray luminosities from the literature. Our X-ray faint pairs on the other hand may represent a phase in the dynamical evolution of these X-ray detected poor groups, where the recent or ongoing interaction, in which the pair E is involved, has destroyed or at least decreased the luminosity of the IGM.

Published work

Parts of the work presented in this thesis, mainly Chapters 2, 3 and 4 have already been published in:

— Grützbauch R., Trinchieri G., Rampazzo R., Held E.V., Rizzi L., Sulentic J.W. and Zeilinger W.W., 2007, "Small-scale systems of galaxies. III. X-ray detected elliptical+spiral galaxy pairs in low-density environments", AJ **133**, 220

The results of the new VIMOS observations, Chapters 5 and 6, will be presented in:

— Grützbauch R., Zeilinger W.W., Rampazzo R., Held E.V., Sulentic J.W. and Trinchieri G., 2007, "Small-scale systems of galaxies. IV. The faint galaxy population of X-ray detected E+S galaxy pairs in low-density environments", in preparation

Other work related to the topic of the thesis was published in the following 3 articles:

— Grützbauch R., Kelm B., Focardi P., Trinchieri G., Rampazzo R. and Zeilinger W.W., 2005, "Small-scale systems of galaxies. III. Properties of the NGC 4756 group of galaxies", AJ **129**, 1832

— Grützbauch R., Annibali F., Bressan A., Focardi P., Kelm B., Rampazzo R. and Zeilinger W.W., 2005, "Optical properties of the NGC 5328 group of galaxies", MNRAS **364**, 146

— Rampazzo R., Marino A., Tantalo R., Bettoni, D., Buson, L. M., Chiosi, C., Galletta, G., Grützbauch, R., Rich, R. M., 2007, "The Galaxy Evolution Explorer UV emission in shell galaxies: tracing galaxy rejuvenation episodes", MNRAS **381**, 245

Other work carried out during the thesis will be published in:

— Trinchieri G., Rampazzo R., Chiosi, C., Grützbauch, R., Marino A., Tantalo R., 2007, "`XMM-Newton` X-ray and `Optical Monitor` UV observations of the shell galaxies NGC 7070A and ESO 2400100", in preparation

VI

Observing programs

The work presented in this thesis is based on the following observing programs:

– The optical imaging presented in Chapter 2 was carried out with the Wide Field Imager (WFI) on the 2.2m telescope in La Silla, Chile operated by MPG and ESO under Program 68.B-0598. The program was executed between Oct 2001 and Oct 2003. The Principal Investigator (PI) of the program is R. Rampazzo.

– X-ray data presented in Chapter 3 were observed with `XMM-Newton` under Program-ID 0148580101 on July, 17 and Oct, 19 2003. The PI is G. Trinchieri

– The spectroscopic observations of the faint candidates presented in Chapter 5 were observed under Program 076.A-0616 with the VIsible Multi-Object Spectrograph (VIMOS) on the ESO Very Large Telescope (VLT). The PI of this program is R. Grützbauch.

Future observations continuing the work presented here are going to be carried out in the next observing period under Program 380.A-0269 with PI R. Grützbauch

VIII

Acknowledgements

Contents

List of Figures

List of Tables

Chapter 1

Introduction

How do galaxies form? How is the mass of today's galaxies assembled and why do they appear in basically two very different morphological types? We know that galaxy properties depend on the galaxies' local environment, but the question is to what extent does the surrounding density influence galaxy evolution? Does this environmental dependence reflect the conditions at the time of initial galaxy formation or is it caused by physical processes that occur afterwards?

More than half of the galaxies in the nearby universe are clustered in galaxy groups. This result is supported by observations (see eg. Geller & Huchra 1983) as well as cosmological simulations (Jenkins et al. 2001). Groups have higher galaxy densities compared to the field and lower relative velocities between individual galaxies than galaxy clusters. Therefore we expect galaxy interactions and merging to play a significant role in these environments. The typical encounter velocities are comparable to the galaxies' internal velocities leading to strong dynamical responses and very efficient transformation of galaxies. To understand galaxy formation and evolution it is inevitable to look at galaxy groups and the physical processes occuring in these environments.

1.1 How to make an elliptical galaxy?

So how are massive galaxies assembled? Massive galaxies with stellar masses $M_* > 10^{11} M_\odot$ are mostly elliptical galaxies. They are spheroidal and dynamically hot systems, supported by anisotropic velocity dispersion rather than rotation (like disks). Their stellar populations are supposed to be old, metal rich, and show no (or little) gradient with distance from the centre. They are considered to have no or very little (cold) Interstellar Medium (ISM) and almost no current star formation (SF). They are known to be a very homogeneous family of objects over a large range of magnitudes following a relation between their velocity dispersion (mass), effective radius

(size) and surface brightness (stellar density), the so-called Fundamental Plane (FP) (Dressler et al. 1987).

Does this argue for an early, fast and unique formation mechanism for all elliptical galaxies?

1.1.1   Monolithic collapse

The formation mechanism for elliptical galaxies was argued to be a dissipative monolithic collapse with a very early, very fast and very efficient burst of star formation. There are several arguments for this view:

− Relations between colour and magnitude or Magnesium abundance and velocity dispersion (σ) and especially increasing α-element ratios ($[\alpha/Fe]$) with σ suggest that for massive galaxies the timescale of gas consumption and re-ejection into the ISM was shorter than the dynamical (collapse) timescale (Matteucci 1994). Since α-elements are produced through the α-process in massive stars they are released relatively fast in Type II supernova (SN) explosions. Fe is mainly produced in SNe Type Ia, where matter accretion from a giant star onto a white dwarf leads to the collapse. The timescale of this process depends on the time that the companion star needs to evolve into a red giant. For most stars this timescale is significantly longer than the timescales of SNe Type II. Therefore, if the ratio between α-elements and Fe is enhanced, most of the gas was consumed by star formation before the SNe Ia could eject their Fe.

− Structural properties of elliptical galaxies like the de Vaucouleurs law (saying that the surface brightness decreases with $r^{1/4}$) or the decreasing σ with radius are reproduced by a cold dissipationless collapse, which is supposed to be the final stage of dissipative collapses. This means that the stars form during the early collapse phase "in flight", making the subsequent collapse a dissipationless collapse.

− Dark matter (DM) halo scaling relations: eg. the virial velocity dispersion σ_{vir} of DM halos increases with halo-mass. Parabolic merging would not reproduce this relation (Ciotti et al. 2007).

However, the problem of this picture is the conservation of angular momentum, that prevents the fast collapse of the gas and results in the formation of disks (see eg. Steinmetz & Navarro 2002).

1.1.2 Hierarchical galaxy formation

The evidence for the build-up of massive spheroids through merging of disk galaxies is numerous. Simulations started decades ago, a famous early example are the models of Toomre & Toomre (1972) reproducing the observed tidal features of nearby merging galaxies.

Galaxy formation through hierarchical merging is the basic idea of the Cold Dark Matter (CDM) scenario (White & Rees 1978). The currently favoured model of the universe is the Λ (=inflationary) CDM model: galaxies form inside dark matter halos that develop from primordial density fluctuations and hierarchically assemble to form more and more massive halos (and galaxies). The stars form initially in disks which are then possibly transformed into spheroids during the subsequent evolution. The CDM is very successful at large scales, reproducing the observed luminosity function and density profiles, it also predicts an increasing merger rate with redshift. However, the predicted richness of substructures on small scales (dwarf galaxies, companions) is not observed. In the CDM scenario small groups and even individual galaxy halos are downsized versions of galaxy clusters. A Milky Way sized halo should have an incredible number of about 500 companions larger than 1 kpc (Moore et al. 1999).

1.1.3 Producing massive spheroids through merging

Taking into account the higher density of the universe at earlier times, galaxy merging and accretion should have played a very important role in the early universe. Observations show that the bulk of the stellar mass in massive (mostly elliptical) galaxies formed between $z \sim 2 - 3$ and that these galaxies are in place at $z \sim 1$. However, there seem to be significantly less massive galaxies at $z > 1.5$ than at $z \sim 1$. Additionally, observations show that a large fraction of massive galaxies at z > 1.5 is involved in major (equal mass) merging events (for a review see Conselice 2007). By integrating the merger rate up to $z \sim 3$, Conselice (2006) found that a typical massive galaxy has experienced 4-5 major mergers.

The outcome of the merging process is highly dependent on the presence of large amounts of gas, i. e. the influence of dissipation is critical (Ciotti et al. 2007). Traditionally it was believed that the merging of gas-rich spirals ("wet merging") produces a spheroidal, elliptical-like remnant that subsequently evolves passively into a mature elliptical. However, more recent simulations suggest that the most massive ellipticals are not produced by merging spirals, but through "dry merging", i.e. merging of smaller early-type (E or S0) galaxies (Naab et al. 2006). It seems that the properties of low luminosity ellipticals, their faster rotation and rather disky isophotes are consistent with being produced by wet merging, while the very luminous slowly rotating, boxy giant ellipticals are assembled from these galaxies

via dry merging without the formation of new stars. This is supported by studying the impact of galaxy merging on the Fundamental Plane (see eg. Evstigneeva et al. 2004; Boylan-Kolchin et al. 2005). Merging of gas rich galaxies produces remnants that lie on the FP, whereas dissipationless merging preserves the FP. This means that merging of galaxies that already lie on the FP results in remnants also following the FP, however having larger sizes and lower densities.

1.1.4 Galactic cannibalism - evidence from line strength indices

The most direct estimate of star formation histories revealing past accretion and merging events is provided by the study of absorption line strength indices. The measured spectral indices are compared with models of simple stellar populations (SSP) of a certain age and metallicity.
Annibali et al. (2007) studied the indices of a large sample of early-type galaxies predominantly located in low density environments (LDE). They found that early-type galaxies in LDEs are fitted by SSPs with a wide spread in ages and metallicities, whereas none of the galaxies in denser environments is younger than $4 - 5$ Gyr. Additionally, they found that about 15% of all galaxies are rejuvenated and that the rejuvenation involves not more than 25% of the galaxy mass. This suggests that most of the stellar mass is formed in a very early epoch with a minor contribution of merging in the subsequent life of a galaxy.

After all there is little doubt that significant evolution in the properties of galaxies takes place after the initial time of galaxy formation. However, to what extent the properties of today's galaxies are determined by the environment and through which physical processes this happens is still a debated question. Whichever of the above scenarios may be the dominant one in creating the galaxies that we observe today, they are most likely to take place in groups. There is strong evidence that the physical processes that are building up and transforming galaxies are dependent on the very local environment of a galaxy and that the preferential site for this evolution are groups of galaxies.

1.2 What are galaxy groups?

It was found that the majority of galaxies resides in groups, both, in the local universe (Tully 1987) and at least out to z $\sim$ 1.4 (Gerke et al. 2005). However, there is no strict definition or classification of galaxy groups. Generally, the term group refers to a poor structure with less than 5 bright ($\lesssim L^*$) members with a low velocity dispersion of $\lesssim 300$ km s^{-1}. L^* is the characteristic luminosity of the luminosity

function as described by Schechter (1976). A detailed description is given in section 6.2.2. Diffuse X-ray emission from a hot intra group medium (IGM) was detected in some poor groups, preferentially in groups dominated by an early-type galaxy population (see eg. Mulchaey et al. 1993).

1.2.1 Classification of galaxy groups - the role of the hot IGM

A classification of galaxy groups based on their hot IGM content, early-type fraction and faint galaxy population was suggested by Zabludoff & Mulchaey (1998). There are 2 main types:

— groups without hot IGM composed of late-type galaxies and few dwarf elliptical galaxies (although a significant number of very faint dIrr and dSph galaxies). These groups are considered to collapse for the first time like our own Local Group (LG),

— groups with a relaxed hot IGM, centered on a giant elliptical with a numerous intermediate and faint galaxy population. This groups exhibit a morphology-density-relation, i.e. the early-type galaxies are located in the denser regions of the group, usually the group center, while the late-type galaxies orbit at a large distance from the center.

The authors furthermore suggest that there is evolution from the first into the second group type. This should then produce a third, transition type exhibiting a perturbed hot IGM not centered on some bright galaxy and a mixed population of early and late type galaxies. The group centres would show signatures of dynamical evolution (interacting group members).

1.2.2 Fossil groups

Fossil groups are thought to be the final stage of the evolution of a galaxy group, where all the bright member galaxies have merged to form an isolated giant elliptical galaxy, leaving the former group's hot IGM and faint galaxy population around the giant E (Ponman et al. 1994). The term "fossil" is a bit misleading, since they are not the conserved early stages of group evolution but their outcome. They were discovered through the identification of extended luminous X-ray halos around isolated, "X-ray over-luminous" ellipticals and are therefore defined by their X-ray properties and isolation by the following criteria:

— having 1 giant elliptical galaxy coinciding with an X-ray source with a luminosity of $L_X > 10^{42}$ erg s^{-1},

– this galaxy should be brighter than the characteristic luminosity (L*) of the luminosity function of its surrounding group, while the second brightest galaxy within the system's virial radius should be at least 2 magnitudes fainter.

These strict criteria keep the number of identified fossil groups small: up to now there are 15 known fossil groups out to a redshift of $z \sim 0.6$ (Mendes de Oliveira et al. 2006). Additionally the known fossil groups have very high velocity dispersions, more similar to clusters than to groups (Mendes de Oliveira & Carrasco 2007).

Fossil groups defined in this way are most probably not the outcome of the collapse of a typical poor group, but only of the most massive ones. Especially the high X-ray luminosity criterion may exclude many of the structures produced by merging typical poor groups.

1.3 How do groups and their members evolve?

1.3.1 Morphology-density relation

The morphology-density relation known from the study of galaxy clusters was found to be present already in poor groups (Tran et al. 2001). This relation says that the bulge-dominated galaxies are found in denser local environments (centres of clusters and groups) than disk dominated objects. This translates into a inverse star formation-density relation, meaning that star formation is halted in some way by denser local environments. This relation was also found for Local Group (LG) dwarf galaxies (Grebel 2005): although the spread in ages and metallicities is large, there is a decreasing amount of recent star formation and more dominant older stellar populations the closer the dwarfs are to the MW. The gas-rich dwarfs are not clustered around a bright galaxy. However, the star formation is not shut off completely. It seems that galaxies are transformed by their very local environment and quite independently of the global large-scale density.

Groups have a wide range of early-type fractions, similar to the field ($\lesssim 20\%$) and similar to rich clusters ($\sim 55\%$), whereas the large early-type fraction is connected to the presence of a hot IGM (Zabludoff & Mulchaey 1998). This suggests that there is a saturation point in early-type fraction which is reached in groups, not in clusters. This either reflects the similar formation conditions of galaxies that are now in groups and in clusters or that the physical processes that are active in the group environment are responsible for the properties of the galaxy population in both, low and high density environments. In other words, it seems that the group environment processes field galaxies and turns them into galaxies observed in galaxy clusters. Cluster specific processes certainly can have an influence on galaxy properties, however they are not required to explain the observed galaxy morphologies.

1.3.2 Luminosity functions

Similar evidence comes from the study of luminosity functions (LFs), i.e. the number of galaxies with a certain luminosity per unit of volume.

The luminosity function of the field (see eg. Lin et al. 1996, for the Las Campanas Redshift Survey) is characterized by a flat (or even decreasing) faint end, i.e. the number of faint and intermediate luminosity galaxies is constant or slightly increasing going to brighter magnitudes. The LF of galaxy groups is not universal and expected to vary with local density. Zabludoff & Mulchaey (2000) found that groups with extended luminous X-ray halos have luminosity functions that are remarkably similar to the luminosity functions of galaxy clusters. They can be fitted by a single Schechter function (Schechter 1976) with parameters (characteristic luminosity and faint end slope) similar to derived nearby cluster LFs. This means that there is also a saturation point in the ratio between faint (dwarf) and bright (giant) galaxies, the dwarf-to-giant ratio (D/G), that is reached in early-type-dominated, X-ray bright galaxy groups.

The luminosity function of dynamically very evolved groups, i.e. massive groups with a very high early-type fraction (eg. the group around NGC 5846, Mahdavi et al. 2005) shows a slightly different behaviour: it is split in two separate distributions of high and low surface brightness galaxies. While the faint end (low surface brightness) is fitted by a Schechter function with similar slope to the X-ray bright groups of Zabludoff & Mulchaey (2000), the bright end is better fitted by a Gaussian function. This can be translated into a lack of galaxies of intermediate luminosity ($-20 \leq M_R \leq -19$) and an overabundance of bright galaxies.

Even the large D/G-ratios found in X-ray bright groups are still not reaching the large number of faint galaxies expected from the ΛCDM scenario. Either there is a problem in the theory or there are physical processes at work destroying faint galaxies or better, influencing the evolution of the visible central part of low mass halos in a way that their luminosity is somehow more reduced in less dense environments.

1.3.3 Evolution of the group structure

There is evidence that poor loose groups dominated by late-type galaxies (eg. the Local Group, or a bit more massive) evolve through successive merging into X-ray bright groups with an early-type population. It was shown indeed that gas-rich merging can result over the timescale of a few Gyrs in the build-up of a halo of diffuse hot gas as observed around elliptical galaxies (O'Sullivan et al. 2001b). However, it is hard to imagine that a structure like the Local Group is transformed into a group with a significant early-type population and a high D/G-ratio. The question is, where do the faint galaxies come from? One possibility is that they are formed during the interaction as tidal dwarf galaxies. However, a large amount of gas is

necessary to reproduce the central densities of observed dwarf galaxies (Wetzstein et al. 2007). An other option is that galaxies are accreted from the surroundings of the group, which can only happen if the group is embedded in a dense global environment. The number of dwarf galaxies would then be connected to the large-scale density.

Once that the X-ray bright group is in place there are 2 possibilities dependent on global environment:

  − Infalling groups build up galaxy clusters, the brightest cluster galaxies (cD galaxies) are formed from merged groups. This view is supported by the similarity of some groups with clusters in their X-ray emission, early-type fraction and dwarf-to-giant ratio as described above. (Khosroshahi et al. 2006) argue that the brightest group galaxy (BGG) in fossil groups show disky isophotes, consistent with being the outcome of gas-rich merging of spirals. However, cD galaxies (the dominant ellipticals in clusters) are characterized by boxy isophotes. This means that if cD galaxies are built up in groups these galaxies should experience further dry merging in galaxy clusters.

  − The X-ray bright group evolves through merging of the bright group members into one isolated giant elliptical. This process is caused by dynamical friction (Binney & Tremaine 1987): the galaxies loose their kinetic energy to the surrounding halo and spiral into the center of the group, where they merge with the central (elliptical) galaxy. The impact of dynamical friction is dependent on galaxy mass. While the massive group members (around the characteristic magnitude M^*) are moving towards the center of mass, the faint galaxies can follow their orbits almost unaffected. The timescale for an M^* galaxy to fall into the center of a $\sigma \sim 250$ km s^{-1} group from an initial radius of ~ 300 kpc is a few tenth of the Hubble-time (Zabludoff & Mulchaey 1998). With a typical characteristic magnitude M_R^* of around -20 to -21, there should be a dip in the LF at this magnitude and a bit below in dynamically evolved groups. At fainter magnitudes ($M_R \sim -18$) the LF should rise again.

    And what happens to the X-ray halo of the group? The cooling timescale at X-ray temperatures is dependent on the gas temperature, density and the cooling function at this temperature. A hot plasma at a temperature of $\sim 10^7$ K, which is typical for groups, has a cooling timescale of about a Hubble-time, i.e. the age of the Universe (Mulchaey & Zabludoff 1999). Therefore the X-ray emission should still be observable long time after the bright galaxies merged to form the giant E.

The result of this evolution in low density environments is then an isolated E with a numerous faint galaxy population and group-like X-ray halo, a fossil group (if its X-ray luminosity is high enough).

1.3.4 Problem: The scatter in X-ray luminosity of early-type galaxies

However, the above picture may be too straightforward. Recent merger remnants identified by their fine structure (tidal signatures, shells,...) were found to be under-luminous in X-ray compared to unperturbed ellipticals of similar luminosity (Sansom et al. 2000; Rampazzo et al. 2006). Galaxy merging therefore seems to have a crucial impact on the hot IGM. This may be connected to the scatter in the X-ray luminosity found for elliptical galaxies: Es of similar optical luminosity (L_B or L_K) have X-ray luminosities ranging over 2 orders of magnitude (Fabbiano et al. 1992). It was found that many of the very X-ray luminous Es are located in poor groups (see eg. Helsdon et al. 2001).

This scatter can be partly explained by the presence of extended emission in higher L_X systems (Matsushita 2001). However, also the low L_X systems require an extended soft emission component, apart from the emission coming from low-mass X-ray binaries (Trinchieri et al. 2000).

One possible origin for the scatter might be connected to the mass of the galaxy's host halo: Mathews et al. (2006) argue that L_X correlates with M_{vir} of the surrounding DM halo, while L_B (or alternatively L_K) is only a measure of the stellar mass of the central E. Only the more massive satellite halos merge at the center with the dominant E, increasing its luminosity. Due to the intrinsic scatter in the presence of massive companions the same massive halo can contain central ellipticals with more or less luminous mass.

Another explanation following the above evidence from merger remnants would be the dynamical age of the elliptical. Recent merging increases the luminosity of the elliptical but reduces the luminosity of the X-ray halo. This is supported by Brassington et al. (2007), who studied the evolution of the X-ray luminosity in pre- and post-merging objects. They found that the X-ray luminosity peaks shortly before nuclear coalescence and dips at about 1 Gyr afterwards. The halo regeneration takes place over a timescale of several Gyrs and is continued long time after the interaction signatures are detectable (O'Sullivan et al. 2001b).

1.4 Galaxy pairs - the missing link?

What happens on the way from the poor group to the isolated giant elliptical? How are X-ray faint groups connected to X-ray bright ones? Are we observing different evolutionary phases or the effects of an intrinsic difference in the dark matter halo mass?

If groups in low density environments are commonly evolving into giant Es, we should observe an intermediate phase, where the central group galaxy is already in

place but still dynamically evolving, possibly interacting with the remaining bright group member: isolated galaxy pairs dominated by a bright elliptical galaxy. The presence of an extended, diffuse X-ray halo would enhance the probability that the pair is indeed a massive and bound structure. However, to investigate the role of the IGM we should take a look at pairs with and without luminous X-ray emission. Of special interest in the above context is the environment of the pairs and the faint galaxies possibly connected to them. If these pairs represent a way station in the coalescence process of poor groups towards isolated ellipticals, they should be surrounded by a significant population of faint galaxies.

In this thesis, four mixed morphology galaxy pairs composed of a giant elliptical and a $\sim L^*$ spiral are investigated. The properties of the pair, especially the pair elliptical, obtained from Wide Field Imager observations are presented in Chapter 2. The properties of the X-ray emission of the 4 pairs are described in Chapter 3. The emphasis of this work is put on the characterization of the faint galaxy population around the galaxy pairs. Their detection and likelihood of being associated to the pair is presented in Chapter 4. The subsequent spectroscopic observations of the faint galaxy candidates and the results concerning their group membership are described in Chapter 5. Finally, Chapter 6 presents the new group members and the resulting properties of the newly defined groups.

Chapter 2

The E+S pair sample

The E+S pairs in our sample were taken from the Reduzzi & Rampazzo (1995a) catalogue of isolated galaxy pairs in the Southern Hemisphere. The pairs were chosen to be similar in their structure, optical luminosity and velocity dispersion, but are very different concerning their X-ray emission. Despite the small number of 4 pairs in our sample, we explore the full range of L_X/L_B ratios found for elliptical galaxies.

Table 2.1 summarizes photometric, structural and kinematical properties of the pair members extracted from the literature. In the following section the properties of the pairs at different wavelengths, basically the optical and X-ray, found in the literature are presented.

Section 2.2 describes the new observations of the 4 pairs with the Wide Field Imager (WFI) at ESO in order to perform detailed surface photometry, quantify signatures of interaction and to search for diffuse stellar light. The data reduction procedures and methods of data analysis are described in detail. The WFI frames were also used to investigate the surrounding field of the pairs for the presence of a faint galaxy population that may be associated to the pair, but this procedure is described in a separate chapter (Chapter 4). The results for each pair extracted from analysing these observations are presented in Section 2.3.

Finally, the environment of the 4 pairs is investigated out to a radius of $1.5°$ using data from the literature. The influences of the large scale density on the group and group member properties is discussed.

2.1 The picture so far

2.1.1 RR 143: NGC 2305 + NGC 2307

RR 143 is a very isolated pair with a projected separation of R $\approx$ 51 kpc and a velocity difference of ΔV $\approx$ 270 km s^{-1}. The much larger velocity difference implied by NED[1] results from an older and less accurate measurement for NGC 2307 (see Table 2.1).
A study of the ellipticity profile for NGC 2305 (Reduzzi & Rampazzo 1996) shows that the outer regions of the galaxy (r$\geq$ 20$''$) are on average flatter ($\epsilon \approx 0.3$) than the inner ones ($\epsilon \approx$ 0.22-025) consistent with the presence of sub-structure. Isophotal shape analysis also supports the presence of sub-structure being boxy within 20$''$ of the center and disky between 20$''$ and 35$''$. A recent bulge/disk decomposition study (de Souza et al. 2004) suggests that the galaxy is lenticular rather than an elliptical. Kinematical studies however show that the galaxy has a maximum rotation velocity $\leq$50 km s^{-1} (Rampazzo 1988) which is more typical of an E than an S0.

2.1.2 RR 210: NGC 4105 + NGC 4106

RR 210 forms a strongly interacting pair (Arp & Madore 1987) separated only by projected 7.7 kpc and 258 km s^{-1}. It was also described as a loose triplet by Tully (1988) including IC 764 that has a similar recession velocity (2127 km s^{-1}) and is situated at a projected distance of 46.3$'$ ($\approx$ 363 kpc) from the pair. Reduzzi & Rampazzo (1996) obtained B, V and R surface photometry for both pair galaxies which show almost constant colour profiles $(B - V) \approx 0.9 - 1$ suggesting that both are early-type galaxies (ETGs). NGC 4105 shows no evidence of perturbation while NGC 4106 is strongly perturbed with arms/tails that are likely a product of the interaction with the companion. NGC 4105 shows evidence for a dusty center and disky outer structure. NGC 4106 shows a disky central structure.
Longhetti et al. (1998a,b) obtained kinematic and spectro-photometric properties for both pair members. Evidence for strong interaction also comes from the velocity and velocity dispersion profiles along a line connecting the nuclei of the two galaxies. The study of line-strength indices (Longhetti et al. 1999) suggests the presence of very recent star formation episodes. In particular NGC 4106 shows a value for the H+K(Ca II) index larger than 1.3, i.e. larger than the maximum value attainable in post-starburst models (both with solar and super-solar metallicity) which suggests the presence of Hε in emission. This feature is considered a good indicator of recent star formation (Rose 1984, 1985). The detection of [O II] λ 3727-9 Å emission in the

---

[1]NED is the NASA/IPAC Extragalactic Database which is operated by the Jet Propulsion Laboratory, California Institute of Technology, under contract with the National Aeronautics and Space Administration.

nucleus of NGC 4105 is also suggestive of a recent star formation episode (Longhetti et al. 1998a).

Caon et al. (2000) showed the extended nature of the ionized gas distribution with mapping Hα kinematics in NGC 4105. The ionized gas counterrotates with respect to the stars and shows a different behaviour on opposite sides of the slit (P.A. 151°) centred on the nucleus: the NW side shows a less steep central gradient, and a dip at about 13″. This data point towards a past cross-fuelling or accretion event. The stellar velocity dispersion is quite high in both galaxies (see Table 2.1). NGC 4105 shows slow stellar rotation ((36±7 km s^{-1}) Caon et al. 2000) in contrast to the ionized gas rotation which reaches 240±20 km s^{-1}. Longhetti et al. (1998b) report a higher stellar rotation velocity of $\approx$ 116 km s^{-1} for NGC 4106. Modeling of kinematics and surface photometry of NGC 4105 (Samurović & Danziger 2005) do not support the presence of significant dark matter at least inside $\approx$1 r_e, although their models neglect any interaction with NGC 4106.

2.1.3 RR 216: IC 3290 and NGC 4373

RR 216 forms an isolated pair according to both Sadler & Sharp (1984) and Arp & Madore (1987) with a projected separation of 26 kpc and ΔV = 54 km s^{-1}. The system is in the Hydra-Centaurus region, but located on the outskirts at 4.9° ($\approx$ 4 Mpc) from the cluster center (Dickens et al. 1986). B, V, and R surface photometry (Reduzzi & Rampazzo 1996) shows that $(B - V) \approx 1$ throughout both galaxies, although IC 3290 shows a well developed bar and a "grand design" spiral pattern. NGC 4373 shows a disky structure in the isophotal shape profile but the luminosity profile is well represented by a r$^{1/4}$ law suggesting that the galaxy is a disky E.

2.1.4 RR 242: NGC 5090 and NGC 5091

RR 242 has parameters similar to the other pairs (R = 17 kpc, Δ V = 108 km s^{-1}), but it is found in a richer local environment than the previous systems. Available NED data suggest that the pair is part of a loose group. Four additional luminous galaxies with comparable redshifts can be found within a radius of 300 kpc around NGC 4105: NGC 5082 (at 5.8′ or 78 kpc, Δ V$_{pair}$= 421 km s^{-1}), NGC 5090A (at 20.3′ or 298 kpc, Δ V$_{pair}$= 45 km s^{-1}), NGC 5090B (at 13.8′ or 184 kpc, Δ V$_{pair}$= 773 km s^{-1}) and ESO 270 G007 (at 24.4′ or 326 kpc, Δ V$_{pair}$= 275 km s^{-1}). If we consider all the above galaxies as a group, this has an average recession velocity of 3681 km s^{-1} and a velocity dispersion of 327 km s^{-1}.

NGC 5090 appears to be a "bona fide" elliptical without signatures of interaction according to the surface photometry of Govoni et al. (2000). The galaxy hosts an FRI radio source (PKS B1318-434) with two jets aligned perpendicular to a line connecting the two galaxies' nuclei (see e.g. Lloyd et al. 1996, and references therein).

Lloyd et al. (1996) have obtained the velocity dispersion and rotation velocity profiles of NGC 5090 which show a high central velocity dispersion and low rotation velocity, both characteristic of E galaxies. Bettoni et al. (2003) estimate a mass of 1.1×10^9 M$_\odot$ for the central super massive black hole in NGC 5090.
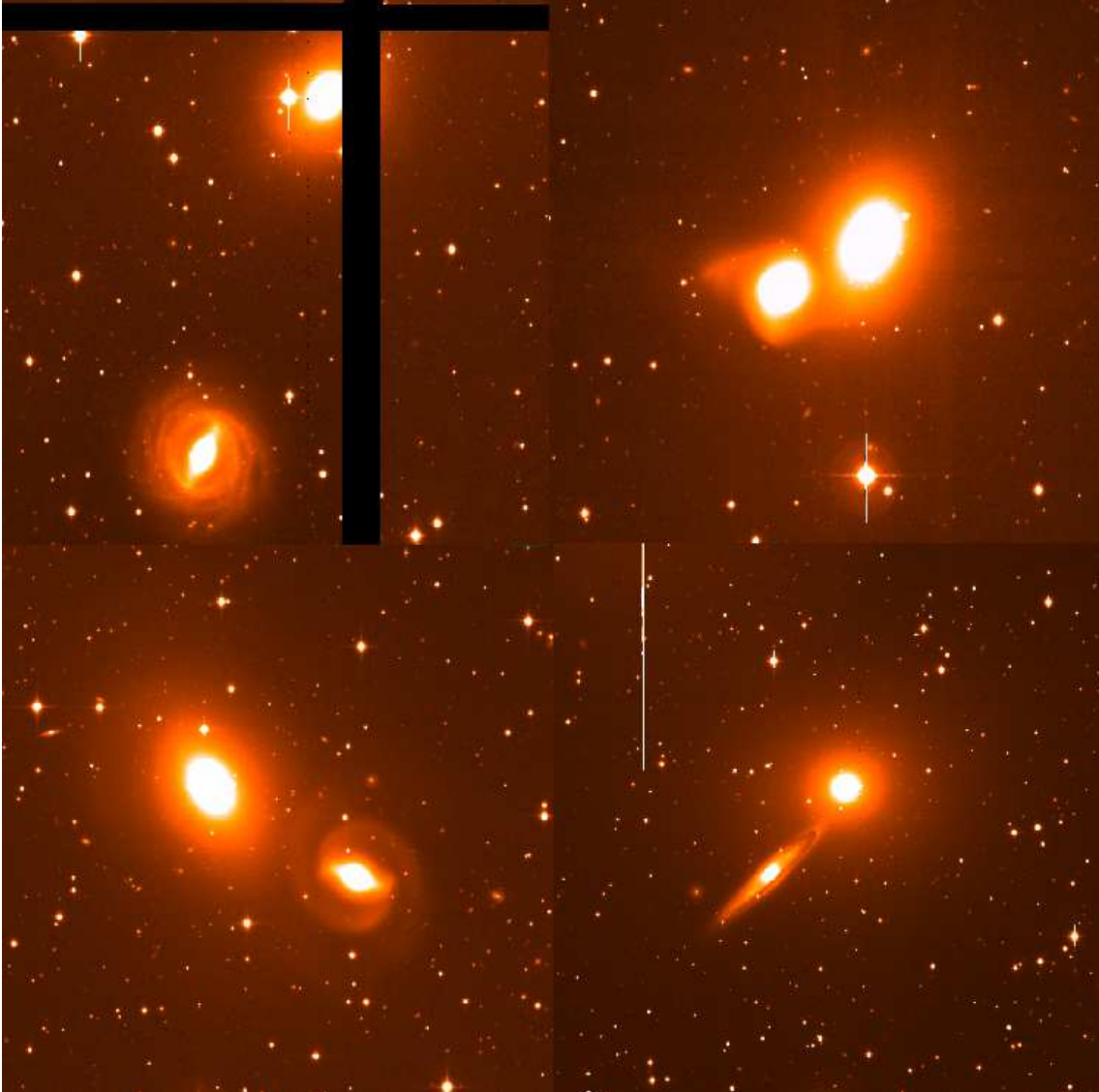
Figure 2.1: Close-up of the 4 pairs, RR 143 (top left), RR 210 (top right), RR 216 (bottom left) and RR 242 (bottom right). The width of the frames is $\sim 5'$.

Table 2.1: Overview of the pairs and their members.

	RR 143		RR 210		RR 216		RR 242		
	NGC 2305	NGC 2307	NGC 4105	NGC 4106	IC 3290	NGC 4373	NGC 5090	NGC 5091	notes
ESO ident	870440	870450	4400540	4400560	3220040	3220060	2700020	2700040	
RA (2000)	06 48 36	06 48 50	12 06 41	12 06 45	12 25 09	12 25 18	13 21 12	13 21 18	
Decl. (2000)	-64 16 24	-64 20 01	-29 45 42	-29 46 06	-39 46 31	-39 45 37	-43 42 16	-43 43 10	
Morphol. Type	E2: pec	SB(rs)ab	E3	SB(s)0+	SB(s)a	SAB(rs)0-:	E2	Sb pec sp	[1]
App. magnitude and color:	NGC 2305	NGC 2307	NGC 4105	NGC 4106	IC 3290	NGC 4373	NGC 5090	NGC 5091	notes
B_T	12.74	12.92	11.60	12.36	12.96	11.90	12.57	13.91	[1]
$(B-V)_T^0$	0.92	0.77	0.87	0.90		0.86			[1]
$(J-H)_{2MASS}$	0.68	0.68	0.53		0.63	0.66	0.79		[1]
$(H-K)_{2MASS}$	0.22	0.30	0.32		0.36	0.27	0.23		[1]
$IRASS_{12\mu}$ [Jy]	<0.029	<0.089	<0.023	<0.023		<0.027	0.120±0.031		[1]
$IRAS_{25\mu}$ [Jy]	<0.024	<0.081	<0.039	<0.029		<0.030	0.200±0.028		[1]
$IRAS_{60\mu}$ [Jy]	<0.039	0.271	0.260±0.039	0.220±0.022		<0.044	0.170±0.045		[1]
$IRAS_{100\mu}$ [Jy]	<0.103	1.572	0.830±0.152	0.710±0.170		<0.191	0.860±0.477		[1]
X-ray and B luminosity:	NGC 2305	NGC 2307	NGC 4105	NGC 4106	IC 3290	NGC 4373	NGC 5090	NGC 5091	notes
log L_X [0.5-2.0 keV]	41.6		39.6	39.1		40.5		41.0	[8]
log L_B	10.4		10.4	9.9		10.7		10.5	[8]
log L_X/L_B	31.2		29.2	29.2		29.8		30.6	[8]
Galaxy structure:	NGC 2305	NGC 2307	NGC 4105	NGC 4106	IC 3290	NGC 4373	NGC 5090	NGC 5091	notes
Mean Eff. Surf. Bright. μ_e(B)	20.83±0.44	22.44 ±0.30	21.27±0.36	21.48±0.94	22.26±0.35	21.26±0.64	21.58±0.56	21.86±0.35	[2]
Average ellipticity $\langle\varepsilon\rangle$	0.29	0.07	0.25[4]	0.33	0.21	0.3[4]	0.15	0.60	[2]
$\langle P.A.\rangle$ $(\Delta P.A.)$ [deg]	142 (≈40)[4]		143 (<10)[4]	94.2 (≈50)[4]	22.5	38 (<10)[4]	109	122	
shape parameter [a4/a]	irr		irr	irr		disky			[4]
Kinematical parameters:	NGC 2305	NGC 2307	NGC 4105	NGC 4106	IC 3290	NGC 4373	NGC 5090	NGC 5091	notes
Hel. Sys. Vel. [km s^{-1}]	3241±20 [5]	3515±27	1912±23 [7]	2170±18 [7]	3342	3396	3421	3529	[1]
Vel.disp. σ_0 [km s^{-1}] stars	244		277±22[7]	253±17[7]		234±23	272±27		[3]
Pairs parameters:	RR 143		RR 210		RR 216		RR 242		
Arp-Madore ident.	AM0648-641		AM1204-292		AM1222-392				
Projected separation [arcsec] (kpc)	234 (51.1)		59 (7.7)		118 (25.7)		77 (17.2)		[6]
Δ V [km s^{-1}]	274		258		54		108		
Adopted distance [Mpc]	45		27		45		46		

[1] NED
[2] LEDA
[3] Hypercat http://www-obs.univ-lyon1.fr/hypercat
[4] Reduzzi & Rampazzo (1996)
[5] Rampazzo (1988)
[6] Reduzzi & Rampazzo (1995b)
[7] Longhetti et al. (1998b)
[8] The original ROSAT data published in Trinchieri & Rampazzo (2001) are converted to the 0.5 - 2 keV band and to H_0=75 km s^{-1} Mpc^{-1}.

2.2   Optical wide-field imaging

2.2.1   Observations

CCD imaging of all 4 galaxy pairs and their surrounding fields was obtained with the MPG/ESO 2.2 m telescope (shown in Figure 2.2) using the Wide Field Imager (WFI). The mosaic is composed of 8 EEV "CCD 44" type CCDs, each having 2048×4096 pixels. The pixel scale is 0.238 pixel^{-1} yielding a field-of-view of 34×33 arcmin^2. A single field centered on each galaxy pair was observed in Service Mode between Nov. 2001 and June 2004. Each field was observed in the Johnson-Bessell V and R bands (ESO filters V/89–ESO843 and Rc/162–ESO844) with total exposure times of 3000 s in both filters (see the Observing Log in Table 2.2). The observing conditions were generally photometric. Standard stars from Landolt (1992) were also observed each night in one or two reference CCDs. In order to fill the gaps between the CCDs, as well as to remove bad columns and cosmic ray hits, multiple 500 s images were recorded for each field. To this purpose, the images were suitably dithered in all cases except one (RR 143).

Table 2.2: Log-book of Wide Field Imaging observations.

Pair	Observing nights	Filter	Dithering	Exposure time [s]	Seeing [arcsec]	Airmass	Zeropoint [mag arcsec^{-2}]
RR 143	18-11-2001	V	N	6×500	0.7	1.22	24.19
RR 143	17-11-2001	R	N	6×500	0.7	1.22	24.53
RR 210	17-04-2002	V	Y	6×500	0.8	1.18	24.12
RR 210	22-01-2002	R	Y	6×500	0.7	1.03	24.48
RR 216	25-01-2002	V	Y	6×500	0.7	1.02	24.15
RR 216	17-04-2002	R	Y	6×500	0.7	1.08	24.44
RR 242	08-06-2004	V	Y	6×500	0.9	1.13	24.06
RR 242	08-06-2004	R	Y	6×500	0.9	1.05	24.41

2.2.2   Reduction and calibration

Reduction of the CCD mosaic data was accomplished with `IRAF`[2] using standard procedures. All multi-extension images were bias-subtracted and divided by twilight flat fields using the Mosaic reduction package `mscred` (Valdes 1998). Images were then astrometrically calibrated and registered onto a common distortion-free coordinate grid using `mscred` and the pipeline script package `wfpred` developed by our collaborators at the Padua Observatory. Astrometric calibration was done using the USNO Catalogue (Zacharias et al. 2000). The internal (image-to-image)

---

[2]`IRAF` is distributed by the National Optical Astronomy Observatories, which are operated by the Association of Universities for Research in Astronomy, Inc., under cooperative agreement with the National Science Foundation.

Figure 2.2: The MPG/ESO 2.2 m telescope dome (foreground) in La Silla, Chile.

astrometric precision is on the order of $0.1''$ while the systematic error of object coordinates is $\sim 0.2 - 0.3''$ reflecting the intrinsic accuracy of the USNO Catalogue.

Before co-addition all CCD images had their counts rescaled ("normalized") to match the photometric zero point of a reference CCD. We adopted CCD#2 as our reference frame and used the relative zero points of the eight CCDs determined by Rizzi (2003). All CCDs, once referred to a common zero point, were combined into a single 8000×8000 image in each band/exposure. All exposures were finally registered and median-combined to create a final image for each target, which covers an area of approximately $32' \times 32'$. In these images all CCD blemishes and gaps are cancelled out, except for RR 143. Figures 2.3, 2.5, 2.7 and 2.9 show the regions of the sky covered by the frames of RR 143, RR 210, RR 216 and RR 242, respectively.

Since the images in each dataset were taken consecutively under photometric sky conditions the median-combined images were calibrated by adopting the average airmass of each observation (see Table 2.2).

Photometric calibration was accomplished separately for each dataset using standard stars obtained on the same nights in order to monitor the nightly zero point variation using the reference CCD#2. A set of linear calibration relations was then computed for each night:

$$V = v' + a_V(V - R) + zp_V \tag{2.1}$$

$$R = r' + a_R(V - R) + zp_R \tag{2.2}$$

where v' and r' are the instrumental magnitudes normalized to 1 s exposure and corrected for atmospheric extinction. The following extinction coefficients were adopted: $k_V = 0.12$, $k_R = 0.09$.

The adopted colour terms of the calibration were $a_V = -0.140 \pm 0.013$ and $a_R = -0.004 \pm 0.016$, while the zero points zp_V and zp_R are those given in the last column of Table 2.2. The zero point uncertainties of the calibration relation are of the order of 0.03 mag in both V and R.

These relations were also used to calibrate the instrumental magnitudes in our photometric catalogues of the candidate member galaxies in the target fields (see Appendix A).

2.2.3   Surface photometry of the pair

Surface photometry of the 2 bright pair members was carried out with the ellipse fitting routine in the `STSDAS` package of `IRAF` and with the `GALFIT` package (Peng et al. 2002). The 2 programs are measuring the surface photometric parameters with different approaches.

Using `ELLIPSE`

The `ELLIPSE` task computes a Fourier expansion for each successive isophote (Jedrzejewski 1987), leaving the ellipticity, position angle and higher order Fourier coefficients free to vary. The higher order coefficients of the Fourier expansion determine the shape of the fitted ellipse, i.e. the isophote's deviation of a pure ellipse. The 3rd order coefficients a_3 and b_3 produce triangular deviations, e.g. egg-like shapes, but of special interest for the interpretation of the galaxy structure are the 4th order coefficients that produce so-called disky (positive values) or boxy (negative values) isophotes. Diskiness is an excess of light along the semi-major and minor axes, whereas the boxiness is a light deficit along the axes, in strong cases leading to the so-called peanut shape indicative of an accretion or merging event (Dettmar & Luetticke 1999). The isophotal shape is directly related to the stellar orbits, playing a significant role in merger and accretion models. The disky- or

boxyness of isophotes can reveal structures that are not detectable by eye, but can give important clues to the galaxy's formation history.

The integrated intensity along the fitted ellipse is measured and output together with the other parameters. The next isophote is then fitted with the values of the previously fitted isophote which is closest in semi-major axis length to the current one. This procedure will be continued until the signal-to-noise ratio falls below a given value, a certain semi-major axis length or the edge of the image is reached. The resulting radial profiles of surface brightness, ellipticity, position angle, higher order coefficients (a_3, b_3, a_4, and b_4) and $(V - R)$ colour are plotted in Figures 2.4, 2.6, 2.8 and 2.10.

Using `GALFIT`

`GALFIT` is fitting a two dimensional model to the galaxy image. Various components with various types of profiles can be fitted at the same time, so it can be used to perform a bulge-disk decomposition, if needed. In our case a one component Sersic profile was fitted to the galaxy images. The Sersic profile is a generalisation of the de Vaucouleurs law with $\mu(r) \sim r^{1/n}$, where the Sersic parameter n is a free parameter (Sersic 1968). This structural parameter is dependent on galaxy type and mass, declining towards lower masses in spherical systems, whereas disk-dominated galaxies show an exponential decline ($n \sim 1$). This profile is thus sensitive to structural differences between different kinds of bulge-dominated galaxies, providing a better fit to real galaxy profiles (see also Section 4.4).

2.2.4   Signatures of interaction

Two methods were used to search for fine structure and signatures of interaction.

First, a model of the elliptical in each pair was derived from the `ELLIPSE` output using the `BMODEL` task and subtracted from the original image. This method is of course very sensitive to the quality of the ellipse fitting procedure. Residuals can be caused for example by foreground stars projected close to the galaxy center, that are difficult to mask out, or by light contamination from a close companion.

To cross-check the presence of residual structure, a second and completely different approach was used: the image was convolved with an elliptical Gaussian function, yielding an unsharpened version of the image which was then subtracted from the original image. The crucial point with this method is to find the appropriate width of the Gaussian function. it should be wide enough to reveal the small scale variations we are searching for but not too wide to account for the large scale variations in the profile. Different widths between 5 and 15 pixels were used.

The output of both methods can be seen in Figures 2.3, 2.5, 2.7 and 2.9 together with the WFI-frames around the pairs.

2.2.5   Detection of diffuse light around the pairs

Galaxy encounters may lead to the stripping of a significant amount of stellar material form the involved galaxies into the intergalactic space. The presence of this diffuse optical light is an evidence for the past extensive interaction between the group members and their dynamical evolution. The shape and distribution of the diffuse light can help to determine the timescales of this co-evolution: irregular shapes and individual plumes indicate a more recent interaction event than the presence of a smooth halo around the group members (see eg. Da Rocha & Mendes de Oliveira 2005).

A search for optical diffuse light and larger-scale structures around the pairs was carried out with the `SourceExtractor` (see also Section 4.1). All sources detected as "object" were masked yielding a background-only image where large-scale diffuse light becomes visible. This procedure is very sensitive to errors in the background determination which, in our case, are caused by the gaps between individual CCDs (for RR 143) or the presence of bright foreground stars (for RR 242).

The most important parameter for this procedure is the background mesh size. If it is too small, the structures and variations we search are subtracted with the background. So, unlike for the object detection, were small scale background variations should be subtracted for an accurate photometry, here a large mesh size, at least 256 pixels should be chosen.

The typical background fluctuations were used to estimate upper limits above which diffuse light becomes undetectable in our observations. The background level was estimated in 10 squares of 20×20 pixel across the images. This procedure yielded RMS values of $\sim 0.3\,\%$ - $1\,\%$ for the different fields. From this values we determined the following limits in mag arcsec^{-2} for the 4 frames: 25.8 for RR 143, 25.4 for RR 210, 26.5 for RR 216 and 25.9 for RR 242.

The surface brightness of the last detected isophote of the E and its semi-major axis are 25.45 ± 0.01 mag arcsec^{-2} at 64 kpc (RR 143), 25.48 ± 0.01 mag arcsec^{-2} at 38 kpc (RR 210), 26.39 ± 0.02 mag arcsec^{-2} at 137 kpc (RR 216) and 24.85 ± 0.01 mag arcsec^{-2} at 65 kpc (RR 242). These values are close to the detection limit determined from the background fluctuations, apart from RR 242, where a bright foreground star close to the pair inhibits a deeper detection.

Table 2.3: Parameters of the `GALFIT` model of the E pair members.

ID	m_R [mag]	n	r_e ['']	r_e^1 [kpc]	μ_0	μ_e [mag arcsec^{-2}]	q [2]	c [3]
RR 143a	10.55	6.2	47.6	13	9.2	22.3	0.79	0.05
RR 210a	9.48	6.5	95.2	13	9.1	22.8	0.85	-0.04
RR 216b	9.52	8.0	154.7	33	6.8	23.9	0.71	0.18
RR 242a	9.30	7.5	404.6	98	9.8	25.7	0.72	0.13

[1] computed with $H_0 = 67$ km s^{-1} Mpc^{-1}.
[2] axis ratio $q = b/a$.
[3] disky/boxiness parameter c.

2.3 Results

All the physical sizes given in this chapter are computed with $H_0 = 67$ km s^{-1} Mpc^{-1}.

2.3.1 Optical surface photometry

RR 143

The WFI image of RR 143 is shown in Figure 2.3 together with a close-up of the pair after the subtraction of an isophotal model of the elliptical to reveal possible fine structure.

Surface photometry of RR 143a is shown in Figure 2.4. Unfortunately the non-dithered frames of this object introduce large errors in the isophotal fit especially from about 1.5' onwards. The isophotal ellipticity was fixed at $\epsilon = 0.3$ in order to extend the fit despite the large area masked by the gaps. This may lead to an overestimation of the surface brightness at the outskirts of the galaxy with resultant overestimation of the structural parameter n. However the surface brightness profile shows evidence for a flat outer slope indicating large n. The model obtained with `GALFIT` gives $n = 6.2$ with an effective radius of $r_e \sim 50''$ (13 kpc). The boxiness of the inner isophotes noted by Reduzzi & Rampazzo (1996) can be confirmed out to $\sim 20''$ (5 kpc) whereas the shape of the subsequent isophotes is certainly affected by the presence of a foreground star $\sim 50''$ from the center of RR 143a. This star is also responsible for the bump in the $(V - R)$ colour profile as well as for the residuals in the model-subtracted image in Figure 2.3. A shell-like feature can be seen in the residual image while the unsharp-masked image shows no signatures of fine structure. We conclude that apart from a maximum 2% boxiness of the inner

isophotes no fine structure is present in RR 143a.
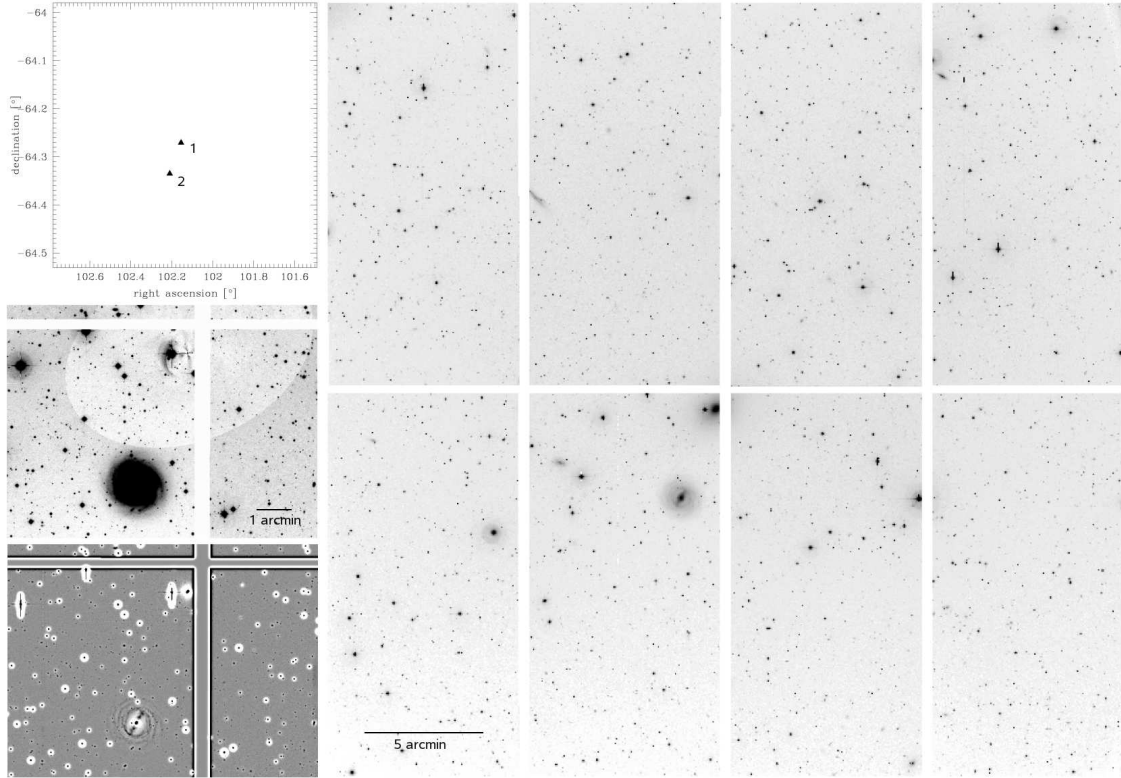
Figure 2.3: The WFI field of RR 143. Small panels: top: galaxies with similar redshift in the WFI field, labelled as in Table 2.4; middle: residual image after subtraction of a galaxy model for the E member of the pair, constructed with BMODEL from the ELLIPSE output; bottom: residual image after subtraction of a Gaussian-convolved image to reveal fine structure. Notice the gaps between the CCDs due to the missed dithering of this field.

RR 210

Figure 2.5 shows the interacting pair RR 210 and its environment. Obvious inter-action induced features are seen, especially in RR 210b. The Gaussian smoothed image reveals tidally disturbed arms, a possible bar-like structure and fine structure also in the E pair member RR 210a. The latter feature is probably caused by a dust-lane: dust filaments surround the core of RR 210a at a radius of $\sim 15''$ (2 kpc) and extend out to $\sim 30''$ (4 kpc) on the NW side. Other features in the model subtracted image probably belong to the highly perturbed RR 210b which can be argued to be in the foreground. No shell structure is detected in the elliptical.
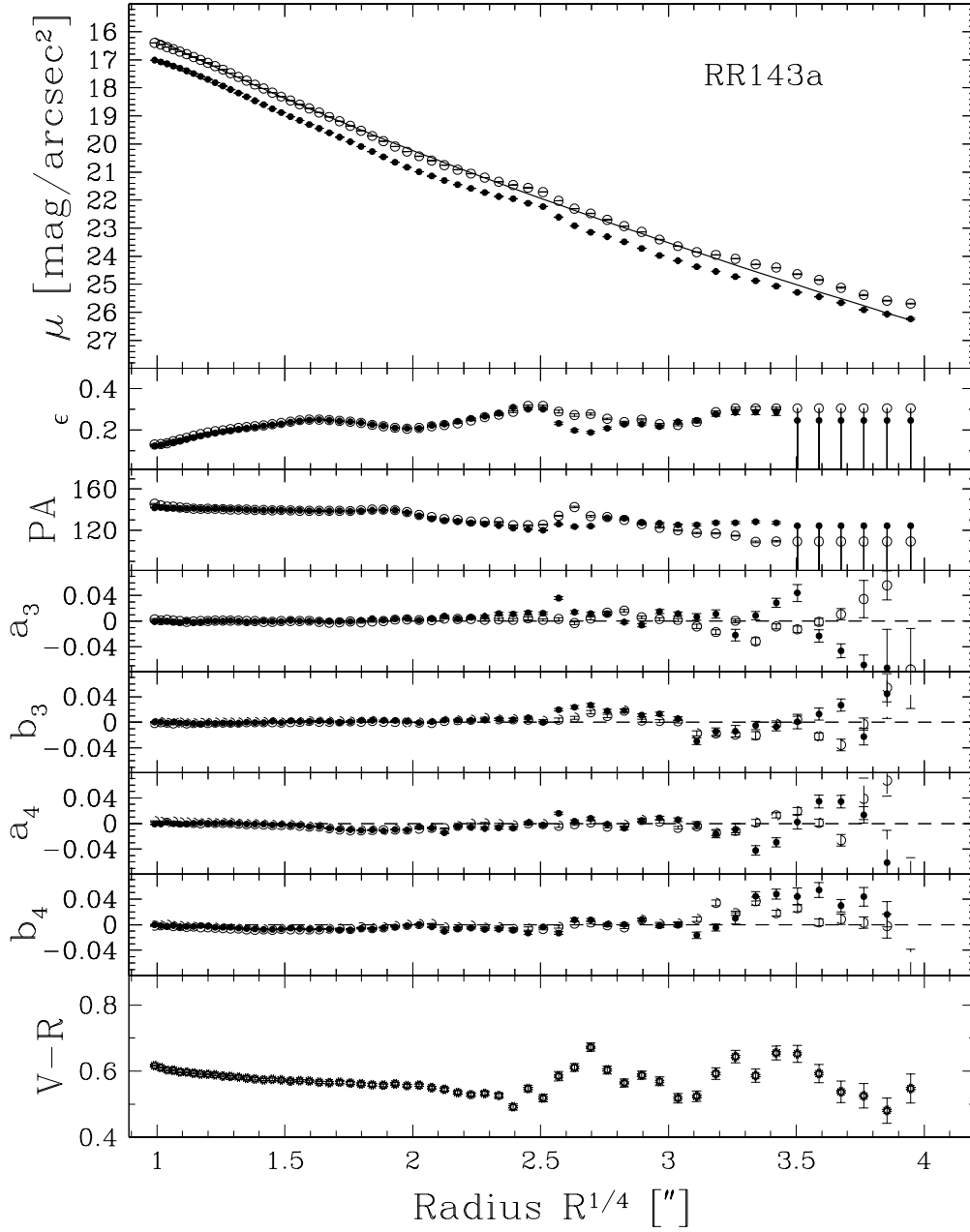
Figure 2.4: Surface photometric profiles of the E member of RR 143 in R (open symbols) and V (filled symbols). The solid line is the surface brightness profile of the GALFIT model. From top to bottom: surface brightness μ, ellipticity ϵ, position angle PA, coefficients of the Fourier expansion a_3, b_3, a_4, b_4 and $(V - R)$ colour profile.
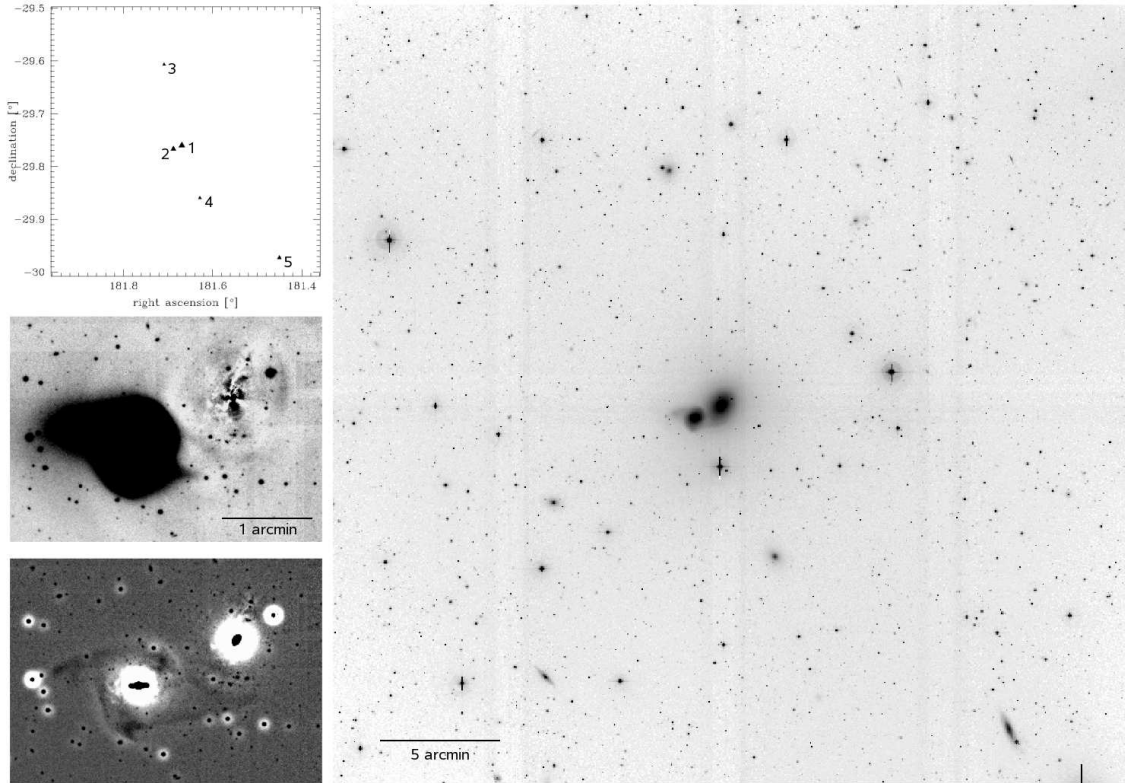
Figure 2.5: The WFI field of RR 210. Small panels: top: galaxies with similar redshift in the WFI field, labelled as in Table 2.4; middle: residual image after subtraction of a galaxy model for the E member of the pair, constructed with BMODEL from the ELLIPSE output; bottom: residual image after subtraction of a Gaussian-convolved image to reveal fine structure.

The surface brightness profile for RR 210a is not well fit with a single component model, most likely due to the presence of RR 210b. At $\sim 40''$ (6 kpc) light contamination from the neighbour becomes dominant. The outer halo of the elliptical seems to be disturbed, the ellipticity drops instead of raising continuously, on the other hand the PA of the isophotes starts to increase. The pair seems to be embedded in a common stellar halo, indicating that the close encounter between this pair is not an unbound encounter. We find no evidence for substructure in the extended halo surrounding the pair.

RR 216

Surface photometry of the elliptical RR 216b (Figure 2.8) reveals homogeneous profiles out to a radius of about $80''$ (19 kpc) with smoothly decreasing μ and $(V-R)$ colour, slightly increasing ϵ and constant position angle and Fourier coefficients. In
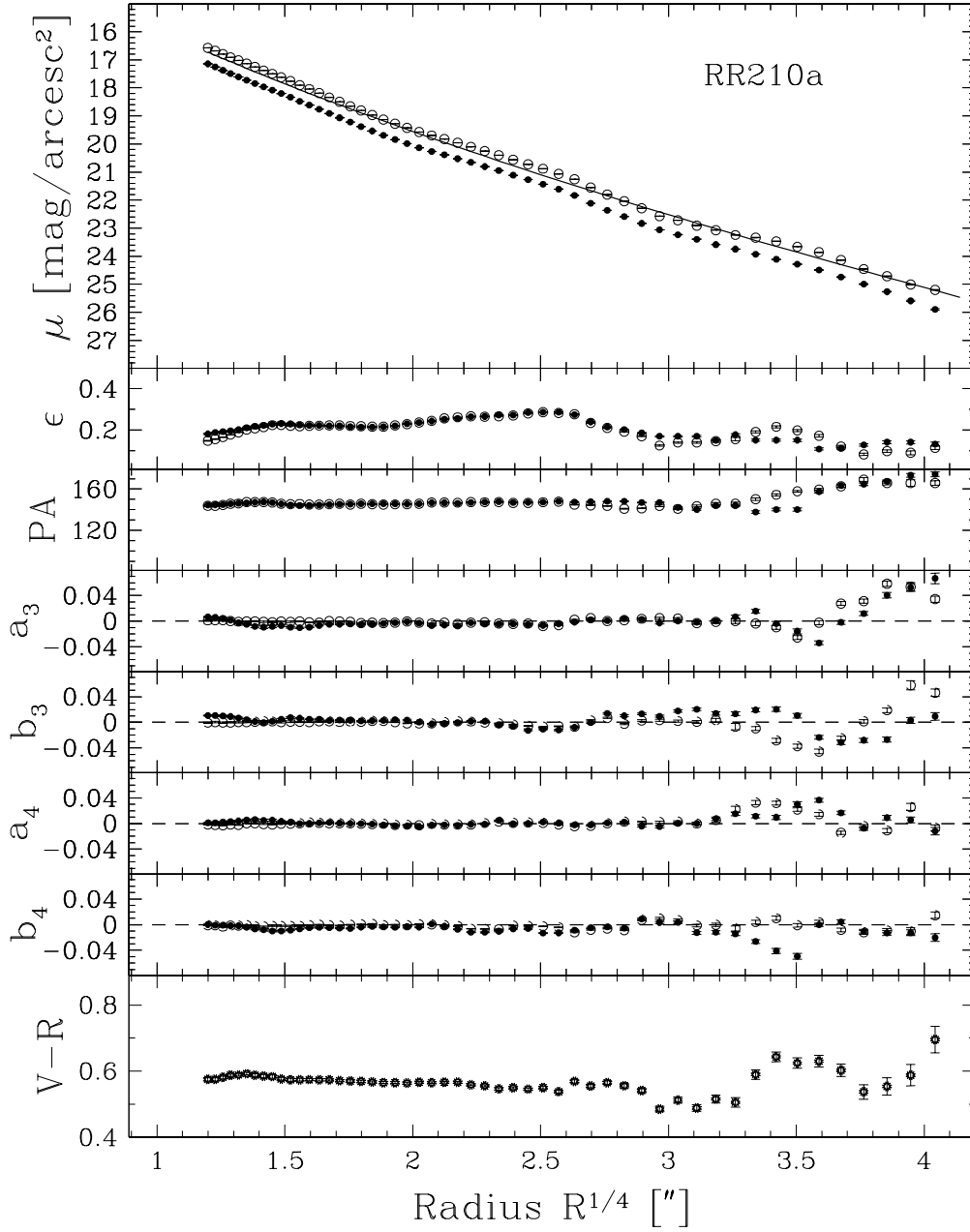
Figure 2.6: Surface photometric profiles of the E member of RR 210 in R (open symbols) and V (filled symbols). The solid line is the surface brightness profile of the GALFIT model. From top to bottom: surface brightness μ, ellipticity ϵ, position angle PA, coefficients of the Fourier expansion a_3, b_3, a_4, b_4 and $(V - R)$ colour profile.
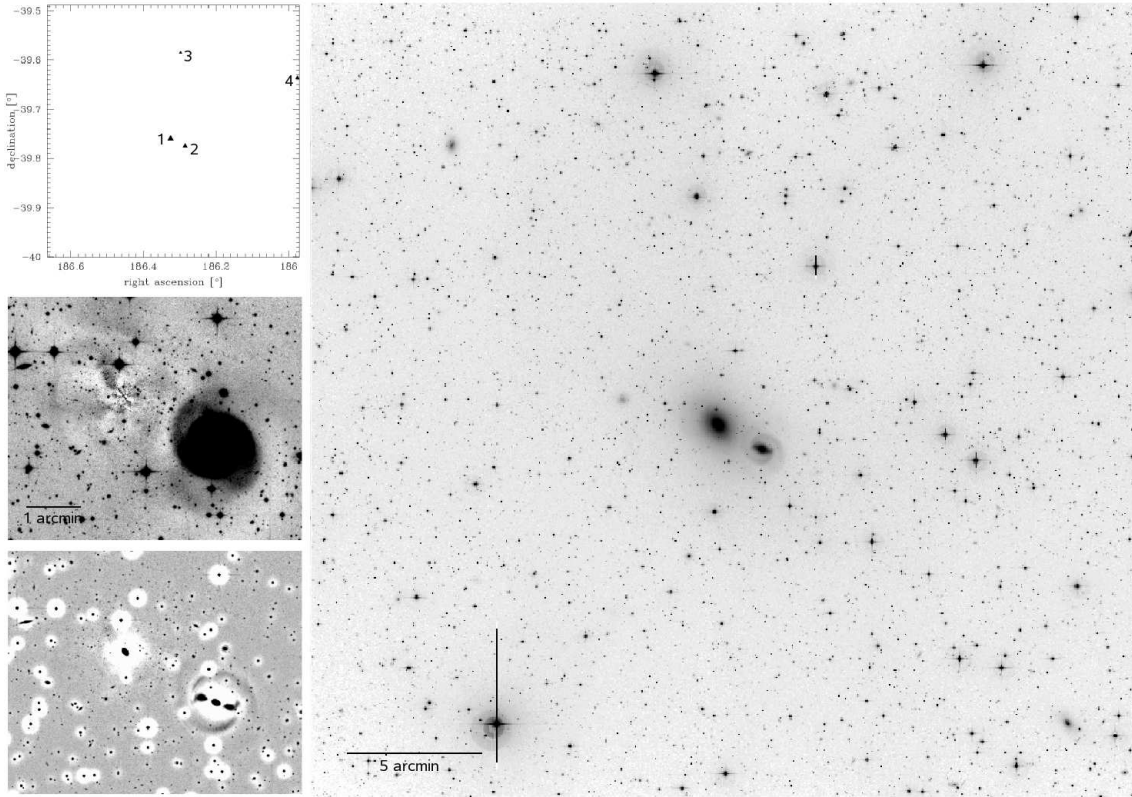
Figure 2.7: The WFI field of RR 216. Small panels: top: galaxies with similar redshift in the WFI field, labelled as in Table 2.4; middle: residual image after subtraction of a galaxy model for the E member of the pair, constructed with BMODEL from the ELLIPSE output; bottom: residual image after subtraction of a Gaussian-convolved image to reveal fine structure.

the galaxy's outer parts ($\sim 1.5'$, 20 kpc) the surface brightness profile becomes very flat. It is best fit with a very high value of $n = 8$ and an extended $r_e \sim 150''$ (33 kpc). This flattening coincides with strong boxiness of the isophotes (more than 5%) and an increased ellipticity. This may argue for the presence of a second physically distinct component of diffuse stellar light surrounding the pair. However a large value of n is also needed to model the central part of RR 216b and the one component fit is a good representation of the surface brightness profile over $\sim$8 magnitudes.

Evidence for recent interaction is detected in the model subtracted image in Figure 2.7, revealing a ripple east of the center at a radius of about $80''$ ($\sim$20 kpc) and an asymmetric excess of light along the major axis (North). One of the grand design spiral arms in RR 216a shows a sharp bend towards the elliptical. The homogeneous colour profile throughout the pair (first reported by Reduzzi & Rampazzo (1996))
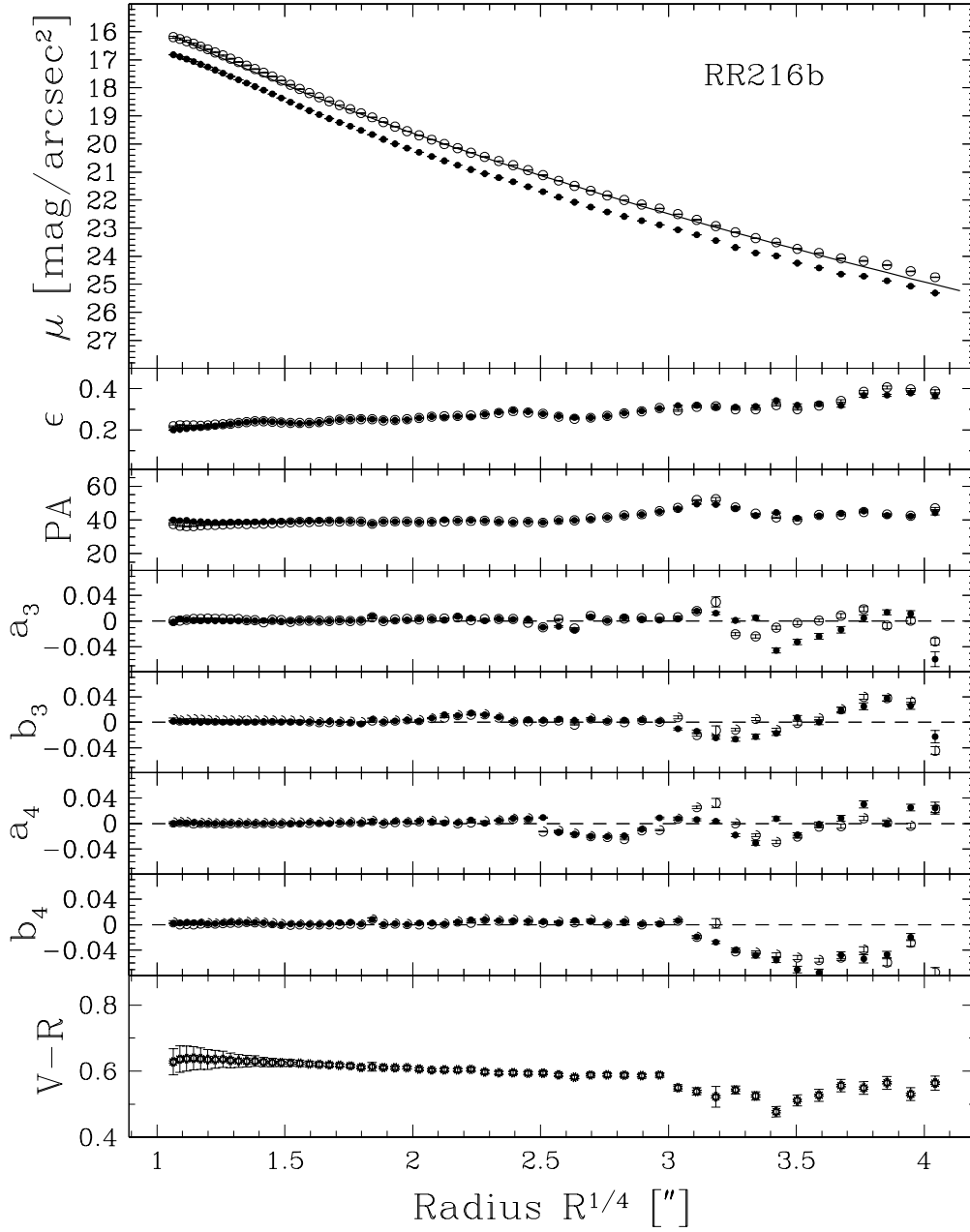
Figure 2.8: Surface photometric profiles of the E member of RR 216 in R (open symbols) and V (filled symbols). The solid line is the surface brightness profile of the GALFIT model. From top to bottom: surface brightness μ, ellipticity ϵ, position angle PA, coefficients of the Fourier expansion a_3, b_3, a_4, b_4 and $(V - R)$ colour profile.

argues for RR 216a not being a true spiral but probably an early-type galaxy with tidally excited arms (tails).
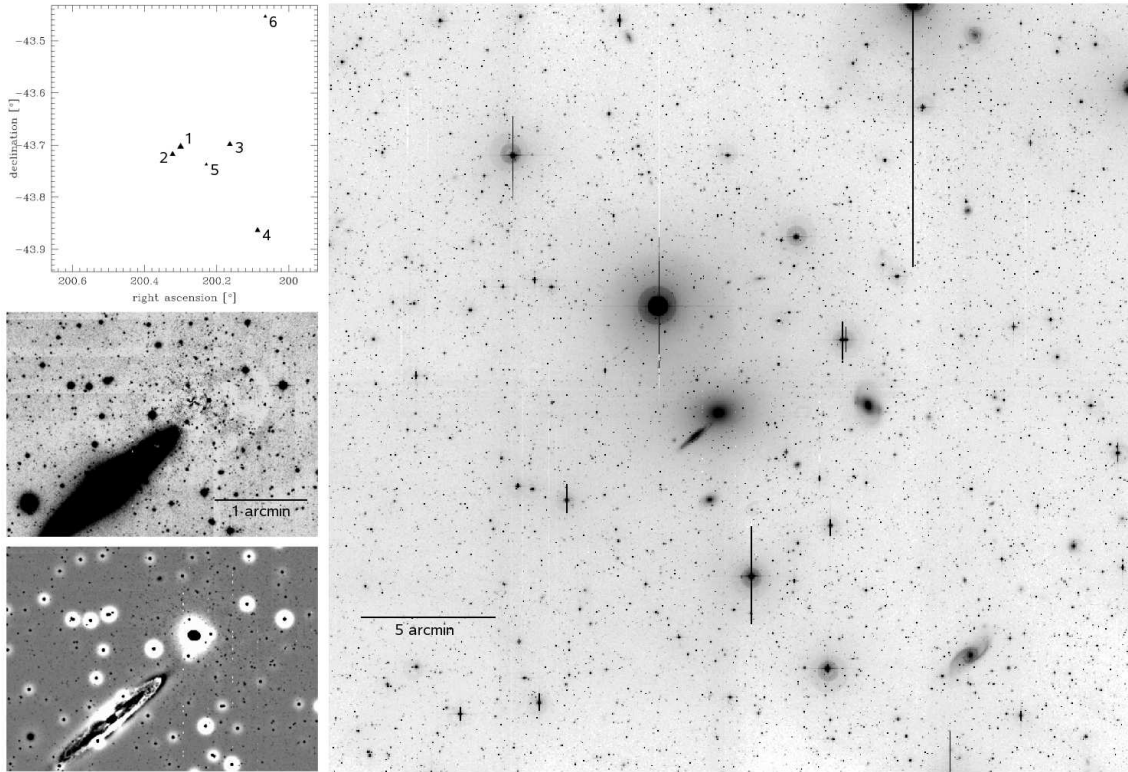
Figure 2.9: The WFI field of RR 242. Small panels: top: galaxies with similar redshift in the WFI field, labelled as in Table 2.4; middle: residual image after subtraction of a galaxy model for the E member of the pair, constructed with BMODEL from the ELLIPSE output; bottom: residual image after subtraction of a Gaussian-convolved image to reveal fine structure.

RR 242

The surface brightness profile of the bright elliptical RR 242a is well represented by a Sersic law with a high $n = 7.5$ and a very extended $r_e \sim 400''$ (98 kpc), a value typical for bright cluster ellipticals. Residuals of the one component fit point toward the presence of a second physically distinct component representing the outer extended halo of the galaxy. Of course the outer slope may be affected by a bright foreground star that can bias n towards a higher value. However, the central part of RR 242a shows a luminosity excess, redder colour and flattening of the profile towards the center (coinciding with a change in position angle). This is due to a circumnuclear disk of absorbing material that is also responsible for variations in
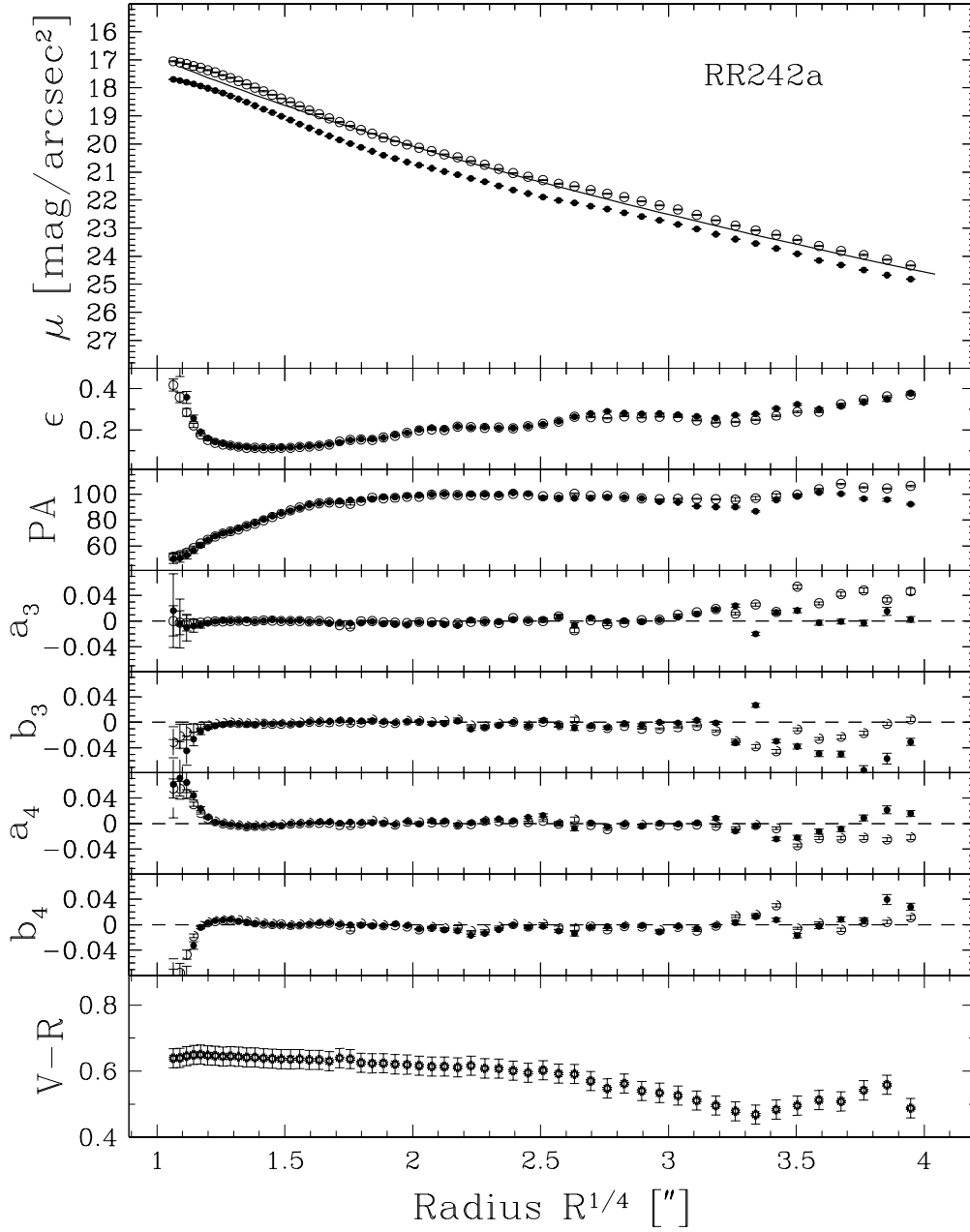
Figure 2.10: Surface photometric profiles of the E member of RR 242 in R (open symbols) and V (filled symbols). The solid line is the surface brightness profile of the GALFIT model. From top to bottom: surface brightness μ, ellipticity ϵ, position angle PA, coefficients of the Fourier expansion a_3, b_3, a_4, b_4 and $(V - R)$ colour profile.

the other profiles in the central part (within 2-3″ radius). The visible extension of
the disk is $\sim 2''$ (0.5 kpc). This nuclear disk has the same position angle as the
spiral RR 242b which shows an asymmetric dust distribution in its disk with more
absorbing material on the side towards RR 242a (see Figure 2.9, *bottom left*). We
therefore argue that material transferred (cross-fuelled) from the spiral to the center
of the elliptical is assembled in a central disk and may be responsible for fuelling
the AGN in RR 242a.

No signatures of fine structure were found in this pair. RR 242a appears to be an
old and unperturbed system sharing some photometric characteristics with bright
cluster ellipticals.

2.3.2   Diffuse stellar light

Diffuse light was detected only in RR 216 (Figure 2.11). An extended plume emerges
from the north side of the galaxy and curves towards the east and southeast. The
plume is detected out to a radius of about $4'$ (56 kpc) from the center of the elliptical
and spans more than $8'$ ($\sim$110 kpc) in projection. To quantify the significance of
this detection we compared the typical background fluctuation in this field (see
above) with the excess light of the plume. The detection limit for this field was
determined to be in the order of 0.3 %, while the intensity of the plume exceeds the
mean background value by ~ 3 % corresponding to a surface brightness of ~ 24 mag
arcsec^{-2}. This feature represents clear evidence for recent or ongoing interaction in
this system, either between the pair members or with a fainter companion.

All the ellipticals of the 4 pairs show very high Sersic indices between 6 and 8, i.e.
larger than the typical $n = 4$. This values are more typical of bright cluster ellipticals
and not of galaxies in LDEs. The highest Sersic parameter, which means the flattest
profile, has RR 216b with $n = 8$, whereas RR 242 shows the largest effective radius.
The profile of RR 210 shows that the outer halo has a slightly different isophotal
ellipticity and position angle relative to the main body of the galaxy, indicative of
a distinct extended halo around the galaxy. Although such extended halos appear
to be connected with the presence of diffuse light (see e.g. Gonzalez et al. 2005) we
did not detect such emission in our data.

We also examined $40' \times 40'$ fields around the 4 pairs using the POSS II digital
R-band images. Low-pass median filtering of the images revealed in all cases the
existence of a faint, spatially extended envelope which appears roughly symmetrical
around the ETG. The largest envelope was found for the early-type component in
RR 216 with a diameter of about 120 kpc (consistent with the high n obtained by
GALFIT). In this context it is interesting to note that two of the most isolated ETGs,
with luminosity and distance comparable to our pairs, do not show such extended
envelopes (Verdes-Montenegro et al. 2005; Sulentic et al. 2006).
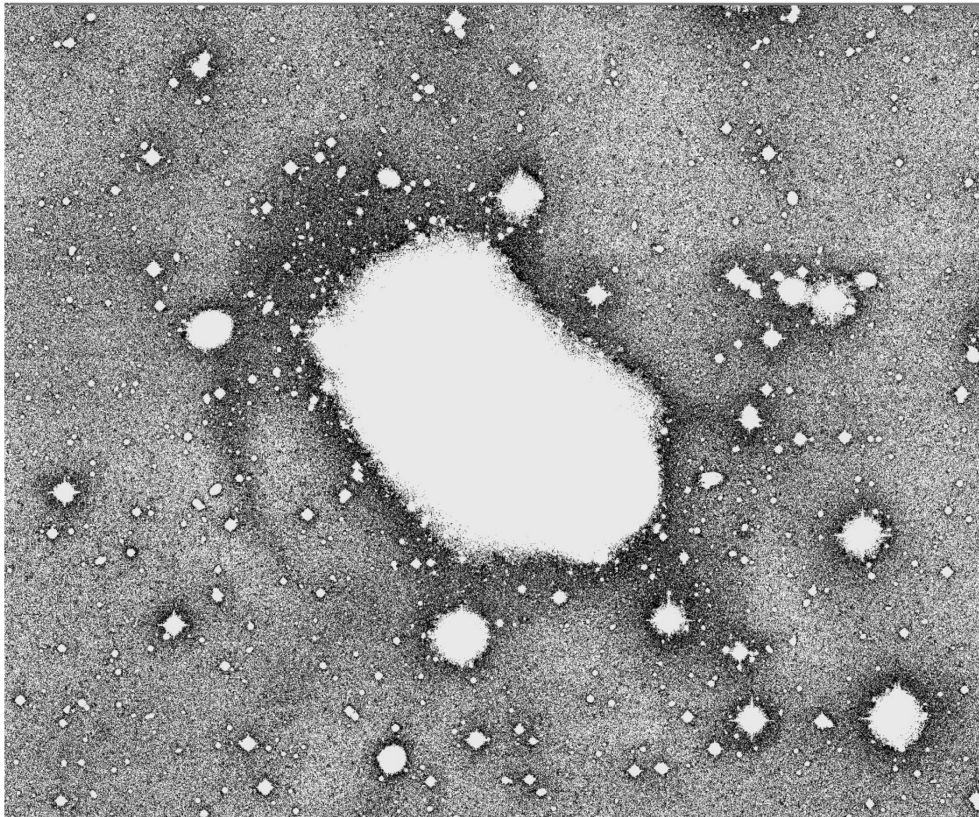
Figure 2.11: Extended plume detected around RR 216. The white part in the center is the pair, not only the elliptical. White regions are masked pixels (detected as belonging to an object by `SExtractor`). The image is inverted, i.e. dark regions are brighter. The curved structure in the NE is clearly visible. Most probably it is stellar material "lost" by a companion or torn out of the elliptical during a past interaction.

2.3.3 Quantification of interaction signatures with Σ

Neither signatures of interaction nor fine structure are found in the elliptical pair members of RR 143 and RR 242 (NGC 2305 and NGC 5090 respectively), they appear to be relaxed systems. Consistently also the spirals of this 2 pairs lack any evidence for perturbations.

The ETGs in RR 210 and RR 216 display unambiguous signatures of recent interaction with the presence of fine structure. An extended dust-lane is observed in NGC 4105, whereas ripples and plumes were detected in NGC 4373 after model subtraction.

The presence of fine structure can be quantified with the parameter Σ (see e.g. Sansom et al. 2000, and reference therein). This parameter is an empirical measure

of the optical disturbance present in a galaxy. It is not an objective way of measure, since it relies on the visual impression of the observer. Nevertheless it provides a good estimation of the dynamical state of a system. The value of Σ was defined by Schweizer et al. (1990) as:

$$\Sigma = S + \log(1 + N) + J + B + X \qquad (2.3)$$

where S is the optical strength of the most prominent ripple ($S = 0 - 3$), N the number of detected ripples, J the number of plumes or jets, B is an estimation of the maximum boxiness of the isophotes ($B = 0 - 3$) and X gives the absence or presence of an X-structure ($X = 0$ or 1).

The higher the value of Σ the higher the morphological disturbance and the probability that the galaxy is *dynamically young*. We estimate a value of $\Sigma = 0$ for NGC 2305 and NGC 5090 and conservatively $\Sigma = 1$ (dust) and $\Sigma = 3.5$ (ripple, plume and boxy isophotes) for NGC 4105 and NGC 4373 respectively. The Σ values of NGC 2305 and NGC 5090 are both indicative of the "relaxed" nature of these galaxies, while NGC 4105 and in particular NGC 4373 seem to be in a considerably less relaxed state.

2.4   The environment

The environment of the 4 pairs was investigated using the NASA Extragalactic Database (NED). We searched for galaxies with comparable redshifts in the *local environment* of each pair, i.e. inside a radius of 20′ (corresponding more or less to the area covered by the WFI field). This local sample is complemented by galaxies in the *large-scale environment*, i.e. within a radius of 90′ from the E pair member. This large-scale radius is a typical radius for poor groups of galaxies at the pair's distance (corresponding to > 1 Mpc) and was already chosen by other authors (see eg. Zabludoff & Mulchaey 1998). In radial velocity space the galaxies should be separated by less than 1000 km s^{-1} from the mean pair velocity. This group membership criterion is motivated by the typical velocity dispersion of poor groups of galaxies (~ 300 km s^{-1}) and was used by numerous previous authors to define group memberships (see eg. Hickson et al. 1992).

The properties of galaxies found within these radii are given in Table 2.4 for the local environment and in Table 2.5 for the large-scale environment. The respective physical distances covered by this search radii are also quoted in the respective table for the respective pair.

The different environments of the 4 pairs are shown in Figure 2.12. Galaxies are plotted with their morphological type quoted in NED. If no classification was available a question mark was used as plot-symbol. RR 143 resides in a significantly
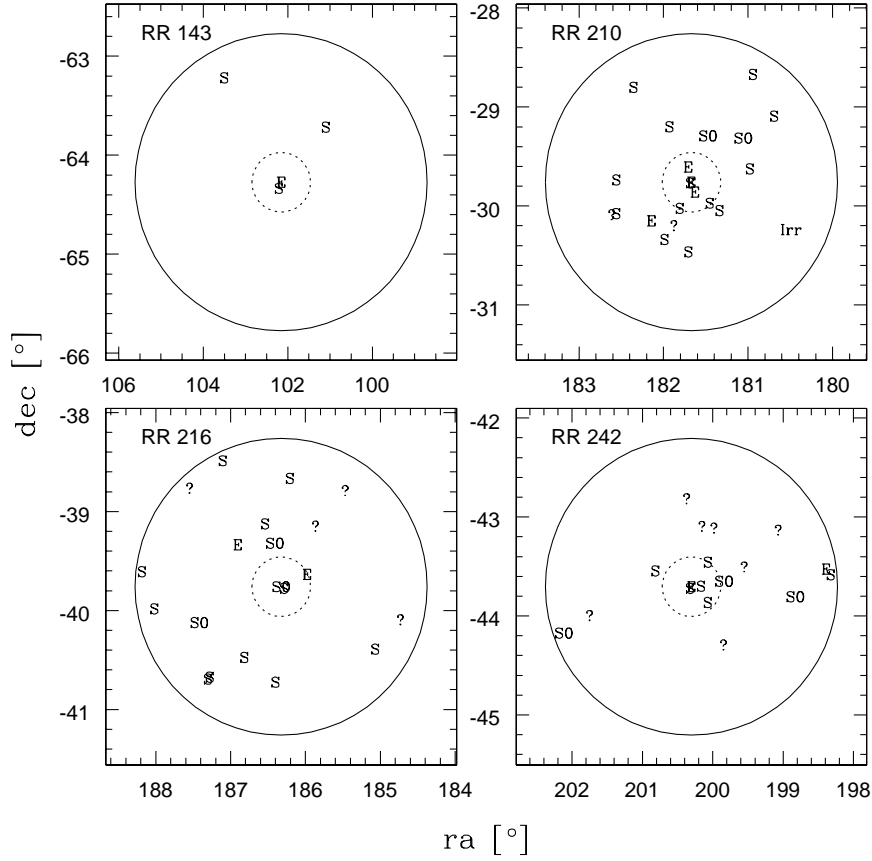
Figure 2.12: The environment of the 4 galaxy pairs. The solid circle indicates the $90'$ radius of the large-scale environment, the dotted circle shows the $20'$ radius of the local environment representing more or less the WFI-field of view. Galaxies are plotted with their morphological type given in NED. If no type was quoted in NED a ? is used as plot symbol.

sparser environment than the other 3 pairs. Only two other spirals are associated to this pair. The other 3 pairs are embedded in loose groups of about 20 members. RR 210 is situated in the most dense environment of all groups. However, it should be noted that RR 210 is significantly closer (~ 2000 km s^{-1}) than the other 3 pairs (~ 3500 km s^{-1}). Due to this closer distance the number of galaxies with available redshift in NED is most probably higher than in the other pairs.

The galaxies in RR 216 seem to be equally distributed over the investigated area without showing any central concentration towards the pair. This pair is located in a different large-scale environment in the vicinity of the Hydra-Centaurus Cluster at

Table 2.4: Galaxies within the WFI fields (search radius $20'$) with similar radial velocities. All data in this table is taken from NED.

ID	m_R [mag]	v_{rad} [km s^{-1}]	type	a[1] [']	d[2] [']	label
RR 143: search radius $20'$ ($= 281$ kpc)						
NGC 2305 (RR 143a)	10.98	3241±20	E2: pec	2.0	0.0	1
NGC 2307 (RR 143b)	11.76	3515±27	SB(rs)ab	1.7	4.0	2
RR 210: search radius $20'$ ($= 169$ kpc)						
NGC 4105 (RR 210a)	9.53	1912±23	E3	2.7	0.0	1
NGC 4106 (RR 210b)	12.36[3]	2170±18	SB(s)0+	1.3	1.0	2
2MASX J12063106-2951336	14.60	2198± 7	E	0.8	6.3	3
2MASX J12065029-2936236	15.30[3]	2019± 0	E	0.9	9.4	4
!! IC 2996	13.28	2256± 5	S	1.5	17.0	5
IC 3005	12.71	1724± 2	SBcd	2.3	17.4	−
RR 216: search radius $20'$ ($= 275$ kpc)						
NGC 4373 (RR 216b)	10.90	3396±18	SAB(rs)0−	3.4	0.0	1
IC 3290 (RR 216a)	11.43	3342±44	SB(s)a	1.7	1.9	2
6dF J1225118-393507	16.30	2140± 0	−	−	10.5	3
ESO 322-IG 002	14.23	3264± 0	E?	0.5	17.6	4
RR 242: search radius $20'$ ($= 272$ kpc)						
NGC 5090 (RR 242a)	10.84	3421± 21	E2	2.9	0.0	1
NGC 5091 (RR 242b)	12.43	3529±145	Sb pec sp	1.8	1.3	2
NGC 5082	12.05	3896± 42	SB(r)0+	1.7	5.9	3
NGC 5090B	12.71	4248± 8	SAB(rs)ab	1.9	13.9	4
ESO 270- G 001	15.57	2960±100	E	0.3	3.7	5
2MASX J13201668-4327195	16.43[3]	3067± 7	Sbc	0.8	18.1	6

[1] semi major axis of the object.
[2] projected distance from the E.
[3] B band magnitude.

$\sim 5°$ from the cluster center. Also in redshift space this group is embedded in a richer environment with a foreground group at ~ 2100 km s^{-1}. The faint 6dF J1225118-393507 (Nr. 3 in Table 2.4) was first considered a member of the group around RR 216 but then found to belong most likely to this foreground structure, which is separated by more than 1000 km s^{-1} from the pair. This object is therefore not further considered in the analysis of group properties (Chapter 6) and is not plotted in Figure 2.12.

Table 2.5: Galaxies in a larger scale environment (search radius $90'$) with similar radial velocities. All data in this table is taken from NED.

ID	α (2000)	δ (2000)	M_R [mag]	v_{rad} [km s^{-1}]	type	a[1] $[']$	d[2] $[']$	label
RR 143: search radius $90'$ (= 1.26 Mpc)								
NGC 2297	06 44 24.6	-63 43 02	12.31	3242±28	SAB(rs)b	1.4	43.4	3
ESO 087- G 050	06 54 00.0	-63 13 08	14.70	3538±10	Sc	1.8	72.6	4
RR 210: search radius $90'$ (= 0.76 Mpc)								
2MASX J12052132-3002465	12 05 21.3	-30 02 46	16.40[3]	2016± 0	Sp	0.7	24.3	7
6dF J1207305-301156	12 07 30.5	-30 11 56	16.00	2534± 0	−	−	28.4	8
IC 0760	12 05 53.5	-29 17 31	12.05	2226±25	S0	1.7	29.9	9
2MASX J12083457-3008549	12 08 34.5	-30 08 55	16.00[3]	2157±24	E	0.5	33.9	10
ESO 441- G 004	12 07 43.6	-29 11 58	15.20	2318± 0	SB	1.1	36.3	11
MCG -05-29-004	12 03 55.2	-29 37 29	15.50[3]	2138± 0	SB	0.6	36.9	12
IC 3010	12 07 57.4	-30 20 22	11.68	1982±12	SAB(s)0/a	1.9	38.5	13
2MASX J12041324-2918486	12 04 13.3	-29 18 49	16.2[3]	2003± 0	S0	0.8	41.8	14
6dF J1206496-302745	12 06 49.6	-30 27 45	16.3[3]	2295± 0	Sp	0.9	42.2	15
IC 0764	12 10 14.2	-29 44 13	11.90	2132± 3	SA(s)c	4.8	46.3	16
ESO 441- G 014	12 10 14.1	-30 04 41	13.89	2146± 8	S	2.1	50.0	17
AM 1207-294 NED02	12 10 27.2	-30 05 21	15.00[3]	2164±81	−	0.4	52.9	18
ESO 440- G 044	12 02 46.4	-29 05 33	13.20	2198± 2	SB(s)m pec	1.6	64.9	19
ESO 440- G 039	12 01 57.9	-30 14 13	14.97	2045 ±71	IB(s)m	1.6	67.6	20
ESO 441- G 011	12 09 25.2	-28 48 06	14.78	2136± 4	Scd	2.1	67.8	21
6dF J1203467-284015	12 03 46.7	-28 40 15	16.50[3]	1907± 0	Sp	0.5	75.6	22
RR 216: search radius $90'$ (= 1.24 Mpc)								
NGC 4373A	12 25 37.7	-39 19 11	11.42	2935±32	SA0+: sp	2.6	26.7	4
IC 3370	12 27 37.3	-39 20 16	10.39	2930±24	E2-3	2.9	36.9	5
ESO 322- G 009	12 26 09.8	-39 07 26	12.88	3576± 7	SB(rs)b	1.6	39.4	6
ESO 321-IG 028	12 23 28.0	-39 08 56	13.26	3072±35	2 obj.?	0.4	42.3	7
ESO 322- G 011	12 27 16.1	-40 28 28	13.58	3242±56	S	1.1	48.5	8
2MASX J12294019-4007220	12 29 40.2	-40 07 22	17.71[3]	3112±22	S0	0.2	54.8	9
ESO 322- G 007	12 25 36.3	-40 43 29	14.62	3197± 9	SB(s)m	1.4	58.0	10
MCG -06-27-023	12 24 50.0	-38 39 54	15.00[3]	3399± 0	SAB(r:)ab	0.6	65.9	11
ESO 321- G 021	12 20 16.2	-40 23 27	12.07	3189± 0	Sc	1.2	69.0	12
ESO 322- G 019	12 29 07.2	-40 40 24	13.60	3100±10	SB(s)cd sp	1.5	70.2	13
ESO 321- G?026	12 21 52.5	-38 47 23	14.15	3115±10	Galaxy?	1.9	70.5	14
ESO 322- G 020	12 29 12.8	-40 41 31	13.12	3423±59	SB(rs)d	1.3	71.7	15
2MASX J12185570-4005358	12 18 55.7	-40 05 36	14.20[4]	3195± 0	−	0.5	75.9	16
NGC 4499	12 32 04.9	-39 58 57	12.20	3729±42	SB(rs)b	1.8	79.2	17
2MASX J12301164-3845537	12 30 11.6	-38 45 54	13.07[5]	3483± 0	−	0.4	82.4	18
ESO 322- G 017	12 28 25.0	-38 29 14	14.38	3398± 0	Sc	1.6	84.5	19
ESO 322- G 024	12 32 44.5	-39 36 31	15.20	3157± 0	S	1.0	86.4	20
RR 242: search radius $90'$ (= 1.23 Mpc)								
NGC 5090A	13 19 21.1	-43 38 58	12.26	3427±32	S0	1.7	20.5	7
ESO 270- G 007	13 23 15.7	-43 32 38	12.97	3750±200	(R)SB(rs)0	1.2	24.2	8
2MASX J13181305-4330182	13 18 13.0	-43 30 19	15.10	3526± 0	−	−	34.7	9
AM 1317-425	13 20 36.8	-43 05 43	−	3323±10	−	0.5	37.1	10
2MASX J13195606-4306498	13 19 56.1	-43 06 50	14.00[4]	3364± 0	−	0.8	38.1	11
2MASX J13192359-4417358	13 19 23.6	-44 17 36	14.90	3358± 0	−	−	40.4	12
2MASX J13212941-4248564	13 21 29.4	-42 48 57	16.00	3463± 0	−	−	53.4	13
2MASX J13161705-4307595	13 16 17.0	-43 08 00	14.80	3910± 0	−	−	63.7	14
ESO 269- G 076	13 15 18.1	-43 48 21	14.50	2983± 0	S0	1.6	64.3	15
2MASX J13270026-4359472	13 27 00.2	-43 59 47	12.70[4]	3178± 0	−	0.7	65.0	16
ESO 270- G 014	13 28 27.3	-44 10 19	12.87	3848±37	S0 pec	1.2	83.1	17
ESO 269- G 072	13 13 33.8	-43 31 34	12.34	3300±200	E4	1.3	83.8	18
ESO 269- G 069	13 13 17.4	-43 34 59	13.47	2965±56	SB(r)a	1.1	86.3	19

[1] semi major axis of the object.

[2] projected distance from the E.

[3] R band magnitude.

[4] I band magnitude.

[5] J band magnitude.

The kinematical and dynamical group properties are computed together with the new faint group members in Chapter 6.

2.5   Summary and conclusions

We investigated structural and photometric properties of 4 galaxy pairs consisting of an elliptical and a spiral galaxy taken from the Reduzzi & Rampazzo (1995a) catalogue of southern isolated galaxy pairs. A field of roughly $0.5° \times 0.5°$ around each pair was observed with the Wide Field Imager (WFI) at ESO. The main results of this chapter are the following:

— The E members of the pairs show very similar optical (colour) and kinematical (velocity dispersion) properties. However we found that RR 143a and RR 242a are dynamically more relaxed objects with an extended regular halo and without signatures of past or recent interactions. The early-type galaxies in RR 210 and RR 216 on the other hand display unambiguous signs of recent or ongoing interaction as evidenced by the model-subtracted and unsharp-masked images. Extended dust lanes (RR 210a) and diffuse stellar light plumes (RR 216b) were detected in these two galaxies.

— The same is found for the spiral pair members, which are unperturbed in RR 143 and RR 242 and distorted in RR 210 and RR 216.

— The signatures of interaction are quantified with the Σ parameter and will be discussed together with the X-ray information presented in the following chapter.

— The 4 pairs are situated in different environments ranging from very sparse (RR 143) to quite rich (RR 216). The galaxies around RR 210 and RR 242 seem more centrally concentrated than in the other 2 pairs.

Chapter 3

X-ray observations with XMM-Newton

In this chapter the new observations in the X-ray domain carried out with `XMM-Newton` are described. First, the X-ray picture given by earlier observations with `ROSAT` is presented. The new observations were necessary to confirm the presence of diffuse, extended X-ray emission suggested by `ROSAT` and to characterise the physical properties of the intra group medium (IGM).

Iso-intensity contours and radial profiles of the emission are presented, asymmetries and perturbations in the IGM are investigated. The spectral energy distribution shows that the emission is a soft emission mainly caused by a hot plasma and a small bremsstrahlung contribution. The abundances were not constrained.

The properties of the IGM are discussed in comparison with the properties of the pairs and other group members found from the analysis of the optical data.

3.1 Early X-ray observations of the 4 pairs

The X-ray picture given by earlier `ROSAT` observations (Trinchieri & Rampazzo 2001) indicates that the X-ray luminosities and L_X/L_B ratios of galaxy pairs encompass a very wide range, in spite of the very small number of pairs studied so far. In particular, the 4 systems studied in this work show very different luminosities and X-ray morphologies in contrast to their relatively similar optical ones (see Table 2.1). In RR 143 and RR 242 the X-ray emission is much more extended than the optical light. The emission seems to be centered on the elliptical pair member, but from its extension and flattened profile it seems to be not only confined to the galaxy. This diffuse extended X-ray emission is indicative of a Intra Group Medium (IGM) and it suggests the presence of a deeper, "group-like" potential. However, this quite tentative result has to be confirmed with deeper and higher resolution X-ray

observations.

Relatively faint and compact emission (i.e. within the optical galaxies) is detected in RR 210 and RR 216. Although no spectral properties could be derived from the `ROSAT-HRI` data, the observed luminosities would point to emission from the galaxy only, most probably from the evolved stellar population, with very little or no contribution from a group component. Especially for RR 210, the X-ray emission is very faint, in fact it is below the value of expected emission from discrete sources for a galaxy at this luminosity. The presence of an IGM in this pair can be almost ruled out.

The `ROSAT` observations of the two faint or almost not detected pairs RR 210 and RR 216 were deeper than the observations of RR 143 and RR 242 found in the `ROSAT` archive. To check the diffuse extended nature of the emission of the two latter and to investigate the spatial, photometrical as well as spectral properties of the emission, the 2 pairs were observed with the `XMM-Newton` satellite.

3.2   Instrument description

`XMM-Newton` is operated by the European Space Agency (ESA). It carries 3 X-ray telescopes with different detector types and a 30 cm telescope sensitive for optical and UV photons (`Optical Monitor OM`) allowing simultaneous X-ray and optical/UV observations. The `OM` data suffer from various problems, like reflections on the detector window and are due to their minor quality not further considered in this work.

The X-ray detectors combine a high angular resolution (PSF of $\sim 6''$ FWHM) with a big field of view ($\sim 30'$ diameter), ideal for our search for extended diffuse emission. The `EPIC` (European Photon Imaging Camera) instrument used for our purposes features 2 different types of detectors, called `MOS` and `PN`. This detectors function in a fundamentally different way, with the `MOS` being front- and the `PN` back-illuminated. The 2 `MOS` fields consist of 7 CCDs each, with one central CCD and the other 6 arranged in a circle around it. The 2 fields are rotated by $90°$ with respect to each other. The `PN` consists of 12 CCDs in a 2×6 rectangle but covering the same circular field as the `MOS` detectors. The `PN` features a fast readout time, making it suitable for observations with a high time resolution, but since we are not dealing with a variable source, this doesn't concern our observations. The single instruments can operate separately and independently.

The covered energy range is $0.15 - 15$ keV, but with the effective photon collecting area of the mirrors being strongly dependent on the photon energy. The highest collecting power is reached at around 1.5 keV with a sharp drop at ~ 2 keV and then a smooth decline beyond $\sim$10 keV. The sensitivity of the `PN` is higher, because the `MOS` detectors are partly obscured by the reflection grating array.

Figure 3.1: Artistic view of the `XMM-Newton` space telescope. Image courtesy of ESA.

3.3 Observations and reduction methods

We obtained `XMM-Newton` observations of RR 143 and RR 242 with `EPIC` in the medium filter as reported in Table 3.1.

We used the `XMM-Newton` Science Analysis System `SAS` version `6.5` to clean the data from flaring events, which reduced the original exposure by $> 30\%$ (see Table 3.1) and to filter them with the standard "FLAGS" (see the science threads at `http://xmm.vilspa.esa.es`). We retain single, double and quadruple events for morphological and `MOS` spectral analysis, while for the spectral analysis of the `PN` data we consider only single events. We also made use of both `CIAO`[1] and `DS9-Funtools`[2]. CCD gaps are masked out during the spatial analysis. In order to improve statistics and to avoid having to take into account the different CCD gap patterns of the two instruments, we summed all `EPIC-MOS` data and kept the `EPIC-PN` data separate. These two datasets will be used for all except the spectral analysis in this work.

---

[1]`http://cxc.harvard.edu/ciao/`
[2]`http://head-cfa.harvard.edu/RD`

Table 3.1: Log-book of `XMM-Newton` observations.

Pair	Observing nights	Original Time PN/MOS [s]	Used live time PN/MOS [s]
RR 143	2003-10-19	9325/11850	7289/9250
RR 242	2003-07-17	18032/21650	11794/14318

3.3.1   Source extent

We smoothed the `EPIC-MOS` data with an adaptive filter in order to better visualise the emission. The iso-intensity contours in the $0.5 - 2$ keV range superposed on our optical images are shown in Figure 3.3.

We employed azimuthal averaging to assess the extent of the diffuse emission in different energy bands. This is only an approximation, because the emission is not azimuthally symmetric around either pair. This approximation allows us to measure a total average extent and to determine the background level. We excluded discrete sources from the profiles which are all centered on the early-type components.

A number of additional sources can be seen in both fields of the pairs. However in all but one case (Galaxy # 13627 in RR 242, Table A.4, coincident with the X-ray source #23 in Table B.2), the X-ray sources are most likely background objects unrelated to the pairs. We present them in the Appendix for completeness, but we will not use them in the present discussion.

3.3.2   Background evaluation

Evaluation of the background for extended sources is always a challenge, as shown by several authors (see Nevalainen et al. 2005) and notes to the use of the `xmmsas` software. Background maps can be obtained as a byproduct of the detection procedure with `xmmsas`. A central extended source is not excised, however, since the program is designed to also provide a correct background for sources embedded in diffuse emission. Blank sky fields are available at `http://xmm.vilspa.esa.es/` and can be used to determine the background. They are unfortunately based on thin filter data while ours are medium filter observations. We therefore analyzed several images, both from the archive and from our own data, to evaluate the shape of the background with the medium filter. A comparison with the thin filter data indicates no significant differences, except for a different relative normalisation for profiles obtained in different energy bands. We have therefore evaluated the background from the deep field blank sky data, and normalized them to our own fields in the outer regions, where the radial profiles show an almost constant surface brightness, very similar in shape to that of the background fields. The results of this procedure for

RR 143 are shown in Figure 3.2 as an example. The same figure also shows that the emission is prominent in the 0.5-2.0 keV profile and becomes negligible above 3.0 keV. Since the contribution in the 2-3 keV range is not significant, and it is confined to the inner regions, we have used the 0.5-2.0 keV data to study the radial distribution of the emission. The same considerations apply to RR 242.
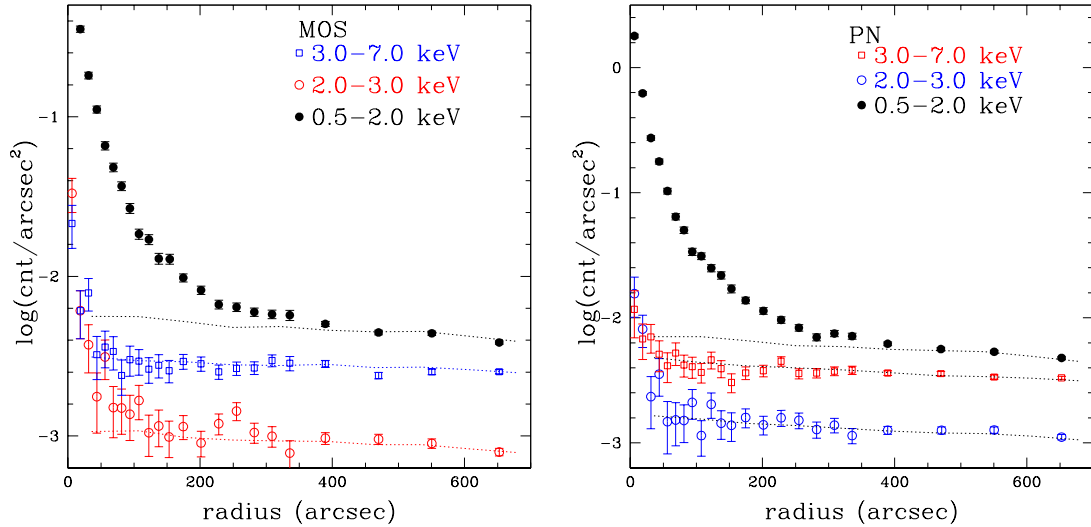
Figure 3.2: Surface brightness profile of the raw XMM data of RR 143 in different energy bands, centered on NGC 2305 (RR 143a). Left: MOS data. Right: PN data. The background shapes from the blank sky fields, normalized to each profile are plotted as dotted lines.

3.3.3 Radial profiles and asymmetry

We produced radial profiles at different position angles in order to quantify the degree of asymmetry. We find that the asymmetry is also a function of radial distance from the center. This motivated us to divide the emission into different azimuthal and radial zones (Figure 3.4, central and right panels). Figure 3.4 confirms significant azimuthal differences in the data which confirm the visual impression from the iso-intensity contours. Asymmetries are also visible in the X-ray emission of NGC 5082, an SB(r)0 galaxy, which is a member of the group around RR 242 and is also embedded in the IGM. In Figure 3.5 we show the comparison of radial profiles obtained in different quadrants to illustrate the evidence for azimuthal asymmetry. The photon distribution is clearly compressed to the SE, while the NW quadrant appears more extended.

3.3.4   Spectral analysis

In order to measure the spectral properties of the X-ray emission we extracted photons from different regions, including background regions appropriate for the emission region we want to investigate. Given the pattern in the `PN` detector, regions in `MOS` and `PN` are often not the same. The central region is typically the same because it fits on the same CCD on PN. The more extended emission is taken from `MOS` while `PN` is limited to the region that fits on a single CCD. For this reason the relative normalisation between instruments is left free to vary in order to compensate for the different regions considered.

We used a local determination of the background, when possible, from an annulus around the region considered (in general this is true for the `MOS1` and `MOS2` data sets, and for the central source in the `PN` data). This also implies that the surrounding "galaxy" is used as background for the central source in RR 242. For `PN`, the background is taken from a region free of source emission and also free of gaps close to the region of interest. Since the emission from the source does not fill the whole field of view in either galaxy, and the background level where the source ends is not significantly reduced relative to the central parts we have used a local determination also for the whole source; this reduces uncertainties due to the background variations between different observations, unavoidable when using a different set of data (like the blank fields, that we cannot use in any case due to the different filters).

The data are binned to increase the statistics. We have considered binning to a specific number of photons, which is reasonable for some regions. However, since the contribution of the background is not uniform with energy, and is larger at high energies, we have also considered larger bins mostly at high energies to increase the signal-to-noise of the net emission in each bin. In all cases we have considered only bins that have a S/N of at least 2 σ after background subtraction. The data are fitted in `XSPEC` with either a plasma (namely `MEKAL` in the `XSPEC` acronyms) or a combination of plasma and bremsstrahlung or power law to account for high energy tails. Low energy absorption is also taken into account and abundances are according to Wilms et al. (2000). The results are given in Table 3.2 and discussed later for each source.

3.4   Results

X-ray maps of RR 143 and RR 242 reveal the presence of a diffuse intra group medium in both systems. The iso-intensity contours in the $0.5 - 2$ keV range superposed on our optical images are shown in Figure 3.3. The extended emission is

Table 3.2: Basic X-ray properties of the extended component.

Pair	Radius	Counts	Count	Flux	log L_X	Temperature[1]
	['] / [kpc]	[0.5-2.0keV]	rate	[0.5-2.0keV]	[erg s^{-1}]	kT [90% confidence]
RR 143	8 / 120	5220±95	0.72	1.2×10^{-12}	41.48	0.54 [0.52-0.56]
RR 242	12 / 160	5750±135[2]	0.49	1.1×10^{-12}	41.46	0.3 [0.25-0.37];2.7 [2.4-3.3]

[1] Best fit temperature(s) and 90% confidence limits assuming a MEKAL code. Low energy absorption is left free, but it is always consistent with the line of sight value. Abundance ratios are consistent with the solar value.

[2] Estimated excluding the central source.

centered on the brighter early-type component (NGC 2305 in RR 143 and NGC 5090 in RR 242) in both pairs. The spiral galaxies (NGC 2307) in RR 143 and NGC 5082 west of RR 242 are also detected as discrete sources.

3.4.1 X-ray morphology

RR 143

The morphology of the X-ray emission from RR 143 is rather disturbed with an anisotropic distribution of photons that is not an artefact of the smoothing process. Figure 3.4 shows that the photon distribution is not the same at different position angles and radial distances. `ROSAT-HRI` data (Trinchieri & Rampazzo 2001) already revealed an elongated source associated with RR 143. One of the directions of elongation is toward the companion galaxy which could indicate a link or interaction artefact. However no optical evidence of tidally generated asymmetries has been detected in either galaxy. The bulk of the emission is centered on the early-type component although the late-type companion (NGC 2307) is also detected (source # 21 in Table B.1). The energy distribution of photons from this galaxy (namely below and above 2 kev) suggests a mildly absorbed source, which would point towards a nuclear source as the origin of most of the X-ray emission with a luminosity $L_{(2.0-10.0)}$ $\sim 3\times 10^{40}$ erg s^{-1}.

RR 242

The distribution of X-ray photons in RR 242 is more extended and less asymmetric than in RR 143. The source shows a prominent peak centered on the nucleus of RR 242a (NGC 5090) and consistent with the position of the radio source PKS B1318 -434 whose axis is oriented perpendicular to the line joining the pair components. This suggests that the tidal interaction may be influencing the way that the central engine of the elliptical is fuelled. The spiral companion is not detected with certainty as a discrete source; however, a source with a maximum likelihood parameter ≤ 10 is found coincident with the position of the galaxy (with $f_{0.5-2.0} \sim 2 \times 10^{-14}$ erg
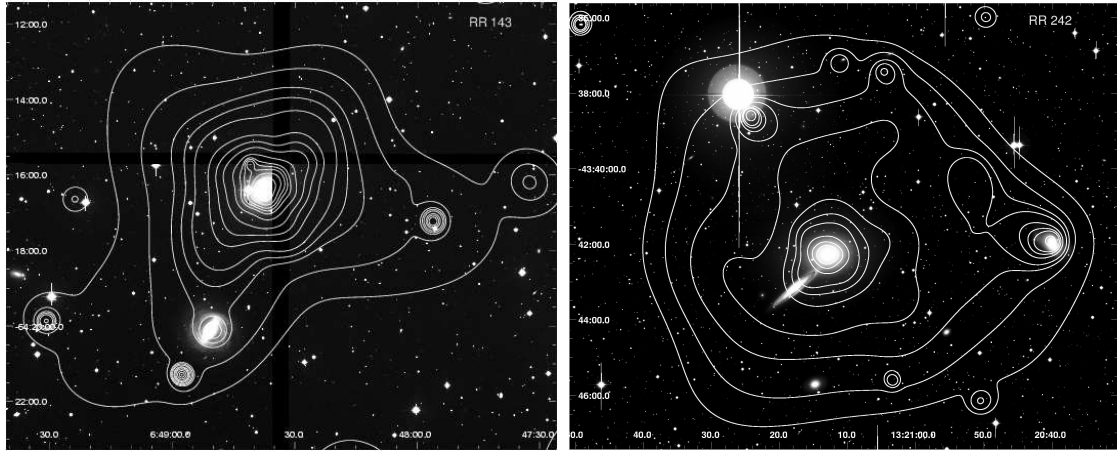
Figure 3.3: Iso-intensity contours of the adaptively smoothed X-ray emission around RR 143 (right panel) and RR 242 (left panel) detected with `XMM-Newton`. Contours are superposed on the R-band WFI images (see Section 2.2). The galaxy west of NGC 5090 is NGC 5082.

cm^{-2} s^{-1}, or L$_X \sim 6 \times 10^{39}$ erg s^{-1}). This would be consistent with the expected luminosity of a normal spiral galaxy. A distortion in the isointensity contours at the position of the galaxy is visible in Figure 3.3 which also suggests some contribution from it.

NGC 5082 located W of the pair is clearly detected as source # 8 in Table B.2 with a 0.5-2.0 keV luminosity of $\sim 8 \times 10^{40}$ erg s^{-1}. The emission in the vicinity of NGC 5082 appears disturbed with indications of a tail towards the NW and of compression towards the SE. This can also be seen in Figure 3.5 at a distance of 20-50″ (5-13 kpc). This might indicate transverse motion of this galaxy relative to the group. Optical data do not show morphological asymmetries that might be a signature of ongoing interaction. At the same time the prominent bar in NGC 5082 could represent the signature of interaction involving the group members (Noguchi 1987).

3.4.2   Radial profiles

Figures 3.4 and 3.5 show the net, azimuthally averaged profiles from `PN` and `MOS` data separately. Emission in RR 143 extends to almost 500″ radius ($\sim$ 120 kpc). The profile of RR 242 shows a very prominent central source that dominates emission in the inner $\sim$ 1′ region. A more extended component extends to r $\sim$ 700″ (160 kpc). The radial profile of the extended emission that is shown in Figure 3.5 can be modelled with two, or even three, components (right panel): at r $<$ 30″, the
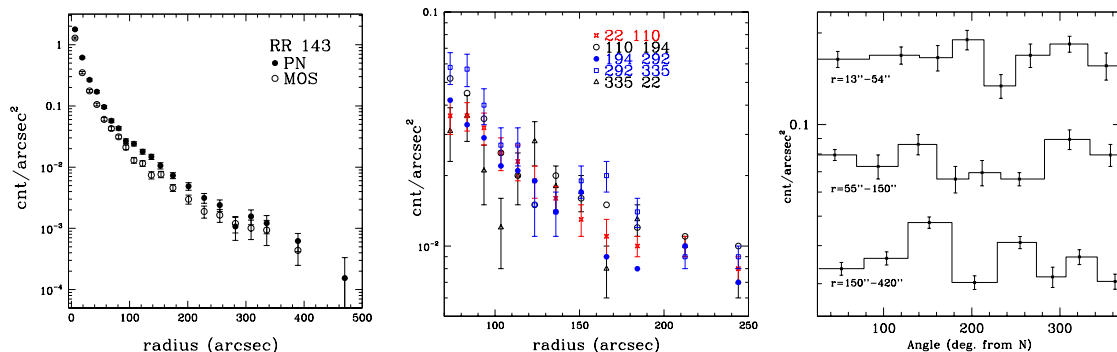
Figure 3.4: Surface brightness profile of the net emission in RR 143: azimuthally averaged from MOS and PN separately (left), in different quadrants (middle) and at different angles and radial distance from the center (right). All plots are in the 0.5-2.0 keV band.

emission is consistent with the instrumental PSF [1]. A significantly flatter component is present at r > 200″ that can be modelled with a β-profile with a core radius $r_c \sim$ 420″ and $\beta \sim 1$ (see Figure 3.5). These two components do not completely describe the data: the central region appears more extended than a simple PSF. The addition of a β-profile with $r_c \sim 45″$ and $\beta \sim 1$ could account for the excess emission. This would imply that the central peak is due to both a nuclear component and a galactic component.

3.4.3 Spectral characteristics

RR 143

The spectral characteristics of the extended component can be modelled with a ~ 0.53keV plasma (0.52-0.56 at 90% confidence level, $\chi^2_\nu \sim 1.4$). The addition of a power law or a bremsstrahlung model with fixed $\Gamma = 1.5/kT=10$ keV gives a significant improvement ($\Delta\chi^2 > 10$ with one additional parameter) and accounts for the excess above 2-3 keV. Figure 3.6 shows the data and best fit model using the data from all three instruments. We find no significant differences if we limit ourselves to the central 20″ radius or if we consider a larger area. In all cases we find a feature in the residuals around 1-1.5 keV that we are not able to model even taking into account variable abundances, multi-temperatures, and a cooling flow. All consistently yield temperatures around 0.5 keV (the cooling flow range is 0.3-0.8) and solar abundances. We find marginally improved results with a model where the

---

[1]We have used the analytical formula given by the "EPIC status of calibration and data analysis" document [XMM-SOC-CAL-TN-0018], of 11/02/05
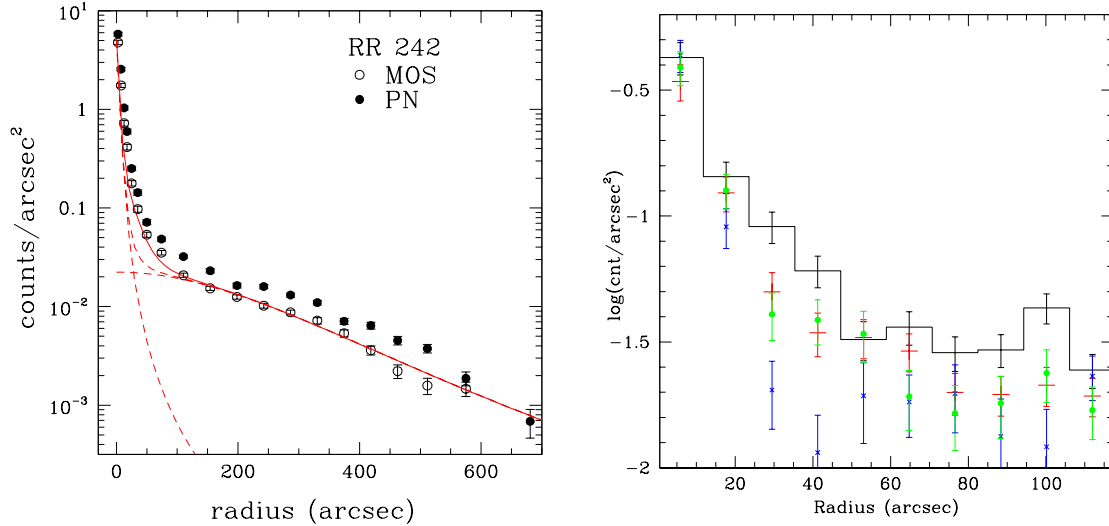
Figure 3.5: Left: Surface brightness profile of the azimuthally averaged net emission in RR 242 in the 0.5-2.0 keV band from `MOS` and `PN` separately. A three component model, due to the sum of the `MOS` point spread function (PSF) and two β-profile functions with $r_c = 420''$ and $r_c = 45''$ and $\beta \sim 1$, is shown with a solid line. The PSF and the larger β-profile are also plotted with a dashed line. Right: Asymmetry of the emission centered on the spiral NGC 5082: radial profiles in 4 different azimuthal sectors. The histogram refers to the $27 - 117°$ quadrant, red plus to $177 - 207°$, blue crosses to $207 - 297°$, and green dots to $297 - 27°$ (clockwise from N). The data are in the 0.5-2 keV energy range.

abundance ratio between different elements is not fixed: i.e. with Fe overabundant and C under-abundant relative to the other elements. The residuals at 1-1.5 keV are somewhat smaller but are still present. Results are given in Figure 3.6 for the `PN` data alone. The absolute values of the abundances are not constrained so we put little weight on their relevance in the discussion.

The total X-ray luminosity of the intra group medium is $L_X \sim 3 \times 10^{41}$ erg s^{-1} (0.5-2.0 keV) with an average density of $n_e \sim 8 \times 10^{-4}$ cm^{-3} in the inner $200''$ and a corresponding gas mass of 8×10^9 M$_\odot$.

RR 242

The spectral results for emission within a $30''$ radius are consistent with the presence of a low luminosity ($L_X \sim 10^{41}$ erg s^{-1}, 2.0-10 keV) and mildly absorbed ($N_H \sim 10^{22}$ cm^{-2}) AGN surrounded by emission from a moderately sub-solar 0.61 keV plasma.
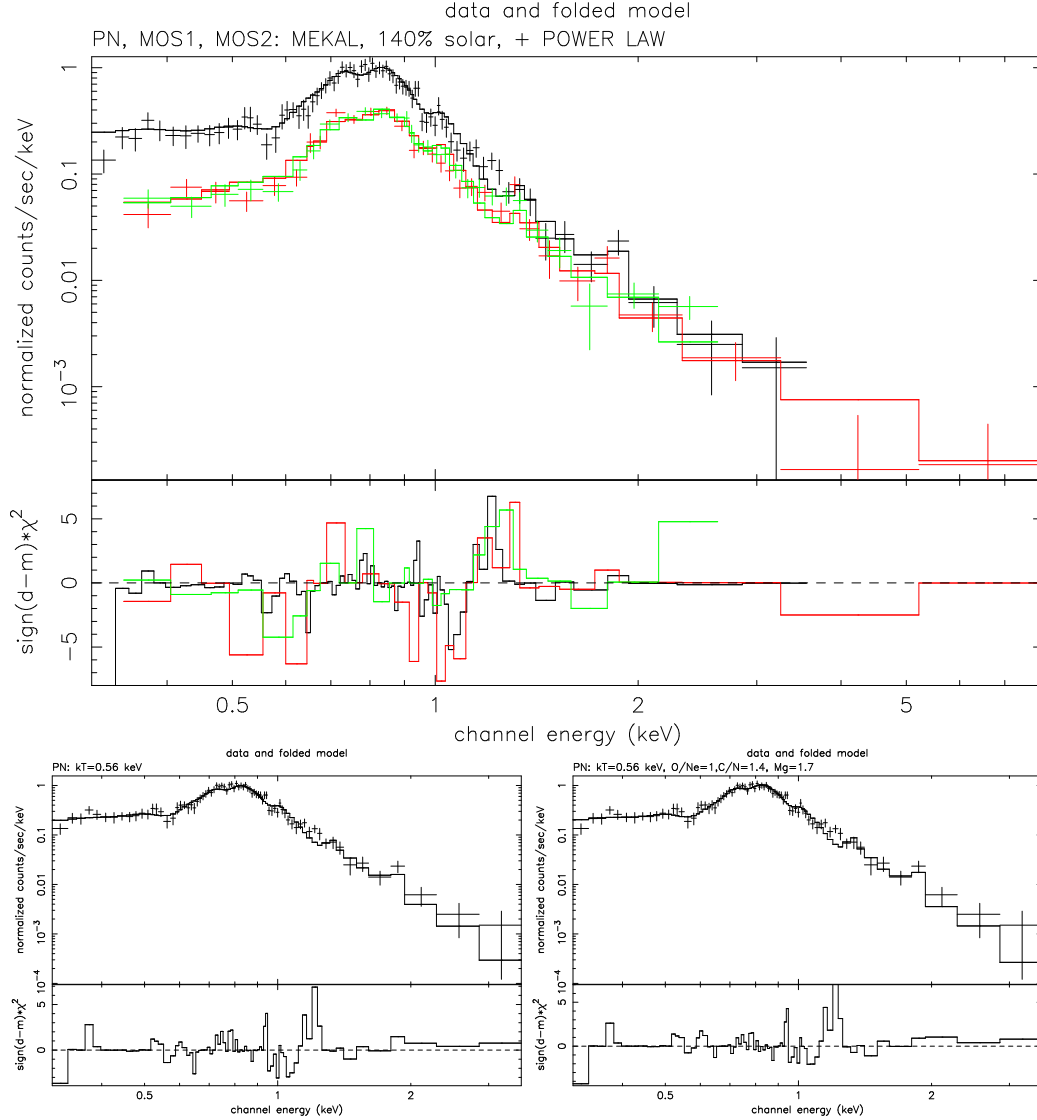
Figure 3.6: Spectral distribution of the diffuse emission in RR 143. Note that since the emission extends over several CCDs in `EPIC-PN`, spectral data are obtained from smaller regions that would fit within a single CCD. To compensate for different areas in `EPIC-PN` and `EPIC-MOS`, the relative normalisation is left free. Top: `EPIC-PN` and `EPIC-MOS` data. The model is a `MEKAL` (kT= 0.5 keV, 100 % solar abundances) plus and power law (fixed $\Gamma = 1.5$), with galactic N_H. Bottom: `PN` data only. The model is a kT= 0.5 keV `MEKAL`, 90% abundances with ratios between elements fixed at the solar values, and a kT= 0.5 keV `MEKAL`, with Mg at 170%, O–Ne at 100% and C–N at 140% of the solar value, respectively.

The luminosity of the latter component ($L_X = 5 \sim 10^{40}$ erg s^{-1}) is consistent with emission from the ISM of the galaxy also taking into account a possible contribution from the surrounding IGM. The larger scale component is also consistent with emission from a hot plasma. The emission is best modelled using a two-temperature plasma ($kT_1 \sim 0.3$ keV and $kT_2 \sim 2.5$ keV) both with approximately solar abundance.

The total luminosity of the extended component is $L_X(0.5\text{-}2.0) \sim 3 \times 10^{41}$ erg s^{-1} and is dominated by the contribution from the hotter one (ratio about 10:1). The average density in the inner $\sim$50 kpc is $n_e \sim 2$ and 7×10^{-4} cm^{-3} for the softer and harder components respectively. This decreases to $n_e \sim 0.9$ and 2×10^{-4} cm-3 in the 50-100 kpc region. The mass of the X-ray emitting gas is $\sim 9 \times 10^9$ M$_\odot$.

3.5 Optical - X-ray comparison

In the following we compare the X-ray emission of the 4 pairs with their properties found from the optical study. The presence and properties of the hot gas halo are compared with the dynamical age of the E indicated by the signatures of recent interaction.

3.5.1 The L_X-L_B plane

Early `ROSAT` observations (Trinchieri & Rampazzo 2001) already indicated that luminosities, L_X/L_B ratios and morphologies are very different in the 4 systems of our pair sample. The distribution of L_X for the four ETGs encompasses nearly the full range found for early-type galaxies.

Figure 3.7 (left panel) shows the location of our four elliptical pair members in the log L_B - log L_X plane. For comparison we plot also early-type galaxies from the sample of Sansom et al. (2000). We have labelled the galaxies in this sample that are members of poor groups (see e.g. Helsdon et al. 2001). However, we did not consider NGC 3605, NGC 3998 and NGC 4203, because their X-ray emission is dominated by LINER/AGN activity. The X-ray luminosities are taken from the catalogue of O'Sullivan et al. (2001a). We have also used their recipe to re-calculate the luminosities given in Table 3.2.

Extended X-ray emission is also detected in poor groups containing very few galaxies, overlapping the domain of classical pairs. NGC 2300 (marked in the figure) is the best known example for this overlap (Mulchaey et al. 1993). The group is dominated by a bright E+S pair (NGC 2300 and 2276) that is isolated enough to satisfy the criterion used in the compilation of the Catalog of Isolated Pairs (Karachentsev
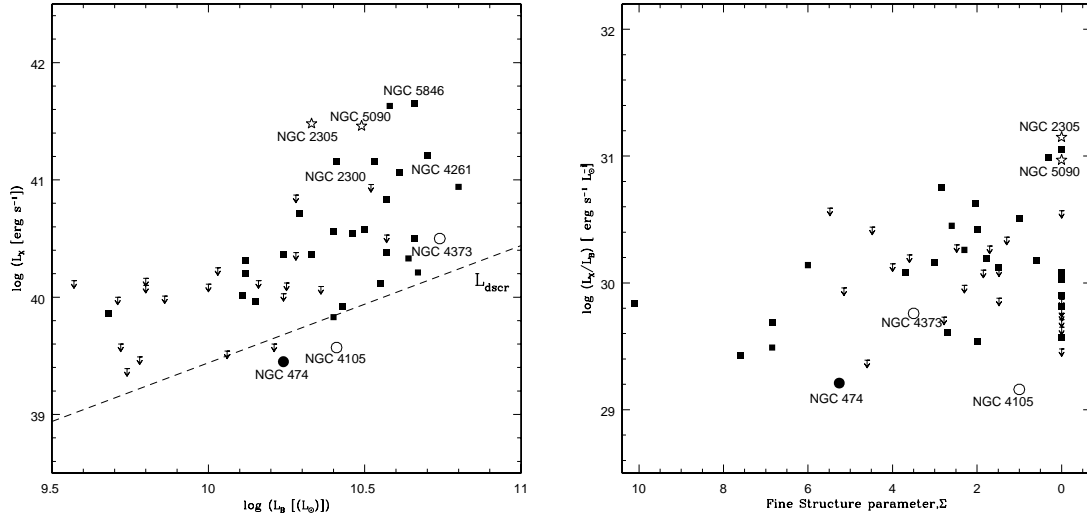
Figure 3.7: Left: Location of the elliptical pair members in the L_B - L_X plane. Right: Logarithm of X-ray luminosity normalized by optical luminosity L_X/L_B versus fine structure parameter Σ. With open stars we plot the location of the 2 systems observed with `XMM-Newton`, with open circles we plot NGC 2305 and NGC 4373 observed with `ROSAT` by Trinchieri & Rampazzo (2001). The Sansom et al. (2000) sample is plotted with filled squares (detections) and arrows (indicating upper limits). Galaxies in this sample that are members of poor groups (see e.g. Helsdon et al. 2001) are labelled. NGC 474 (taken from Rampazzo et al. 2006), which is also member of an E+S pair, is plotted with a filled circle. The dashed line (L_{dscr}) represents the expected emission from discrete stellar X-ray sources from Ciotti et al. (1991).

1987, KPG 127). The other members of this loose group (NGC 2268 and IC 455) are significantly fainter ($\sim$ 2 mag. Mulchaey et al. 1993). Notice also the location of NGC 474, a member of an E+S galaxy pair, which has a large system of shells and is interacting with the spiral NGC 470 (Rampazzo et al. 2006).

The 4 pairs studied in this work have comparable optical luminosities but spread over a wide range of X-ray luminosities. The dashed line in Figure 3.7 represents the expected emission from discrete sources, i.e. from the evolved stellar population, in a galaxy of a given optical luminosity. It can be considered the lower limit of expected emission from an unperturbed galaxy. Similar to the shell galaxy NGC 474, the elliptical of RR 210 - NGC 4105 - is located below this line, indicating that hot gas has been stripped from its halo. The luminosity of NGC 4373 (RR 216b) is consistent with the expected X-ray emission from discrete sources, whereas the X-

ray luminosities of NGC 2305 (RR 143a) and NGC 5090 (RR 242a) are 2 orders of magnitude above this limit, similar to NGC 5846, the dominant member of a supposedly dynamically evolved poor galaxy group (Mahdavi et al. 2005).

3.5.2 L_X/L_B as a function of interaction-signatures

The right panel of Figure 3.7 plots the normalized X-ray luminosity L_X/L_B for the same set of galaxies as a function of the Σ parameter (see Section 2.3.3) tracing the dynamical age of an interaction or merging.

Sansom et al. (2000) and O'Sullivan et al. (2001a) discuss the anti-correlation between L_X/L_B and Σ. The observation that only apparently relaxed ellipticals are strong X-ray emitters is argued to be consistent with the hypothesis that strong disturbances, such as mergers, cause the build up of hot gas halos over a time-scale of several gigayears (Sansom et al. 2000). O'Sullivan et al. (2001a) further suggest that some of the scatter seen in the global L_X versus L_B relation is due to the evolutionary state and past merger history of early-type galaxies.

Read & Ponman (1998) found that after an increase in the emission from hot gas at earlier stages of a merger, relaxed remnants (about 1.5 Gyr after a merger) appear relatively devoid of hot gas. The X-ray deficiency of recent merger remnants was also noted by Fabbiano & Schweizer (1995). They suggest that a merger-induced starburst could drive a galactic superwind which clears the remnant of most of the hot gas. After the starburst subsides the hot gas is gradually replenished by stellar mass loss (for a review, see Sarazin 1997) and, perhaps to some small extent, also by the thermalization of returning tidal debris (Hibbard & van Gorkom 1996).

All this evidence points towards the existence of a sequence of merging phases characterized by differences in the X-ray emission. This sequence was investigated in detail by Brassington et al. (2007), who investigated the X-ray properties of pre- and post-merging objects. They found that the X-ray emission peaks about 300 Myr *before* nuclear coalescence. The emissivity of the gas is then reduced during the merging process by starburst-driven galactic winds, reaching its minimum at ~ 1 Gyr after nuclear coalescence. At a higher dynamical age of about 3 Gyr the resulting remnant has rebuilt the hot gas halo and resembles an evolved elliptical galaxy.

The unperturbed galaxies RR 242a and RR 143a (NGC 5090 and NGC 2305) as well as RR 216b (NGC 4373), which displays the clearest evidence of ongoing interaction are consistent with the $L_X / L_B - \Sigma$ relation derived from the Sansom et al. (2000) sample. The moderately perturbed NGC 4105 (RR 210a) is a very weak X-ray source with a luminosity similar to NGC 474 the E member of Arp 227 which displays a

complex system of shells, presumably due to strong past interactions (Rampazzo et al. 2006).

In the picture of the merger-age sequence RR 143 and RR 242 are in a post-merger phase with an old dynamical age, whereas RR 216 and especially RR 210 are dynamically young.

3.6 Summary and conclusions

The X-ray properties of our E+S pair sample can be summarized as follows:

- The X-ray emission of RR 210 and RR 216 is relatively faint and compact, i.e. within the optical galaxy. The luminosity of the detected sources is consistent with the expected emission from the evolved stellar population of the galaxy. The presence of an IGM is very unlikely.

- RR 143 and RR 242 are more luminous and their emission is extended, indicating the presence of a large amount of hot gas or IGM. The `XMM-Newton` observations confirm the presence of diffuse extended emission with luminosities of around $L_X \sim 3 \times 10^{41}$ erg s^{-1} and extensions of r $\sim 500''$ (120 kpc) in RR 143 and r $\sim 700''$ (160 kpc) in RR 242.

- The high spatial resolution of the new observations also show that this emission encloses both pair members (in the case of RR 143) and even another group member (NGC 5082 in RR 242). This can be interpreted as evidence that the pairs are bound and embedded in a "group-like" potential (see eg. Mulchaey 2000).

Morphologies

The X-ray morphologies also suggest that these two systems may be at different stages of evolution. RR 242 appears more relaxed with a more regular and azimuthally symmetric emission. The emission in RR 143, though centered on the early-type galaxy, has a clear elongation towards the companion possibly indicating dynamical effects (tidal/ram pressure stripping). However, no optical distortion can be seen in the spiral of RR 143.

Bound structures

The above considerations suggest that RR 143 and RR 242 form bound structures on the basis of their extended X-ray emission. Note however that, at odds with RR 242, RR 143 is a very poor structure without luminous companions. RR 210

and RR 216 do not have extended X-ray emission but both have some luminous companions and probably represent the active part of very poor and loose evolving groups. The activity is seen in the optically distorted morphology traced by diffuse light plumes. The presence of these structures, at least in RR 216, argues in favour of a bound nature of the pair. The bound nature of RR 210 can not be confirmed. However, it should be noted that also this pair seems to be embedded in a group with other luminous members with a low velocity dispersion. Additionally, the strong interaction between this pair could have destroyed a previously existing X-ray halo. The investigation of the presence of a faint galaxy population associated to the pairs will help to clarify this point.

Evolutionary stage

The combined optical and X-ray analysis suggest that the X-ray luminous E+S pairs RR 143 and RR 242 are likely the dominant members of **evolved** poor groups, whereas RR 210 and RR 216 are likely the dominant members of **evolving** groups. At odds with their optical, kinematic (mass) and environmental similarities, the ETGs in our E+S pairs have remarkably different X-ray properties. We suggest that this can be explained either in terms of the present evolutionary phase of the system or the past histories of the ETGs.

Chapter 4

The candidate faint galaxy population

The following chapter describes the procedure of detecting and selecting the faint galaxy population that may be associated to each pair.

First, the objects were detected in the WFI frames of the pairs. Only extended (non-stellar) sources with a minimum size and magnitude were considered as candidates. Then, a colour restriction based on the expected colour-magnitude relation (CMR) was applied to the candidates. This procedure is considered a successful method to remove background galaxies from the sample. Additionally, the spatial distribution of the candidates around the pair and the local projected number density was investigated, to see if the candidates are smoothly distributed and concentrated around the pairs or if there are denser clumps not connected to the pair, indicative of a background structure.

Surface photometry of all candidates was carried out to investigate structural parameters of the objects. A one-component Sersic model was fitted to each galaxy image. The resulting parameters for all candidates are given in Appendix A. Expected relations between the photometric parameters like central and effective surface brightness, Sersic parameter and total magnitude are investigated as well as the connection of these parameters to other galaxy properties like global $(V - R)$ colour and a possible connection to the galaxy's position in the group (morphology-density relation).

Finally, the evidence gained from this analysis in favour and against the candidates being dwarf galaxies connected to the respective pair is summarized and discussed.
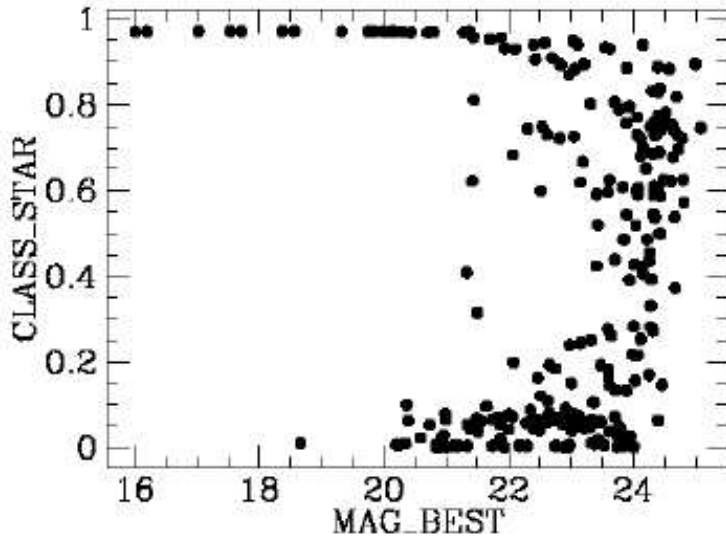
Figure 4.1: SExtractor's Star/Galaxy classifier as a function of magnitude. The reliability of the classification fades with fainter magnitudes. Stellar sources have a `CLASS_STAR` of 1, close to 0 the source is extended (figure taken from Bertin & Arnouts 1996).

4.1   Object detection with SourceExtractor

The faint galaxy population around each pair was identified running the SourceExtractor (Bertin & Arnouts 1996) on the WFI frames. SExtractor is a program to find and catalogue sources in astronomical images and perform a quick but decent photometry on the identified sources. It distinguishes between point- (stellar) and extended sources with a stellarity parameter `CLASS_STAR` based on a neural network output, comparing the "fuzziness" of the image given by the seeing with the object's profile. This classifier can have a value between 0 (non-star) and 1 (star) and is found to be quite robust up to a certain magnitude. Since we are interested in a sample of faint galaxies (non-stars) we considered only sources with a stellarity parameter ≤ 0.5 (Bertin & Arnouts 1996). Furthermore the sample was limited to candidates with a detection radius larger than $a \geq 1.5''$ corresponding to $a \geq 400$ pc (200 pc for the closer pair RR 210), which is smaller than the smallest Local Group dwarf galaxies found by Mateo (1998) and is reaching into the domain of dwarf spheroidal galaxies (dSph) that are typically smaller than 500 pc. The sample was also limited in magnitude. Only candidates brighter than $R = 21$ mag were considered, which is the magnitude below which the star/galaxy classifier was found to become unreliable (see Figure 4.1, Bertin & Arnouts 1996). This corresponds to a limiting absolute magnitude of $M_R \sim -12.5$ mag ($M_R \sim -11.5$ mag for RR 210).
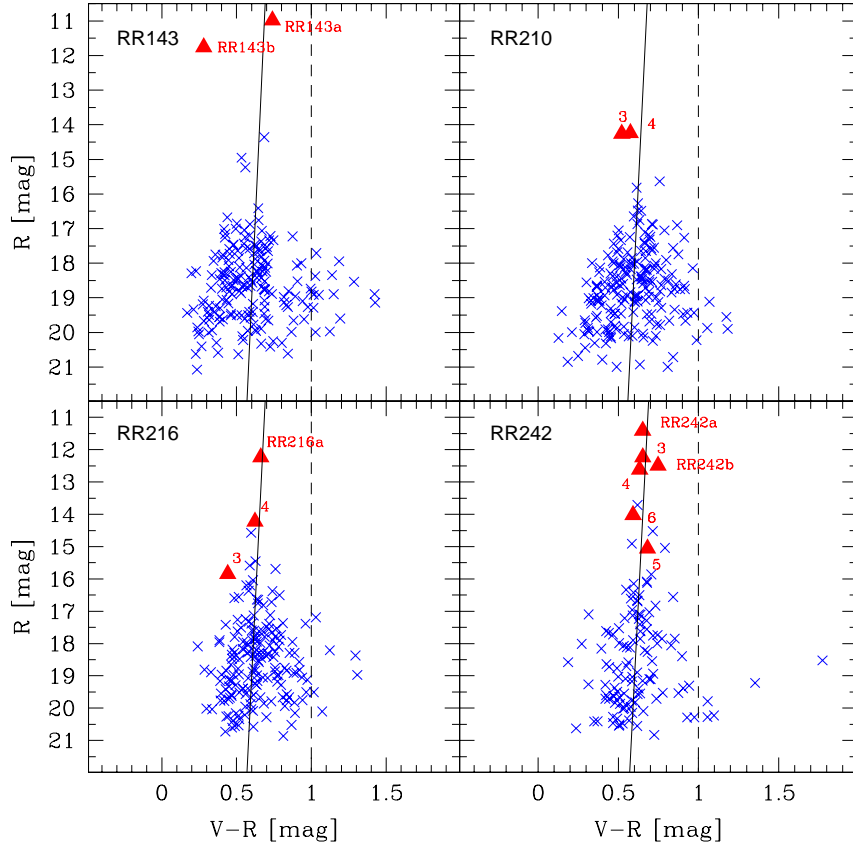
Figure 4.2: Colour-magnitude relation of the candidate faint galaxy sample around the 4 pairs. The dashed vertical lines represent the applied colour limit above which galaxies are considered to be likely background galaxies and were therefore excluded from our sample.

4.2 Colour restriction via the CMR

The colour-magnitude diagrams of the detected and selected galaxies in the four respective fields are shown in Figure 4.2. Our sample galaxies follow the well known trend (see e.g. Faber 1973), where fainter objects have bluer colours, reflecting the expected lower metallicities of less massive galaxies, since the enriched material ejected by supernovae is more easily blown out of the galaxy. This trend is well defined in the blue colour regime while contamination with background objects becomes evident at the red end of the distribution. The bold line in Figure 4.2 represents the colour-magnitude relation for the Virgo cluster (Visvanathan & Sandage 1977) adjusted for the respective pair recession velocities. The red triangles are the galaxies

in the WFI-field with similar recession velocities from NED, labelled as in Table 2.4. Apart from the spiral RR 143b, they all follow the red sequence valid for early-type galaxies and bulges, showing a very small spread in colours.

Colour restrictions are the most common way to exclude likely background objects when no redshift information is available and were used by many authors (see e.g. Khosroshahi et al. 2004). The magnitude of an object in a certain filter changes with redshift dependent on the wavelength of the used filter and the shape of the object's spectral energy distribution, i.e. its morphological type. To account for this shift the so-called K correction for the respective bandpass has to be added to the observed magnitude, changing the colour of the object. Fukugita et al. (1995) found from synthetic galaxy colours that the K-correction for a typical elliptical galaxy at $z \sim 0.2$ corresponds to a shift in colour of $\Delta(V - R) \sim 0.2$ mag. Adopting an intrinsic colour of ellipticals of $(V - R) \sim 0.7$, galaxies with a colour of $(V - R) > 0.9$ are already most likely in the background. Therefore, for the sake of simplicity, all objects with $(V - R) \geq 1$ were excluded from the sample (dashed line), leading to the exclusion of 4 - 15 objects/system. The colour limit is shown as a dashed line in Figure 4.2. The resulting colour-restricted candidate populations do not differ in colour in the respective groups. The mean colour of the whole sample of candidate group members around all 4 pairs is $(V - R) = 0.58 \pm 0.17$ mag.

4.3 Projected spatial distribution of the candidate member galaxy population

The spatial distribution of the faint candidate members was investigated by computing the local projected density around each object. This estimate is based on a method described by Dressler (1980). It consists of determining the radius and the corresponding area in Mpc^2 within which the 10 nearest neighbours of each galaxy reside and hence computing the projected number density of galaxies per Mpc^2 for each galaxy position. To construct iso-density contours these values have to be interpolated to a grid. The mapping software `EasyMapping`[1] was used for this purpose. The thin plate splines interpolation was found to give the best results within a reasonable computing time. The resulting iso-density maps of the colour-restricted candidate samples are shown in Figure 4.3 for each of the four systems of galaxies. The positions of galaxies with known and similar redshift within the WFI field are marked with triangles sized according to their absolute magnitude (the intervals are given in the figure), while the candidates are marked with small crosses. The X-ray contours are also shown as black contours around RR 143 and RR 242. The

---

[1] `EasyMapping` is a mapping software developed by Olivier Monnereau and is available from *http://perso.wanadoo.fr/olivier.monnereau/EasyMapping.htm*

distribution of candidates around RR 242 seems to be smoother than in RR 143 and RR 216, where some high density clumps probably not connected to the pair are visible. Most of the candidates around RR 210 seem to be concentrated in a high density clump northwest of the pair, most probably a background structure. Interestingly, the density maps of RR 242 and RR 216, one pair with extended IGM and one without, seem to be more similar than - as we would expect - the maps of the two pairs with IGM or the two pairs without respectively.
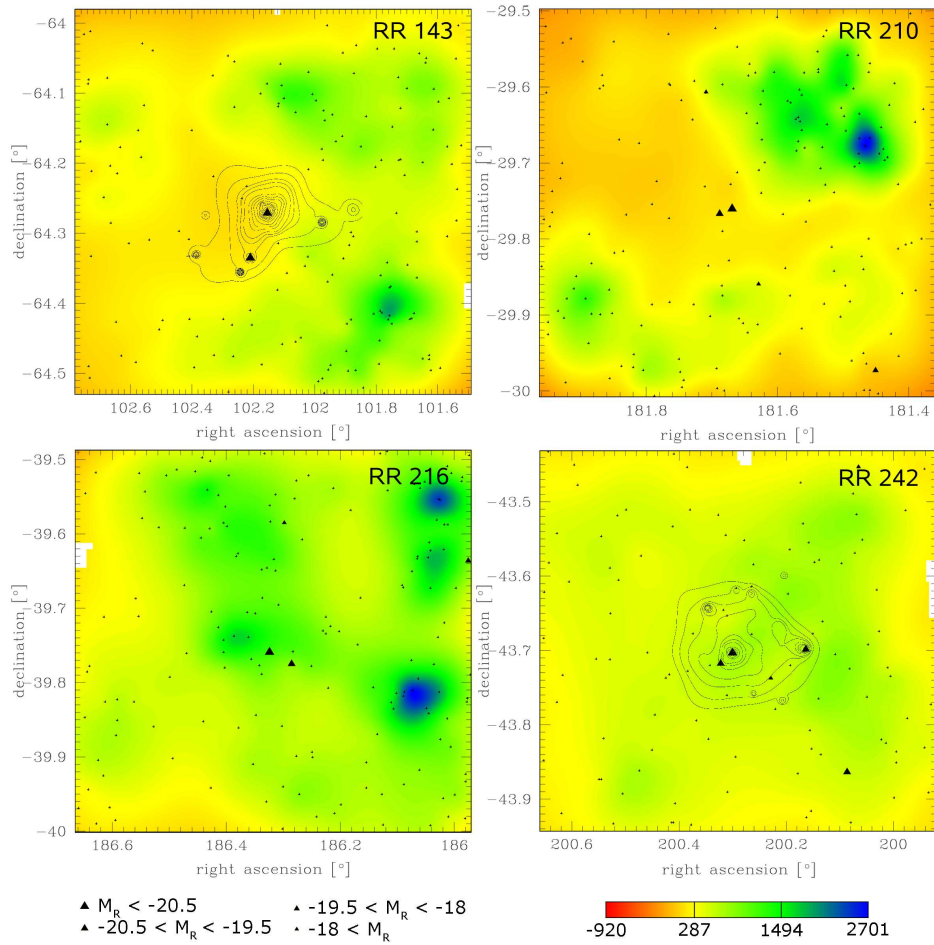
Figure 4.3: Number density distribution of candidate members in the field of each pair. Galaxies with similar radial velocity are marked with triangles sized according to their magnitude. The candidates are marked with small crosses, whereas the contours around the pair are the contours of the X-ray emission. The projected number density is computed in galaxies Mpc^{-2} from red (low) to blue (high).

4.4   Surface photometry of the candidate member galaxies

4.4.1   Why fitting a Sersic law?

Surface photometry was performed on this sample using the `GALFIT` package (Peng et al. 2002). `GALFIT` fits a 2-dimensional model to galaxy images, where the radial luminosity profile may be fitted by different functions. The surface brightness profile of bright ellipticals is known to follow the de Vaucouleurs law (de Vaucouleurs 1948):

$$I(r) = I_e \exp\{-7.67\,[(\frac{r}{r_e})^{1/4} - 1]\} \tag{4.1}$$

where $I(r)$ is the intensity at radius r and I_e the intensity at the effective radius r_e. Extending the study of the family of ellipticals to systems of lower mass, it became obvious that the shape of the radial surface brightness profile, described by the exponent $1/n$, is changing with mass. The de Vaucouleurs law, where $n = 4$, seems to be only a special case of the generalized Sersic law (Sersic 1968):

$$I(r) = I_e \exp\{\kappa\,[(\frac{r}{r_e})^{1/n} - 1]\} \tag{4.2}$$

where the shape parameter n is a free parameter of the fit, decreasing with mass and κ a factor dependent on n. The different shape of profiles with different n is shown in Figure 4.4. There seems to be a continuous trend for n decreasing with galaxy luminosity, extending over ten orders of magnitude from bright ellipticals to the class of dEs (Graham 2005), which were found to have exponentially decreasing surface brightness profiles ($n \sim 1$), similar to disk dominated galaxies. This shape parameter (or Sersic parameter) n may therefore be an efficient way of discriminating between nearby faint disk galaxies or dEs ($n \sim 1$), that are possibly associated to the pair and bright background Es with a higher n.

4.4.2   Automatic fitting with `GALFIT`

We performed an automatic fit for all selected candidates with a 1 component Sersic law to obtain the photometric parameters such as central and effective surface brightness (μ_0 and μ_e respectively), effective radius r_e and, of course, the Sersic parameter n. `GALFIT` is quite sensitive on the given input parameters of the model. To prevent the program from crashing or finding only a local minimum instead of the true global minimum and best solution, reasonable parameters should be given as a first approximation. Therefore, an input file for each galaxy was constructed taking the geometric and photometric parameters determined by SExtractor as input parameters for the Sersic model. Sextractor's detection radius for example can
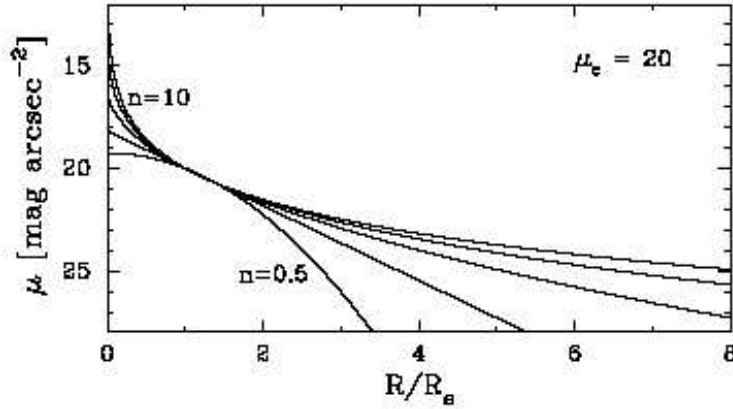
Figure 4.4: The dependence of the profile shape on the Sersic parameter n. The figure shows profiles from $n = 0.5$ to $n = 10$ with the same r_e for $\mu_e = 20$ mag arcsec^{-2} (taken from Graham & Driver 2005). Profiles with higher n (bright ellipticals) are more centrally concentrated and also more extended.

be used as reasonable approximation of the effective radius r_e. The free parameters within GALFIT are the galaxy's center coordinates (x,y), the total flux F_{tot}, the effective radius r_e, Sersic index n, axis ratio $q = b/a$, the position angle PA and the diskiness-boxiness parameter c. F_{tot} is converted into a magnitude using the exposure time keyword EXPTIME from the image-header and the photometric zeropoint given in Table 2.2. Σ_e and Σ_0, the effective and central surface brightness are not fitted but can be calculated from the other output parameters:

$$\Sigma_e = \frac{F_{tot}\kappa^{2n}c}{8nqr_e^2 e^\kappa \Gamma(2n)\beta(1/c, 1 + 1/c)} \quad (4.3)$$

where $\beta(x, y)$ is the Beta-function defined as $\beta(x, y) = \Gamma(x)\Gamma(y)/\Gamma(x + y)$ and $\Gamma(x)$ is the Gamma function. κ is a function of n defined in a way that half of the total flux F_{tot} is within r_e. It can be approximated by $\kappa \approx 2n - 0.3271$ (Capaccioli 1989). The central surface brightness Σ_0 follows from Σ_e:

$$\Sigma_0 = \Sigma_e e^\kappa \quad (4.4)$$

Σ_e and Σ_0 are then converted to magnitudes with the photometric zeropoint, yielding μ_e and μ_0 via $\mu = zp - 2.5 \log \Sigma$.

GALFIT also has difficulties dealing with big images. To minimize the computing time, the fit was carried out on small thumbnail images copied from the WFI frame. For each galaxy a square thumbnail centered on the galaxy with a size of 5× the detection radius given by SExtractor was copied.

The resulting surface photometric parameters of the fit (m_R, n, r_e, μ_0 and μ_e) of all four samples can be found in Tables A.1 − A.4 given as Appendix A.

Figure 4.5 compares the input magnitudes (measured by `SExtractor`) with the fitted output magnitudes of `GALFIT` as a function of magnitude. There is no significant difference between the respective samples (RR 143: red, RR 210: blue, RR 216: magenta and RR 242: green). There is also no significant trend with magnitude. The median differences are $\langle mag_{fit} - mag_{sex} \rangle < 0.02$ in all magnitude bins with a rms of ~ 0.1 mag. Both, the median as well as the rms scatter (solid line and dashed line in Figure 4.5 respectively) are more or less constant with magnitude.
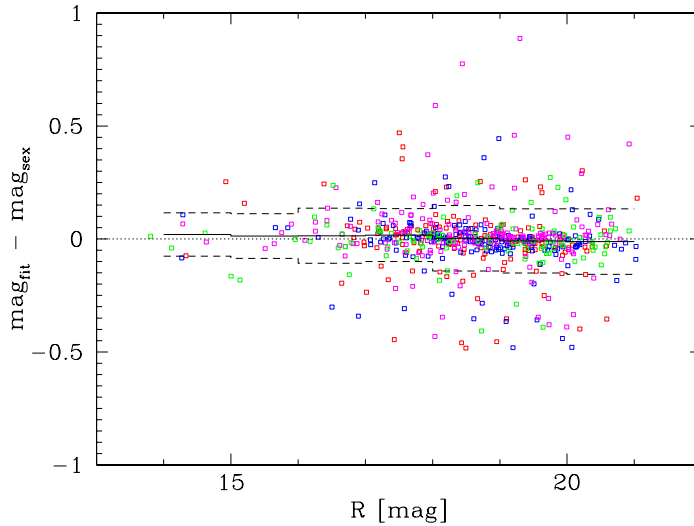
Figure 4.5: Comparison between magnitudes measured by `SExtractor` and fitted by `GALFIT` plotted vs. magnitude. The 4 samples are coloured in red (RR 143), blue (RR 210), magenta (RR 216) and green (RR 242). The bin size for the median (solid line) is 1 mag. The dashed line gives the rms scatter of the magnitude difference in each magnitude bin.

4.4.3   Fitting isophotal profiles with `ELLIPSE`

To test the reliability of the automatic fitting procedure a random sample of candidates was also fitted isophote by isophote with the `IRAF` task `ELLIPSE` (see also Section 2.2.3) higher n. The resulting radial profiles of surface brightness, ellipticity, position angle, Fourier coefficients and $(V - R)$ colour are shown in Figures 4.6 and 4.7. The central area affected by the seeing (usually $\sim 0.8''$) is not shown in the plots. We then compared the isophotal profile (open circles: R band, filled circles:

V band) with the respective `GALFIT` model. The surface brightness profile in the R band of the model for each galaxy is plotted as solid line in the surface brightness panel of each figure. Obviously, the surface brightness profile of the galaxy model corresponds very well with the measured isophotal surface brightness profile of the example galaxies. The model parameters (fitted R band magnitude, absolute magnitude M_R computed with the distance of the pair, central and effective surface brightness μ_0 and μ_e and n) are also given in the surface brightness panel. The left side of Figures 4.6 and 4.7 shows the R band thumbnail of the galaxy together with the residual image after subtraction of the galaxy model. Our sample galaxies are galaxies of different morphological types, ranging from prototypical dE galaxies (object 3519) over faint spirals (object 12209) to brighter galaxies, here a SB0 (object 4052) with a dominant disk (low n) and a bar, visible as a region of flatter μ profile, different PA and a peak in ϵ.

4.4.4 Resulting photometric parameters

Figure 4.8 shows the histograms of the resulting parameters of the automatic fitting procedure. The Sersic index distribution of candidates around all pairs (bottom left) peaks at $n \sim 1$, consistent with most of our candidates being either faint late-type or low-mass early-type dwarf galaxies (see eg. Binggeli et al. 1984). The absolute magnitude M_R and effective radius r_e in kpc were calculated assuming that all candidates are at their respective pair's distance. The M_R distributions (Figure 4.8, top panel) of our sample objects around RR 143, RR 216 and RR 242 are very similar with peaks at $M_R \sim -14.8$, $M_R \sim -14.3$ and $M_R \sim -14.5$ respectively. Figure 4.8 also shows that the r_e distributions (bottom right) of candidates around these pairs have similar peaks around $r_e \sim 0.5$ kpc.

Although the average Sersic index n of the candidates in the RR 210 field is $n \sim 1$, the distributions of M_R and r_e peak at fainter magnitudes ($M_R \sim -13.5$ mag) and at smaller effective radii ($r_e \sim 0.3$ kpc) with a noticeable lack of objects with r_e between 0.5 and 1 kpc. Furthermore the M_R distribution shows a lack of candidates in the range $-15 \geq M_R \geq -18$ and an excess between $-12 \geq M_R \geq -14$. The smaller distance of this pair would explain the larger number of candidates with fainter absolute magnitudes but does not account for the deficiency of objects between $-15 \geq M_R \geq -18$. If we further consider that the objects appear concentrated in a clump to the northwest of the pair (see Section 4.3), we expect that most of them are in a separate structure, most likely a background group.

Figure 4.9 shows the dependence of the Sersic parameter n on the galaxy's R band magnitude. The 4 samples are coloured as in Figure 4.8. The correlation shows a large spread, but indeed, the higher n galaxies in our sample tend to be brighter. If we transform the apparent magnitude into absolute magnitude M_R, a shift between
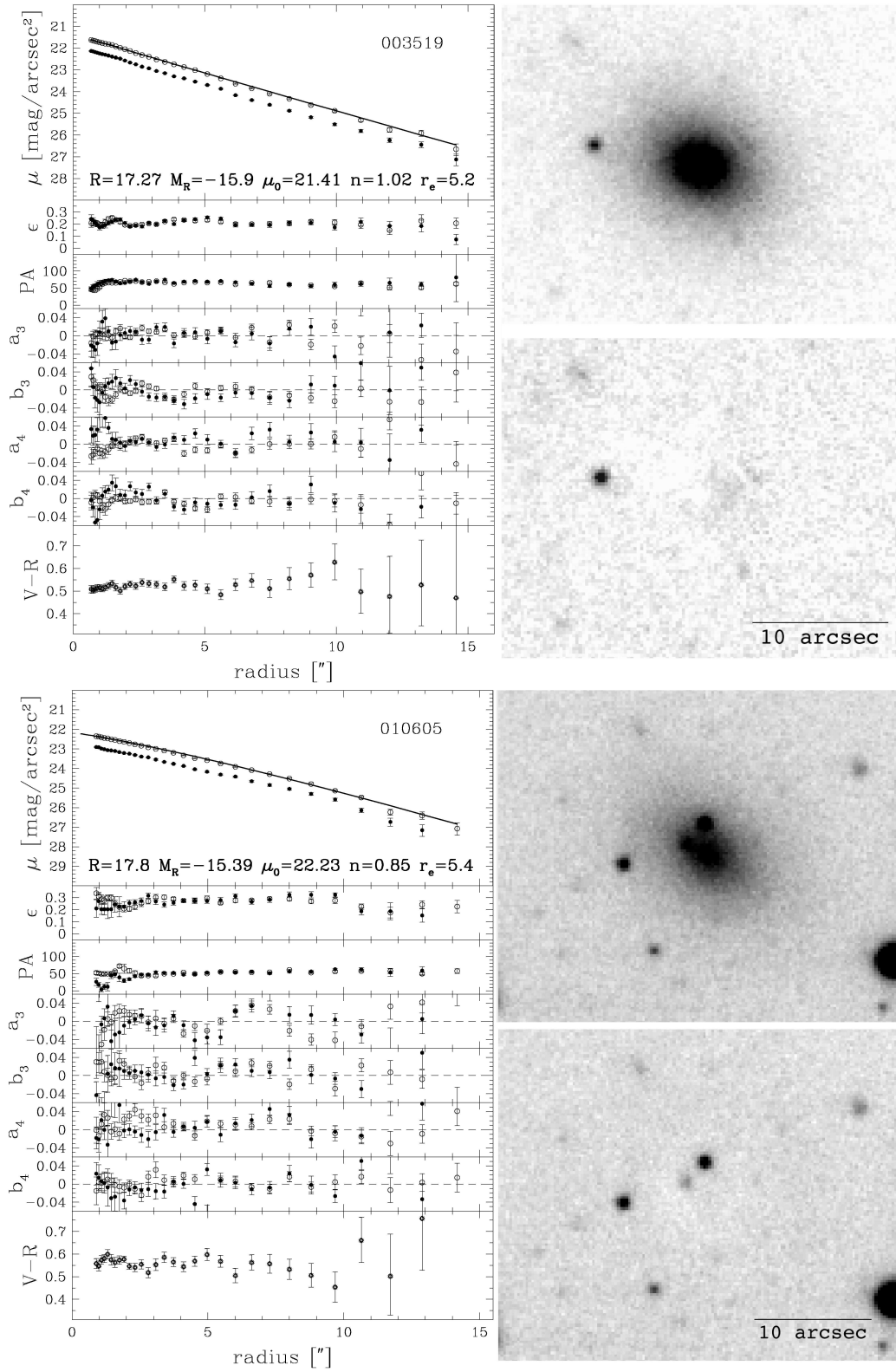
Figure 4.6: Surface photometry of candidate faint member galaxies: objects 3519 and 10605.
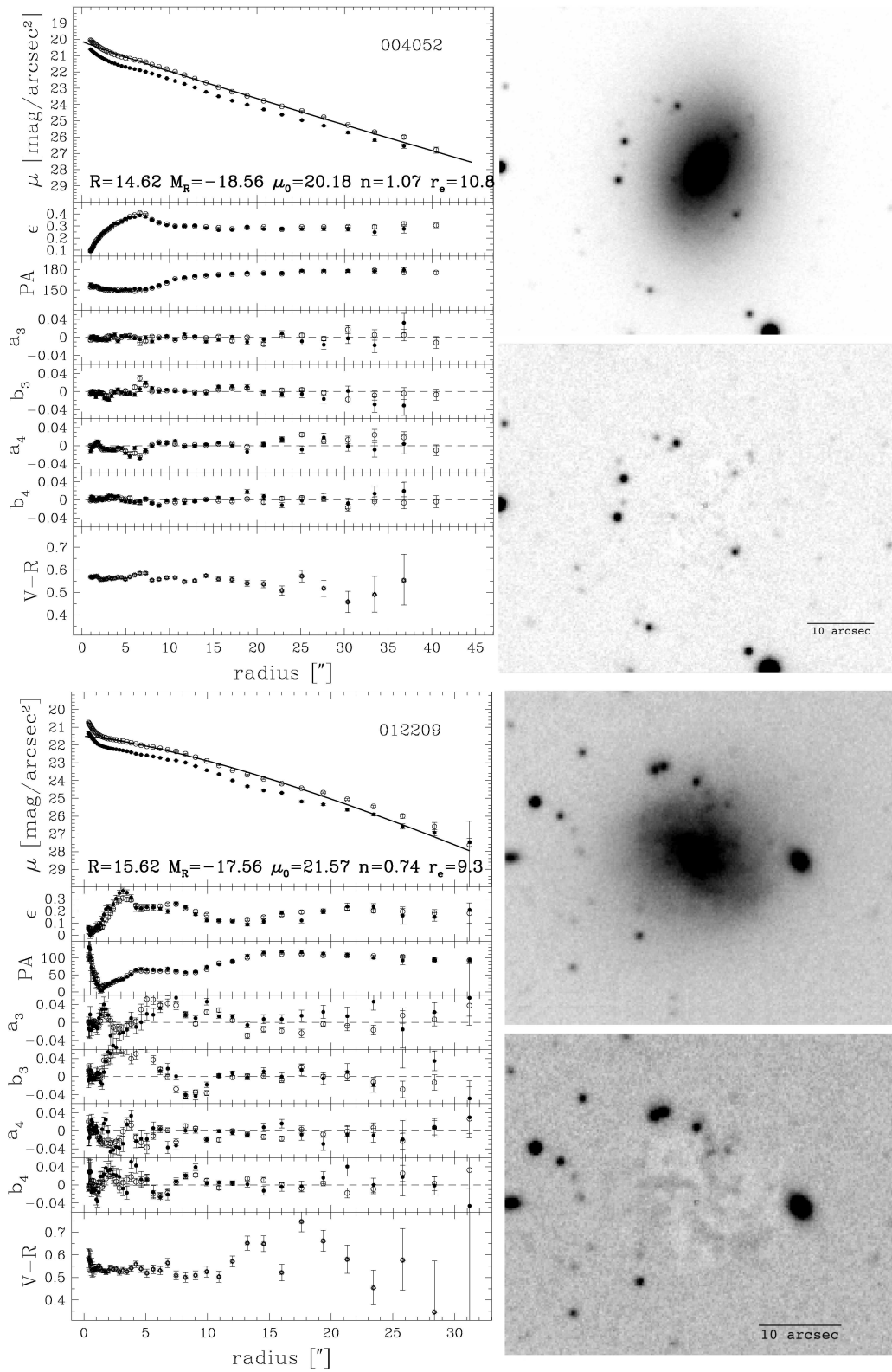
Figure 4.7: Surface photometry of candidate faint member galaxies: objects 4052 and 12209.
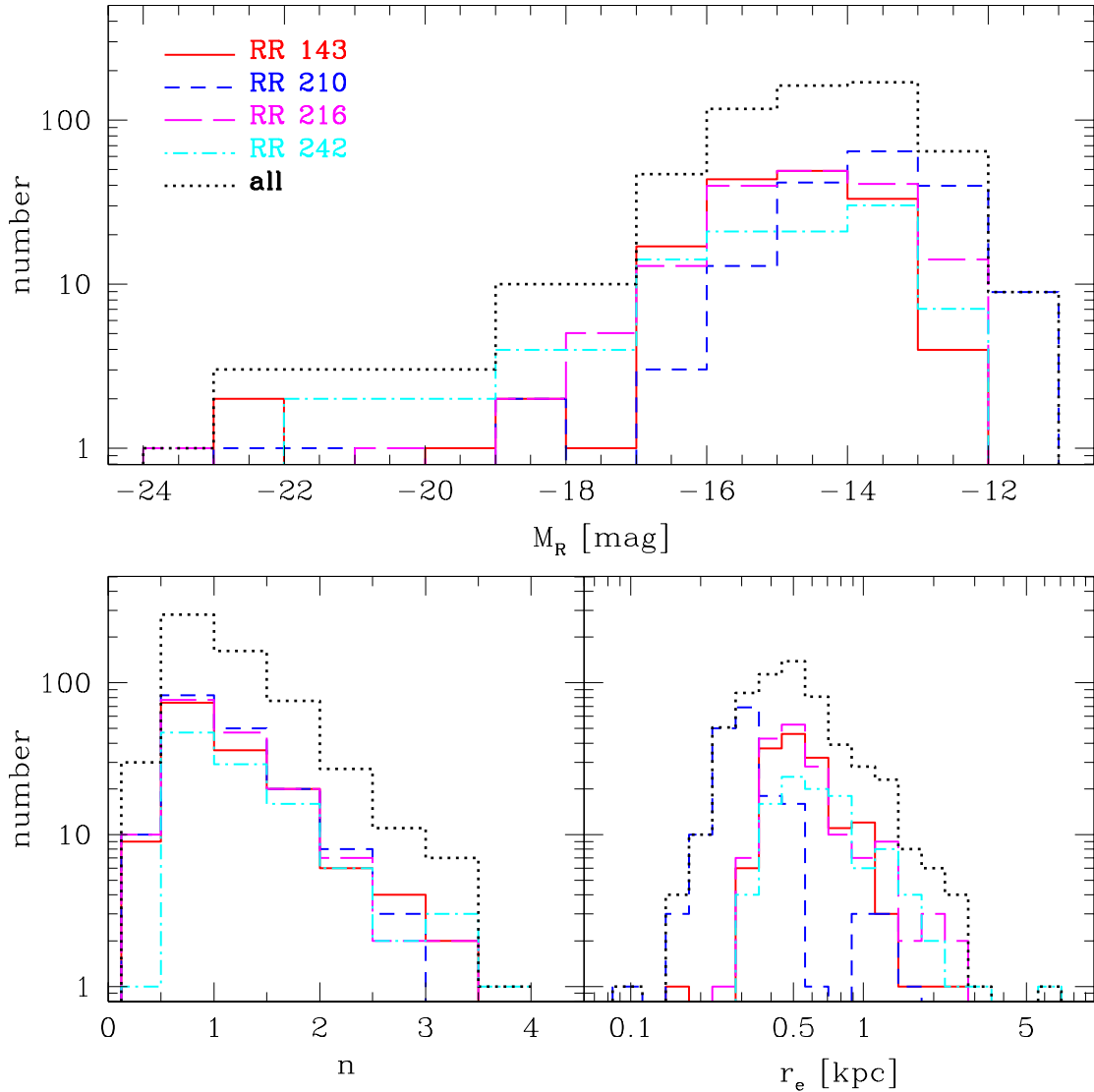
Figure 4.8: Histogram of absolute Magnitude M_R (*top*), Sersic index n (*bottom left*) and effective radius r_e (*bottom right*).

the different samples becomes visible, especially the sample around RR 210 seems to be offset in M_R. Of course, due to its smaller distance, the limiting magnitude of 21 mag corresponds to a fainter absolute magnitude than in the other fields (~ -11.5 vs ~ -12.5 for the other 3 fields). This effect is even better visible in the plots of r_e vs. magnitude in Figure 4.10, since the different distance affects also the physical size of the objects. Now one could argue that in this field (RR 210) we sample the faint galaxy population down to a fainter magnitude and a smaller
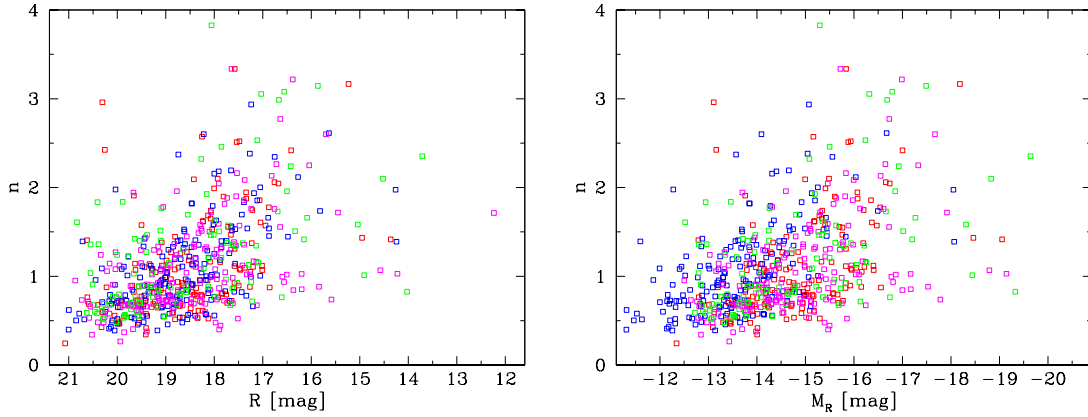
Figure 4.9: Sersic parameter n plotted against R band magnitude and absolute magnitude M_R. The 4 samples are coloured in red (RR 143), blue (RR 210), magenta (RR 216) and green (RR 242).

size, which is certainly true. But if this would be the only difference in the samples, the RR 210 sample should show the same continuous distribution in magnitude and size, down to fainter magnitudes and smaller sizes. Obviously, this is not the case. Most of the candidates in this sample are small and faint (see also histograms in Figure 4.8), but have the same n as brighter galaxies in the other samples. Galaxies at $M_R \sim -14$ already show values of $n > 2$ (see blue symbols in Figure 4.9), whereas the exponential galaxies ($n \sim 1$) lack from $M_R \lesssim -15$.
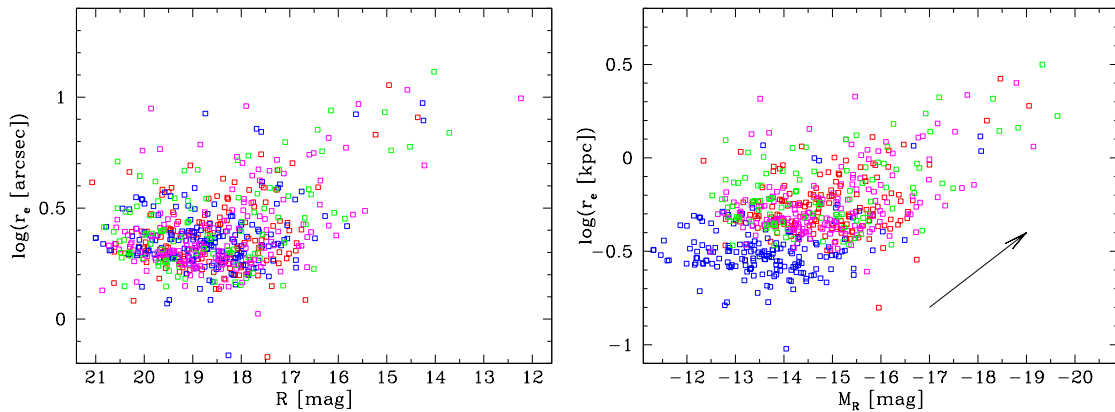
Figure 4.10: Effective radius r_e plotted against R band magnitude and absolute magnitude M_R. The arrow indicates the direction in which galaxies would move in the plot if their distance would be larger. Colour-coding like in Figure 4.9.

From the number distribution of n in Figure 4.8 this difference is not visible, because there are many galaxies with $n \sim 1$ at very faint magnitudes. These very faint galaxies could easily be $\sim 3mag$ brighter dwarf elliptical galaxies in a background group at $\sim$ 4-5 times the pair's distance and would still follow the $M_R - n$ relation. For the $M_R - r_e$ relation the distance has no effect, since the galaxies would move exactly along the predicted relation if their distance is changed (arrow in Figure 4.10).

4.4.5 M_R - μ_0 - n relations

In order to further investigate the properties of candidate dwarfs and the likelihood of their association to the central galaxy pair we studied the relations between M_R, μ_0 and n as proposed by Graham (2005). They investigated the structural and photometric parameters of a large sample of galaxies from bright E to dE covering a range of about 10 magnitudes and found that these parameters follow a linear relation (logarithmic for n) over the whole magnitude range. The interesting thing for us is the connection between distance-dependent (M_R) and distance-independent (μ_0, n) quantities.

Figure 4.11 shows our 4 samples in the planes of $M_R - \mu_0$, $M_R - n$ and $\mu_0 - n$ plotted with the relation found by Graham (2005). The candidates are plotted in blue, whereas the red triangles are the galaxies within the field with similar redshift found in the literature, labelled as in Table 2.4.

The top left panel shows the plane of $M_R - \mu_0$ and obviously most of our candidates follow the predicted relation, although shifted in absolute magnitude. The most conspicuous case is - again - RR 210, where almost the whole sample seems to be offset systematically. We fitted our samples with the slope fixed at the value given by Graham (2005) to determine the likely shift in magnitude and found the following: RR 242 and RR 143 are offset by $\sim$ 1 mag, RR 216 is offset by $\sim$ 1.5 and RR 210 is offset by $\sim$ 2.5 mag. This suggests that there is moderate background contamination in the X-ray pairs RR 242 and RR 143, but also a significant population of probably new group members, as well as around RR 216, which seems to have a larger background contamination than the X-ray pairs but also a larger fraction of possible faint companions than RR 210. I contrast to this, the sample of RR 210 seems to consist mainly of background objects. The magnitude shift of the RR 210 sample corresponds to a shift in distance of a factor of > 3, which is consistent with the implications of the other photometric properties as well as the number density maps (see Section 4.3). Notice also that the 2 confirmed members (red triangles labelled 3 and 4, which is *not* the central pair) are close to the value expected from the correlation. The confirmed members that deviate from the relation (3, 6 and RR 242b in RR 242 and RR 216a) are spiral galaxies.
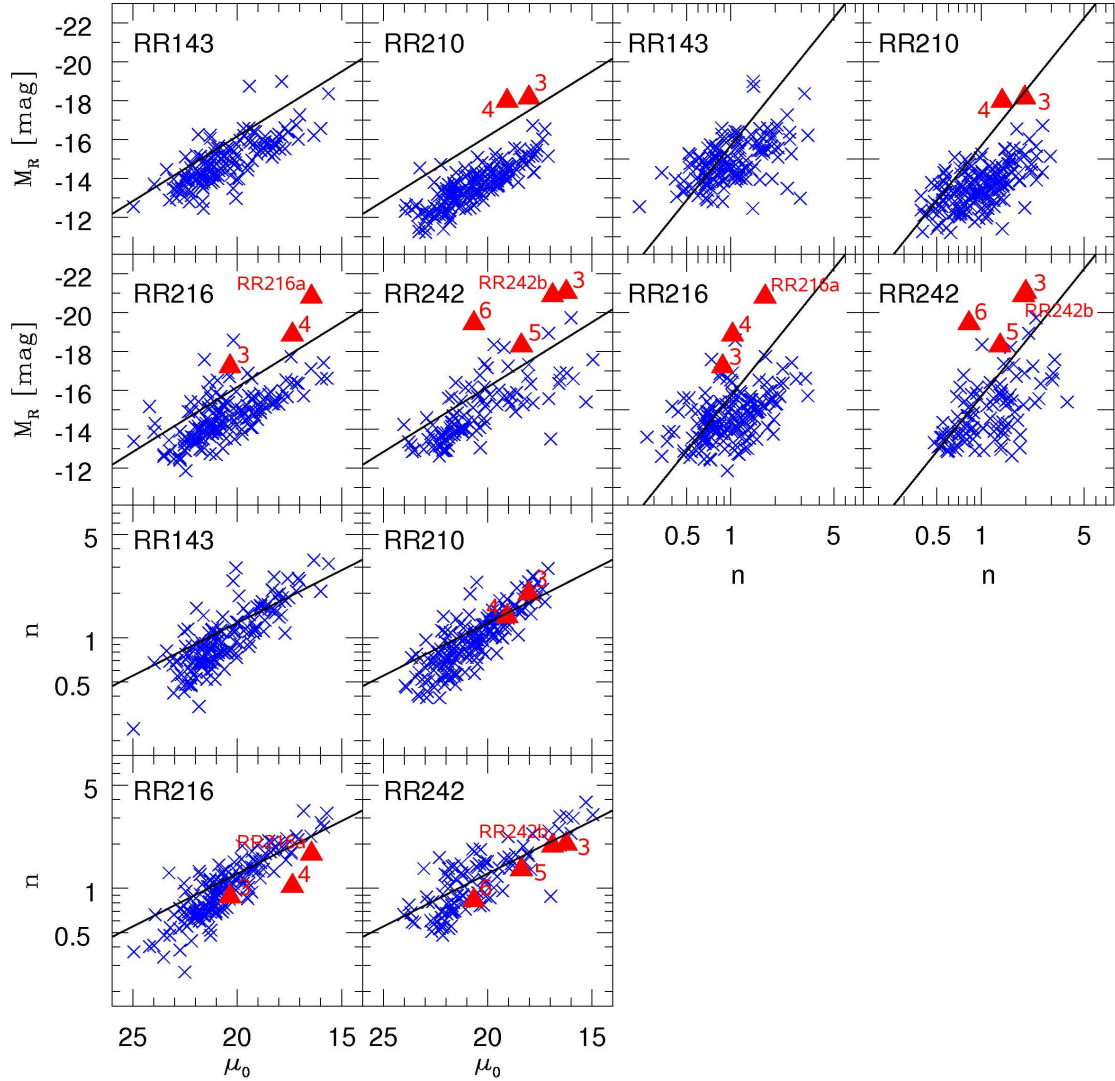
Figure 4.11: $M_R - \mu_0 - n$ Relation. The blue crosses are the candidates, the red triangles are galaxies in the WFI-field with similar redshift found in NED (also called confirmed members). The solid line is the respective relation found by Graham (2005) for a large sample of early-type galaxies from bright Es to dEs.

The relation between $M_R - n$ doesn't seem to be as tight as the $M_R - \mu_0$ relation, but nevertheless it is worth looking at it in more detail. It supports the implications of Figure 4.9, which is basically the same plot but with n in a linear scale and without the Graham (2005) relation plotted. As suggested by Figure 4.9, more faint galaxies in RR 210 deviate from the relation than in the other pairs' samples. The galaxies
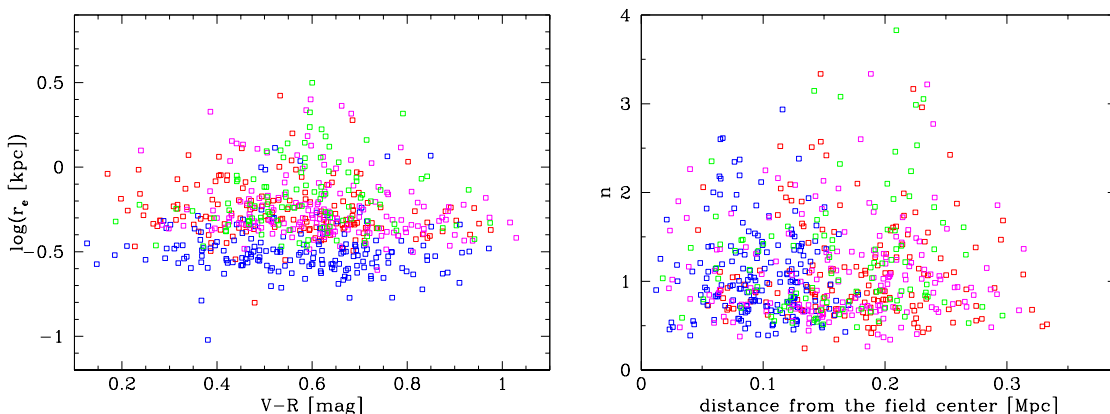
Figure 4.12: Left panel: effective radius r_e plotted against global $(V - R)$ colour. Right panel: candidates' projected distance from the geometric center of the pair in Mpc plotted against the Sersic index n to probe the presence of a morphology-density relation. Colour-coding like in Figure 4.9

with higher n are all off the relation, in contrast to the two confirmed member galaxies that follow the relation quite well. But also in the other samples, most of the galaxies with high n are displaced from the relation, which is consistent with the expectations not to find galaxies with high n at low luminosities and that the high n galaxies are more probably background galaxies than the galaxies with exponential profiles.

4.4.6 Structural parameters in connection to other properties

From the correlation between magnitude and effective radius and magnitude and colour, we would expect a correlation between effective radius and colour. Figure 4.12 shows the plot of r_e against $V - R$ colour. Obviously, this plot mirrors the colour-magnitude relation, but with a larger spread. The (merely visible) peak at $V - R \sim 0.6$ is exactly the position of the red sequence for early-type galaxies. Obviously, a significant background contribution, which is very difficult to remove without redshift measurements is still present in our samples.

Another interesting correlation is the so-called morphology-density relation. This relation says that more centrally concentrated galaxies (high n) are located in environments with higher local density, usually the center of galaxy clusters. However, this correlation was found to hold also for galaxy groups even poor groups, mostly for those with extended X-ray emission. The question is therefore, in which environment this correlation starts to build up and if very local density enhancements are

sufficient to change the galaxies' morphologies or if a global high density field and deep potential well is needed. The projected distance from the geometrical center of the pair in Mpc is plotted against n in Figure 4.12 (right panel). Interestingly, the highest n are found in medium distance from the center. Although, if we consider the highest n galaxies to be most likely in the background (as argued in the previous sections), the picture changes to a more constant distribution of n with distance. If there is a trend in n with distance from the pair, there is obviously too much background contamination and projection effects that make this trend undetectable without having the redshift information.

4.5 Expected number of background galaxies

The expected contribution from background galaxies was estimated using the program `GalaxyCount`[2] (Ellis & Bland-Hawthorn 2007). The program calculates the number of background galaxies (and standard deviation) expected in a magnitude limited observation of a given field. This number of expected galaxy counts is mainly dependent on the characteristics of the observations, that can be simulated with `GalaxyCount`. We adopted an average seeing of $0.8''$, a search area of $33' \times 33'$, and an exposure time of 50 minutes with the collecting area of a 2.2 m telescope. We further adopted a throughput of 60% for the WFI instrument. Using a range of S/N values we derive for the interval $15.0 < m_R < 19.5$ mag $\sim 170 - 200 \pm 20$ galaxies with a completeness of about 95%.

This number is compatible with the number of galaxies we found in our fields of view, suggesting that we are dealing with background galaxies only. However, we used additional selection criteria for galaxy identification with SExtractor, for example the cutoff in size of $1.5''$, which is not reproduceable within `GalaxyCount`. We choose this cutoff of $\sim 2\times$ the seeing FWHM to carry out a reasonable surface photometry of the objects. However, this cutoff is highly influencing the resulting number of candidates. Changing the minimum detection radius from $1.5''$ to $1''$ for example, results in a $\sim 5\times$ larger number of detections. Therefore it is very difficult to compare our numbers to the expected background galaxy counts given by the program.

Anyway, from this analysis we can confirm that we are exploring very low density environments and that the expected number of member galaxies around the respective pair is small - in the order of $\sim 20\%$ - as suggested already from the study of the photometric parameters and what was also found by other authors (see eg. Zabludoff & Mulchaey 1998).

---

[2]http://www.aao.gov.au/astro/GalaxyCount/

4.6   Summary and conclusions

In this Section the results of the search for faint galaxies possibly associated to the 4 galaxy pairs RR 143, RR 210, RR 216 and RR 242 are summarized.

   – We detected a sample of candidate faint galaxies in the WFI fields around the 4 pairs using the SExtractor (Bertin & Arnouts 1996). The candidates were selected to have a stellarity parameter ≤ 0.5 to exclude stellar sources, furthermore $R < 21$ mag and $a > 1.5''$ corresponding to a reasonable physical size similar to the faintest dwarfs in the Local Group and allowing a reasonable surface photometry on the candidates.

   – The selected sample was limited in $(V - R)$ colour via the colour-magnitude relation to exclude likely background galaxies.

The final selected and colour restricted samples comprise 151, 172, 160 and 102 candidate galaxies in the RR 143, RR 210, RR 216 and RR 242 fields respectively. An important thing to keep in mind before we compare the properties of the different samples, is the fact that three of the pairs (RR 143, RR 216 and RR 242) show very similar recession velocities around 3500 km s^{-1}, whereas RR 210 is situated at a smaller distance of ~ 2000 km s^{-1}. This is affecting the properties of the candidates connected to their distance, which are absolute magnitudes and sizes and distances in physical scales.

   – Automated fitting of a Sersic profile ($\mu \sim r^{1/n}$) to all selected candidates showed that our candidate populations in all fields peak at $n \sim 1$, suggesting that they are indeed faint galaxies possibly physically connected to the pair.

   – The distributions of absolute magnitude M_R and effective radius r_e show that RR 210 is different from the other pairs, but not only as it would be expected from its smaller distance. The smaller distance would imply that the distributions have the same shape, but with the RR 210 sample extending towards fainter magnitudes. In contrast to this, the distributions are not more extended, but *shifted* in absolute magnitude, suggesting that most of them are indeed a few magnitudes brighter and belonging to a background structure. An other possibility would be that the shape of the luminosity function in RR 210 is different from the other pairs with a dip between $-18 > M_R > -16$ and lots of faint dSph members, which we missed in the other pairs due to the size criterion.

   – Relations between fitted parameters and absolute magnitude suggest that only a small percentage of candidates is really associated to their respective pair.

This relations also suggest that RR 210 is different from the other samples, showing an even larger background contamination than the other pairs.

— This suggestion is also supported by the surface density maps, where most of the candidates in RR 210 are concentrated in a clump to the northwest of the pair. The field of RR 242 shows the smoothest distribution of candidates with the number density also peaking in the center. The same is the case for RR 216, whereas it also shows some prominent high density clumps in the outskirts. In the field of RR 143, the number density of candidates does not peak in the center, although the distribution is not as clumpy as in RR 210 and RR 216.

We conclude that the analysis of photometric and structural properties of the faint galaxy populations around the pairs yields evidence for the presence of an associated dwarf galaxy population in three cases, where the candidates around RR 242 show the highest membership probability. RR 143 and RR 216 probably have a smaller faint galaxy population, while RR 210 seems to have very few associated faint galaxies. However, for conclusive evidence spectroscopic data are required. The process of proposing and successively preparing spectroscopic observations, with the subsequent data reduction and analysis is described in the following chapter.

Chapter 5

The VIMOS Data

The candidate faint galaxy population detected in the WFI field around each of the four pairs (see previous chapter) was observed with VIMOS, the multi-object spectrograph on the ESO VLT. The observations were carried out in service mode, i.e. by the ESO staff astronomers, giving us no influence on the scheduling of the single Observation Blocks (OBs), which can for convenience be carried out in an arbitrary order. Since each pointing of the telescope is a single OB and since we had 4 telescope pointings per pair, this means that not all pointings per pair are carried out in one go, some may be not carried out at all due to time constraints, bad weather or more important programs. Unfortunately, this was the case and our program was not completed. For 2 pairs (RR 143 and RR 242) all 4 pointings were observed, whereas for RR 210 we got only 2 pointings and for RR 216 only 1 of 4. Furthermore this means that the largest incompleteness concerns the pairs without IGM, making a comparison between the two cases very difficult. Nevertheless, we tried to apply a reasonable completeness correction of member galaxies at each magnitude leading to interesting and promising results. With this first results in hand we reapplied for observing time and proposed the completion of our program, which was approved and will hopefully be carried out in the next observing period (Period 80). However, despite the incompleteness of our sample we can present some interesting results.

The following sections describe the whole path from proposing the observations in March 2005 (Period 76) via preparing the so-called Phase 2 material in summer and autumn to finally receiving the data in May 2006. The data reduction pipeline is described as well as the data analysis including redshift measurements to determine the objects that are most probably associated to the pair and the important correction for incompleteness.

Figure 5.1: The primary mirror of UT2, one of the 4 8.2m telescopes of the VLT, seen from the Nasmyth platform.

5.1 Instrument description

The best instrument to cover the whole WFI field containing the candidates and to reach down to the faint magnitudes of our objects was found to be VIMOS (VIsible Multi-Object Spectrograph) on the creatively named Very Large Telescope (VLT) of ESO on Cerro Paranal, Chile. The instrument is mounted on the Nasmyth focus B of UT3 and has four identical arms - the 4 quadrants of the whole field - each having a field of view of $7' \times 8'$ and a gap between each quadrant of $\sim 2'$. This means that we can cover the whole WFI field of $34' \times 34'$ very efficiently with 2×2 VIMOS pointings.

Different instrument configurations, dependent on the scientific goal of the observations, are available. Having in mind the goal of measuring absorption line indices, we choose a high resolution grism covering the spectral region of Hβ, Mg and Fe, which is the HR blue grism. This has a wavelength coverage from 415 – 620 nm at a resolution of 2050 (using a $1''$ slit) and a dispersion of 0.51 Å /pix, allowing only one slit in dispersion direction, i.e. each single spectrum covers the whole length of the detector. The wavelength range is dependent on the position of the slit on the CCD along the dispersion direction. For an object at the edge of the frame it shifts to 480 – 690 nm ($+4'$, upper edge) and 365 – 565 nm ($-4'$, lower edge). The slits are positioned on the targets with masks, that are prepared on Paranal.
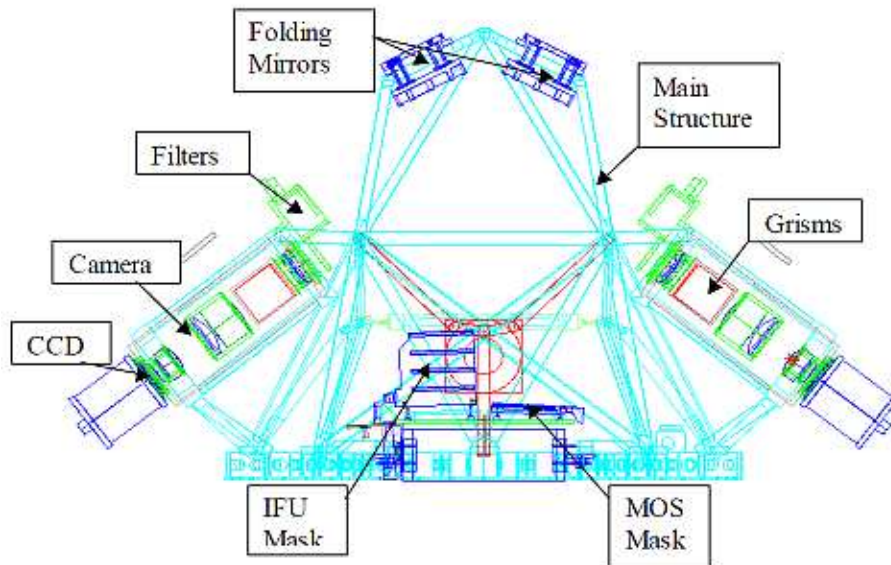
Figure 5.2: Opto-mechanical layout of the VIMOS instrument (image taken from the VIMOS user manual).

For each quadrant of the instrument the user has to define a mask and construct a file containing the position, length and width of each slit using `VMMPS`, the VIMOS Mask Preparation Software. This software has to be used on the pre-images made by VIMOS about 2 month before the spectroscopic observations to ensure a correct positioning of the slit on the galaxy (see Section 5.3).
Figure 5.2 shows the optical-mechanical layout of the instrument with 2 of its four arms, whereas Figure 5.1 shows a picture of the primary mirror of one of the UTs from the platform below the Nasmyth focus.

5.2   The proposal

5.2.1   How to write a successful observing proposal?

To enhance the probability of getting your proposal approved, the following points should be considered:

– Let a PhD student be the principal investigator (PI) of the program. Programs that have a PhD student as PI and are therefore crucial for the completion of a PhD thesis are treated preferentially by the OPC, the committee responsible for ranking the proposals and allocating observing time or not.

– Ask for the observations to be performed in service mode. If the observations are performed in service mode, the single OBs do not have to be carried out in a row (like it is done in visitor mode for obvious reasons) but can be carried out whenever there is a free time slot for a single OB. Therefore the scheduling of your observations should be more easy.

– Have as many data as possible concerning your target already in hand, reduced, analysed and published. Then make clear that this is the final set of data needed by any means to reach the scientific goal. Keep in mind that the number of proposals usually exceed the available time by a factor of ~ 3, this means that you should leave no doubt about the absolute necessity of your observations.

– Don't ask for too much time. Try to find a good balance between absolutely necessary but short integration time with the best possible result. If you manage to keep the whole program below 10 hours of observing time, you can apply in the separate category of `short proposals`, that have a higher chance of being approved, since they are easier accommodated in the available time slots.

– Try to avoid technical mistakes. Even an excellent scientific case can not compensate for mistakes in calculating observing times, overheads, signal-to-noise and so on. In other words, technical mistakes or doubts about the feasibility of the program are an invitation to reject a program, that will thankfully be accepted by the OPC.

– Avoid trying to disprove the results of a rival working group. Most probably one of them is part of the OPC.

5.2.2   Structure and contents of an ESO proposal

The scientific description of the proposed program is divided into the `Scientific Rationale`, giving the scientific motivation of your observations and the `Immediate Objective`, describing what exactly is going to be observed, which methods of analysing the data will be used and what detailed results and conclusions are expected to be drawn from this analysis.

The technical part consists of the justification for the need of exactly this telescope and instrument configuration, the justification of the requested observing mode (visitor or service), the justification of the amount of observing time needed and the justification of the requested lunar phase. If ESO facilities were used in the last 2 years, the results or at least the progress of the data analysis has to be reported.

Finally, all publications within the last 2 years that are related to the proposed scientific case should be listed.

5.2.3   Technical details of our proposal

The amount of requested observing time should be calculated with the exposure time calculator provided by ESO[1]. The best way to get a meaningful value for the exposure time is to quantify the necessary signal-to-noise ratio (S/N) for the resulting spectra. For measuring redshifts with cross-correlation, the S/N is not that important, while for the calculation of absorption line indices, the S/N is crucial and should not be lower than 25. Using the ETC, we calculated that a S/N of ~ 25 at the central wavelength of the HR blue grism of 5100 Å for a galaxy with $\mu_0 \sim 18$ mag arcsec^{-2} in R band is reached within ~ 1 hour of exposure. A central surface brightness of ~ 18 mag arcsec^{-2} means that we can probably get good indices for the brighter third of our sample. Trying to reach down to fainter magnitudes, the exposure time starts to explode, so we accepted this compromise. The requested lunar phase is dark time around new moon ($\pm$ 3 days) given the intrinsic faintness of the objects.

5.3   Phase 2 - Pre-imaging and preparation of spectroscopic observations

After a proposal is accepted, the Phase 2 preparations can start. This Phase 2 preparations are carried out with the Phase 2 Preparation tool P2PP, which is used to manage Observation Blocks (OBs). All observing sequences at ESO instruments are controlled by these OBs, they have to be prepared by the user regardless whether the observations are carried out in visitor or service mode.

5.3.1   Pre-imaging

First, OBs for pre-imaging have to be prepared. Pre-imaging is mandatory for all spectroscopic observations with VIMOS and are carried out in service mode usually 2 month before the spectroscopic observations. The relevant parameters of the pre-imaging observations have to be entered into one OB for each telescope pointing. Within an OB different templates are available. For pre-imaging, the OB has to include the target information, the set of constraints (seeing, airmass,...), an image acquisition template and the science template defining the parameters of the imaging observation like integration time, filter, number of integrations and guide star coordinates.

Due to the big field of view of VIMOS, the area where suitable guide stars can be located is very small, it can be difficult to find a star for which the field is not

---

[1]http://www.eso.org/observing/etc/

vignetted by the shadow of the guide probe. To simplify the selection of suitable
guide stars, the `GuideCam` tool is provided by ESO and can be downloaded from
the ESO web page[2]. This `SkyCat` based tool displays the field around the target,
marking the positions of possible guide stars from catalogues, the VIMOS field of
view and the projected shadow of the guide probe to avoid blocking scientific targets
in the pre-images. Finding charts for the pre-images have to be prepared by the user
and attached to each OB. For VIMOS pre-imaging observations the use of `GuideCam`
is mandatory for producing these finding charts. Figure 5.3 shows an example for
a submitted finding chart, here the field RR 242-b, the upper right quadrant of the
WFI field. The green rectangle is the field of view of VIMOS, which should not
be cut by the yellow line, indicating the shadow of the guide probe. The red circle
marks the maximal search radius for guide stars.

If no guide star without vignetting of the VIMOS field can be found, the guide
star should be selected in a way that the guide probe obscures a part of the image
where no scientific target is located. The vignetting is not checked by the service
astronomer and has to be checked carefully by the user.

5.3.2   Slit assignment with `VMMPS`

Once the pre-imaging is carried out, the pre-images have to be used for assigning the
slit positions for each target. One slit mask has to be produced for each quadrant
of the VIMOS field of view. This masks are produced at the VLT site but have to
be defined by the user. For this purpose the VIMOS Mask Preparation Software
`VMMPS` has to be used. This software is also a `SkyCat` plug-in and can be downloaded
from the ESO web page. Based on an input catalogue it produces an output file
containing the Aperture Definition in Pixels (ADP) for all slits on the respective
mask. The input catalogue (`contributed catalogue`) with precise astrometry of all
scientific targets and some reference stars is cross-correlated to the VIMOS `pre-image`
`catalogue` of reference stars obtained by running SExtractor on the VIMOS pre-
image. The `contributed catalogue` should containing an ID number, RA and
DEC for all targets and reference stars, whereas the VIMOS `pre-image catalogue`
contains the ID, X_IMAGE and Y_IMAGE coordinates of a number of reference
stars from the pre-image. With this VIMOS `pre-image catalogue` the `contributed`
`catalogue` is then translated into the VIMOS coordinate system. The reference stars
that the two catalogues have in common and that are used for the transformation
appear on the frame as well as the `rms` of the transformation, which should be
around $0.2''$.

The output VIMOS catalogue can then be used for assigning slits automatically.
First, the reference stars (at least 3) have to be selected, optionally compulsory

---

[2]http://www.eso.org/observing/p2pp/OSS/GUIDECAM/
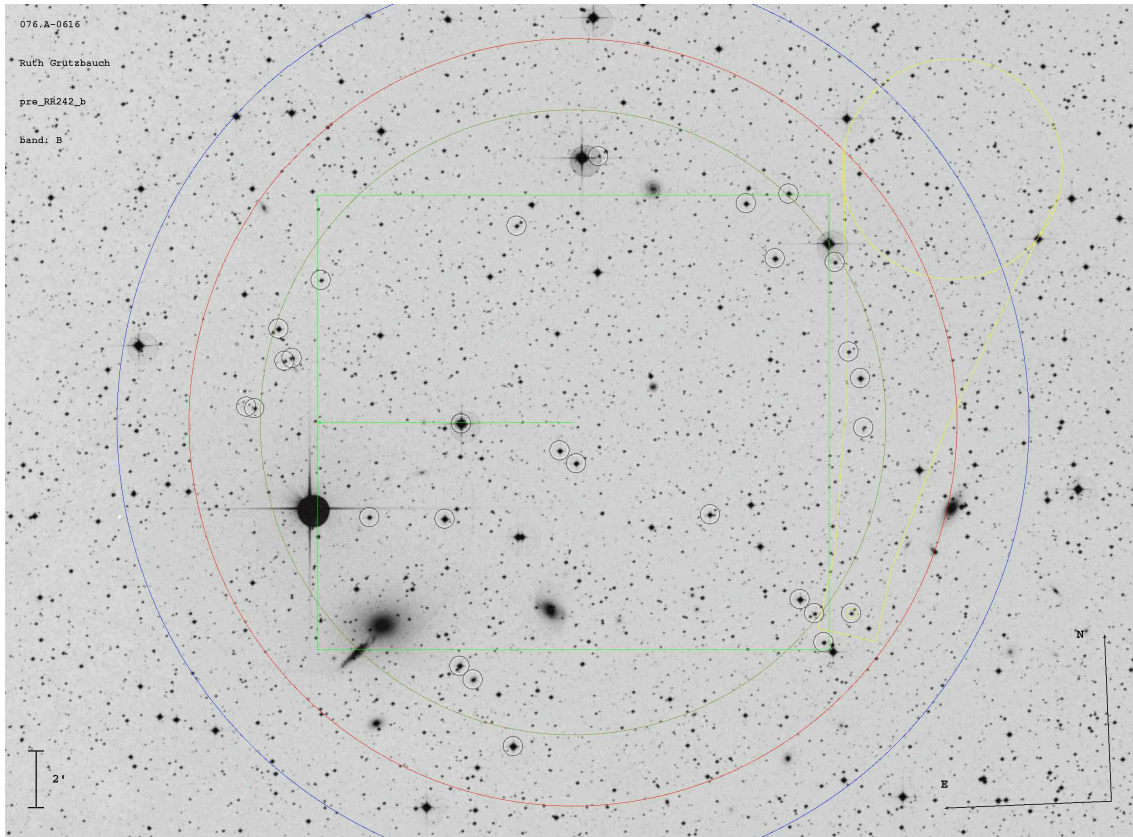
Figure 5.3: Finding chart for RR 242-b, the upper right quadrant of the WFI field. The pair can be seen in the lower left corner. The green rectangle is the VIMOS field of view, the red circle the maximal search radius for guide stars and yellow the projected shadow of the guide probe. Guide stars are marked with small circles. The guide probe shadow should not cut the VIMOS field of view

objects that should be treated with higher priority or forbidden objects can be defined. Then the slit width and the sky region around the objects can be modified. Finally, the program computes the best solution for positioning as many slits as possible without overlapping in spacial or dispersion direction.

Now the allocated slits can be modified or additional slits can be defined manually. This is considered dangerous because the manually entered slits are not checked for overlap. Since for the HR blue grism only one slit can be placed in dispersion direction, only the spacial overlap has to be checked. Moreover, the number of ~ 10 objects per quadrant is low, so the danger of producing overlaps and screwing things up is low too.

All slits were checked by eye and modified if needed, for example if the slit was not exactly positioned on the nucleus of the galaxy or the object seemed to be more spatially extended than the length of the assigned slit.

Finally, the resulting ADP-files of the set of 4 masks for each VIMOS field of view has to be attached to the respective spectroscopic OB. Figure 5.4 shows the slits assigned to one quadrant of RR 242-b.

5.3.3   Submitting spectroscopic OBs

The spectroscopic OBs are prepared and submitted again with P2PP (see above). The procedure and needed parameters are similar to the pre-imaging OBs with the difference that the ADP-files have to be attached to the acquisition template of the OB. For an accurate wavelength calibration a night-time calibration template for an arc-spectrum for has to be added after the science template. The total exposure time for each pointing is 3600 seconds, which were split up in two integrations of 1800 seconds each. VMMPS can be used to plot the ADP-file onto the pre-image to produce the spectroscopic finding charts that have to be submitted with each OB. An example for a spectroscopic finding chart is shown in Figure 5.4.

5.4   The spectroscopic Observations

5.4.1   Characteristics of the observations

The log of the spectroscopic observations is given in Table 5.1. The fields have been observed between January and March 2006. Each pointing was split into 2 identical exposures that were combined during the procedure of spectra extraction. Table 5.1 lists the parameters of each single exposure, which are the integration time, the airmass, the FWHM of the seeing, the angular distance of the moon and its fractional illumination.

5.4.2   Incompleteness and Constraints

Not all submitted OBs were observed, i.e not all 4 pointings per WFI field are available for all pairs. The 2 pairs with detected diffuse X-ray emission RR 143 and RR 242 were observed completely, whereas the other 2 pairs RR 210 and RR 216 were partially observed, covering only the northern (upper) half and the northeastern (upper left) quarter of the total field for RR 210 and RR 216 respectively.

The respective OBs were also observed under different observing conditions, the constraints for airmass, seeing, moon distance and illumination were not fulfilled for all OBs. For example RR 242-b was observed with a very high fractional lunar
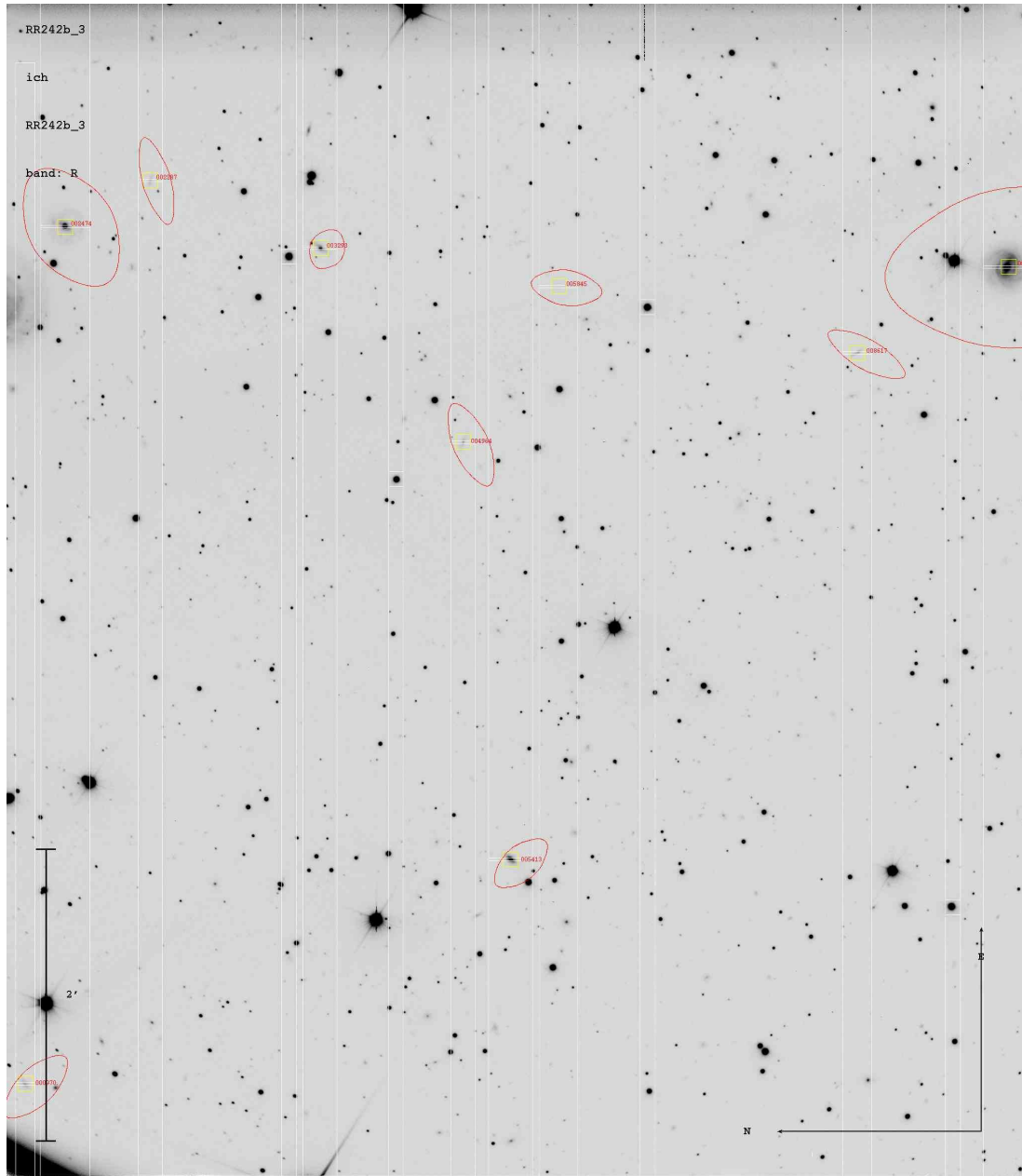
Figure 5.4: Finding chart for spectroscopic OB showing the slits allocated in one of the quadrants of the VIMOS field RR 242-b. The yellow squares and red ellipses mark the scientific targets, whereas the white squares mark reference stars. The slits on the targets are marked in white (the small horizontal lines), the extensions of the resulting spectra are the white long vertical lines (this is the dispersion direction).

illumination of $> 0.7\%$, while the constraint was 0.2%. This leads to a brighter sky background and a lower S/N, which may result in a lower fraction of galaxies with measured redshifts in this quadrant with respect to the others. Also for RR 143-b and RR 143-d and RR 242-a the lunar illumination constraint was exceeded.

One exposure of RR 242-c was observed at a high seeing of $1.4''$, violating the constraint of $1.2''$. However, for measuring the global radial velocity of the objects this is not as problematic as it would be for example for the surface photometry.

Table 5.1: Log of spectroscopic VIMOS observations.

Pointing	OB ID	observation date JJJJ-MM-DD	exp. time [s]	airmass	seeing ['']	moon dist.[1] [°]	lunar ill.[2] %
RR 143-a	218955	2006-01-29	1800	1.298	0.64	90.7	0.005
RR 143-a	218955	2006-01-29	1800	1.308	0.65	90.8	0.004
RR 143-b	218973	2006-01-23	1800	1.297	0.84	85.2	0.446
RR 143-b	218973	2006-01-23	1800	1.306	0.78	85.2	0.444
RR 143-c	218964	2006-01-30	1800	1.359	0.85	92.1	0.006
RR 143-c	218964	2006-01-30	1800	1.408	0.69	92.1	0.006
RR 143-d	218946	2006-01-22	1800	1.319	0.83	85.1	0.550
RR 143-d	218946	2006-01-22	1800	1.304	0.82	85.1	0.547
RR 210-a	219249	2006-03-31	1800	1.018	0.66	150.3	0.041
RR 210-a	219249	2006-03-31	1800	1.006	0.66	150.1	0.042
RR 210-b	219258	2006-03-26	1800	1.073	1.03	121.6	0.138
RR 210-b	219258	2006-03-26	1800	1.135	1.05	121.9	0.136
RR 216-a	219285	2006-03-29	1800	1.052	1.03	143.1	0.000
RR 216-a	219285	2006-03-29	1800	1.081	1.03	143.3	0.000
RR 242-a	219759	2006-03-24	1800	1.104	0.82	76.3	0.328
RR 242-a	219759	2006-03-24	1800	1.150	0.94	76.6	0.326
RR 242-b	219750	2006-03-09	1800	1.093	0.82	110.0	0.730
RR 242-b	219750	2006-03-09	1800	1.175	0.73	109.5	0.734
RR 242-c	219741	2006-03-25	1800	1.208	1.40	89.2	0.221
RR 242-c	219741	2006-03-26	1800	1.069	1.17	100.5	0.141
RR 242-d	219732	2006-03-26	1800	1.132	1.06	101.9	0.132
RR 242-d	219732	2006-03-26	1800	1.191	1.09	102.1	0.131

[1] angular distance of the moon on the sky.

[2] fractional illumination of the moon.

5.5 Data reduction pipeline

For the basic reduction of data observed with VLT instruments an automatic data reduction pipeline was developed by ESO. The data are reduced automatically and sent to the user together with the raw data and all calibration files.

The VIMOS pipeline applies bias and flat-field corrections and processes arc lamp spectra, standard star and science frames. For each science frame a spectral curva-

ture correction as well as wavelength calibrations are applied. The detected objects in each slit are extracted and co-added if the OB was split into more exposures. The bias, flat-field and standard star calibration files are produced automatically by ESO and do not need to be observed by the user, whereas the arc lamp spectrum for the wavelength calibration should be observed directly after the science target in exactly the same configuration (night-time calib template within the OB).

The calibration cascade, automatically delivered calibration and science products and an example of data reduction with the pipeline is presented in the following.

5.5.1 The calibration cascade

The calibration cascade for the `imaging` mode applied to the pre-images consists of the following steps:

1. combine the bias frames into a `master bias`. The product type code of the resulting calibration file is `MBII`

2. use this `master bias` to create the `master sky-flat` from the twilight sky flat-field exposures (code of the master flat: `MSFI`)

3. use the `master bias` and `master sky-flat` to reduce the photometric standard star images and compute the night zeropoint (code `PSMI` for the magnitude table and `PZPI` for the zeropoint table)

4. use the `master bias`, the `master sky-flat` and the night zeropoint value to reduce the science image (code of the resulting reduced science frame: `SREI`)

The calibration cascade for the `MOS` mode consists in:

1. create the `master bias` (product type code `MBIS`)

2. use this `master bias` to create the `master flat` (code `MSFS`)

3. use the `master bias` and `master flat` to reduce the arc lamp spectra and compute the `inverse dispersion solution table` (code `PWDM`)

4. use the `master bias`, `master flat` and `dispersion solution` to reduce the science frame

A correction for the instrument response is currently not applied automatically, but can be applied afterwards. A spectro-photometric standard star is therefore observed and reduced automatically. The calibration files for the flux calibration are provided to the user together with the calibration files used in the pipeline reduction. The product type codes are `PSRM` for the reduced standard star and `PRSM` for the resulting response function.

5.5.2   Reduced science products

Together with the raw data and calibration files, the following reduced MOS science products are provided to the user:

- one FITS file per quadrant containing all one-dimensional extracted spectra, one per line (aperture). Product type: `MOS_SCIENCE_EXTRACTED`, short code: `SEXM`

- one FITS file per quadrant containing the one-dimensional sky spectra (one per line) that have been subtracted from the target spectra. Product type: `MOS_SCIENCE_SKY`, short code: `SSKM`

- one FITS file per quadrant containing the background-subtracted two-dimensional object spectra. Product type: `MOS_SCIENCE_REDUCED`, short code: `SREM`

- one FITS file per quadrant containing the two-dimensional background spectra that were subtracted from the target spectra. Product type: `MOS_SKY_REDUCED`, short code: `SSRM`

- two FITS tables per quadrant containing information on object positions and which output 1D spectra are extracted from which slit. The product type code is `SWTM` for the `WINDOW_TABLE` and `SOTM` for the `OBJECT_TABLE`

The naming scheme for the science products can be confusing but follows a clear structure:

`VI_<TYPE>_<OB_ID>_<TIMESTAMP>_<PARAMS>.<SUFFIX>`

with `VI` for VIMOS, `<TYPE>` is the product type code of the science product, `<OB_ID>` the ID-number of the OB. `<TIMESTAMP>` gives the date and time of the observation in the format `<YEAR>-<MONTH>-<DAY>T<HOUR>:<MINUTE>:<SECOND>.<MILLISEC>`. `<PARAMS>` includes the parameters of the observation which are order sorting filter, grism, mask ID, quadrant number and instrument gain in the format `<ORDFLT>_<GRISM>_<MASK>_Q<QUAD>_<GAIN>`. Finally, the file extension `<SUFFIX>` is either `fits` for fits images or `tfits` for fits tables.
So, for example the file

`VI_SEXM_219741_2006-03-25T07:56:07.118___HRb_201022_Q2_hi.fits`

is a fits image containing the extracted one dimensional target spectra (SEXM) from OB 219741 observed with no order sorting filter and HR blue grism with the mask number 201022 on quadrant 2 with high gain (always used in spectroscopic mode).

5.5.3 The pipeline running environments `Gasgano` and `Esorex`

Two programs can be used for executing the reduction pipeline, `Gasgano` and `Esorex`. `Gasgano` is a Java based tool with a graphic interface. It can be used for viewing and organizing the data and to execute pipeline recipes. The recipes can also be executed on a command line basis using `Esorex`. This has the advantage that it can be embedded in scripts for automation of the data reduction and that it runs fast and stable without the Java environment. In addition to the Common Pipeline Library (CPL), a specific library of pipeline recipes has to be downloaded for each instrument.

5.5.4 Example of MOS data reduction with `Esorex`

In a perfect world, the user should not have to mess around with the data reduction, since all the reduced data products are delivered and ready to use for science. However, if something unforeseen happened during the observations or a flux calibration should be applied to the spectra or simply if the user doesn't trust too much in reduction pipelines, then the user should get familiar with the basics of the pipeline and its recipes.

In our case, two of the OBs were not observed continuously but were split up in their two separate exposures, due to degrading observing conditions during the second exposure. That is, the two exposures of the same OB were observed on different dates (but in consecutive nights). In this case the pipeline doesn't recognise that the two integrations have to be combined. The reduction of these two OBs was therefore repeated using the same recipes but co-adding the spectra in the end.

Due to some problems with running the VIMOS recipes in `Gasgano` we used `Esorex`. With `Esorex`, the recipes are executed together with so-called `sof`-files (set of frames) that must contain the file names of the files that are necessary for each reduction recipe and their DO-category (for example `MASTER_BIAS`).

After constructing the `sof`-file, the recipe is simply executed with:

```
> esorex <options> <recipe-name> <sof-file>
```

where `<options>` is optional.

The recipes for constructing the master bias (`vmbias`) and the master flat (`vmspflat`) and the one for computing the dispersion solution (`vmspcaldisp`) were not repeated, since the difference should be the combination of the frames *after* the calibration steps but *before* identifying objects in the slits and extracting the 1D spectra.

The recipe for correcting, combining and extracting the target spectra is called `vmmosobsjitter`. It applies the basic reduction steps, wavelength calibration, corrects for known bad pixel patterns, combines the single exposures within the same

OB, searches for objects in each slit and extracts a 1D spectrum from the total signal detected in the slit. The `sof`-file has to contain the raw science frames that have to be co-added before extracting the target spectra and the calibration files master bias, dispersion solution, grism table and bad pixel table. The DO-categories of the single files are not checked by `Esorex`. The files have to be given in exactly the right order as expected by the program.

The `sof`-file for quadrant 1 of OB 219741 (RR 242-c) is shown here as an example:

```
#sof.219741.1
obs/219741/sci_raw/VIMOS.2006-03-26T05_00_38.792.fits MOS_SCIENCE RAW
obs/219741/sci_raw/VIMOS.2006-03-25T07_56_08.182.fits MOS_SCIENCE RAW
mbia/VI_MBIA_060325A_Q1_hi.fits MASTER_BIAS CALIB
gen/grs_HR_blue.1.tfits GRISM_TABLE CALIB
pwdm/VI_PWDM_060325A___HRb_101022_Q1_hi.tfits EXTRACT_TABLE CALIB
gen/badpixel.1.tfits CCD_TABLE CALIB
```

The recipe was then executed with:

```
> esorex -output-dir=219741/Q1 vmmosobsjitter sof.219741.1
```

The procedure was repeated for each quadrant of the VIMOS field in both OBs.

5.5.5 Getting the object ID - who is who

The resulting reduced extracted spectra of each quadrant are stored as different apertures within a single fits-file. To avoid confusion, we decided to copy each 1D spectrum into a single fits-file named with its object ID. For this purpose we need the information from which slit the spectrum in each aperture was extracted and the ID of the object in this slit. The information if a spectrum was found and extracted from each slit is given in the object-table, whereas the object ID is given as `SLITxID` keyword in the image header (where `x` is the number of the respective slit). With this information each aperture (spectrum) was copied into a single file named `<object_id>.fits` with the object ID corresponding to the ID given in the photometric catalogues in Appendix A (Tables A.1, A.2, A.3 and A.4). The resulting 1D one-per-file spectra were then used to measure radial velocities.

5.6 Redshift measurements

5.6.1 The cross-correlation technique

The redshifts were measured using the cross-correlation technique: a stellar template spectrum with known radial velocity is cross-correlated with the object spectrum. The cross-correlation function $c(n)$ is defined in a way that if template and object spectra are identical but shifted by a value d, the correlation function has a peak of 1 at $n = d$. The mathematical background of this procedure is described by Tonry & Davis (1979). Dealing with real spectra, the template and object spectra will never be identical, the peak is therefore a fraction of 1, whereas the width of the correlation peak is a measure for the internal dispersion of the galaxy (assuming that the broadening of the lines in the galaxy spectrum with respect to the stellar spectrum is only caused by the galaxy's internal stellar velocity dispersion). To provide a reliable estimate of velocities and the respective errors, obviously more than one template spectrum should be used. For this purpose a number of template spectra of different spectral type should be observed with the same configuration and reduced with the same routines as the object spectra. Unfortunately, only one of our velocity standard stars was observed during our observing run. Therefore 4 additional template spectra were taken from the literature, two early-type galaxy spectra observed by the WINGS group (Antonio Cava, personal communication) and two late-type giant star spectra extracted from the catalogue of Jacoby et al. (1984). The 5 template spectra were corrected for heliocentric velocity and shifted to zero velocity before being correlated with each object spectrum.

5.6.2 The `rvsao` package

The `IRAF` package `rvsao` provides a useful task to measure radial velocities via cross-correlation called `xcsao`, combining all the necessary steps from rebinning template and object, fitting the continuum, Fourier transformation and filtering, computing the cross-correlation function and fitting the peak of this function to obtain radial velocity and dispersion of the galaxy. To have an idea of the reliability of the measurement the so-called R-value is computed, which is the ratio between the height of the found peak of the correlation function to any spurious peak of this function. For a meaningful and reliable solution this confidence parameter has to be at least $R > 3$ (Tonry & Davis 1979). Additionally, the velocity is accepted only if at least 3 out of 5 template spectra give similar velocities. Spectra with a lower R were inspected by eye to check the solution and in a few cases it was found to be correct. However, a solution with a value of $R < 2$ was never accepted.

To check the results of the cross-correlation procedure by eye, the `xcsao` task can be run interactively. The velocity can be refitted if necessary, excluding regions of
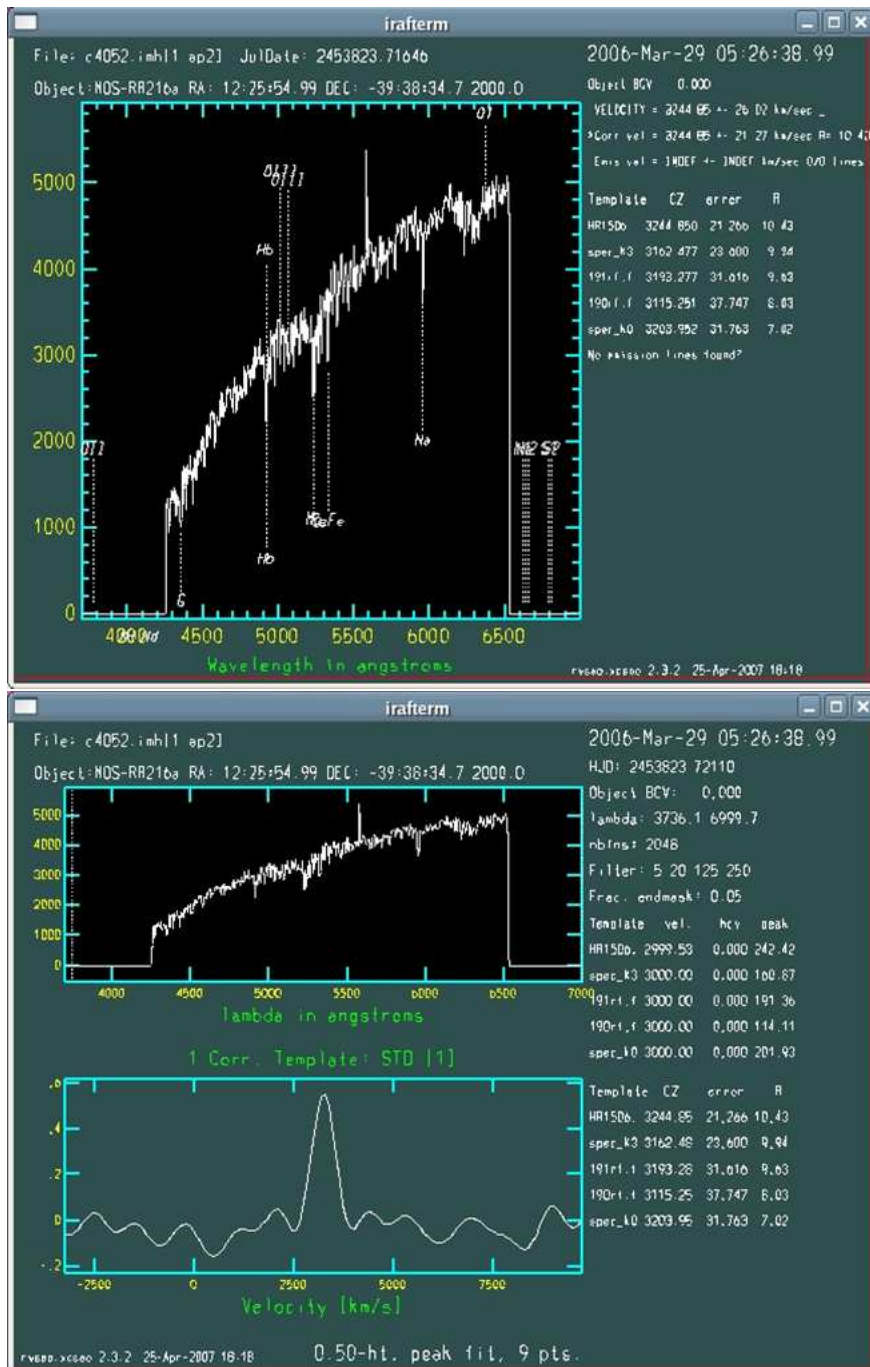
Figure 5.5: Screen shot of the redshift measurement with `xcsao` for object 4052. Top panel: spectrum with identified lines. Bottom panel spectrum and cross-correlation function. Radial velocities, errors and R-values are printed to the right of the correlation function plot.

the spectrum, excluding templates, refitting the continuum, inserting a new velocity guess and many more useful options. An example of this interactive procedure is given in Figure 5.5. It shows the spectrum of object 4052, which was found to be associated to RR 216. The top panel shows the spectrum with the identified lines, whereas in the bottom panel the spectrum and correlation function is plotted. The peak of the correlation function for this spectrum is very clear with a height of ~ 0.6, the corresponding velocities and R-values for the different templates are printed to the right of the correlation function plot. The R-values range from ~ 7 to 10.5, which means that the measurement has a high reliability. The velocities range from $3115 - 3245$ km s^{-1} with errors of around 30 km s^{-1}. The radial velocity and velocity error quoted in Table C.1 are the median and standard deviation of the measurements with the different templates.

During the interactive cross-correlation procedure all spectra were investigated by eye. In some cases, usually for emission line dominated spectra, the lines could not be identified by `xcsao` and were measured by hand using the `IRAF` task `splot`. With this task a Gaussian fit of each spectral line can be performed. The final radial velocity is then the average of all fitted lines and the error their standard deviation. The last column in Table C.1 indicates if the redshift measure comes from the cross-correlation procedure (giving the R-value of the cross-correlation) or if the lines were fitted by hand with `splot` (giving R=0). Table 5.2 gives the total number of galaxies with measured redshift as well as the number of redshifts obtained with `xcsao` and with `splot` respectively.

5.7 Membership results

With the redshift measurements in hand, the galaxies that are most probably associated to each system can now be identified.

5.7.1 Group membership definition

The group membership can be defined in different ways:

1. strict criterion: a galaxy is considered a member of the structure if the difference between the galaxy's velocity and the mean (or median) group velocity $\Delta v = |(v_{galaxy} - v_{group})|$ is lower than a certain value. Depending on the expected compactness of the group in redshift space different values of Δv were used by previous authors, usually either $\Delta v < 1000$ km s^{-1} (see eg. Hickson et al. 1992) or $\Delta v < 1500$ km s^{-1} (see eg. Ramella et al. 1994),

2. flexible criterion: the group membership is defined via the group's velocity dispersion. Usually a limit of $\Delta v < 3\sigma_{group}$ is used, reflecting the approximate dynamical boundaries of the group (Cellone & Buzzoni 2005; Firth et al. 2006).

Both criteria were applied to our sample of galaxies with measured redshifts. We found that in our case the 2 methods yield the same results, there are no galaxies close to the limit in velocity difference in both cases (see also the radial velocity histograms in Figure 5.6). This means that the structures including the supposed new member galaxies are well defined in redshift space and it is supporting the view that they are real bound physical associations.

5.7.2   Radial velocities

Figure 5.6 shows the number distribution of radial velocities in the WFI fields of the 4 pairs. The distribution of supposed member galaxies of each group is shaded in red. The pair plus other galaxies in the WFI field with already known and similar radial velocities (see Table 2.4) are also included in this plot to show the shape of the whole structure in redshift space. There are no nearby background objects, the group structure is well defined in redshift space.

The coordinates, radial velocity, velocity error and R band magnitude computed by `SExtractor` of the supposed new member galaxies of all four groups are given in Table 6.1.

A prominent background concentration is present in 3 of the 4 fields. For RR 143 and RR 210 the background group is centered at ~ 45000 km s^{-1}, while for RR 242 it is located at ~ 16000 km s^{-1}, i.e. well separated from our group structures. The galaxies in the field of RR 216 seem to be more equally distributed. Note however, that in this field only 1 quadrant of the whole WFI field was observed with VIMOS, so the number of galaxies with redshifts is considerably smaller than in the other fields.

The resulting numbers of new group members and background galaxies for each field are given in Table 5.2. These numbers are compared with the total number of galaxies in the respective colour-selected sample, the number of galaxies observed with VIMOS and the number of galaxies for which a reliable redshift could be measured (with cross-correlation or by hand respectively).

A total number of 213 redshifts could be measured corresponding to 83% of all observed objects.
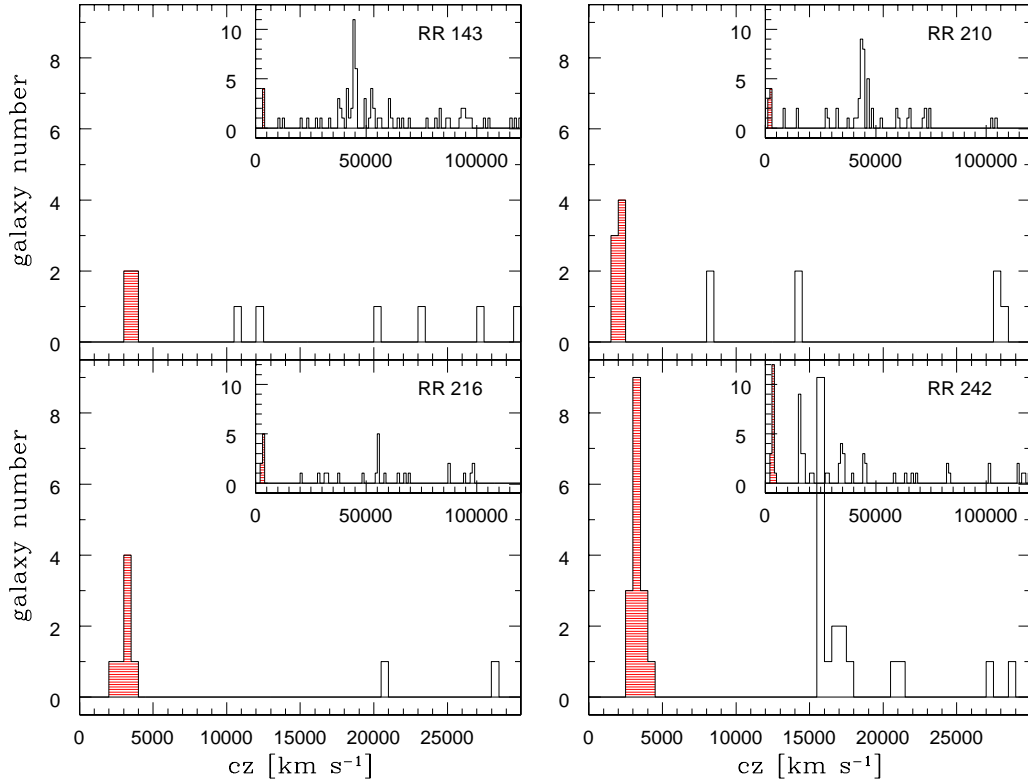
Figure 5.6: Histogram of radial velocities of galaxies in the WFI fields. The plots show the velocity range close to the pairs' velocity from $0 - 30\,000$ km s^{-1}, which is ~ 10 times the velocity of the pairs. The whole range of found velocities (up to $\sim 130\,000$ km s^{-1}) is plotted in the small window in the upper right corner of each plot. Shaded in red are the galaxies that are considered group members. The pair and galaxies with previously known similar redshift in the WFI field are also added to this distribution. The bin size is 500 km s^{-1}.

5.7.3 Spatial distribution

The spatial distribution of objects in each WFI field separated in new group members, background objects, galaxies that were observed but too faint to measure their redshift and not observed objects is shown in the Figures 5.7, 5.8, 5.9 and 5.10. The different number and distribution of faint members in the 4 fields can be seen. The members of RR 143 and RR 210 are scarce and not concentrated around the pair, whereas the members of RR 242 seem to be more clustered around the central elliptical. This trend is discussed in more detail later.
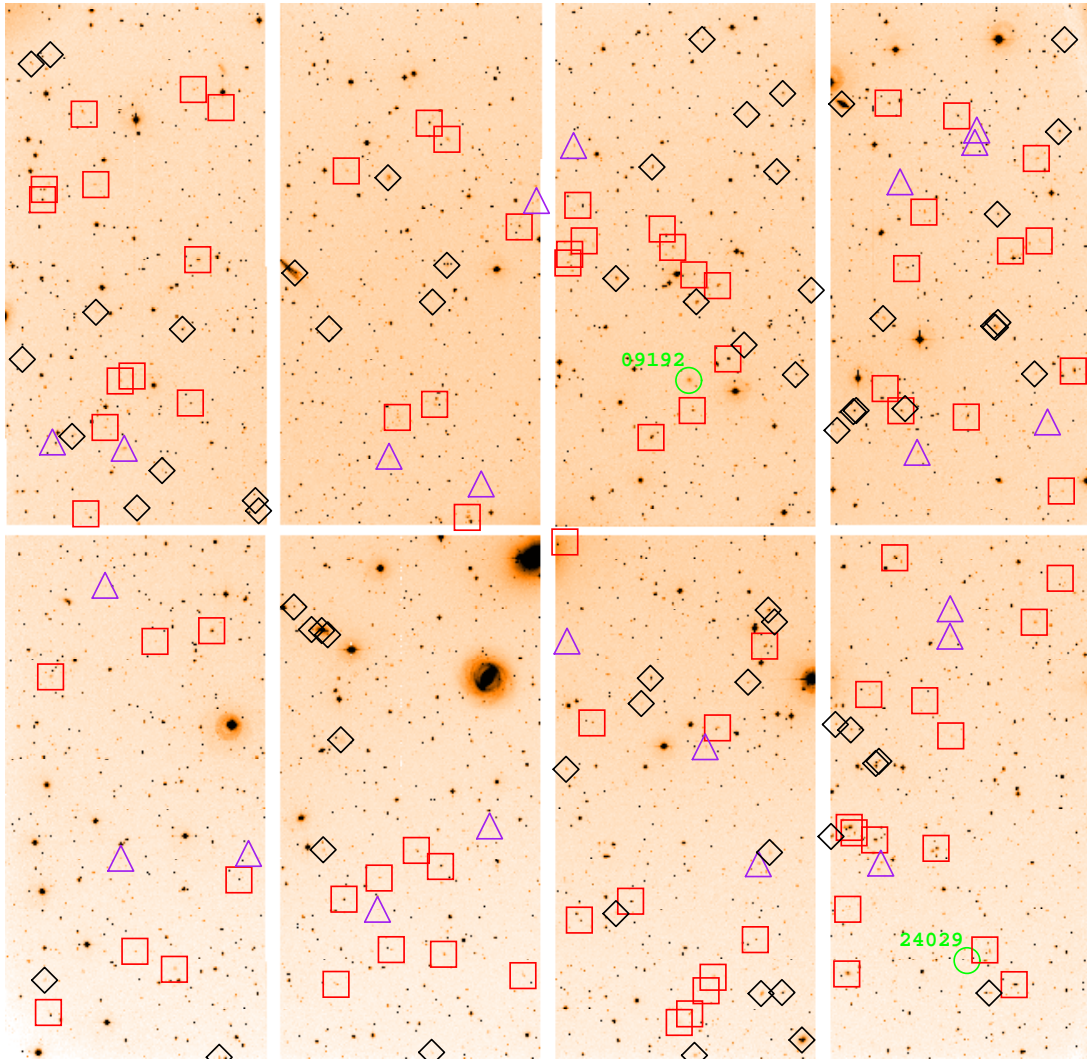
Figure 5.7: Results of VIMOS observations in the field of RR 143. Marked with different symbols are: group members (green circles), background galaxies (red squares), objects observed but too faint for redshift measurement (blue triangles) and not observed objects (black diamonds). The group members are additionally labelled with their object ID.

5.7.4   Completeness correction

Considering the high level of incompleteness and especially the different degree of completeness of the different groups, a completeness correction has to be applied to these numbers. There are basically two reasons for the incompleteness in our sample:
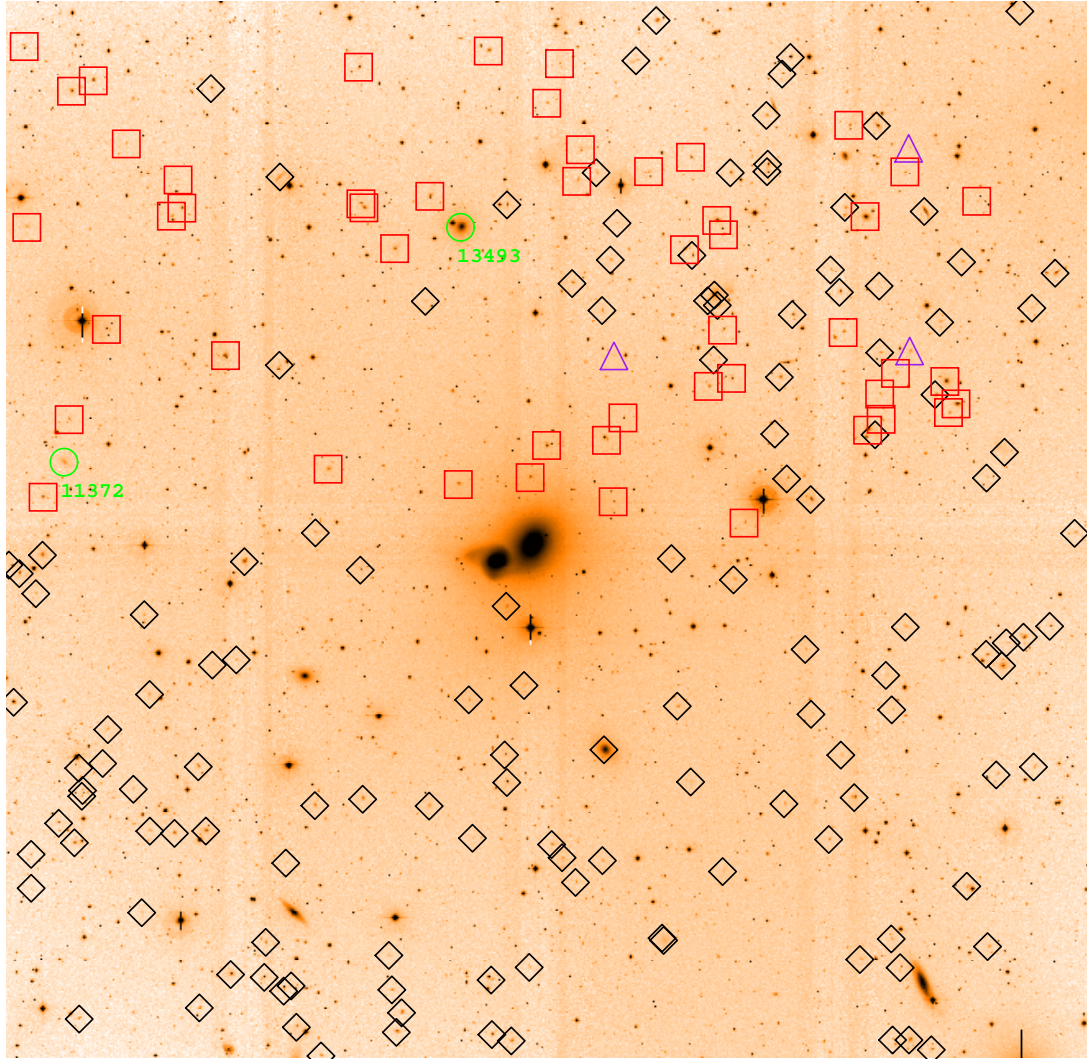
Figure 5.8: Results of VIMOS observations in the field of RR 210. Marked with different symbols are: group members (green circles), background galaxies (red squares), objects observed but too faint for redshift measurement (blue triangles) and not observed objects (black diamonds). The group members are additionally labelled with their object ID.

1. Incompleteness due to technical constraints of the observations, which are:

   – The gaps between the 4 CCDs of the VIMOS field of view. Objects situated in these gaps can obviously not be observed. The gap width of $2'$ leads to a loss of 22% of the area of the WFI field.

   – The HR_blue grism allows only one slit in dispersion direction. That means that objects with similar declination (closer than the slit length)
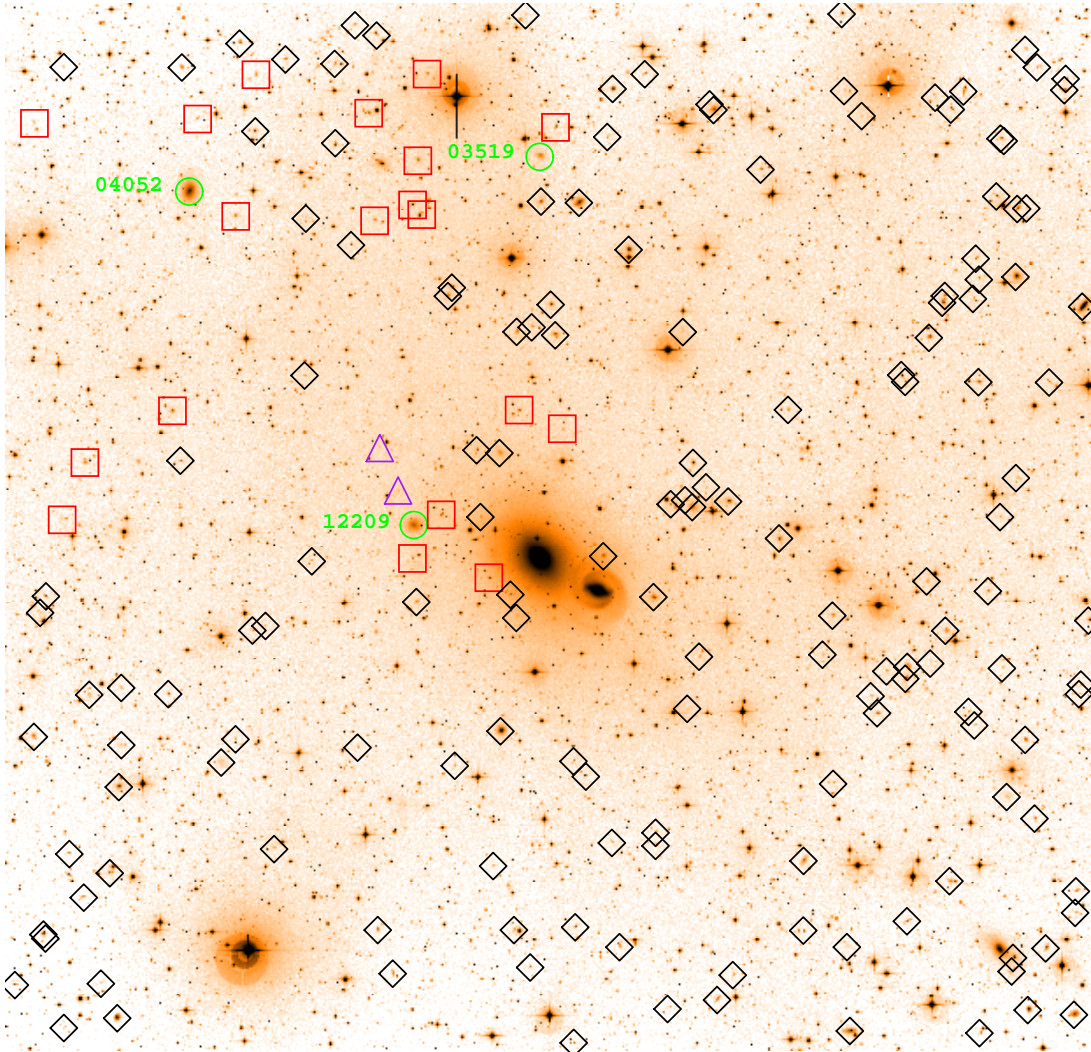
Figure 5.9: Results of VIMOS observations in the field of RR 216. Marked with different symbols are: group members (green circles), background galaxies (red squares), objects observed but too faint for redshift measurement (blue triangles) and not observed objects (black diamonds). The group members are additionally labelled with their object ID.

can not be observed at the same time. If none of the targets is defined as compulsory the slit-assignment software chooses randomly which object to observe.

— Not all scheduled pointings were carried out. RR 143 and RR 242 were observed completely, but RR 210 and RR 216 were observed 50% and 25% respectively.
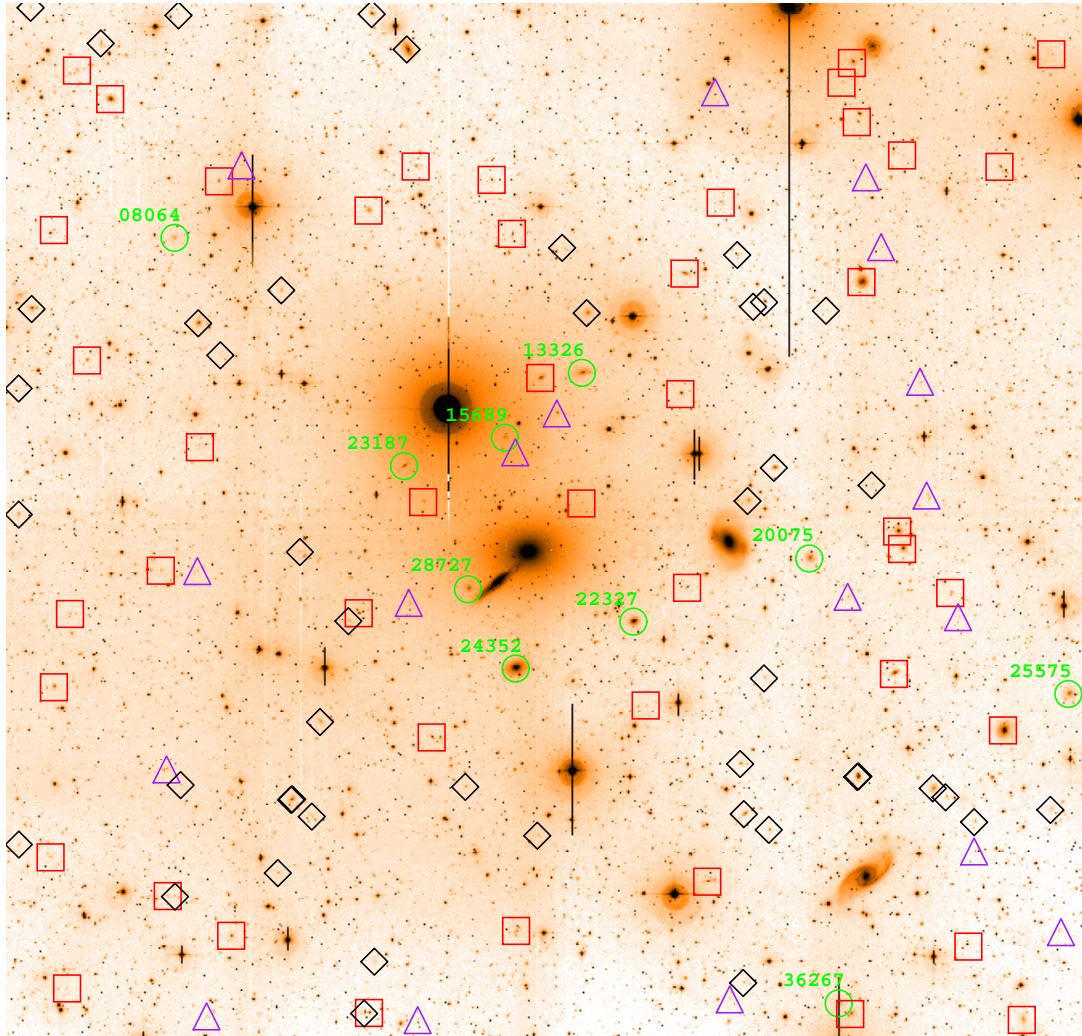
Figure 5.10: Results of VIMOS observations in the field of RR 242. Marked with different symbols are: group members (green circles), background galaxies (red squares), objects observed but too faint for redshift measurement (blue triangles) and not observed objects (black diamonds). The group members are additionally labelled with their object ID.

2. Incompleteness due to not measured redshifts. Considering all 4 samples, the redshifts of 83% of all observed galaxies could be measured. This level of completeness is expected to be dependent on magnitude, since redshifts of faint objects are more difficult to measure.

Therefore the sample has to be corrected for incompleteness depending on the magnitude of the objects. Figure 5.11 shows the numbers of galaxies in the whole sample

Table 5.2: Number of galaxies in the complete colour-selected sample, number of galaxies observed with VIMOS and number of galaxies for which a redshifts could be measured, separated in how the redshift was obtained (cross-correlation or fitting single lines). The last line gives the number of the supposed new member galaxies in each field.

	RR 143	RR 210	RR 216	RR 242
complete sample	171	190	178	118
observed[1]	106 (62%)	55 (29%)	24 (13%)	73 (62%)
measured z from xcsao	69	50	22	45
measured z from splot	15	2	–	10
measured z total[2]	84 (79%)	52 (95%)	22 (92%)	55 (75%)
members[3]	2 (2%)	2 (4%)	3 (14%)	10 (18%)
members corrected[4]	4.4	4.9	15	15.4
total number of observed objects	258			
total number of measured redshifts	213 (83%)			

[1] In brackets the percentage of observed galaxies out of the complete sample.
[2] In brackets the percentage of galaxies with measured redshift out of all observed galaxies.
[3] In brackets the percentage of member galaxies out of all galaxies with measured redshifts.
[4] Expected number of members after completeness correction.

(white), observed sample (red), sample with redshifts (magenta) and sample of new members (black) in each magnitude bin (bin size 1 mag). The different degrees of completeness in the 4 samples and the magnitude dependence of the completeness is clearly visible. The fields of RR 143 and RR 242, where all 4 pointings were observed, show a reasonable degree of completeness, whereas for RR 210 (2 pointings) and especially RR 216 (1 pointing) the number of missed objects is very high (see Table 5.2 for the total numbers). The magnitude dependent incompleteness (due to not measurable redshifts in observed spectra) starts at ~ 18.5 mag, the incompleteness at brighter magnitudes is caused by technical constraints of the observations.

The completeness correction for the number of member galaxies is based on the assumption that the fraction of member galaxies in the sample of not observed galaxies is the same as the one we found in the sample of observed galaxies. Thus, the fraction of members out of all galaxies with redshifts is computed for each magnitude bin and multiplied with the total number of galaxies in this magnitude bin, yielding the total number of expected members per magnitude bin:

$$N_{corr}(mag) = \frac{N_{members}(mag)}{N_{with\ redshift}(mag)} \times N_{sample}(mag) \qquad (5.1)$$
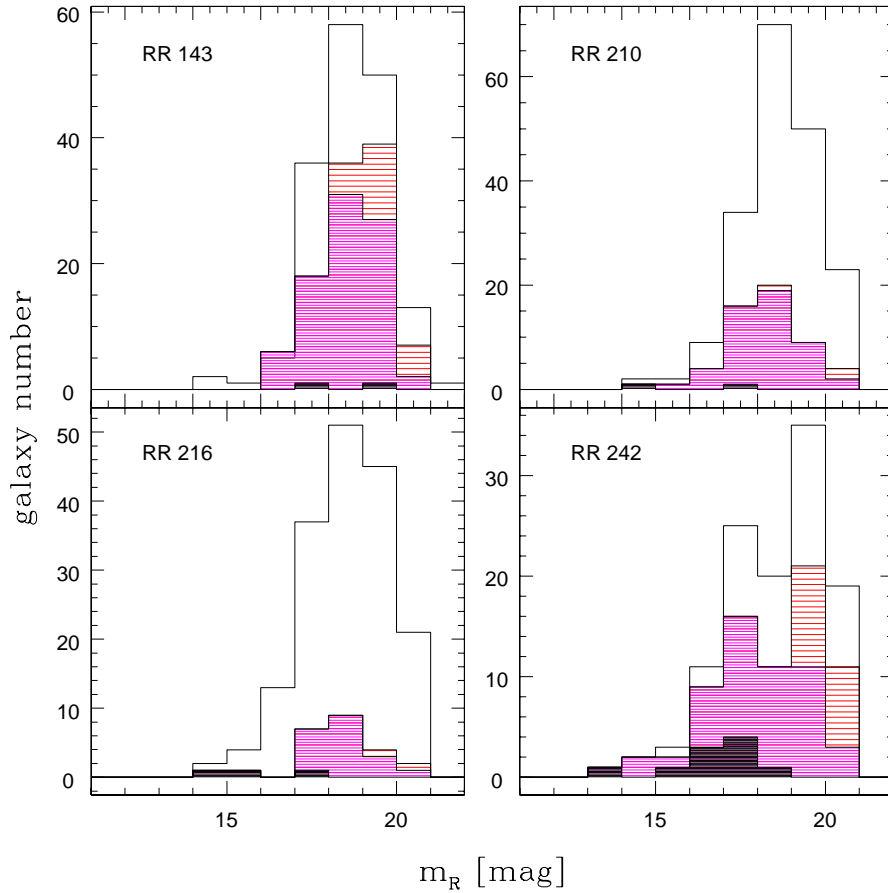
Figure 5.11: R band magnitude histogram of all sample galaxies (white), observed galaxies (red), galaxies with measured redshift (magenta) and new member galaxies (black). The bin size is 1 magnitude.

Figure 5.12 shows the completeness-corrected number of member galaxies in each magnitude bin: the actual number of galaxies found to be members is shaded in red, whereas the total number of expected members per magnitude bin is plotted as histogram. Each magnitude bin is labelled with the percentage of completeness reached in this magnitude bin, i.e. percentage of galaxies with measured redshift out of the complete sample.

The incompleteness above $\sim -15 + 5 \log h$ mag is caused by technical constraints of the observations, for example the 3 brightest candidates in RR 143 were missed and the completeness in the 2 brightest bins is therefore 0%. Below $\sim -15 + 5 \log h$ mag the completeness is clearly decreasing with magnitude.
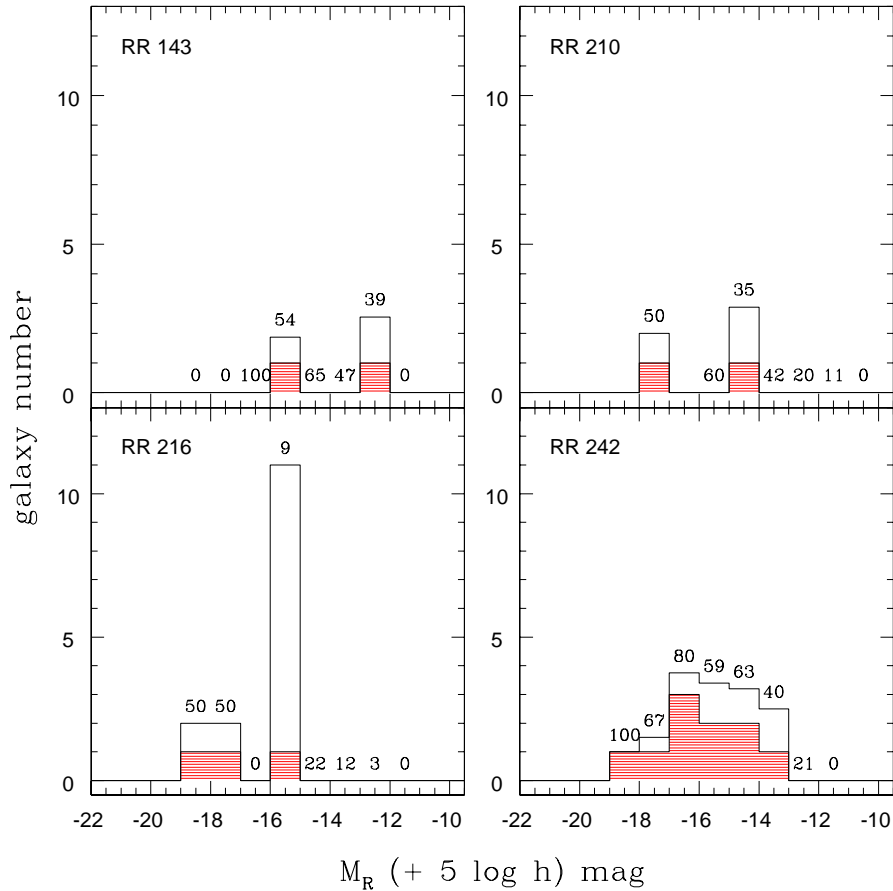
Figure 5.12: Completeness correction of the number of supposed member galaxies in each bin of absolute magnitude M_R. The bin size is 1 magnitude. The actual number of identified members per magnitude bin is shaded in red, whereas the number of expected members is plotted in white.

Problems

The completeness-corrected number of members is highly dependent on the binning, which is especially problematic for structures with few member galaxies. Furthermore, no completeness correction can be applied for magnitude bins in which no members were found. Due to the poor number statistics in RR 216 it is difficult to apply a reasonable correction. Note for example the high number of expected members in the bin $-15 > M_R > -16$: the only galaxy observed in this magnitude bin was found to be a member, so following the above procedure, all galaxies in the sample at this magnitude were assumed to be members as well. However, also from the absolute numbers (Table 5.2) we expect a higher number of galaxies to be

associated to RR 216, reaching a number of companions similar to that of the X-ray luminous RR 242.

The completeness-corrected galaxy numbers are used in the calculation of luminosity functions, but are not considered in the determination of other group properties.

5.8 Summary and conclusions

We observed the candidate faint galaxy population detected in Wide Field Imager (WFI) frames around the four pairs RR 143, RR 210, RR 216 and RR 242 with the VIsible Multi-Object Spectrograph (VIMOS) on the Very Large Telescope (VLT) at ESO. The proposal was accepted for Period 76 and observed between January and March 2006.

– From the 258 observed objects we could measure redshifts for 213, a success rate of 83%. Out of these 213 objects we found that only 17 are faint galaxies associated to the pairs: 2 members in RR 143 (2% of galaxies with measured redshift), 2 members in RR 210 (4%), 3 members in RR 216 (14%) and 10 members in RR 242 (18%). The majority of background galaxies are clustered in a background structure well separated from our groups in redshift space.

– The observing program was not completed. The fields of the 2 X-ray luminous pairs were fully observed, whereas the fields of the 2 X-ray faint pairs were only partly covered, 50% in RR 210 and 25% in RR 216.

– The reasons and effects of incompleteness in our sample were investigated and intensively discussed in the last section. A magnitude dependent completeness correction was applied to each group sample assuming that the fraction of missed members in the not observed sample is the same as the fraction of members found in the observed sample. From this completeness correction we expect a high number of missed members in RR 216.

– We conclude that the presence of an IGM is not connected to the presence of a numerous faint galaxy population surrounding the pair. Out of 85 galaxies with measured redshift in the WFI field of the X-ray luminous RR 143 only 2 very faint companions could be identified. Furthermore they are located at a relatively large distance from the pair.

– The presence of companions could be connected with the pair's environment. The lack of companions around RR 143 is continued in the sparse larger-scale environment around this pair.

– To support this tentative results the observations of the partly observed 2 X-ray faint pairs have to be completed. A new observing program proposing the continuation of the observations was accepted and will be carried out in Period 80 (October 2007 - March 2008).

Chapter 6

Group and group member properties

In the following only the spectroscopically confirmed member galaxies are considered. Their basic properties are summarized in Table 6.1. The new members are used together with the previously known group members presented in Section 2.4 to compute the group properties. To account for the different degrees of completeness and depth of the group sample within and outside the WFI field, all quantities are computed for the whole sample and the WFI subsample separately and compared in the discussion.

The group kinematics and dynamics are presented in the first section, following a luminosity-weighted approach in the determination of all mass related quantities. Distribution of members, group compactness, crossing times and mass-to-light ratios are analysed and compared with the literature.

The luminosity functions (LFs) of the individual and combined group samples are presented in the next section. The LFs of our X-ray faint and X-ray luminous groups are compared with the LF of a sample of X-ray detected poor groups, the LF of a sample of galaxy clusters and the LF of the local field.

We then investigate the morphologies of group member galaxies and their connection to other group properties as well as the spectral properties of the faint member galaxies observed with VIMOS.

Table 6.1: New member galaxies of the 4 pairs/groups.

ID	α (2000)	δ (2000)	v_{rad} [km s^{-1}]	R[1]	D[2] [Mpc]	m_R [mag]	$(V-R)$ [mag]	n	r_e [kpc]	μ_0	μ_e [mag arcsec^{-2}]
RR143_09192	06 47 53.2	-64 10 55.05	3296 ± 46	3.34	0.122	17.25	0.56	1.05	1.30	21.30	23.23
RR143_24029	06 46 33.0	-64 28 49.95	3724 ± 73	3.87	0.307	19.93	0.62	0.73	0.58	21.64	22.87
RR210_11372	12 07 43.3	-29 43 10.91	1927 ± 183	3.08	0.117	17.59	0.50	0.83	0.97	22.24	23.68
RR210_13493[3]	12 06 50.3	-29 36 23.47	2008 ± 45	9.08	0.080	14.26	0.52	1.98	1.30	18.03	21.97
RR216_03519	12 25 17.8	-39 33 45.63	3716 ± 134	2.13	0.165	17.26	0.51	1.02	1.22	21.41	23.28
RR216_04052[4]	12 26 11.3	-39 34 47.12	3193 ± 50	9.63	0.209	14.57	0.60	1.07	2.52	20.18	22.15
RR216_12209	12 25 37.0	-39 44 36.36	2697 ± 62	5.32	0.054	15.58	0.59	0.74	2.17	21.57	22.82
RR242_08064	13 22 10.4	-43 32 55.57	3441 ± 60	2.58	0.202	17.85	0.64	1.21	1.32	21.88	24.15
RR242_13326	13 21 3.9	-43 36 58.06	3172 ± 45	3.42	0.080	16.15	0.60	1.42	2.11	20.15	22.87
RR242_15689	13 21 16.5	-43 38 53.21	3731 ± 81	7.20	0.050	17.73	0.74	1.38	0.73	20.47	23.11
RR242_20075	13 20 26.7	-43 42 27.53	3045 ± 52	6.63	0.120	16.33	0.55	1.51	1.38	20.02	22.95
RR242_22327[5]	13 20 55.5	-43 44 20.18	3237 ± 70	9.63	0.054	15.06	0.69	1.34	0.98	18.38	20.94
RR242_23187	13 21 33.0	-43 39 43.04	3400 ± 88	0.00	0.058	17.37	0.44	0.75	0.95	20.54	21.82
RR242_24352[6]	13 21 14.8	-43 45 43.16	2697 ± 45	10.05	0.050	13.71	0.62	2.35	1.68	16.00	20.76
RR242_25575	13 19 44.2	-43 46 27.97	2655 ± 84	4.26	0.239	16.42	0.60	2.24	1.73	19.02	23.53
RR242_28727	13 21 22.6	-43 43 21.55	3017 ± 87	6.80	0.030	17.05	0.64	1.16	0.69	20.08	22.25
RR242_36267	13 20 21.8	-43 55 38.41	2997 ± 40	3.19	0.245	18.67	0.50	0.89	1.07	22.32	23.90

[1] confidence parameter R from the cross-correlation procedure. If R = 0 the redshift was determined by measuring lines by hand with `splot`.

[2] projected distance from the E member of the pair.

[3] RR210_13493 = 2MASX J12065029-2936236

[4] RR216_04052 = 2MASX J12261133-3934474

[5] RR242_22327 = ESO 270- G 001

[6] RR242_24352 = ESO 270- G 003

6.1 Group kinematics and dynamics

All mass related quantities are calculated by luminosity-weighting the contribution from each object (see eg. Firth et al. 2006). Each galaxy is weighted by its relative luminosity calculated from the galaxy's R band magnitude:

$$w_i = 10^{-0.4 \ m_{Ri}} \tag{6.1}$$

The coordinates of the center of mass α_{group} and δ_{group} are given by averaging the luminosity weighted coordinates α_i and δ_i of all group members:

$$\alpha_{group} = \frac{\sum_i \alpha_i \ w_i}{\sum_i w_i} \ \ and \ \ \delta_{group} = \frac{\sum_i \delta_i \ w_i}{\sum_i w_i} \tag{6.2}$$

The luminosity-weighted mean velocity, i.e. the velocity of the group center of mass is calculated similarly:

$$v_{group} = \frac{\sum_i v_i \ w_i}{\sum_i w_i} \tag{6.3}$$

The luminosity-weighted line-of-sight velocity dispersion is calculated by summing over the weighted squared deviation of each group member from the group velocity:

$$\sigma_r = \left[\frac{\sum_i w_i \ (v_i - v_{group})^2}{\sum_i w_i} \right]^{\frac{1}{2}} \tag{6.4}$$

6.1.1 Distribution of radial velocities

The distribution of radial velocities of the whole sample and the WFI-subsample (in red) is shown in Figure 6.1. v_{group} of each sample is plotted as a vertical dashed line. The horizontal line above each histogram shows 3 σ_r, representing the approximate dynamical boundaries of each group. The mean velocities of the two samples do not differ significantly, apart from RR 216, where the velocity of the WFI-subsample is dominated by the very bright pair E (no other bright members are present in the WFI-field) and is therefore biased towards a higher value.

The full range of radial velocities is already present in the WFI-subsample. The unweighted velocity dispersions of the two samples are either comparable or higher in the WFI-subsample. The weighted dispersion of the WFI-subsample are also comparable to the full sample, again apart from RR 216 where the velocity difference between the 2 dominating pair galaxies is very small, which biases the dispersion towards a small value.
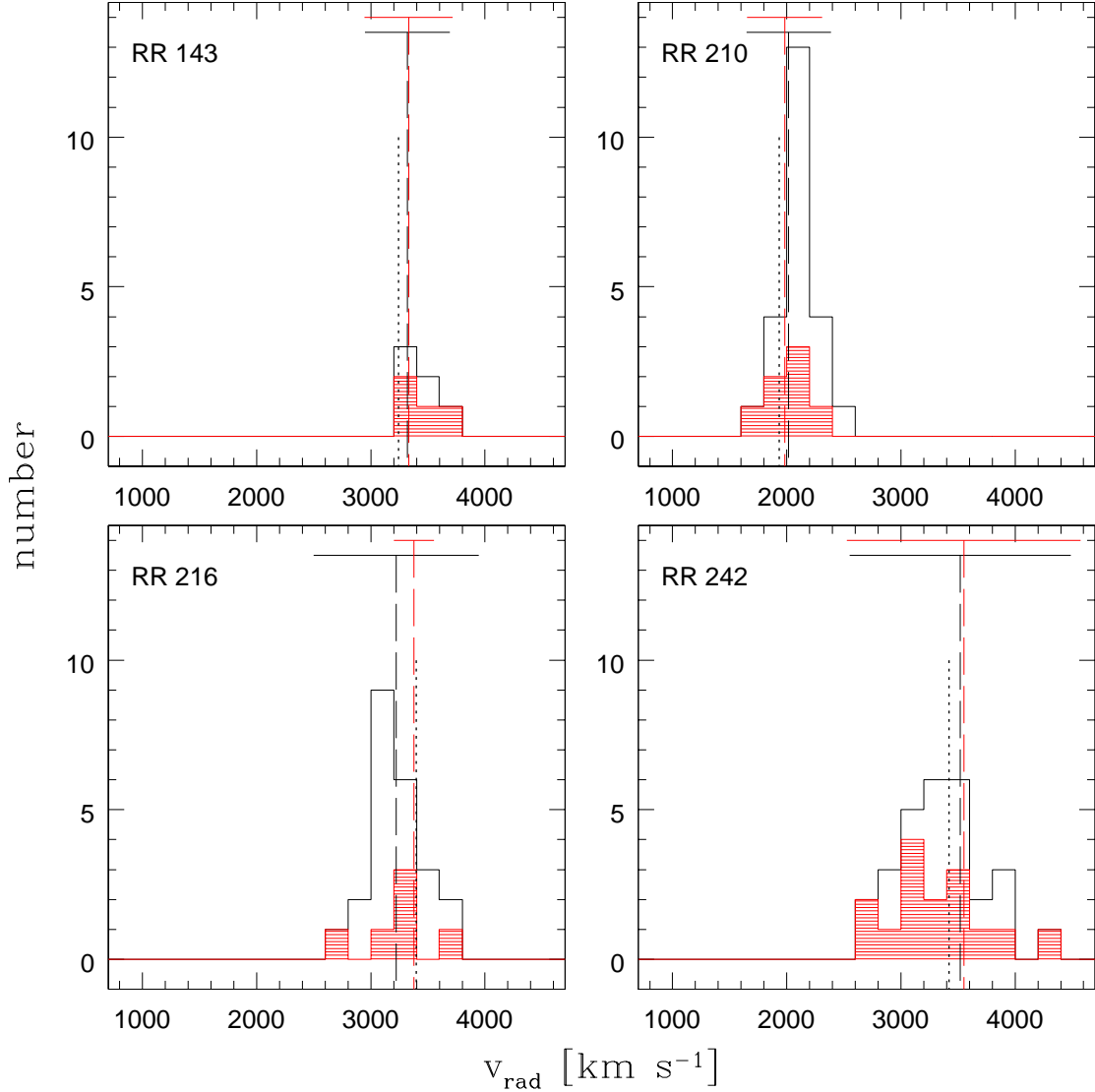
Figure 6.1: Distribution of radial velocities in the 4 groups, including previously known and new member galaxies. The luminosity-weighted mean velocity and 3σ velocity dispersion are plotted as vertical dashed and horizontal solid line respectively. The WFI-subsample is plotted in red, the line indicating the 3σ velocity dispersion of the WFI-subsample is drawn above the black line indicating the 3σ velocity dispersion of the whole sample within $90'$ from the pair E. The velocity of the elliptical pair member is indicated by the shorter dotted line.

6.1.2   Peculiar velocities

The peculiar velocity is the difference between the individual galaxy velocity and the group center velocity ($v_{galaxy} - v_{group}$). It is usually normalized by the groups velocity

dispersion to compare different groups (see e.g. Zabludoff & Mulchaey 2000).

Figure 6.2 shows the peculiar velocities of galaxies versus their projected radial distance from the center of mass. The peculiar velocities are binned every 0.1 h^{-1} Mpc in projected offset from the center of mass, the dispersion in each bin is shown as vertical bars. Each group is plotted in a separate panel, the bottom panel of Figure 6.2 shows the combined sample of galaxies in all 4 groups with the dispersion in each bin plotted in red. The group members are also separated in *giants* and *dwarfs* following Zabludoff & Mulchaey (2000). Galaxies with absolute magnitudes brighter than $-19 + 5 \log h$ are considered giants, fainter objects are defined as dwarfs. Each group is plotted with a different symbol, the giants with big and the dwarfs with small symbols of the same type.

The first interesting implication of this plot is that the position of the pair is not coinciding with the position of the center of mass of the group. The projected offset of RR 216 and RR 242 and RR 143 is around 0.1 h^{-1} Mpc, only RR 210 is located close to the center of mass.

To analyse the dependence of the velocity dispersion on the projected distance, the 4 group samples are combined to increase the number statistics. The bottom panel in Figure 6.2 shows that the velocity dispersion of the combined sample is not constant with projected radius. The maximal dispersion is reached at around 0.2 h^{-1} Mpc ($\sim$ the border of the WFI field of view), from where it starts to decrease out to $\sim$ 0.5 h^{-1} Mpc. Outwards the dispersion is rising again, indicative of the transition between the potential of the group concentrated around the E and the influence of the global large-scale density. An other possibility is that mass has been stripped from this region. Although the dispersion changes by a factor of ~ 3, this is a tentative result due to the intrinsically low number of members in our groups.

Since the kinematics in the region outside the 0.5 h^{-1} Mpc radius may not trace the group potential (as traced by the IGM), the dynamical quantities are calculated also without galaxies lying outside this radius.

To compare the distribution of members in projection and velocity space the R-statistic was proposed by Zabludoff & Mulchaey (2000). It is defined as $R^2 = (d/\delta_d)^2 + (|v_{pec}|/\delta_{|v_{pec}|})^2$, where δ_d and $\delta_{|v_{pec}|}$ denotes the rms deviations in projected distance and peculiar velocity of the whole sample respectively. A galaxy with a large distance d from the group center or a large peculiar velocity v_{pec} will also have a large value of R, while the average member should have $R \sim 2$. We compared the distribution of R values for 3 magnitude limited subsamples: the brightest group galaxies (BGGs) with $M_R < M^*$, the giants with $M_R < -19 + 5 \log h$ and the dwarfs. Additionally, the sample was divided into the full sample and galaxies within 0.5 h^{-1} Mpc from the group center. Figure 6.2 shows the distribution of R for the BGGs (heavily shaded), giants (shaded) and dwarfs (unshaded) in the
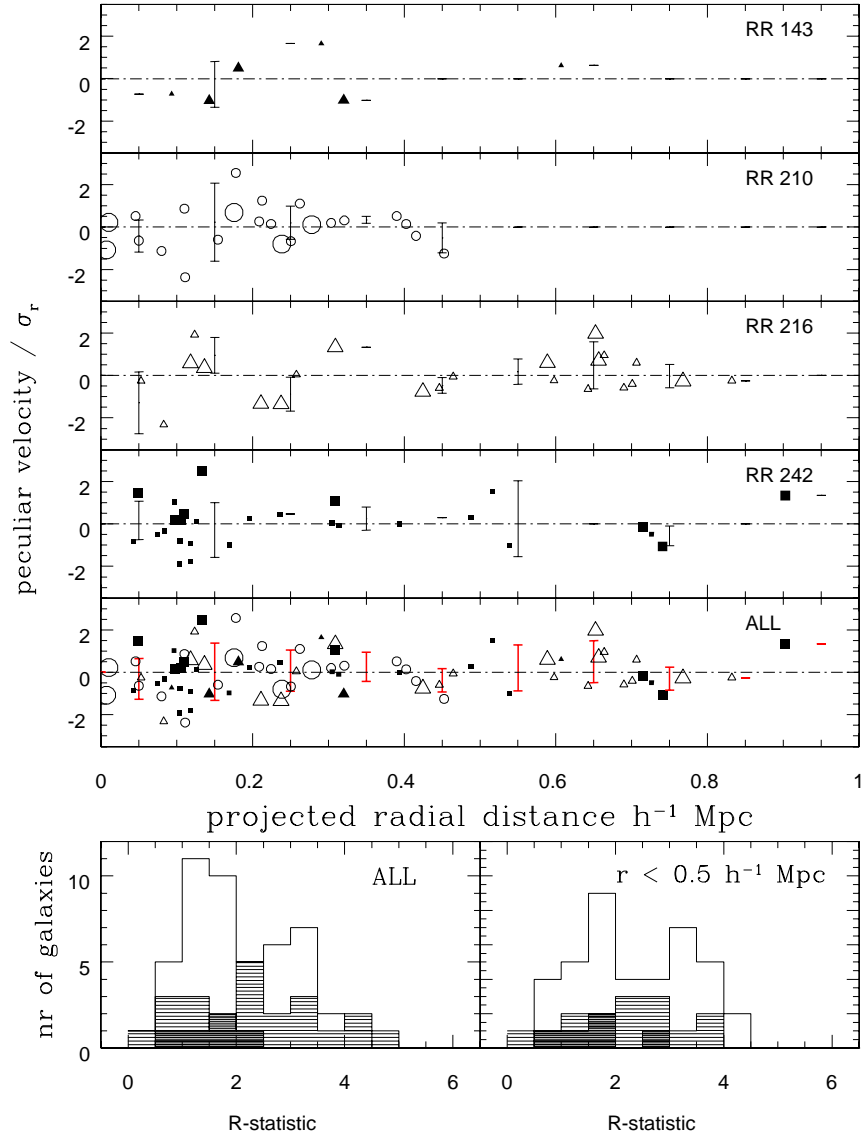
Figure 6.2: Peculiar galaxy velocities ($v_{galaxy} - v_{group}$) normalized by the luminosity-weighted line-of-sight velocity dispersion σ_r as a function of the projected radial distance from the center of mass. Each group is plotted separately, while the bottom panel shows the members of all 4 groups together. The galaxies are binned in projected radial distance every 0.1 h^{-1} Mpc, the red vertical bars show the dispersion in each bin. The dispersion rises from the center out to $\sim$ 0.2 h^{-1} Mpc, then it decreases before rising again beyond $\sim$ 0.5 h^{-1} Mpc, maybe indicating an influence from outside the group. The R-statistic quantifies the offset in velocity and distance of each galaxy. BGGs (heavily shaded), giants (shaded) and dwarfs (unshaded) show different distributions of R suggesting that they occupy different orbits.

full sample (left panel) and for the galaxies within 0.5 h^{-1} Mpc (right panel). In both samples the BGGs are more centrally concentrated than dwarfs and giants with $\langle R_{BGG} \rangle = 1.5$ and $\langle R_{BGG,0.5} \rangle = 1.7$. Considering all galaxies out to $\sim 1\ h^{-1}$ Mpc also the dwarf population follows a different distribution in phase-space than the giants with $\langle R_{dwarfs} \rangle = 2.0$ and $\langle R_{giants} \rangle = 2.3$. This trend is consistent with the results of Zabludoff & Mulchaey (2000), who argue that this suggests that the 3 populations (BGGs, giants, dwarfs) move on different orbits and have not mixed yet. Inside the 0.5 h^{-1} Mpc radius this difference vanishes, the R values of dwarfs and giants are comparable ($\langle R \rangle \sim 2.2$).

6.1.3 Definition of dynamical quantities

The mean harmonic radius is a measure of the compactness of the group and is calculated from the projected separations R_{ij} between the i-th and j-th group member and corrected for projection effects (Binney & Tremaine 1987):

$$R_H = \frac{\pi}{2} \left[\frac{\sum_i \sum_{j<i} (w_i w_j)/R_{ij}}{\sum_i \sum_{j<i} w_i w_j} \right]^{-1} \tag{6.5}$$

The virial radius is connected to R_H as:

$$R_{vir} = \frac{R_H \pi}{2} \tag{6.6}$$

The crossing time t_c is computed from the mean distance of group members from the group centre of mass, $\langle r \rangle$, and the mean velocity relative to the centre of mass, $\langle v \rangle$, following the definition of Rood & Dickel (1978):

$$t_c = \frac{\langle r \rangle}{\langle v \rangle} \tag{6.7}$$

Different mass estimators can be found in the literature. Following the discussion in Heisler et al. (1985) we computed the virial mass M_{vir} and the projected mass M_P:

$$M_{vir} = \frac{3}{G} \sigma_r^2 R_{vir} \tag{6.8}$$

$$M_P = \frac{32}{\pi G} \frac{\sum_i w_i (v_i - v_{group})^2 r_{\perp i}}{\sum_i w_i} \tag{6.9}$$

Both mass estimators assume spherical symmetry and an isotropic distribution of velocities. The projected mass M_P is based on the projected separation from the group center of mass $r_\perp$ of each galaxy, whereas the virial mass M_{vir} is calculated

with the virial radius of the system. M_P is supposed to be more sensitive to inter-lopers than M_{vir}.

The mass-to-light ratio $M_\odot/L_\odot$ is computed from the virial mass and the group luminosity obtained by summing up the luminosities of the individual galaxies. These are calculated from the absolute magnitude of the galaxies obtained by the distance modulus given in Table 6.2 and the absolute magnitude of the sun $M_{R\odot} = 4.42$ mag (taken from Binney & Merrifield 1998):

$$L_i = 10^{0.4(M_{R\odot}-M_{Ri})} \tag{6.10}$$

The dynamical mass estimates are also assuming that the system is composed of particles of equal mass, i.e. equal contribution to the group potential. Since the group member galaxies in our investigated groups span a wide range of masses, we adopted a luminosity-weighted calculation of the dynamical quantities. The group members and their weights normalized to the sum over all weights, i.e. their contribution to the total luminous mass, is given in Table 6.3. However, the unweighted results are also shown in Table 6.2. Table 6.3 gives also the peculiar velocity ($v_{pec} = v_i - v_{group}$) and projected radial distance of each member from the group center of mass $r_\perp$, as well as the absolute magnitude M_R and luminosity L_R used for the calculation of the group luminosity.

6.1.4 Dynamical results

The dynamical properties of the 4 groups are given in Table 6.2, in the first row for the whole sample and in the second row for the group members inside the radius of 0.5 h^{-1} Mpc. Both, the luminosity-weighted and the uniformly-weighted results are given in the Table.

The different weighting is influencing the results dramatically in all systems, but especially in RR 210, where the parameters of the bright pair are dominating the resulting values. The 2 galaxies are separated by only 6 h^{-1} kpc and are close to the center of mass and velocity. R_H and M_{vir} rise by an order of magnitude if the members are uniformly weighted. For the other systems the values change by a factor of ~ 2. The group velocity and velocity dispersion is not so affected by the weighting. The weights given in Table 6.3 illustrate the dominance of the pair elliptical. RR 143a and RR 210a contribute more than 50% to the total luminous mass, the spiral pair companion is clearly the second brightest object. RR 216b and RR 242a contain about 1/3 of the luminous mass and have a few other massive objects brighter or comparable to the spiral pair member in their closer environment.

Table 6.2: Dynamical properties of the 4 groups. The first line gives the luminosity weighted results for the whole sample, while the second line shows the results for galaxies within 0.5 h^{-1} Mpc. In line 3 and 4 the same values are calculated with uniform weights.

Group	Nr. of members	Distance (Modulus) [Mpc (mag)]	Centre of mass α (2000) [h:m:s]	δ (2000) [°:′:″]	v_{group} [km s^{-1}]	velocity dispersion [km s^{-1}]	3D velocity dispersion [km s^{-1}]
RR 143	6	49.6 (33.5)	06:48:05.7	-64:10:52	3320	124	212
	5	49.5 (33.5)	06:47:59.3	-64:11:55	3316	122	207
uniform w_i	6	51.1 (33.5)	06:48:23.2	-64:02:05	3426	180	304
	5	50.8 (33.5)	06:47:15.8	-64:11:52	3404	189	319
RR 210	23	30.1 (32.4)	12:06:55.8	-29:46:47	2018	123	210
uniform w_i	23	31.5 (32.5)	12:06:42.8	-29:44:27	2113	165	273
RR 216	23	48.1 (33.4)	12:26:05.5	-39:38:38	3223	241	414
	12	47.6 (33.4)	12:26:01.5	-39:33:50	3191	229	393
uniform w_i	23	48.6 (33.4)	12:26:17.1	-39:40:19	3255	241	411
	12	47.9 (33.4)	12:25:56.4	-39:37:55	3206	273	463
RR 242	28	52.5 (33.6)	13:20:20.7	-43:42:06	3520	323	537
	21	52.9 (33.6)	13:20:54.8	-43:42:08	3546	314	529
uniform w_i	28	50.1 (33.5)	13:20:21.6	-43:38:07	3356	368	623
	22	50.1 (33.5)	13:20:44.1	-43:37:00	3354	363	617

Group	Harmonic radius (r_h) [Mpc]	Virial radius (r_{vir}) [Mpc]	Crossing time [H$_0$]	Virial mass [10^{12} M$_\odot$]	Projected mass [10^{12} M$_\odot$]	Group luminosity [10^{11} L$_\odot$]	M/L
RR 143	0.169	0.266	0.140	1.43	7.64	1.06	13
	0.160	0.251	0.092	1.30	5.46	1.04	12
uniform w_i	0.441	0.693	0.164	7.79	30.6	1.13	68
	0.319	0.501	0.091	6.24	22.1	1.09	56
RR 210	0.053	0.083	0.136	0.437	6.00	1.56	2
uniform w_i	0.443	0.696	0.166	6.54	16.6	1.71	38
RR 216	0.351	0.552	0.237	11.1	63.2	3.84	28
	0.236	0.370	0.102	6.70	32.0	3.14	21
uniform w_i	0.866	1.360	0.238	27.3	65.4	3.92	69
	0.453	0.711	0.104	18.3	37.5	3.17	57
RR 242	0.221	0.346	0.090	12.5	92.3	2.19	57
	0.141	0.221	0.045	7.56	31.6	1.79	42
uniform w_i	0.407	0.639	0.099	29.9	119	1.99	150
	0.282	0.442	0.061	20.3	59.3	1.61	125

The unweighted R_H of RR 216 is very high, indicative of the higher large-scale density in which this pair is embedded and the probable dynamical link to the Hydra-Centaurus cluster. However, it also means that the brighter members are more concentrated towards the pair than the intermediate luminosity galaxies.

Table 6.3: Properties of group members used for dynamical calculations. Galaxy IDs starting with N are numbered according to Table 2.5.

galaxy	(v_{pec}) [km s^{-1}]	$r_\perp$ [Mpc]	M_R [mag]	L_R [$L_\odot$]	w_i	(v_{pec}) [km s^{-1}]	$r_\perp$ [Mpc]	M_R [mag]	L_R [$L_\odot$]	w_i
			luminosity-weighted					uniform weights		
RR143_09192	-24.	0.013	-16.23	1.81E+08	0.0017	-130.	0.093	-16.29	1.93E+08	0.1667
RR143_24029	404.	0.199	-13.55	1.54E+07	0.0001	298.	0.291	-13.61	1.63E+07	0.1667
RR143_N0001	-79.	0.063	-22.50	5.84E+10	0.5503	-185.	0.143	-22.56	6.21E+10	0.1667
RR143_N0002	195.	0.101	-21.72	2.85E+10	0.2683	89.	0.181	-21.78	3.03E+10	0.1667
RR143_N0003	-78.	0.355	-21.17	1.71E+10	0.1617	-184.	0.320	-21.23	1.83E+10	0.1667
RR143_N0004	218.	0.670	-18.78	1.90E+09	0.0179	112.	0.607	-18.84	2.02E+09	0.1667
RR210_11372	-91.	0.064	-14.80	4.89E+07	0.0003	-186.	0.080	-14.90	5.37E+07	0.0435
RR210_13493	-10.	0.061	-18.13	1.05E+09	0.0067	-105.	0.050	-18.23	1.15E+09	0.0435
RR210_N0001	-82.	0.020	-22.86	8.19E+10	0.5242	-177.	0.007	-22.96	8.99E+10	0.0435
RR210_N0002	132.	0.014	-21.53	2.41E+10	0.1540	37.	0.010	-21.63	2.64E+10	0.0435
RR210_N0003	180.	0.042	-17.79	7.68E+08	0.0049	85.	0.046	-17.89	8.43E+08	0.0435
RR210_N0005	238.	0.109	-19.11	2.59E+09	0.0166	143.	0.110	-19.21	2.84E+09	0.0435
RR210_N0006	-294.	0.089	-19.68	4.38E+09	0.0280	-389.	0.111	-19.78	4.80E+09	0.0435
RR210_N0007	-2.	0.152	-17.49	5.83E+08	0.0037	-97.	0.154	-17.59	6.39E+08	0.0435
RR210_N0008	516.	0.154	-16.39	2.12E+08	0.0014	421.	0.178	-16.49	2.32E+08	0.0435
RR210_N0009	208.	0.189	-20.34	8.05E+09	0.0515	113.	0.176	-20.44	8.82E+09	0.0435
RR210_N0010	139.	0.180	-17.89	8.42E+08	0.0054	44.	0.209	-17.99	9.24E+08	0.0435
RR210_N0011	300.	0.213	-17.19	4.42E+08	0.0028	205.	0.212	-17.29	4.85E+08	0.0435
RR210_N0012	120.	0.236	-18.39	1.34E+09	0.0085	25.	0.224	-18.49	1.46E+09	0.0435
RR210_N0013	-36.	0.212	-20.71	1.13E+10	0.0724	-131.	0.239	-20.81	1.24E+10	0.0435
RR210_N0014	-15.	0.263	-17.69	7.01E+08	0.0045	-110.	0.250	-17.79	7.68E+08	0.0435
RR210_N0015	277.	0.240	-17.59	6.39E+08	0.0041	182.	0.262	-17.69	7.01E+08	0.0435
RR210_N0016	114.	0.253	-20.49	9.24E+09	0.0591	19.	0.278	-20.59	1.01E+10	0.0435
RR210_N0017	128.	0.273	-18.50	1.48E+09	0.0095	33.	0.304	-18.60	1.62E+09	0.0435
RR210_N0018	146.	0.290	-18.89	2.12E+09	0.0135	51.	0.321	-18.99	2.32E+09	0.0435
RR210_N0019	180.	0.398	-19.19	2.79E+09	0.0178	85.	0.390	-19.29	3.06E+09	0.0435
RR210_N0020	27.	0.411	-17.42	5.46E+08	0.0035	-68.	0.416	-17.52	5.99E+08	0.0435
RR210_N0021	118.	0.393	-17.61	6.51E+08	0.0042	23.	0.403	-17.71	7.14E+08	0.0435
RR210_N0022	-111.	0.458	-17.39	5.32E+08	0.0034	-206.	0.453	-17.49	5.83E+08	0.0435
RR216_03519	493.	0.097	-16.15	1.69E+08	0.0004	461.	0.124	-16.17	1.73E+08	0.0435
RR216_04052	-30.	0.037	-18.84	2.02E+09	0.0052	-62.	0.053	-18.86	2.06E+09	0.0435
RR216_12209	-526.	0.075	-17.83	7.95E+08	0.0021	-558.	0.083	-17.85	8.11E+08	0.0435
RR216_N0001	173.	0.107	-23.32	1.25E+11	0.3247	141.	0.118	-23.34	1.27E+11	0.0435
RR216_N0002	119.	0.125	-21.98	3.63E+10	0.0945	87.	0.136	-22.00	3.71E+10	0.0435
RR216_N0003	41.	0.234	-19.18	2.76E+09	0.0072	9.	0.258	-19.20	2.81E+09	0.0435
RR216_N0004	-288.	0.188	-21.99	3.67E+10	0.0954	-320.	0.211	-22.01	3.74E+10	0.0435
RR216_N0005	-293.	0.237	-23.02	9.47E+10	0.2463	-325.	0.238	-23.04	9.66E+10	0.0435
RR216_N0006	353.	0.290	-20.53	9.56E+09	0.0249	321.	0.309	-20.55	9.75E+09	0.0435
RR216_N0007	-151.	0.395	-20.15	6.73E+09	0.0175	-183.	0.425	-20.17	6.87E+09	0.0435
RR216_N0008	19.	0.480	-19.83	5.02E+09	0.0130	-13.	0.464	-19.85	5.12E+09	0.0435
RR216_N0009	-111.	0.468	-17.20	4.45E+08	0.0012	-143.	0.446	-17.22	4.54E+08	0.0435
RR216_N0010	-26.	0.606	-18.79	1.92E+09	0.0050	-58.	0.598	-18.81	1.96E+09	0.0435
RR216_N0011	176.	0.563	-19.91	5.40E+09	0.0140	144.	0.589	-19.93	5.51E+09	0.0435
RR216_N0012	-34.	0.752	-21.34	2.02E+10	0.0524	-66.	0.768	-21.36	2.06E+10	0.0435
RR216_N0013	-123.	0.660	-19.81	4.92E+09	0.0128	-155.	0.642	-19.83	5.02E+09	0.0435
RR216_N0014	-108.	0.658	-19.26	2.97E+09	0.0077	-140.	0.690	-19.28	3.03E+09	0.0435
RR216_N0015	200.	0.674	-20.29	7.66E+09	0.0199	168.	0.656	-20.31	7.81E+09	0.0435
RR216_N0016	-28.	0.810	-3.41	1.36E+03	0.0000	-60.	0.832	-3.43	1.38E+03	0.0435
RR216_N0017	506.	0.671	-21.21	1.79E+10	0.0465	474.	0.652	-21.23	1.82E+10	0.0435
RR216_N0018	260.	0.659	-3.41	1.36E+03	0.0000	228.	0.664	-3.43	1.38E+03	0.0435
RR216_N0019	175.	0.692	-19.03	2.40E+09	0.0062	143.	0.706	-19.05	2.45E+09	0.0435
RR216_N0020	-66.	0.715	-18.21	1.13E+09	0.0029	-98.	0.701	-18.23	1.15E+09	0.0435
RR242_08064	-79.	0.222	-15.75	1.17E+08	0.0005	85.	0.196	-15.65	1.07E+08	0.0357
RR242_13326	-348.	0.095	-17.45	5.61E+08	0.0026	-184.	0.075	-17.35	5.10E+08	0.0357
RR242_15689	211.	0.108	-15.87	1.31E+08	0.0006	375.	0.096	-15.77	1.19E+08	0.0357
RR242_20075	-475.	0.012	-17.27	4.75E+08	0.0022	-311.	0.043	-17.17	4.32E+08	0.0357
RR242_22327	-283.	0.068	-18.54	1.53E+09	0.0070	-119.	0.084	-18.44	1.39E+09	0.0357
RR242_23187	-120.	0.135	-16.23	1.82E+08	0.0008	44.	0.126	-16.13	1.66E+08	0.0357
RR242_24352	-823.	0.106	-19.89	5.31E+09	0.0243	-659.	0.118	-19.79	4.82E+09	0.0357
RR242_25575	-865.	0.080	-17.18	4.37E+08	0.0020	-701.	0.104	-17.08	3.98E+08	0.0357
RR242_28727	-503.	0.115	-16.55	2.45E+08	0.0011	-339.	0.118	-16.45	2.23E+08	0.0357
RR242_36267	-523.	0.138	-14.93	5.51E+07	0.0003	-359.	0.169	-14.83	5.01E+07	0.0357
RR242_N0001	-99.	0.096	-22.76	7.46E+10	0.3413	65.	0.098	-22.66	6.78E+10	0.0357
RR242_N0002	9.	0.105	-21.17	1.73E+10	0.0789	173.	0.109	-21.07	1.57E+10	0.0357
RR242_N0004	376.	0.036	-21.55	2.45E+10	0.1120	540.	0.049	-21.45	2.23E+10	0.0357
RR242_N0005	748.	0.100	-20.89	1.33E+10	0.0610	912.	0.133	-20.79	1.21E+10	0.0357
RR242_N0006	-453.	0.150	-19.58	3.99E+09	0.0182	-289.	0.104	-19.48	3.63E+09	0.0357
RR242_N0007	-93.	0.114	-21.34	2.02E+10	0.0923	71.	0.106	-21.24	1.83E+10	0.0357
RR242_N0008	230.	0.336	-20.63	1.05E+10	0.0480	394.	0.308	-20.53	9.54E+09	0.0357
RR242_N0009	6.	0.263	-18.50	1.48E+09	0.0067	170.	0.237	-18.40	1.34E+09	0.0357

Table 6.3– continued from previous page

galaxy	(v_{pec}) [km s^{-1}]	$r_\perp$ [Mpc]	M_R [mag]	L_R [$L_\odot$]	w_i	(v_{pec}) [km s^{-1}]	$r_\perp$ [Mpc]	M_R [mag]	L_R [$L_\odot$]	w_i
			luminosity-weighted					uniform weights		
RR242_N0010	-197.	0.371	-3.60	1.62E+03	0.0000	-33.	0.314	-3.50	1.47E+03	0.0357
RR242_N0011	-156.	0.361	-3.60	1.62E+03	0.0000	8.	0.305	-3.50	1.47E+03	0.0357
RR242_N0012	-162.	0.376	-18.70	1.77E+09	0.0081	2.	0.394	-18.60	1.61E+09	0.0357
RR242_N0013	-57.	0.555	-17.60	6.44E+08	0.0029	107.	0.489	-17.50	5.85E+08	0.0357
RR242_N0014	390.	0.566	-18.80	1.94E+09	0.0089	554.	0.516	-18.70	1.77E+09	0.0357
RR242_N0015	-537.	0.560	-19.10	2.56E+09	0.0117	-373.	0.539	-19.00	2.33E+09	0.0357
RR242_N0016	-342.	0.756	-3.60	1.62E+03	0.0000	-178.	0.726	-3.50	1.47E+03	0.0357
RR242_N0017	328.	0.939	-20.73	1.15E+10	0.0526	492.	0.903	-20.63	1.05E+10	0.0357
RR242_N0018	-220.	0.755	-21.26	1.87E+10	0.0857	-56.	0.714	-21.16	1.70E+10	0.0357
RR242_N0019	-555.	0.781	-20.13	6.62E+09	0.0303	-391.	0.741	-20.03	6.02E+09	0.0357

The differences between M_{vir} and M_P are quite high, M_P is generally higher than M_{vir} by a factor of 2-5. This effect is expected in systems where individual galaxies are close to each other in projection. M_{vir} was found to underestimate the mass by a factor of ~ 3 or more in such systems (Heisler et al. 1985). Another reason for this difference could be that the groups are not virialized. On the other hand, the crossing times of the groups are a small fraction of the Hubble-time, usually lower than 0.2, apart from RR 216 when calculated with the whole sample. This indicates that the groups or at least their centres are virialized (Ferguson & Sandage 1990).

RR 216 and RR 242 have comparable M_{vir} but very different M/L due to the very high group luminosity of RR 216, twice the group luminosity of RR 242. Since the number of *giant* galaxies is the same in both systems ($N_{giant} = 10$), the individual giants of RR 216 contain more (luminous) mass than the ones in RR 242. The M/L ratios of the groups are consistent with typical values found for poor groups of galaxies, although on the lower limit, indicating that the virial mass is underestimating the total mass of the systems.

6.1.5 Distribution of group members and group compactness

The positions of group members of the 4 groups is plotted in Figure 6.3. The groups are moved to a common distance, so that the shown field of view corresponds to $\sim$ 2.5 h^{-1} Mpc on each side. Plotted are the large-scale environment search radius of 90′ centered on the pair E (solid line), the WFI field of view (central square), the 0.5 h^{-1} Mpc radius (dashed line) and the mean harmonic radius R_H (dotted line), both centered on the group center of mass. The central solid-line circle is R_H calculated only with members inside 0.5 h^{-1} Mpc centered on the respective center of mass.
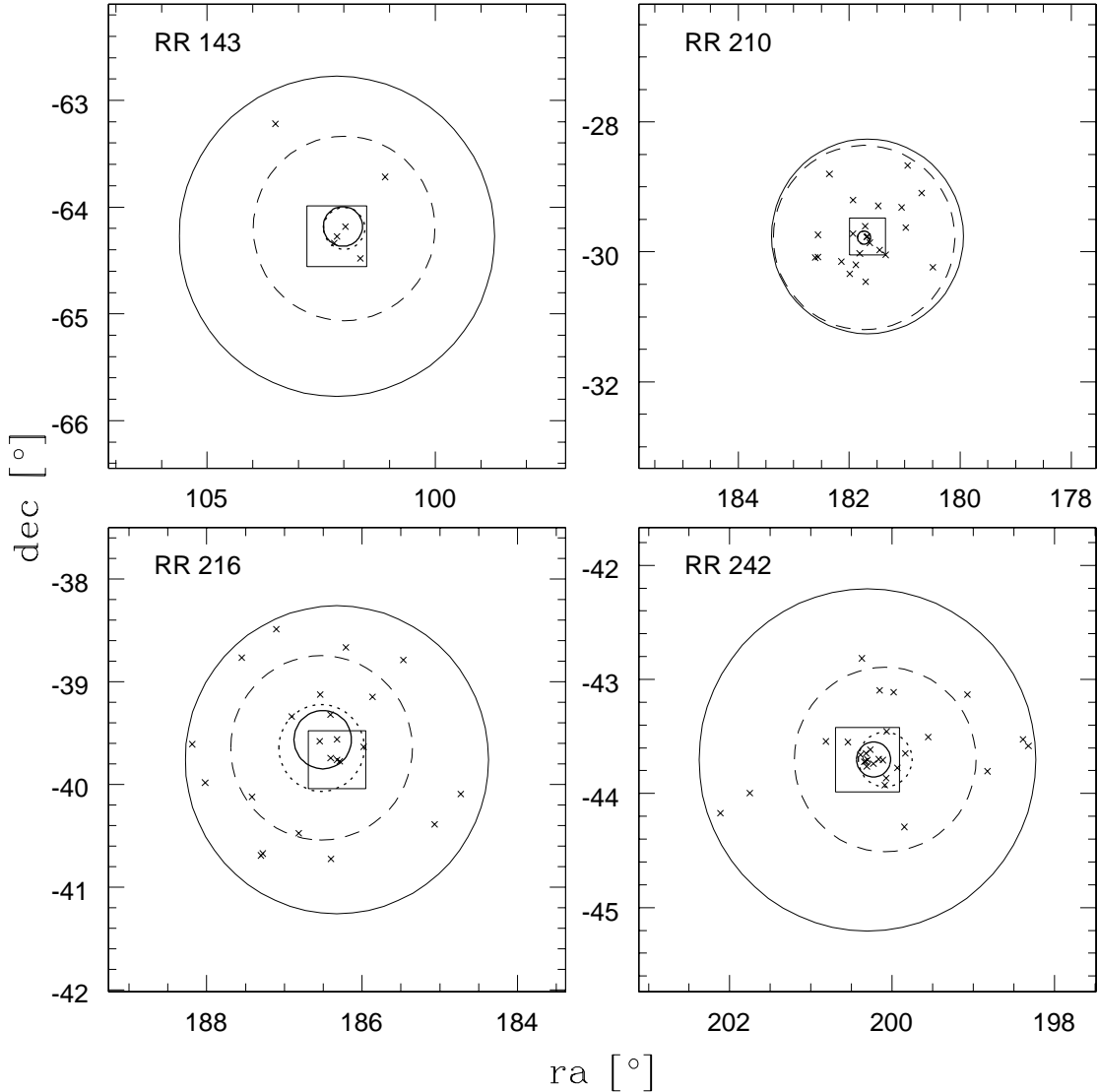
Figure 6.3: Position of member galaxies of the 4 groups moved to a common distance. The field of view of each plot is $\sim 2.5\ h^{-1}$ Mpc on each side. The position of all galaxies with concordant radial velocity within $90'$ are plotted as crosses. The $90'$ search radius around the E pair member is indicated by the solid circle, whereas the dashed circle represents the $0.5\ h^{-1}$ Mpc limit found in Figure 6.2, beyond which the velocity dispersion starts to rise again. The central square represents the WFI field of view. The central circle is the luminosity-weighted mean harmonic radius R_H centered on the group center of mass calculated with group members inside the $0.5\ h^{-1}$ Mpc radius (solid line) and with the whole sample (dotted line), see Table 6.2 for the values.

Again it becomes obvious that the group center of mass does not coincide with the position of the pair, only RR 210 seems to be located in the center of the group potential. It also seems to be the most compact group with a small R_H, although this is probably caused by the higher number of galaxies with intermediate luminosity identified by NED due to the closer distance of this group. Additionally, this is the pair with the smallest projected separation, which is also influencing the luminosity weighted R_H to be smaller. The unweighted R_H is comparable to the other groups (see Table 6.2 for values).

The galaxies around RR 216 are spread over the investigated area without a central concentration, indicative of the higher large-scale density of its environment (outskirts of the Hydra-Centaurus Cluster).

The X-ray luminous pairs RR 143 and RR 242 have a completely different environment, but for both systems the diffuse X-ray emission is not connected to the large-scale distribution of group galaxies. The IGM is centered in the potential well of the elliptical and not on the group center of mass.

Considering only galaxies within the 0.5 h^{-1} Mpc radius, we find that the group center of mass moves towards the pair elliptical in all cases.

6.1.6 Radial density profile of faint group members

The spatial distribution of the faint members can only be investigated for the group centres within the WFI field of view (~ 250 h^{-1} kpc radius around the pair E). The redshift information of galaxies outside this field is taken only from NED, which is highly incomplete at faint magnitudes.

The radial density profile of the faint group members ($M_R > -19 + 5\log h$) is plotted in Figure 6.4 for all four groups. The number of group members is counted in radial bins of 20 h^{-1} kpc width and divided by the area of that bin. The radius is measured from the field centre, i.e. the pair elliptical. The first bin 0 - 20 kpc is not plotted since no galaxies are found there. This is due to the large extent of the bright ellipticals. The effective radius of the smallest of the 4 Es is ~ 12 kpc.

The faint galaxies in RR 242 are clearly concentrated around the bright elliptical, as already suggested by the visual impression from the fields in Figures 5.7 – 5.10, whereas in RR 143 there is no central concentration. The situation for the other two pairs is not clear. Due to the high incompleteness (and its asymmetry) the spatial distribution of members with respect to the pair cannot be determined.
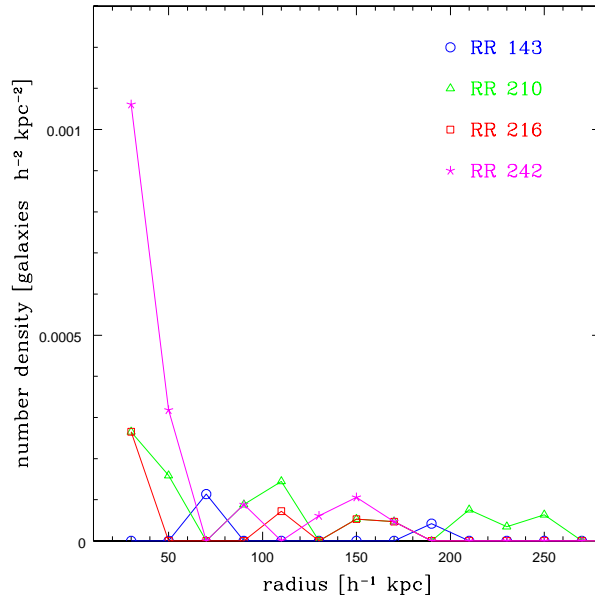
Figure 6.4: Radial density profile of faint group member galaxies. The pairs are colour-coded and marked with different symbols. Note the concentration of faint galaxies towards the center (the pair E) in RR 242, but not in RR 143.

6.2 Luminosity functions

To simplify the comparison with luminosity functions from the literature the absolute magnitudes presented in this section are computed with $H_0 = 100$ and given in $+5$ log h mag, where $h = H_0/100$. First, the distribution of absolute magnitudes of all member galaxies within the WFI field of view and within the $90'$ radius are shown. The then following luminosity functions are computed with the completeness-corrected galaxy counts only within 0.5 h^{-1} Mpc, to compare the same physical regions in all the groups.

6.2.1 Distribution of absolute magnitudes

Figure 6.5 shows the distribution of absolute magnitudes in the 4 groups separated in members located within the WFI field of view and all member galaxies in a $90'$ radius as given in Table 2.4. The mean absolute magnitudes of the WFI field subsamples do not differ significantly from the whole group sample. The values are consistently around $M_R \sim$ -18 mag, apart from RR 216, which has a higher value due to its brighter elliptical pair member, but also due to other very bright members in the larger scale environment.

It is also remarkable that very few faint members were identified. The confirmed companions tend to be of intermediate luminosity in the supposed transition region from "normal" to dwarf galaxies at around $M_R \sim -18$ (Ferguson & Binggeli 1994), which is populated by faint S0s, spirals and dwarf ellipticals. Despite the high number of very faint candidates (the median of all candidate samples is fainter than $M_R \sim -14 + 5 \log h$), no faint dwarf irregular galaxies were found.

The dependency of galaxy magnitudes on their position within the group is also investigated in Figure 6.5. The trend is that the brightest galaxies in the groups are more centrally concentrated than the galaxies of intermediate luminosity, as already suggested by the analysis of peculiar velocities. Outside of $\sim 0.6\ h^{-1}$ Mpc RR 216 and RR 242 again have some brighter members, in contrast to RR 143, while for RR 210 this region lies outside the investigated area. The lack of faint galaxies outside of $\sim 0.2\ h^{-1}$ Mpc is easily explained: this is the approximate extension of the WFI field of view, the spatial limit of our search for faint member galaxies.
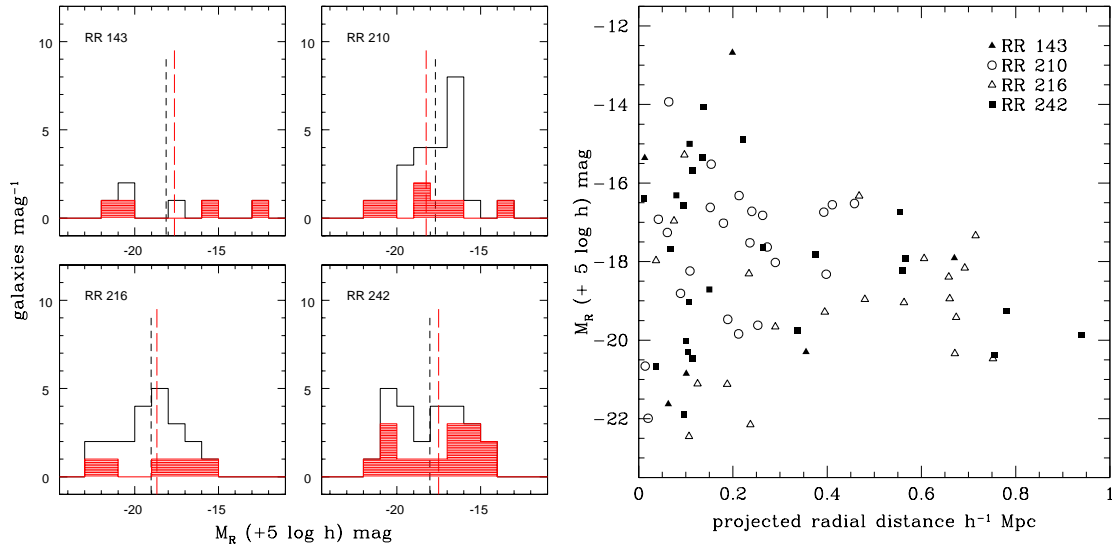
Figure 6.5: Left: Absolute magnitude histogram of members of the 4 groups in the WFI field (red) and in the 90′ radius (Tables 2.4 and 2.5). The vertical dashed lines indicate the mean absolute magnitude of group members within the WFI field (red, long dashed) and the 90′ radius (black, short dashed). Right: Absolute magnitude vs. projected radial distance from the group center.

6.2.2 Definition of the luminosity function

The luminosity functions shown in Figure 6.6 are computed with the completeness-corrected counts as described in Section 5.7.4.

The analytic form of the luminosity function usually fitted to the observed distribution of magnitudes was described by Schechter (1976):

$$\Phi(L)dL = \Phi^* \left(\frac{L}{L^*} \right)^\alpha \exp \left(\frac{L}{L^*} \right) dL \tag{6.11}$$

where L is the galaxy luminosity and $\Phi(L)dL$ the number of galaxies with a luminosity between L and $L + dL$ per Mpc^3. This equation can be transformed into absolute magnitudes, which are easier to obtain than luminosities:

$$\Phi(M)dM = \frac{2}{5} \, \Phi^*(\ln 10) \left[10^{\frac{2}{5}(M^*-M)} \right]^{\alpha+1} \exp \left[-10^{\frac{2}{5}(M^*-M)} \right] dM \tag{6.12}$$

where M is the absolute magnitude of galaxies and $\Phi(M)dM$ is the number of galaxies in the magnitude bin $(M, M + dM)$ per Mpc^3. The parameters Φ^*, α and M^* are the free parameters of the Schechter function, which must be determined empirically. The characteristic magnitude M^* is the transition point between the steep rise of the LF at bright magnitudes and the shallower slope of the faint end of the LF, which is determined by α. An $\alpha < -1$ means that the LF is still rising at faint magnitudes, whereas $\alpha > -1$ gives a decreasing number of galaxies with fainter magnitudes. Φ^* is the number of galaxies per magnitude and per Mpc^3 at the characteristic luminosity, i.e. the normalisation of the LF. To determine Φ^* in physical units the galaxy numbers are usually divided by the surveyed volume. This approach is problematic when the surveyed area is covering only part of a structure, e.g. the central part of a group. In this case the galaxies may be distributed over a larger distance along the line of sight than the size of the projected surveyed field. The normalisation to physical units therefore makes not so much sense.

Usually the normalisation is obtained by integrating the luminosity function with a certain M^* and α down to a faint magnitude limit giving the total number of galaxies within this magnitude range. Then, the number of observed galaxies within the given magnitude range is divided by the number obtained by the integration giving the normalisation factor Φ^*.

The errors are estimated by the Poisson counting statistics, assuming that the error in each magnitude bin is given by the square root of the number of galaxies in that bin.
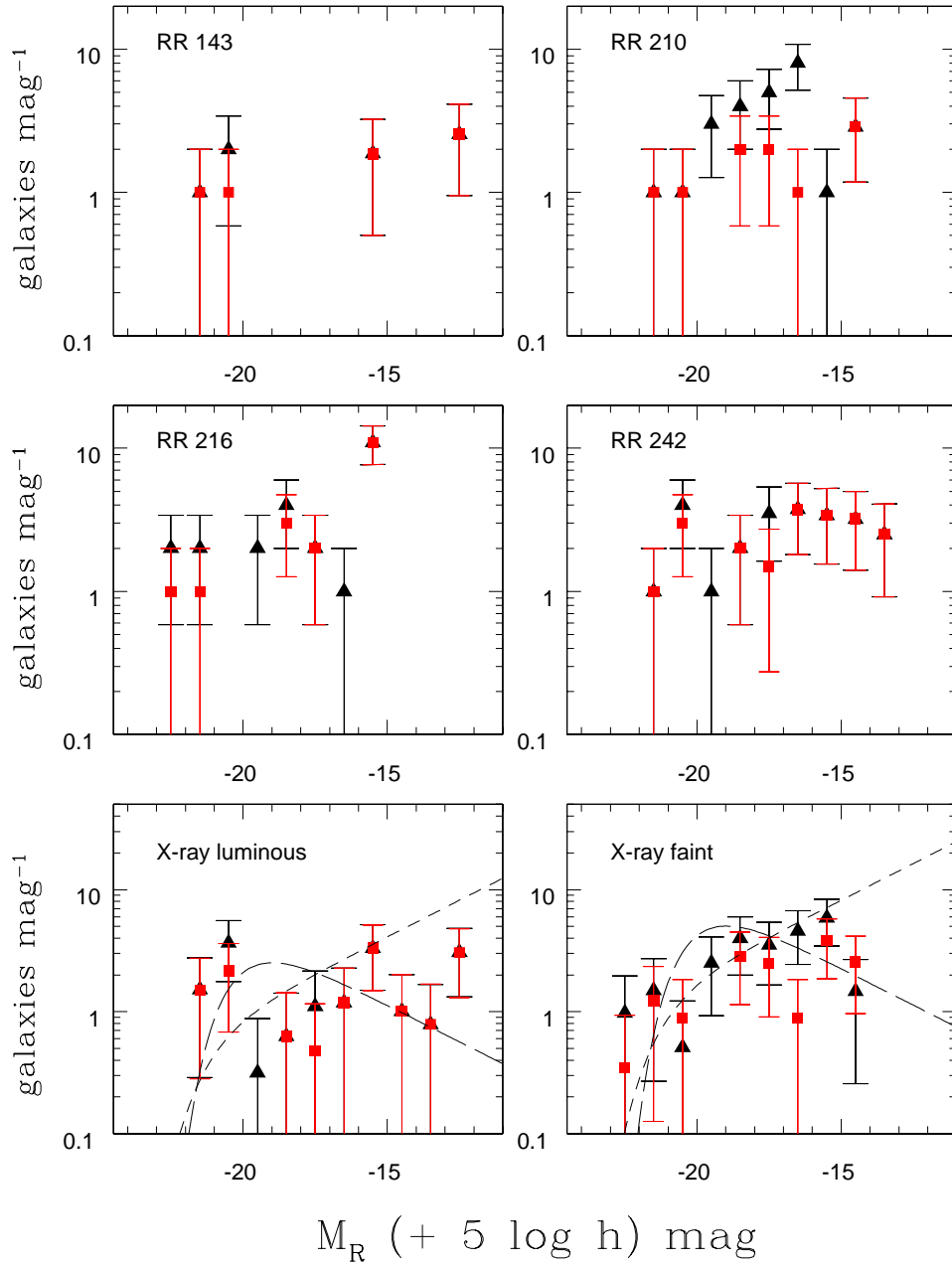
Figure 6.6: Individual and combined luminosity functions of the 4 groups. The LFs of the 2 X-ray luminous and the 2 X-ray faint groups are combined respectively. For this combined LFs the counts of the groups are normalized so that each group contains the same number of galaxies with $M_R < -15 + 5 \log h$. This avoids the shape of the combined LF to be dominated by the richer group. The LFs are computed for the large scale sample (black triangles) and the WFI field subsample (red squares).

6.2.3   Individual and combined group LFs

The top panels of Figure 6.6 show the LF of each group separately. The galaxy counts per magnitude are completeness-corrected but not normalized by the surveyed area. To compare the same physical area in all groups only galaxies within $0.5\ h^{-1}$ Mpc projected distance from the pair elliptical are considered, which is the area sampled in the closest group RR 210. However, also the inclusion of all galaxies within $90'$ does not significantly change the LFs. The LF of the WFI-subsample is plotted in red. The main difference between the LF of the WFI-subsample and the LF within $0.5\ h^{-1}$ Mpc is the lack of galaxies around $M_R = -19 + 5 \log h$, which is partly due to the selection criteria of the pair sample. The selection of galaxy pairs can lead to the selection of poorer local environments as it may be typical for poor groups.

The 2 bottom panels of Figure 6.6 show the combined LFs of the two groups with IGM (X-ray luminous) and the two groups without IGM (X-ray faint) respectively. Before combining them the LF of each group was normalized to have the same number of members brighter than $M_R = -15 + 5 \log h$, i.e. the mean number of members of both groups brighter than $M_R = -15 + 5 \log h$. The LFs of both groups were then averaged. This procedure ensures that the shape of the combined LF is not weighted more by the richer group. Again the WFI-subsample is plotted in red. The dashed line represents the LF of X-ray detected poor groups found by Zabludoff & Mulchaey (2000), hereafter ZM00. They investigated a sample of 5 poor galaxy groups with X-ray halos of comparable luminosity to our 2 X-ray luminous pairs and found that their LF can be fitted by a Schechter function with $M^* = -21.6 + 5 \log h$ and $\alpha = -1.3$. These values are comparable to nearby rich cluster LFs (see eg. Trentham 1997; Driver et al. 1998). The long-dashed line shows the LF of the local field from the Las Campanas Redshift Survey (LCRS) found by Lin et al. (1996) with $M^* = -20.29 + 5 \log h$ and $\alpha = -0.7$. The normalisation of both LFs is adjusted to fit the number of members of our groups.

The combined LF of the two X-ray luminous groups seems to have a non-Schechter form with an excess of bright galaxies and is not consistent with the LF found by ZM00. But also the LCRS field LF cannot fit our observations, there are not enough giants of intermediate luminosity (below $M_R \sim -20 + 5 \log h$). The X-ray faint group LF on the other hand is consistent with the LF of ZM00, although there is still an excess of bright giant galaxies. However, within the errors the ZM00 LF is consistent with our observations.

Dwarf-to-giant (D/G) ratios were determined from the completeness-corrected counts for all individual groups and the 2 combined samples. The limit between giants and dwarfs was again $M_R = -19 + 5 \log h$ following ZM00. The values are computed

Table 6.4: Dwarf-to-giant (D/G) ratios obtained from the LFs.

group	D/G$_{0.5}^1$	D/G$_{0.5,17}^2$	D/G$_{WFI}^3$	D/G$_{WFI,17}^4$
RR 143	1.5	0.0	2.2	0.0
RR 210	4.2	1.8	3.9	2.0
RR 216	3.0	1.0	8.0	2.5
RR 242	3.4	0.9	4.3	0.9
combined X-ray luminous	2.1	0.3	2.9	0.3
combined X-ray faint	3.5	1.4	5.1	2.1

[1] D/G$_{0.5}$: dwarf-to-giant ratio for galaxies within 0.5 h^{-1} Mpc.
[2] D/G$_{0.5,17}$: dwarf-to-giant ratio for galaxies within 0.5 h^{-1} Mpc using only dwarfs brighter than $M_R = -17 + 5 \log h$.
[3] D/G$_{WFI}$: dwarf-to-giant ratio for galaxies within the WFI field of view.
[4] D/G$_{WFI,17}$: dwarf-to-giant ratio for galaxies within the WFI field of view using only dwarfs brighter than $M_R = -17 + 5 \log h$.

for the full dwarf sample and for galaxies brighter than $M_R = -17 + 5 \log h$ to be compared with values from the literature. Additionally, the D/G only for galaxies within the WFI field of view were calculated, since outside this field the information of faint member galaxies is missing. All values are given in Table 6.4.

The average D/G of the ZM00 X-ray luminous poor groups down to $M_R = -17 + 5 \log h$ was found to be 1.9 ± 0.4, compared to a value of less than 1.0 for local group galaxies in this magnitude range (Pritchet & van den Bergh 1999). The D/G ratios of our groups confirm the visual impression from the LFs in Figure 6.6. The X-ray faint groups have higher D/G ratios than the X-ray luminous groups. The value of the combined X-ray faint groups is close to the value found for the ZM00 X-ray luminous poor groups.

Considering that the two X-ray luminous groups are the more complete groups of our sample, the result is unlikely to be caused mainly by incompleteness effects. However, in the field of RR 143 the 3 candidates with M_R between -17 and -19 $+5 \log h$, the range of dwarfs used here, were not observed. Assuming that these 3 galaxies were members of the group would raise the D/G to ~ 1, similar to the one of RR 242. This value is still lower than the D/G of 1.9 from ZM00 as well as the D/G ratio found for our X-ray faint groups.

6.3 Morphology

Figure 6.7 shows R band thumbnails of the new confirmed member galaxies of all 4 groups. The morphologies of the galaxies are investigated with `ELLIPSE` and `GALFIT` (see also Section 4.4). Results are compared with the galaxy morphologies of the X-ray detected groups discussed in Tran et al. (2001), which is the same sample of the groups investigated by ZM00.

6.3.1 Surface photometry with `ELLIPSE`

Detailed surface photometry of all new members was performed with the `IRAF` `ELLIPSE` task already described in Section 4.4. The residual images after subtracting a galaxy model constructed from the isophotal fit is shown in Figure 6.13. A lot of substructure is visible in the residual images: asymmetries (RR143_09192, RR242_23187, RR242_25575), bars (RR143_09192, RR216_04052, RR242_22327), filaments (RR242_13326) and even shells (RR242_24532).
The latter 2 galaxies and their residual image are shown in Figure 6.8 (RR242_13326) and 6.9 (RR242_24532) in more detail. The filament in RR242_13326 might be the debris of an accreted companion. However, the resolution is not high enough to properly identify this feature.
The system of shells in RR242_24532 extends out to a radius of ~ 8 kpc. The shell system is not aligned with the semi-major axis of the galaxy's main body. The shift in position angle is $\sim 30°$. Different formation scenarios for stellar shells have been proposed, ranging from weak interactions, accretion of companions to minor and major merging events (see eg. Barnes 1992). In any case, they are considered a clear evidence of environmental influence on galaxy evolution.

The radial profiles of surface brightness, ellipticity, PA, and higher order coefficients of the Fourier expansion a_3, b_3, a_4, b_4 for each galaxy are shown in Figures 6.11 and 6.12. Together with the isophotal profiles the `GALFIT` 2 component model (see next Section) is plotted. The dotted red lines are the sersic (bulge) and exponential (disk) models, while the solid line represents the resulting total galaxy model. The figures show that that the 2 component model represents a good fit to the real profiles in most cases.

The number of barred galaxies in our faint galaxy sample is high. In 5 objects (out of 17) the bar is clearly distinguishable in the radial profiles, confirming the visual impression from the images, while in one case (RR242_25575) there might be a weak bar. A very strong bar is visible as a bump in the surface brightness profile (e.g. RR242_22327). Another signature of a bar is a high ellipticity. The ellipticity usually rises to a maximum before it settles down to the constant value
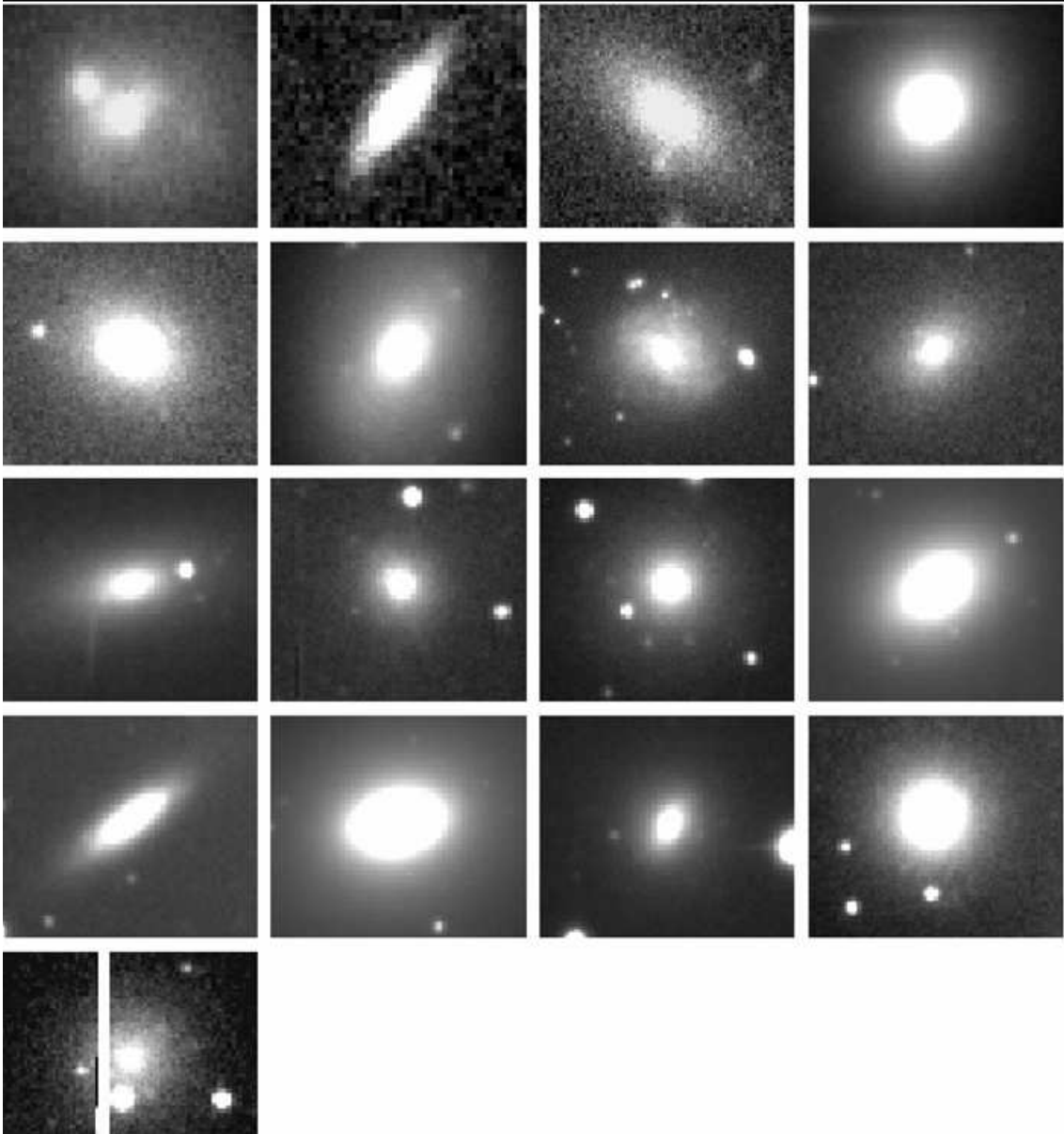
Figure 6.7: R band thumbnails of member galaxies of all pairs. From left to right:
1st row: RR143_09192, RR143_24029, RR210_11372 and RR210_13493;
2nd row: RR216_03519, RR216_04052, RR216_12209 and RR242_08064;
3rd row: RR242_13326, RR242_15689, RR242_20075 and RR242_22327;
4th row: RR242_23187, RR242_24352, RR242_25575 and RR242_28727;
last row: RR242_36267.

of the inclined disk. This ellipticity maximum and a corresponding change in the position angle is a very strong indication for a bar (e.g. RR143_09192). This way of detecting a bar does not work in disks that are highly inclined to the line of sight.

6.3.2   Bulge-disk decomposition with `GALFIT`

In order to investigate the bulge-to-total (B/T) ratios of our member galaxies a bulge-disk decomposition was attempted with `GALFIT` (see also Section 4.4).

Bulge-disk decompositions are usually done by fitting a de Vaucouleurs bulge ($\mu_r \sim r^{1/4}$) and an exponential disk ($\mu_r \sim r$) to the galaxy's surface brightness profile. Tran et al. (2001) found that the galaxy population of poor X-ray detected groups are well fitted by a 2-component model composed of a de Vaucouleurs bulge and an exponential disk. However, the shape of the profile - determined by the exponent $1/n$ - is supposed to change significantly with mass (see Section 4.4). This is not only valid for low mass ellipticals, it means that also the bulges of low mass galaxies are expected to show a different profile shape, i.e. a lower n. It may therefore be more accurate to let n vary as a free parameter of the fit. However, this also introduces a new uncertainty and ambiguity into the fit. To investigate the differences between the use of $n = 4$ (de Vaucouleurs bulge) or n as a free parameter (Sersic bulge), both combinations of bulges with exponential disks were fitted to our member galaxies.

The results of this procedure are given in Table 6.5. Some objects could not be fitted with a bulge and disk model, in which case no bulge magnitude is given in the
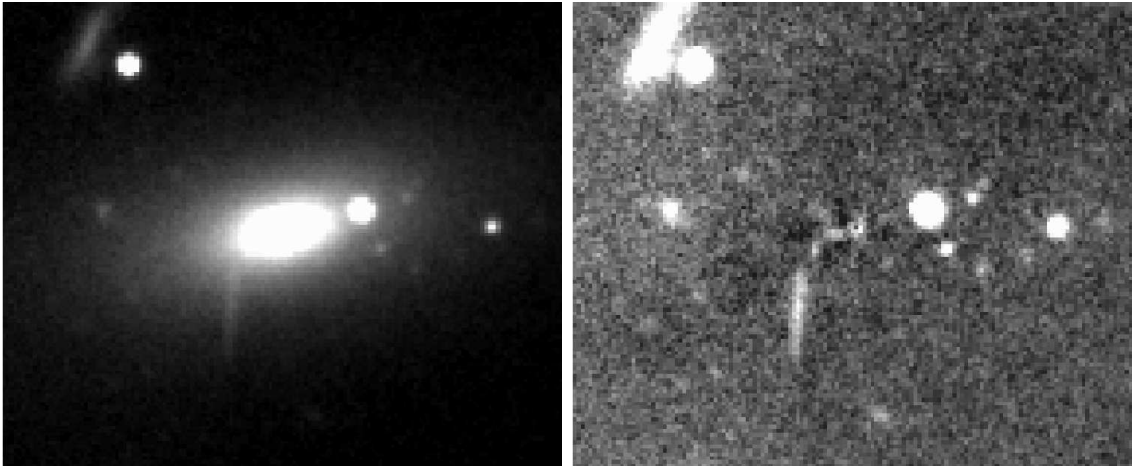
Figure 6.8: Filament in RR242_13326. R band image and residual image after `ELLIPSE` model subtraction. The size of the image is about 30 arcseconds.
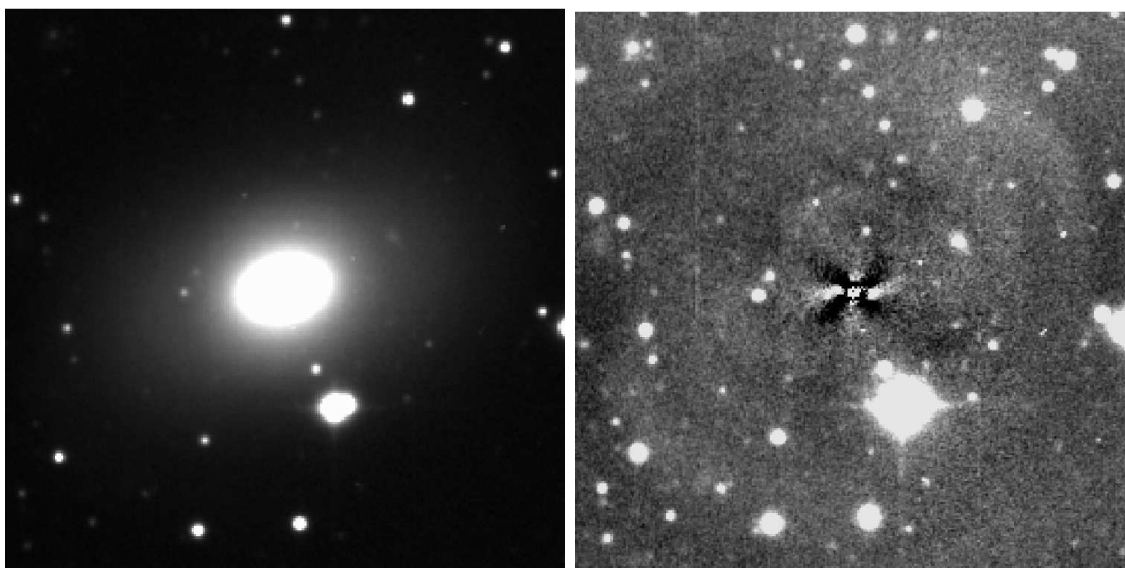
Figure 6.9: Shell structure in RR242_24532. R band image and residual image after `ELLIPSE` model subtraction. The size of the image is about 1 arcminute.

Table. The residual images of each galaxy after subtraction of the respective model are shown in Figure 6.13 for the model with Sersic bulge and in Figure 6.14 for the model with de Vaucouleurs bulge respectively. The differences between the two models are significant, especially for the bulge dominated objects. The comparison between Figures 6.13 and 6.14 shows that the de Vaucouleurs bulges do not fit the galaxies very well. The Sersic bulge seems to be a better representation of real faint galaxy bulges.

Figure 6.15 shows the number distribution of B/T ratios for the Sersic (black, shaded) and de Vaucouleurs model (red, dotted line). The two distributions differ in the higher B/T range: the de Vaucouleurs model tends to overestimate the magnitude of the true bulge and is biasing the B/T ratio towards a higher value. However, both distributions show that our sample is dominated by low B/T - i.e. disk dominated - galaxies.

The comparison between the measured isophotal profiles with `ELLIPSE` and the fitted 2 component model with `GALFIT` is shown in Figures 6.11 and 6.12. The dotted lines represent the bulge and disk model respectively. A model for the bar was added for the brighter bars. The solid line represents the resulting galaxy model where the separate components are added.

The morphological classifications given in Table 6.5 are based on the surface brightness profiles and visual inspection. An automatic classification with the B/T ratio
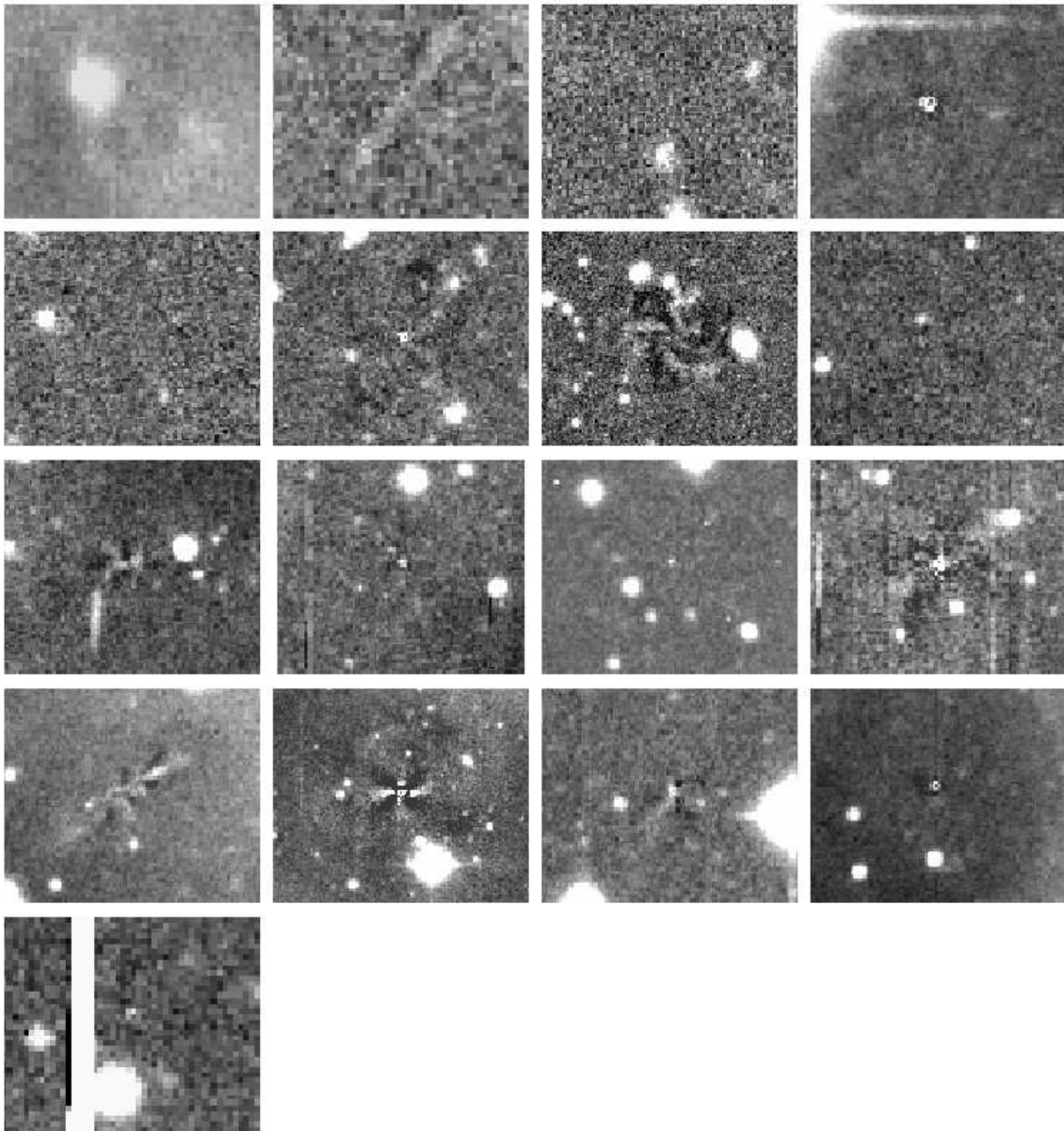
Figure 6.10: Residual images after subtraction of a model constructed from the isophotal fit with ELLIPSE. Objects are in the same order as in Figure 6.7.

was proposed by previous authors and is also used by Tran et al. (2001). This automatic classification is dividing between late (S, disk dominated) and early-type (S0 and E, bulge dominated) galaxies at B/T = 0.4. This may work for distinguishing between bright E and S galaxies, but for DE and especially S0 galaxies this is
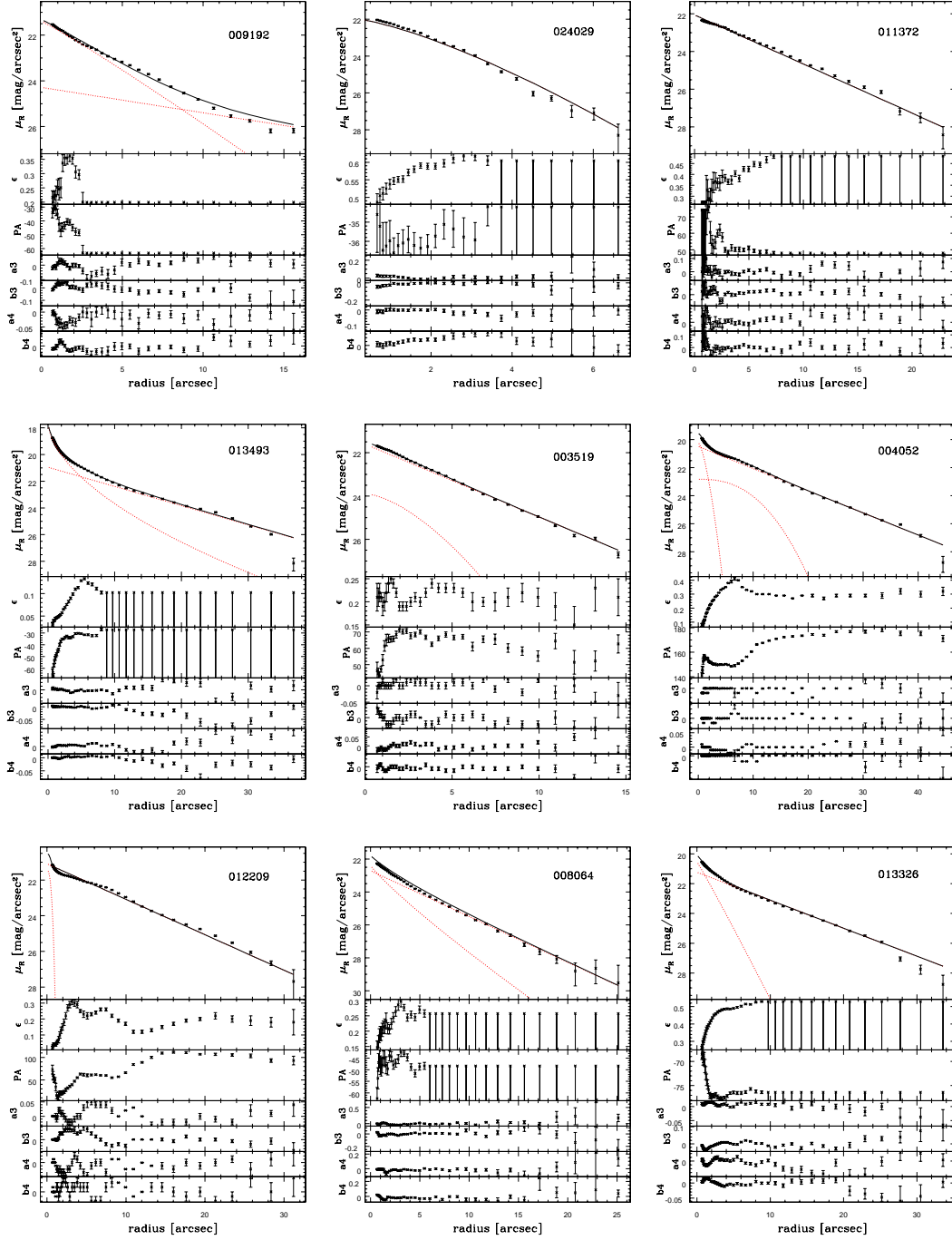
Figure 6.11: Radial isophotal profiles of faint member galaxies in the R band obtained by ELLIPSE. Objects RR143_09192, RR143_24029, RR210_11372, RR21_13493, RR216_03519, RR216_04052, RR216_12209, RR242_08064 and RR242_13326.
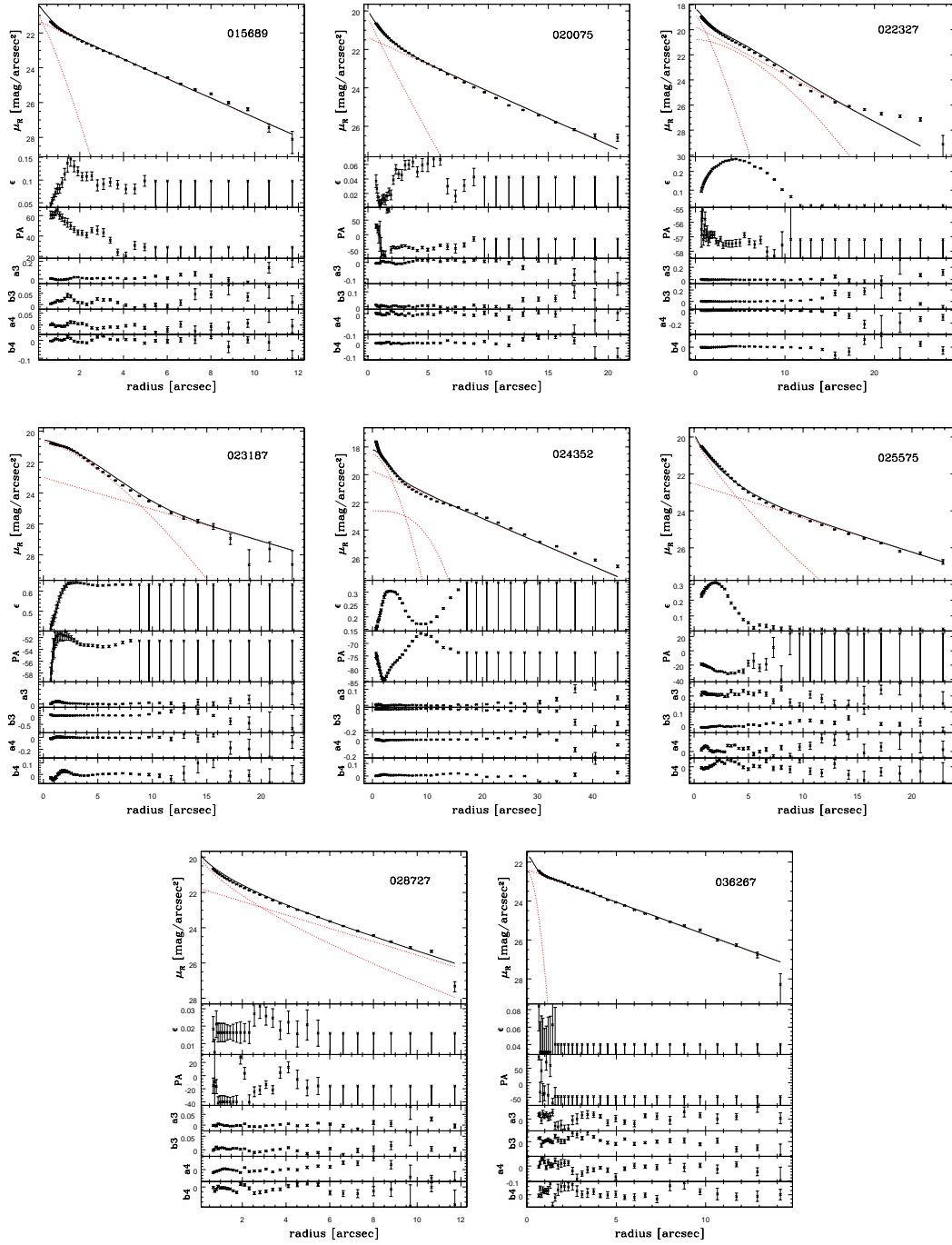
Figure 6.12: Radial isophotal profiles of faint member galaxies in the R   band obtained by ELLIPSE. Objects RR242_15689, RR242_20075, RR242_22327, RR242_23187, RR242_24352, RR242_25575, RR242_28727, RR242_36267.
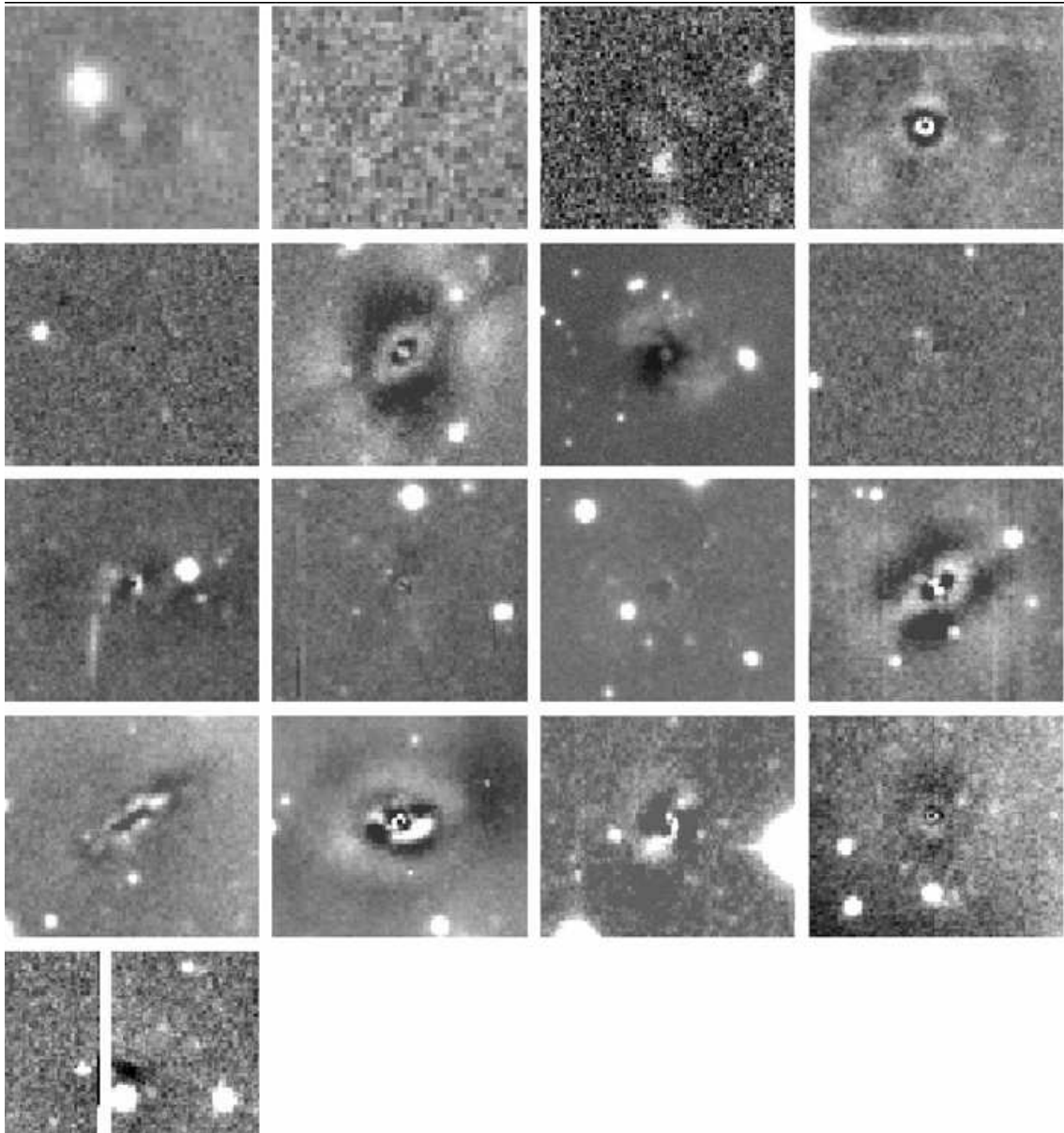
Figure 6.13: Residual images after subtraction of a 2 component model with a Sersic bulge and an exponential disk fitted by `GALFIT`. Objects are in the same order as in Figure 6.7.

problematic. A comparison between the classification by eye and the classification suggested by the B/T ratio shows the problem: S0 galaxies can have a wide range of bulge to disk ratios and are not necessarily bulge dominated systems. The same is the case for dE, which can be purely exponential or nucleated dwarfs with a higher
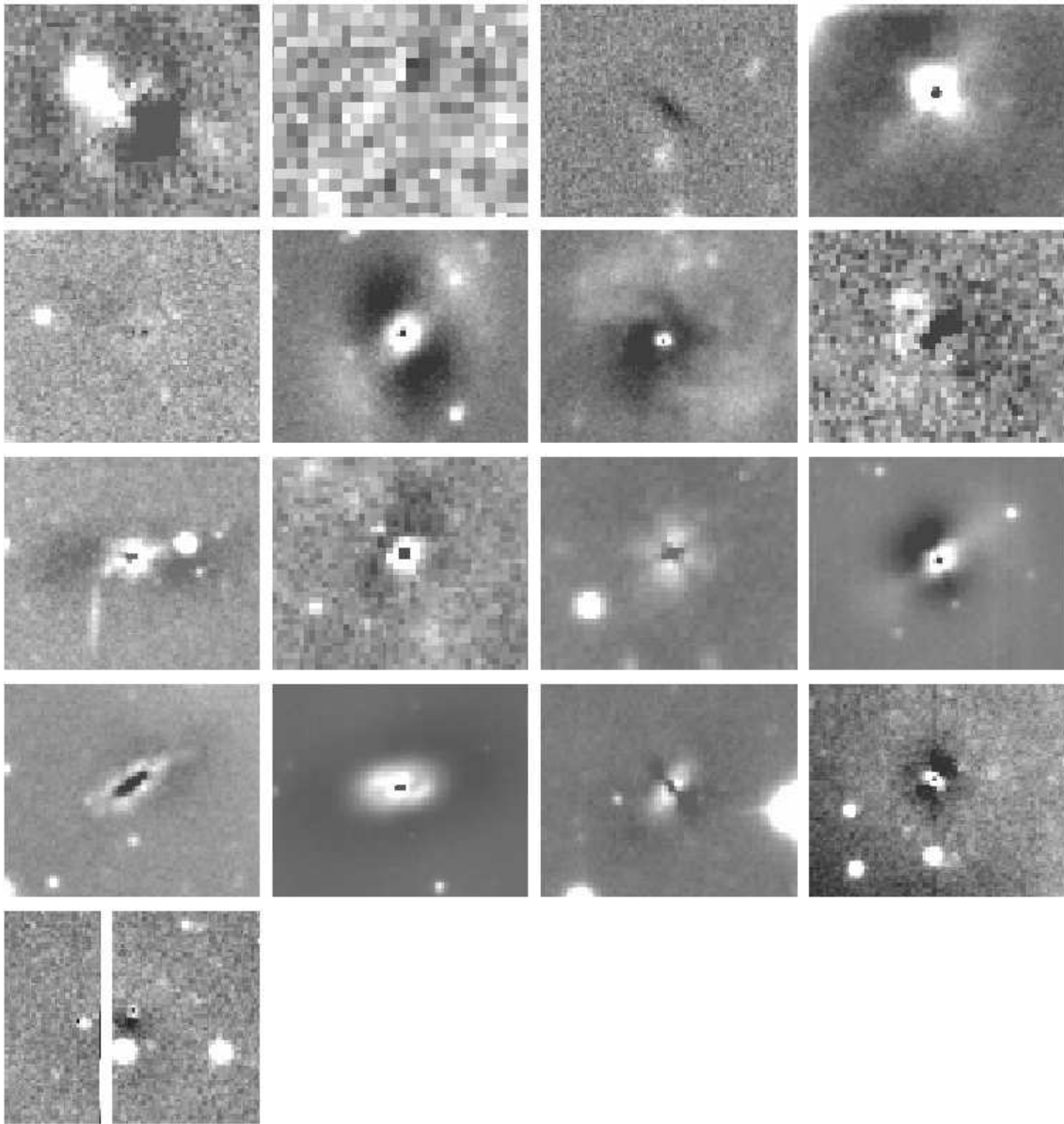
Figure 6.14: Residual images after subtraction of a 2 component model with a de Vaucouleurs bulge and an exponential disk fitted by `GALFIT`. Objects are in the same order as in Figure 6.7.

B/T ratio. Our sample is composed of a high fraction of S0s (6 out of 17, 35%), but only 3 of them have a B/T > 0.4 (18%). This would give an automatically classified early-type fraction that is similar to that of the field, whereas the S0-fraction ob-

Table 6.5: Bulge-disk decomposition: bulge and disk magnitudes and bulge-to-total light (B/T) ratios of the fit with de Vaucouleurs and Sersic bulges respectively.

| object | morph. type | de Vaucouleurs bulge | | Sersic bulge | | | B/T_{deV} | B/T_S | Δ B/T |
		bulge m_R	disk m_R	bulge m_R	bar m_R	disk m_R			
RR143_09192	SB0	19.10	17.33	17.31	20.70	18.55	0.16	0.77	-0.6
RR143_24029	S	–	19.89	–	–	19.89	0.00	0.00	0
RR210_11372	DE	–	17.58	–	–	17.58	0.00	0.00	0
RR210_13493	SB0	15.11	14.87	16.18	17.30	14.53	0.44	0.23	0.22
RR216_03519	DE	21.95	17.29	20.69	–	17.32	0.01	0.04	-0.03
RR216_04052	SB0	17.95	14.67	17.39	–	14.70	0.05	0.08	-0.03
RR216_12209	Sc	22.07	15.63	21.79	–	15.63	0.00	0.00	0
RR242_08064	DE	19.25	18.18	19.28	–	18.30	0.27	0.29	-0.02
RR242_13326	S0	17.17	16.54	18.64	–	16.29	0.36	0.10	0.26
RR242_15689	DE	19.52	18.10	20.93	–	17.95	0.21	0.06	0.15
RR242_20075	DE	17.39	16.79	18.74	–	16.53	0.37	0.12	0.25
RR242_23187	S	–	–	17.63	–	17.96	–	0.57	–
RR242_22327	SB0	16.72	15.51	17.58	16.56	15.79	0.25	0.41	-0.16
RR242_24352	SB0	14.59	14.52	15.31	17.36	14.17	0.49	0.29	0.2
RR242_25575	SB?	16.27	17.70	17.62	–	16.77	0.79	0.31	0.47
RR242_28727	DE	18.25	17.38	17.95	–	17.40	0.31	0.38	-0.07
RR242_36267	DE	21.31	17.92	23.06	–	17.89	0.04	0.01	0.03

tained by eye is more typical of galaxy clusters and X-ray luminous galaxy groups (Tran et al. 2001, and references therein).

The B/T ratios versus the projected distance from the field center (the pair E) is shown in Figure 6.15. The individual galaxies are plotted as small dots, again in red (de Vaucouleurs bulge) and black (Sersic bulge). The mean and dispersion are computed in bins of 50 kpc ($H_0 = 67$ km s^{-1} Mpc^{-1}) and plotted as open circles with respective error bars. A morphology-radius ($\sim$ density) relation seems to be present in our sample: galaxies with higher B/T ratios tend to be more centrally concentrated than pure disks. This result was also found for the groups studied by Tran et al. (2001). However, due to projection effects and the small number of objects the dispersion is very large. The trend is more significant for the de Vaucouleurs model, which was already found to represent a bad fit to the real galaxy bulges and to overestimate the B/T ratios. For the Sersic model the relation is flatter and the dispersion is larger than the slope of the relation. Therefore this result remains quite tentative and has to be used with caution.
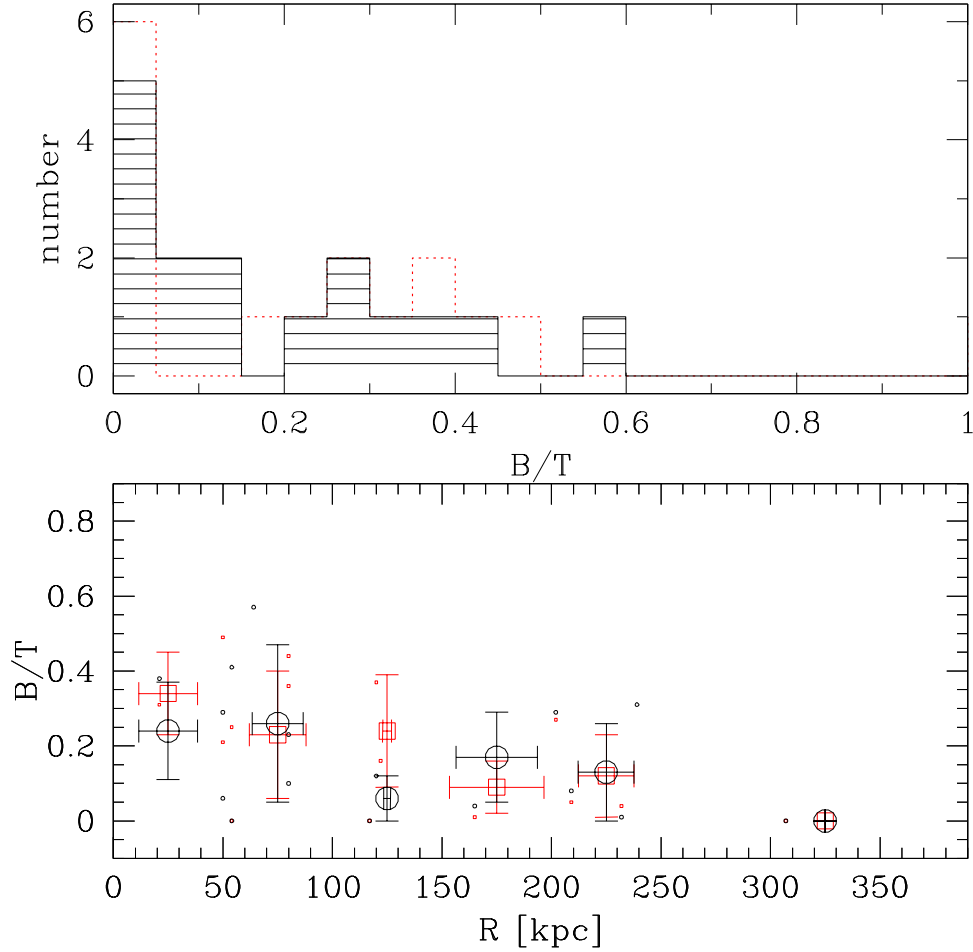
Figure 6.15: Bulge-to-total ratios of member galaxies of the 4 groups: number and spatial distribution of B/T for the fit with Sersic bulges (black) and de Vaucouleurs bulges (red) respectively.

6.4 Photometric relations

6.4.1 CMR for member galaxies

Figure 6.16 shows the colour-magnitude relation of the four samples already shown in Figure 4.2, but now the confirmed member galaxies of each structure were plotted with red crosses. All galaxies follow very well the red sequence for early-type galaxies (solid line), also at faint magnitudes. The new members have very uniform colours, no blue star-forming dwarfs are present in our sample.
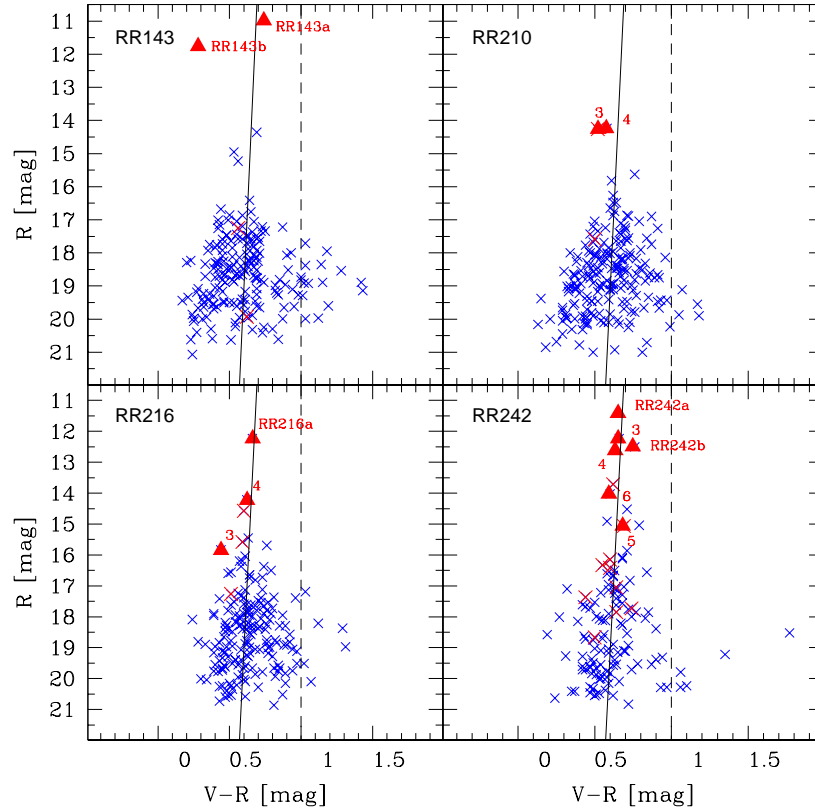
Figure 6.16: Colour-magnitude relation for group member galaxies. Same as in Figure 4.2, but with the confirmed members plotted as red crosses.

6.4.2 Kormendy Relation

Elliptical galaxies and early-type bulges are known to follow a relation between their effective radius r_e and the surface brightness at this radius μ_e (Kormendy 1977), the so-called Kormendy Relation (KR). The $\log r_e - \mu_e$ plane is one projection of the Fundamental Plane of early-type galaxies, which is basically a correlation between velocity dispersion, characteristic sizes and densities of early-type galaxies. The principal message of this plane is that massive ellipticals have different structures than fainter galaxies, they are more extended but also less dense (lower μ_e at higher corresponding r_e). Faint E, S0 or dwarf elliptical (dE) galaxies are not following this relation, but are rather distributed in the $r_e - \mu_e$ plane below the KR and also below $r_e = 3$ kpc. They are considered a distinct family of galaxies, the so-called *ordinary* galaxies, whereas galaxies above $r_e = 3$ kpc belong to the family of *bright* ellipticals (Capaccioli et al. 1992).

The ordinary family is often considered to be the building blocks of galaxies in the bright family, although more recent simulations (Evstigneeva et al. 2004) show that through merging processes the galaxies move on tracks rather parallel to the KR. In this picture the present day ordinary galaxies can not produce the bright ellipticals we observe. However, these authors use dissipationless N-body simulations and admit that dissipation may significantly change the final point of a merging product and move it towards the KR. Merging gas rich ordinary galaxies could therefore produce bright ellipticals on the KR.
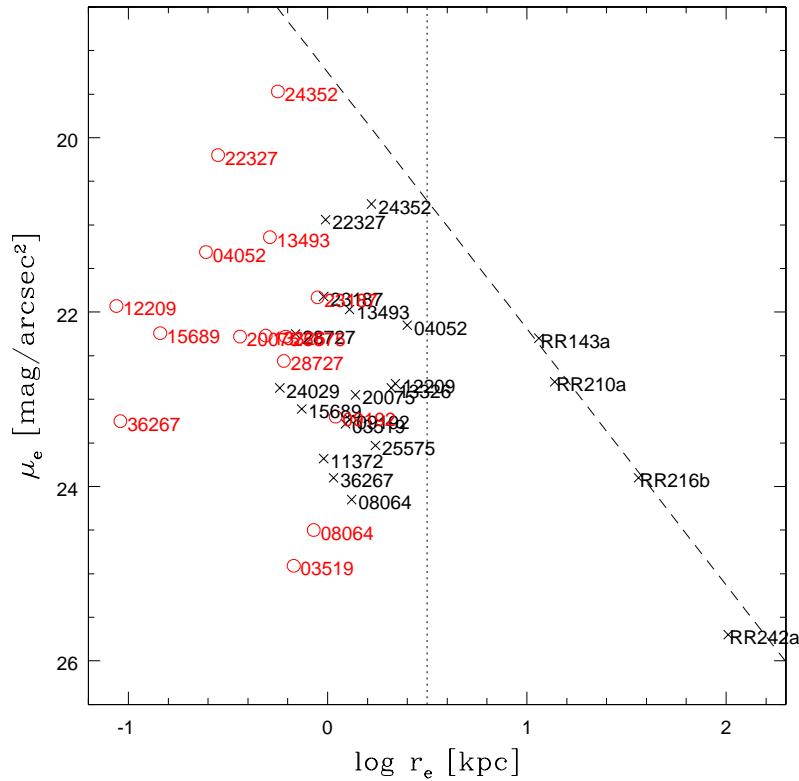
Figure 6.17: Kormendy relation for group member galaxies. The parameters of the 1 component sersic model are plotted as crosses. The red open circles are the parameters of the Sersic model bulge obtained by the bulge-disk decomposition (see section 6.3.2). All galaxies are labelled with their ID.

The plane of r_e and μ_e for our faint group member galaxies is shown in Figure 6.17. The 4 bright pair ellipticals RR 143a, RR 210a, RR 216b and RR 242a are also plotted. The parameters are taken from the 1 component Sersic fit as described in Section 2.2.3. The dashed line shows the KR from Kormendy (1977) shifted to the R

band. The dotted line at $\log r_e = 0.5$ separates the bright from the ordinary family (Capaccioli et al. 1992). The faint group members are plotted as crosses using their r_e and μ_e from the 1 component Sersic fit (described in Section 4.4) and as red open circles using the r_e and μ_e of the bulge component obtained with the bulge-disk decomposition described in section 6.3.2.

The 4 pair ellipticals lie on the KR clearly in the bright galaxy domain, whereas the faint members are distributed in the $\log r_e - \mu_e$ plane below the limit of ordinary galaxies. The brightest galaxy in the sample RR242_24352 is closest to the KR, whereas the faintest galaxies are clearly off the relation in the expected vertical strip of ordinary galaxies (Capaccioli et al. 1992).

Using the values of the bulge component only (red symbols) has an interesting effect: it moves the galaxies with high B/T ratios roughly parallel to the KR, since their bulges are smaller but more concentrated, thus have a higher surface brightness. The bulges of the most disk dominated objects (12209, 36267, 15689 and 03519) are displaced horizontally. Their small low n bulges are not more concentrated than the exponential disk, so they only get smaller, but not brighter, reaching almost the region populated by globular clusters. If these disk dominated objects are gas rich systems they could move horizontally towards the KR when increasing their bulge component via accretion or merging processes.

6.5 Spectral properties

The spectra of member galaxies observed with VIMOS are presented in Figure 6.18 and 6.19.

The spectra shown here are the total object spectra, i.e. the lines of the 2D spectrum are summed over the whole spatial extent of the galaxy. They are wavelength calibrated and sky-subtracted, but not flux calibrated, since spectro-photometric standard stars were not observed during all nights. In principle the available response functions for the nights in March could also be used to calibrate the spectra observed in January, however, this would introduce an additional source of uncertainty. Anyway, for the measure of absorption line indices the flux calibration is not necessary, since the measured values are calibrated with the indices of standard stars from the Lick system. The flux calibration would be needed to estimate star formation rates (SFR) from emission lines, yet there are no emission-line dominated galaxies in our group member sample. The 2 galaxies that show line emission have a dominant underlying absorption component from an older stellar population. Therefore we did not flux calibrate the spectra, they are plotted in the observed counts per unit of wavelength.
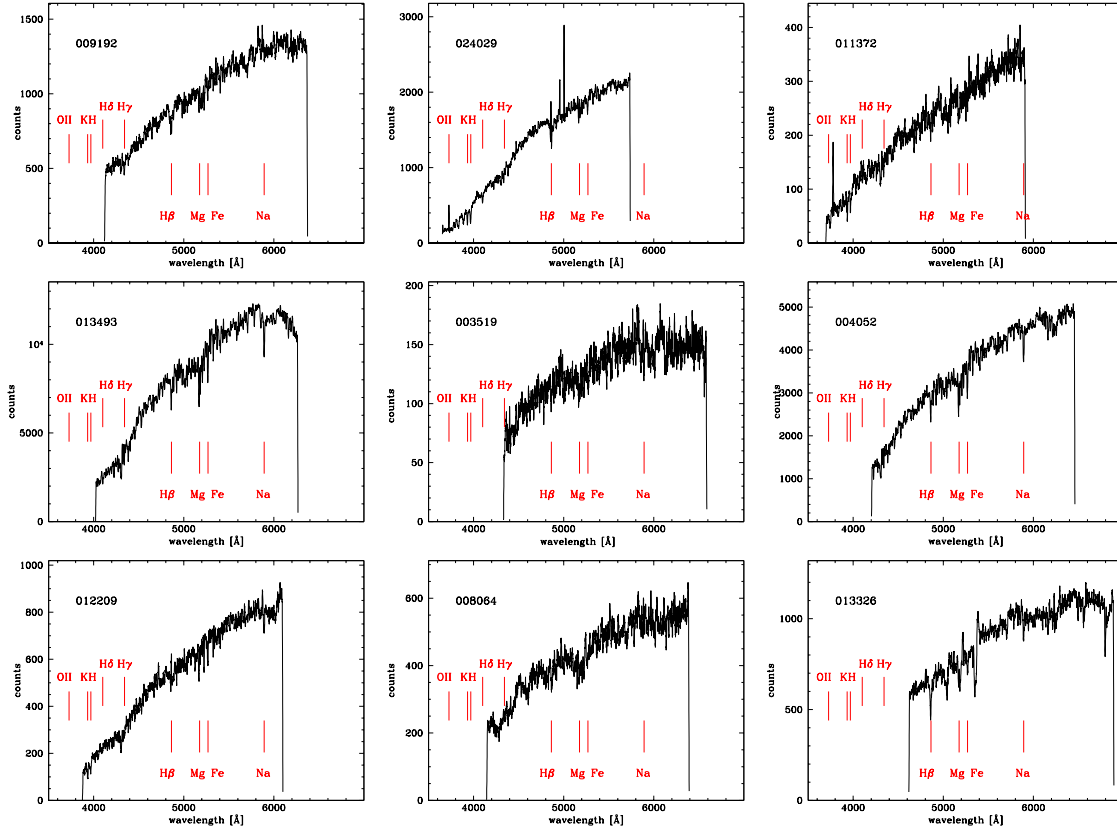
Figure 6.18: Spectra of member galaxies observed with VIMOS. Objects RR143_09192, RR143_24029, RR210_11372, RR21_13493, RR216_03519, RR216_04052, RR216_12209, RR242_08064 and RR242_13326.

6.5.1   Absorption features

The spectra are shifted to the respective rest-frame (z=0). The most prominent absorption lines Ca K+H, Hβ, Mg I (λ 5175 Å) and the Ca+Fe band (λ 5269 Å) are marked in each panel. As already suggested by the colour-magnitude relation, the spectra are characterised by a relatively old stellar population. Deep metal lines (Mg I and Fe) are present in most of the objects. However many galaxies also show strong Hβ absorption indicative of a younger population. The line strength of Hβ is relatively insensitive to the effects of metallicity. Together with the combined MgFe index it gives a robust determination of both, the mean age and mean metallicity of a galaxy (Worthey & Ottaviani 1997). The procedure of measuring line indices in the Lick-IDS system that will be applied to our spectra in future work is described in Rampazzo et al. (2005).
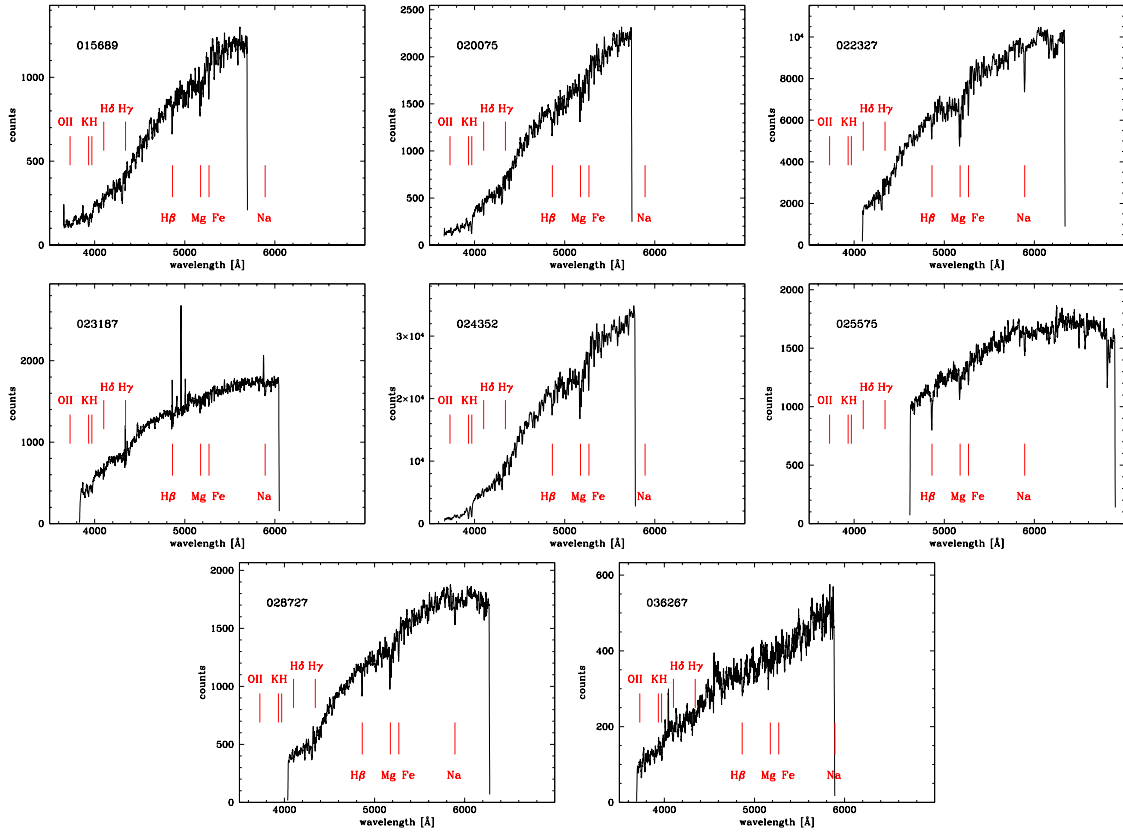
Figure 6.19: Spectra of member galaxies observed with VIMOS. Objects RR242_15689, RR242_20075, RR242_22327, RR242_23187, RR242_24352, RR242_25575, RR242_28727 and RR242_36267.

6.5.2   Emission features

The position of the [O II] emission line at λ 3727 Å, considered a good indicator of recent star formation (Kennicutt 1992), is also marked in each panel. Unfortunately this line is just outside of the spectral range covered in most of the spectra. Only one galaxy (RR143_24029) has a clear detection of [O II]. The two galaxies with detected emission lines (RR143_24029 and RR242_23187) also show clear detections of the [O III] lines at λ 4959 Å and λ 5007 Å (they are not marked in the figure due to the lack of space and to avoid confusion). The strong forbidden line emission relative to the weak emission of Hβ could be indicative of an active galactic nucleus (AGN) in these objects. An easy method to distinguish between star formation and AGN are emission line ratios of Balmer lines vs. forbidden lines such as Hβ/[O II] or Hα/[N II] (Veilleux & Osterbrock 1987). However, the strong Hβ absorption component

makes a reliable determination of line ratios very difficult. Additionally we lack the information about the line emission of Hα and [N II] (λ 6583 Å). In the spectrum of RR242_23187 there is also Hγ and Hδ in emission, suggesting that this galaxy has enhanced star formation. This is consistent with the clumpy circumnuclear structure seen in the model subtracted image, possible star forming regions. [O II] emission, which is also indicating recent star formation activity, is detected in RR143_24029. However, no other Balmer emission lines are detected. With the present data we cannot distinguish between star formation and AGN activity in this galaxy.

6.6   Summary and conclusions

The properties of the newly defined groups around the 4 galaxy pairs and their new members were investigated in this chapter. Galaxies with similar radial velocity to the pair ($\Delta v < 1000$ km s^{-1}) within a 90$'$ radius ($\sim 1\ h^{-1}$ Mpc) taken from NED are complementing the group population at larger radii. We calculated luminosity weighted group dynamics, individual and combined group luminosity functions and investigated the morphology of the new group members. We found the following results:

– The presence of extended diffuse X-ray emission from an IGM is not necessarily connected to the presence of a numerous faint galaxy population. A possible explanation for this is the dynamical age of the central elliptical. Groups in a similar environment can be in a different evolutionary phase traced by the giant central elliptical galaxy: interaction (accretion/merging) disrupts the hot gas halo, which is then built up again during ongoing evolution in a timescale of a few gigayears. In this picture RR 242 would be the most evolved system, RR 216, which is expected to have a significant number of faint companions, would then be in an earlier phase of its dynamical evolution. The same could be the case for RR 210, which is despite of its apparent lack of faint companions embedded in a compact larger-scale structure (in projection and redshift space). The apparent lack of faint companions concentrated around the pair could be a completeness problem. This point will soon be clarified with the completion of the observing program. The case of RR 143 is different. The lack of faint galaxies is real, incompleteness is supposed to play a minor role in this structure. Interestingly, the scarcity of faint members is continued at larger scales. In a radius of $\sim 1\ h^{-1}$ Mpc we found only two other galaxies with similar redshift.

– The IGM is a local phenomenon and is not connected to the large-scale group environment. The X-ray emission is centered on the pair elliptical but neither

of them is in the group center of mass. The velocity dispersion profile suggests that the dispersion is not constant with radius. It shows a maximum at $\sim$ 0.2 h^{-1} Mpc and decreases until $\sim$ 0.5 h^{-1} Mpc before increasing again in the outskirts of the groups. This might suggest either that the groups have a dynamical boundary at $\sim$ 0.5 h^{-1} Mpc or that mass has been stripped from this region. However, due to the low number of members this result has to be speculative.

– The dynamical group properties show that projection effects play a significant role in the groups. Therefore the values are uncertain by a factor of $\sim$ 2. However, the low crossing times indicate that at least the centres of the groups are virialized.
The luminosity weighting affects the values dramatically. Since the pair elliptical dominates the groups by far ($\sim$ 1/2 of the total group light in RR 143 and RR 210 and 1/3 in the other two), the values are dominated by the small separation of the central pair. We suggest that the uniformly weighted quantities provide a more realistic representation of the group properties in our case. There is no trend in the dynamical quantities with group X-ray luminosity. The velocity dispersion is increasing in numerical order from RR 143 to RR 242, the same is the case for the virial mass. Harmonic and virial radius of the groups are similar, apart from RR 216 in which the member galaxies are less concentrated towards the group center. This is probably due to the different large-scale environment of this pair, since it is located in the outskirts of the Hydra-Centaurus cluster region.

– The Luminosity Functions (LF) of X-ray luminous groups are different from the X-ray faint groups. They do not agree with the LF found for a sample of X-ray luminous poor groups by Zabludoff & Mulchaey (2000), neither with the LF of the local field (Lin et al. 1996). Our X-ray luminous groups show a higher number of bright galaxies or, in other words, they lack galaxies between -20 $< M_R <$ -19 $+5 \log h$ mag. This non-Schechter form of the LF is similar to the supposed dynamically evolved group around NGC 5846 (Mahdavi et al. 2005). The X-ray faint groups on the other hand agree with the LF of the ZM00 groups, they have a similar D/G ratio ($\sim$ 2). Despite the environmental differences between the two X-ray luminous groups in our sample their normalized LFs are quite similar showing a lower D/G ratio with equal numbers of dwarfs and giants. This could indicate that our X-ray luminous pairs are more dynamically evolved than the ZM00 groups. The X-ray faint groups on the other hand may show a phase in the dynamical evolution of the ZM00 groups where the recent or ongoing interaction, in which the pair E is involved, has destroyed or at least decreased the luminosity of the IGM.

– The morphological study of the new group members indicates a high number of S0 galaxies in our sample (35%), most of them with a low bulge-to-total light (B/T) ratio. We performed a bulge-disk decomposition and showed that a Sersic model (free n) represents a better fit to the bulges of these faint galaxies than the usual de Vaucouleurs model with $n = 4$. The automatic classification of faint galaxies following their B/T ratios is problematic for faint objects. Usually galaxies with B/T > 0.4 are considered early-type galaxies. However, the term of early-type galaxies combining ellipticals and S0s may not be appropriate for faint S0s.

A morphology-radius relation seems to be present in the combined group sample. Galaxies with higher B/T ratios seem to be more concentrated towards the field center, i.e. the pair elliptical (which is not the center of mass for the whole group!). However, there is a large spread in B/T ratios, the result remains tentative.

Signatures of interactions and merging are present in the group sample. Asymmetries, filaments, and shells are detected in several galaxies. Due to the small number of objects we did not attempt a statistical analysis of these signatures.

– The spectra of the new members are indicative of an old stellar population in the vast majority of galaxies. No blue objects, dIrr or tidal dwarfs are present in our sample. This is also supported by the colour-magnitude relation of group galaxies. Although we reach into the domain of dwarf irregular (dIrr) and dwarf spheroidal (dSph) galaxies that we observe in our local group, a significant part of them may be still to faint for being detected. However, interaction induced rejuvenation episodes resulting in a small fraction of younger stars may have happened in some objects. They can only be identified by the study of absorption line indices that will be carried out in future work.

Chapter 7

Summary, conclusions and outlook

The aim of this thesis is studying the evolution of poor groups of galaxies via the properties of their diffuse X-ray emitting gas component and their faint galaxy population.

We investigated the environment of 4 galaxy pairs composed of a giant elliptical galaxy and its spiral companion. The pairs are very similar from the optical and dynamical point of view, but have very different X-ray properties. Two of them show extended diffuse X-ray emission from a hot Intra Group Medium (IGM), whereas the other two seem to be deficient in hot gas.

Can this difference be caused by the environment of the galaxy pair or is it indicative of a different evolutionary phase of the pair or the elliptical? Are these pairs a way station in the coalescence process of galaxy groups towards giant isolated ellipticals with extended group-like IGM, the famous fossil groups?

The answers to these questions may be hidden in the population of faint galaxies possibly surrounding the pairs. While the brighter objects in a typical loose group can merge within a Hubble-time, the fainter galaxies should remain due to their longer merging timescale. The main conclusions of this study and perspectives of future work are summarized in the following.

7.1 Summary and Conclusions

– **Optical properties of the pairs**
   The E members of the pairs show very similar optical (colour) and kinematical (velocity dispersion) properties. However we found that RR 143a and RR 242a are dynamically more relaxed objects with an extended regular halo and without signatures of past or recent interactions. The early-type galaxies in RR 210 and RR 216 on the other hand display unambiguous signs of recent or ongoing

interaction as evidenced by the model-subtracted and unsharp-masked images. Extended dust lanes (RR 210a) and diffuse stellar light plumes (RR 216b) were detected in these two galaxies.

– **Properties of the IGM around the pairs**
The X-ray emission of RR 210 and RR 216 is relatively faint and compact, i.e. within the optical galaxy and consistent with the expected emission from the evolved stellar population. The presence of an IGM is very unlikely.
RR 143 and RR 242 are more luminous and their emission is extended, indicating the presence of a large amount of hot gas or IGM. The `XMM-Newton` observations confirm the presence of diffuse extended emission with luminosities of around $L_X \sim 3 \times 10^{41}$ erg s^{-1} and radii of ~ 120 kpc in RR 143 and ~ 160 kpc in RR 242.
This emission, though centered on the elliptical, encloses both pair members (in RR 143) and even another group member (NGC 5082 in RR 242), suggesting that the pairs are bound and sitting in a deep potential well. The X-ray morphologies however suggest that these two systems may be at different stages of evolution: RR 242 appears more relaxed with a more regular and azimuthally symmetric emission, while the emission in RR 143 has a clear elongation towards the companion possibly indicating dynamical effects (tidal/ram pressure stripping). However, no optical distortion can be seen in the spiral of RR 143.

– **Properties of the candidate faint galaxy population around the pairs**
We detected a candidate faint galaxy population in WFI-fields around the 4 pairs (radius ~ 0.2 h^{-1} Mpc) down to $M_R \sim$ -12 $+5 \log h$ mag. The detected sample was limited in $(V - R)$ colour via the colour-magnitude relation to exclude likely background galaxies. This yielded 151, 172, 160 and 102 candidate galaxies in the fields of RR 143, RR 210, RR 216 and RR 242 fields respectively. From the analysis of photometric and structural properties of the faint galaxy populations around the pairs we can conclude that the candidates around RR 242 show the highest membership probability. RR 143 and RR 216 probably have a smaller faint galaxy population, while RR 210 seems to have very few associated faint galaxies.

– **Results of the spectroscopic observations**
The observing program was not completed. The fields of the 2 X-ray luminous pairs were fully observed, whereas the fields of the 2 X-ray faint pairs were only partly covered, 50% in RR 210 and 25% in RR 216. From the 258 observed objects we could measure redshifts for 213, a success rate of 83%. Out of these 213 objects we found that only 17 are faint galaxies associated to the pairs: 2 members in RR 143 (2% of galaxies with measured redshift), 2 members in

RR 210 (4%), 3 members in RR 216 (14%) and 10 members in RR 242 (18%). The majority of background galaxies are clustered in a background structure well separated from our groups in redshift space.

A magnitude dependent completeness correction was applied to each group sample. From this completeness correction we expect a high number of missed members in RR 216.

– **IGM vs group environment**
The presence of extended diffuse X-ray emission from an IGM is not necessarily connected to the presence of a numerous faint galaxy population. A possible explanation for this is the dynamical age of the central elliptical. The centres of groups surrounded by a similar environment can be in a different evolutionary phase traced by the giant central elliptical galaxy: interaction (accretion/merging) disrupts the hot gas halo, which is then built up again during ongoing evolution in a timescale of a few gigayears. In this picture RR 242 would be the most evolved system, while RR 216 would be in an earlier phase of its dynamical evolution. The apparent lack of faint companions concentrated around RR 210 could be a completeness problem. The scarcity of faint members in RR 143 could be connected with its very sparse large-scale environment.

The IGM is a local phenomenon and is not connected to the large-scale group environment. The X-ray emission is centered on the pair elliptical but neither of them is in the group center of mass. The velocity dispersion profile suggests that the dispersion is not constant with radius. However, due to the low number of members this is a speculative result.

– **Group dynamics**
The dynamical group properties show that projection effects play a significant role in the groups. Therefore the values are uncertain by a factor of ~ 2. However, the low crossing times indicate that at least the centres of the groups are virialized.

The luminosity weighting affects the values dramatically. Due to the small separation of the dominant central pair, we suggest that the uniformly weighted quantities provide a more realistic representation of the group properties in our case.

The dynamical quantities are not correlated with the group X-ray luminosity, but with the large-scale environment of the pairs.

– **Luminosity functions**
The Luminosity Functions (LF) of X-ray luminous groups are different from the X-ray faint groups. A comparison with LFs of a sample of X-ray bright

groups (ZM00 groups) suggests that our X-ray luminous pairs are more dynamically evolved than the ZM00 groups. The X-ray faint groups on the other hand may show a phase in the dynamical evolution of the ZM00 groups where the recent or ongoing interaction, in which the pair E is involved, has destroyed or at least decreased the luminosity of the IGM.

– **Properties of new group members**
The morphological study of the new group members indicates a high number of S0 galaxies in our sample (35%), most of them with a low bulge-to-total light (B/T) ratio. We performed a bulge-disk decomposition and showed that a Sersic model (free n) represents a better fit to the bulges of these faint galaxies than the usual de Vaucouleurs model with $n = 4$. The automatic classification of faint galaxies in late and early-types following their B/T ratios is problematic for faint objects. The term of early-type galaxies, combining ellipticals and S0s, may not be appropriate for faint S0s.
A morphology-radius relation seems to be present in the combined group sample. Galaxies with higher B/T ratios seem to be more concentrated towards the field center, i.e. the pair elliptical (which is not the center of mass for the whole group!). However, there is a large spread in B/T ratios, the result remains tentative.
The spectra of the new members are indicative of an old stellar population in the vast majority of galaxies. No blue objects, dIrr or tidal dwarfs are present in our sample. This is also supported by the colour-magnitude relation of group galaxies. Although we reach into the domain of dwarf irregular (dIrr) and dwarf spheroidal (dSph) galaxies that we observe in our local group, a significant part of them may be still too faint for being detected.

7.2   Future work

– To support some of our tentative results the observations of the partly observed 2 X-ray faint pairs have to be completed. A new observing program proposing the continuation of the observations was accepted and will be carried out in Period 80 (October 2007 - March 2008).

– The study of the galaxy spectra is going to be continued with the measure of absorption line strength indices in the Lick/IDS system. This work will be carried out together with our collaborators at the Osservatorio Astronomico di Padova, following the procedure described in (Rampazzo et al. 2005).

– Our work suggests that the differences in X-ray properties of the groups are connected to the dynamical age of the brightest group elliptical. Therefore

we have to find out more about the history of the pair E. A new observing program focusing on the star formation history of the pair elliptical revealing past accretion/merging events will be proposed for the next observing period at ESO. With the information we have now in hand we are confident that this proposal will be approved.
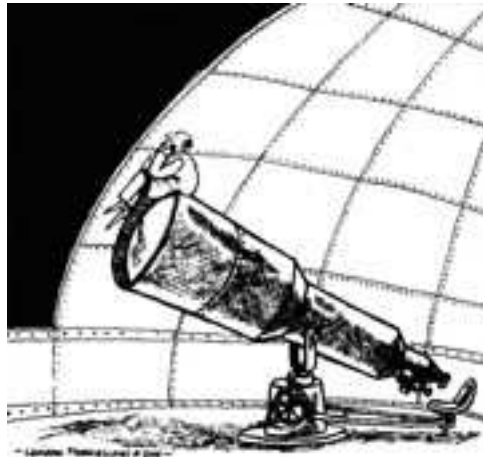
**The universe may
be as great as they say
but it wouldn't be missed
if it didn't exist.**

− Piet Hein −

Bibliography

Annibali, F., Bressan, A., Rampazzo, R., Zeilinger, W. W., & Danese, L. 2007, A&A, 463, 455

Arp, H. C. & Madore, B. F. 1987, A Catalogue of Southern Peculiar Galaxies and Associations 2 volume set (Halton C. Arp and Barry F. Madore, pp. 504. ISBN 0521343364. Cambridge, UK: Cambridge University Press, May 1987.)

Barnes, J. E. 1992, ApJ, 393, 484

Bertin, E. & Arnouts, S. 1996, A&AS, 117, 393

Bettoni, D., Falomo, R., Fasano, G., & Govoni, F. 2003, A&A, 399, 869

Binggeli, B., Sandage, A., & Tarenghi, M. 1984, AJ, 89, 64

Binney, J. & Merrifield, M. 1998, Galactic astronomy (Galactic astronomy / James Binney and Michael Merrifield. Princeton, NJ : Princeton University Press, 1998. (Princeton series in astrophysics) QB857 .B522 1998 ($35.00))

Binney, J. & Tremaine, S. 1987, Galactic dynamics (Princeton, NJ, Princeton University Press, 1987, 747 p.)

Boylan-Kolchin, M., Ma, C.-P., & Quataert, E. 2005, MNRAS, 362, 184

Brassington, N. J., Ponman, T. J., & Read, A. M. 2007, MNRAS, 377, 1439

Caon, N., Macchetto, D., & Pastoriza, M. 2000, ApJS, 127, 39

Capaccioli, M. 1989, Galaxy Photometry (Gerard and Antoinette de Vaucouleurs: A life for Astronomy), 173–+

Capaccioli, M., Caon, N., & D'Onofrio, M. 1992, MNRAS, 259, 323

Cellone, S. A. & Buzzoni, A. 2005, MNRAS, 356, 41

Ciotti, L., Lanzoni, B., & Volonteri, M. 2007, ApJ, 658, 65

Ciotti, L., Pellegrini, S., Renzini, A., & D'Ercole, A. 1991, ApJ, 376, 380

Conselice, C. J. 2006, ApJ, 638, 686

Conselice, C. J. 2007, ArXiv e-prints, 706

Da Rocha, C. & Mendes de Oliveira, C. 2005, MNRAS, 364, 1069

de Souza, R. E., Gadotti, D. A., & dos Anjos, S. 2004, ApJS, 153, 411

de Vaucouleurs, G. 1948, Annales d'Astrophysique, 11, 247

Dettmar, R.-J. & Luetticke, R. 1999, in Astronomical Society of the Pacific Con-
    ference Series, Vol. 165, The Third Stromlo Symposium: The Galactic Halo, ed.
    B. K. Gibson, R. S. Axelrod, & M. E. Putman, 95–+

Dickens, R. J., Currie, M. J., & Lucey, J. R. 1986, MNRAS, 220, 679

Dressler, A. 1980, ApJ, 236, 351

Dressler, A., Lynden-Bell, D., Burstein, D., et al. 1987, ApJ, 313, 42

Driver, S. P., Couch, W. J., & Phillipps, S. 1998, MNRAS, 301, 369

Ellis, S. C. & Bland-Hawthorn, J. 2007, MNRAS, 377, 815

Evstigneeva, E. A., de Carvalho, R. R., Ribeiro, A. L., & Capelato, H. V. 2004,
    MNRAS, 349, 1052

Fabbiano, G., Kim, D.-W., & Trinchieri, G. 1992, ApJS, 80, 531

Fabbiano, G. & Schweizer, F. 1995, ApJ, 447, 572

Faber, S. M. 1973, ApJ, 179, 731

Ferguson, H. C. & Binggeli, B. 1994, A&A Rev., 6, 67

Ferguson, H. C. & Sandage, A. 1990, AJ, 100, 1

Firth, P., Evstigneeva, E. A., Jones, J. B., et al. 2006, MNRAS, 372, 1856

Fukugita, M., Shimasaku, K., & Ichikawa, T. 1995, PASP, 107, 945

Geller, M. J. & Huchra, J. P. 1983, ApJS, 52, 61

Gerke, B. F., Newman, J. A., Davis, M., et al. 2005, ApJ, 625, 6

Gonzalez, A. H., Zabludoff, A. I., & Zaritsky, D. 2005, ApJ, 618, 195

Govoni, F., Falomo, R., Fasano, G., & Scarpa, R. 2000, A&AS, 143, 369

Graham, A. W. 2005, in IAU Colloq. 198: Near-fields cosmology with dwarf elliptical galaxies, ed. H. Jerjen & B. Binggeli, 303–310

Graham, A. W. & Driver, S. P. 2005, Publications of the Astronomical Society of Australia, 22, 118

Grebel, E. K. 2005, in American Institute of Physics Conference Series, Vol. 752, Stellar Astrophysics with the World's Largest Telescopes, ed. J. Mikolajewska & A. Olech, 161–174

Heisler, J., Tremaine, S., & Bahcall, J. N. 1985, ApJ, 298, 8

Helsdon, S. F., Ponman, T. J., O'Sullivan, E., & Forbes, D. A. 2001, MNRAS, 325, 693

Hibbard, J. E. & van Gorkom, J. H. 1996, AJ, 111, 655

Hickson, P., Mendes de Oliveira, C., Huchra, J. P., & Palumbo, G. G. 1992, ApJ, 399, 353

Jacoby, G. H., Hunter, D. H., & Christian, C. A. 1984, A library of stellar spectra (NSSDC/WDC-A-R&S, Greenbelt: NASA, National Space Science Data Center / World Data Center A for Rockets and Satellites, 1984)

Jedrzejewski, R. I. 1987, MNRAS, 226, 747

Jenkins, A., Frenk, C. S., White, S. D. M., et al. 2001, MNRAS, 321, 372

Karachentsev, I. 1987, Moscow Izdatel Nauka

Kennicutt, Jr., R. C. 1992, ApJ, 388, 310

Khosroshahi, H. G., Ponman, T. J., & Jones, L. R. 2006, MNRAS, 372, L68

Khosroshahi, H. G., Raychaudhury, S., Ponman, T. J., Miles, T. A., & Forbes, D. A. 2004, MNRAS, 349, 527

Kormendy, J. 1977, ApJ, 218, 333

Landolt, A. U. 1992, AJ, 104, 340

Lin, H., Kirshner, R. P., Shectman, S. A., et al. 1996, ApJ, 464, 60

Lloyd, B. D., Jones, P. A., & Haynes, R. F. 1996, MNRAS, 279, 1197

Longhetti, M., Bressan, A., Chiosi, C., & Rampazzo, R. 1999, A&A, 345, 419

Longhetti, M., Rampazzo, R., Bressan, A., & Chiosi, C. 1998a, A&AS, 130, 251

Longhetti, M., Rampazzo, R., Bressan, A., & Chiosi, C. 1998b, A&AS, 130, 267

Mahdavi, A., Trentham, N., & Tully, R. B. 2005, AJ, 130, 1502

Mateo, M. L. 1998, ARA&A, 36, 435

Mathews, W. G., Brighenti, F., Faltenbacher, A., et al. 2006, ApJ, 652, L17

Matsushita, K. 2001, ApJ, 547, 693

Matteucci, F. 1994, A&A, 288, 57

Mendes de Oliveira, C. L. & Carrasco, E. R. 2007, ArXiv e-prints, 710

Mendes de Oliveira, C. L., Cypriano, E. S., & Sodré, L. J. 2006, AJ, 131, 158

Moore, B., Ghigna, S., Governato, F., et al. 1999, ApJ, 524, L19

Mulchaey, J. S. 2000, ARA&A, 38, 289

Mulchaey, J. S., Davis, D. S., Mushotzky, R. F., & Burstein, D. 1993, ApJ, 404, L9

Mulchaey, J. S. & Zabludoff, A. I. 1999, ApJ, 514, 133

Naab, T., Khochfar, S., & Burkert, A. 2006, ApJ, 636, L81

Nevalainen, J., Markevitch, M., & Lumb, D. 2005, ApJ, 629, 172

Noguchi, M. 1987, MNRAS, 228, 635

O'Sullivan, E., Forbes, D. A., & Ponman, T. J. 2001a, MNRAS, 328, 461

O'Sullivan, E., Forbes, D. A., & Ponman, T. J. 2001b, MNRAS, 324, 420

Peng, C. Y., Ho, L. C., Impey, C. D., & Rix, H.-W. 2002, AJ, 124, 266

Ponman, T. J., Allan, D. J., Jones, L. R., et al. 1994, Nature, 369, 462

Pritchet, C. J. & van den Bergh, S. 1999, AJ, 118, 883

Ramella, M., Diaferio, A., Geller, M. J., & Huchra, J. P. 1994, AJ, 107, 1623

Rampazzo, R. 1988, A&A, 204, 81

Rampazzo, R., Alexander, P., Carignan, C., et al. 2006, MNRAS, 368, 851

Rampazzo, R., Annibali, F., Bressan, A., et al. 2005, A&A, 433, 497

Read, A. M. & Ponman, T. J. 1998, MNRAS, 297, 143

Reduzzi, L. & Rampazzo, R. 1995a, Candidates for a Southern extension of the Karachentsev catalogue of isolated pairs of galaxies (New York: Gordon and Breach Science Publishers, |c1995)

Reduzzi, L. & Rampazzo, R. 1995b, Astrophysical Letters Communications, 30, 1

Reduzzi, L. & Rampazzo, R. 1996, A&AS, 116, 515

Rizzi, L. 2003, PhD thesis, Research Doctorate Thesis, University of Padua, Italy

Rood, H. J. & Dickel, J. R. 1978, ApJ, 224, 724

Rose, J. A. 1984, AJ, 89, 1238

Rose, J. A. 1985, AJ, 90, 1927

Sadler, E. M. & Sharp, N. A. 1984, A&A, 133, 216

Samurović, S. & Danziger, I. J. 2005, MNRAS, 363, 769

Sansom, A. E., Hibbard, J. E., & Schweizer, F. 2000, AJ, 120, 1946

Sarazin, C. L. 1997, in Astronomical Society of the Pacific Conference Series, Vol. 116, The Nature of Elliptical Galaxies; 2nd Stromlo Symposium, ed. M. Arnaboldi, G. S. Da Costa, & P. Saha, 375–+

Schechter, P. 1976, ApJ, 203, 297

Schweizer, F., Seitzer, P., Faber, S. M., et al. 1990, ApJ, 364, L33

Sersic, J. L. 1968, Atlas de galaxias australes (Cordoba, Argentina: Observatorio Astronomico, 1968)

Steinmetz, M. & Navarro, J. F. 2002, New Astronomy, 7, 155

Sulentic, J. W., Verdes-Montenegro, L., Bergond, G., et al. 2006, A&A, 449, 937

Tonry, J. & Davis, M. 1979, AJ, 84, 1511

Toomre, A. & Toomre, J. 1972, ApJ, 178, 623

Tran, K.-V. H., Simard, L., Zabludoff, A. I., & Mulchaey, J. S. 2001, ApJ, 549, 172

Trentham, N. 1997, MNRAS, 290, 334

Trinchieri, G., Pellegrini, S., Wolter, A., Fabbiano, G., & Fiore, F. 2000, A&A, 364, 53

Trinchieri, G. & Rampazzo, R. 2001, A&A, 374, 454

Tully, R. B. 1987, ApJ, 321, 280

Tully, R. B. 1988, Nearby galaxies catalog (Cambridge and New York, Cambridge University Press, 1988, 221 p.)

Valdes, F. G. 1998, in Astronomical Society of the Pacific Conference Series, Vol. 145, Astronomical Data Analysis Software and Systems VII, ed. R. Albrecht, R. N. Hook, & H. A. Bushouse, 53–+

Veilleux, S. & Osterbrock, D. E. 1987, ApJS, 63, 295

Verdes-Montenegro, L., Sulentic, J., Lisenfeld, U., et al. 2005, A&A, 436, 443

Visvanathan, N. & Sandage, A. 1977, ApJ, 216, 214

Wetzstein, M., Naab, T., & Burkert, A. 2007, MNRAS, 375, 805

White, S. D. M. & Rees, M. J. 1978, MNRAS, 183, 341

Wilms, J., Allen, A., & McCray, R. 2000, ApJ, 542, 914

Worthey, G. & Ottaviani, D. L. 1997, ApJS, 111, 377

Zabludoff, A. I. & Mulchaey, J. S. 1998, ApJ, 496, 39

Zabludoff, A. I. & Mulchaey, J. S. 2000, ApJ, 539, 136

Zacharias, N., Urban, S. E., Zacharias, M. I., et al. 2000, AJ, 120, 2131

List of Abbreviations

ADP	Aperture definition in pixels
AGN	Active galactic nucleus
BGG	Brightest group galaxy
CDM or ΛCDM	Cold Dark Matter (where Λ is the cosmological constant)
CMR	Colour-magnitude relation
CPL	Common Pipeline Recipes
B/T ratio	Bulge-to-total light ratio
D/G ratio	Dwarf-to-giant ratio
dE	Dwarf elliptical galaxy
DEC	Declination
dIrr	Dwarf irregular galaxy
DM	Dark matter
dSph	Dwarf spheroidal galaxy
E	Elliptical galaxy
EPIC	European Photon Imaging Camera
ESA	European Space Agency
ESO	European Southern Observatory
ETC	Exposure time calculator
ETG	Early-type galaxy (E and S0 galaxies)
FWHM	Full width at half maximum
HR	High resolution
IGM	Intra group medium (also: Intergalactic medium)
ISM	Interstellar medium
KR	Kormendy Relation
LCRS	Las Campanas Redshift Survey
LDE	Low density environments
LF	Luminosity function
LG	Local Group
LINER	Low ionization nuclear emission-line region
M/L	Mass-to-light ratio
ML	Maximum likelihood statistic

MOS	Multi-object spectroscopy
MOS (X-ray detector)	Metal Oxide Semi-conductor
MPG	Max Planck Gesellschaft
MW	Milky Way
NED	NASA Extragalactic Database
OB	Observation Block
OM	Optical Monitor
OPC	Observing Programmes Committee
P2PP	Phase 2 preparation tool
PhD	Philosophiae doctor
PI	Principal Investigator
PSF	Point spread function
RA	Right ascension
RMS	Root mean square
S0	Lenticular galaxy
S/N	Signal-to-noise ratio
SAS	Science Analysis System
S	Spiral galaxy
SFR	Star formation rate
SNe	Supernovae
SOF	Set of frames
UT	Unit telescope
VIMOS	VIsible Multi-Object Spectrograph
VLT	Very Large Telescope
VMMPS	VIMOS mask preparation software
WFI	Wide Field Imager
WINGS	WIde-field Nearby Galaxy-cluster Survey
ZM00	Zabludoff & Mulchaey (2000)

Appendix A

Photometric catalogue of the candidate member galaxies around the 4 pairs

Table A.1: Faint candidate group member population around RR 143.

ID	α (2000)	δ (2000)	m_R [mag]	V–R [mag]	n	r_e [arcsec]	μ_0 [mag arcsec^{-2}]	μ_e [mag arcsec^{-2}]
00006	06 47 20.3	-64 31 19	15.23	0.56	3.17	6.77	15.66	22.18
00028	06 49 06.8	-64 31 42	19.27	0.84	1.08	1.63	20.35	22.35
00035	06 47 51.2	-64 31 48	18.04	0.62	1.53	1.58	18.89	21.86
00751	06 47 49.6	-64 00 22	19.51	0.46	0.67	1.94	21.23	22.33
00754	06 46 07.3	-64 00 19	18.66	0.59	0.93	1.81	20.10	21.76
01042	06 47 10.1	-64 02 21	14.36	0.69	1.42	8.11	17.90	20.63
01127	06 50 53.6	-64 00 45	19.97	0.25	0.49	2.22	22.71	23.43
01326	06 50 59.0	-64 01 02	18.81	0.52	0.52	2.71	21.50	22.26
01908	06 50 13.3	-64 01 52	19.08	0.69	1.38	2.38	20.73	23.38
01991	06 47 26.8	-64 02 02	18.23	0.64	1.62	1.69	19.08	22.24
02314	06 50 05.5	-64 02 26	19.41	0.35	0.75	1.96	21.70	22.98
02457	06 47 36.9	-64 02 41	20.62	0.23	1.41	1.45	21.64	24.35
02483	06 46 37.6	-64 02 42	17.65	0.65	1.55	1.98	18.26	21.28
02668	06 49 06.7	-64 02 57	17.37	0.66	1.10	1.41	18.77	20.80
02862	06 46 08.8	-64 03 10	17.34	0.75	1.87	1.86	17.86	21.58
02883	06 46 31.9	-64 03 08	19.95	0.57	0.47	1.80	22.25	22.91
02940	06 46 57.0	-64 02 19	18.12	0.52	0.52	1.89	21.09	21.88
03090	06 49 01.7	-64 03 27	18.34	0.33	0.53	3.19	21.98	22.78
03218	06 46 32.4	-64 03 31	20.32	0.66	0.43	1.95	22.57	23.14
03285	06 48 25.9	-64 03 39	20.22	0.54	0.88	1.21	21.69	23.24
03859	06 48 03.7	-64 04 19	18.24	0.67	0.61	1.97	21.24	22.22
03964	06 47 28.4	-64 04 27	18.09	0.45	1.16	2.13	20.18	22.36
04070	06 49 18.4	-64 04 38	17.26	0.42	0.88	3.82	21.33	22.89
04264	06 46 53.5	-64 04 45	19.46	0.68	0.89	2.51	21.95	23.54
04342	06 50 41.1	-64 04 47	19.40	0.59	3.03	3.03	21.98	22.88
04431	06 50 55.7	-64 04 55	18.13	0.69	1.68	1.58	18.56	21.86
04693	06 50 56.2	-64 05 14	17.65	0.71	1.47	1.57	18.21	21.05
04748	06 48 36.4	-64 05 21	19.34	0.21	1.14	2.37	21.23	23.34
04874	06 48 24.7	-64 05 30	19.67	0.28	0.71	2.06	21.69	22.87
05014	06 46 46.7	-64 05 41	18.98	0.82	1.18	2.35	20.96	23.17
05046	06 46 25.9	-64 05 44	18.00	0.93	1.99	1.71	17.99	21.96
05363	06 48 41.3	-64 06 10	18.01	0.71	1.58	1.74	18.69	21.78
05526	06 48 00.8	-64 06 14	18.52	0.69	1.18	1.37	19.54	21.75
05757	06 46 14.0	-64 06 33	19.10	0.94	0.85	2.45	21.62	23.11
05769	06 48 22.9	-64 06 36	18.75	0.69	0.94	2.94	20.73	22.41
05889	06 47 57.8	-64 06 48	18.23	0.63	1.62	1.86	18.90	22.07
06038	06 46 22.1	-64 06 52	18.89	0.74	1.27	1.86	19.98	22.39
06070	06 48 27.0	-64 07 01	17.81	0.67	1.90	1.84	18.20	21.97
06152	06 50 12.4	-64 07 08	16.87	0.59	1.78	2.03	17.74	21.25
06304	06 48 27.5	-64 07 17	18.43	0.67	0.79	2.69	20.54	21.91
06315	06 49 01.8	-64 07 21	17.58	0.69	3.34	4.00	16.37	23.26
06459	06 46 51.5	-64 07 26	18.25	0.46	0.78	1.78	20.09	21.43
06608	06 47 51.8	-64 07 39	19.65	0.88	1.91	2.34	19.95	23.75
06644	06 48 13.9	-64 07 46	17.34	0.72	1.95	2.63	18.13	22.01
06858	06 47 45.1	-64 07 59	17.58	0.59	1.12	2.12	19.20	21.27
06959	06 47 18.5	-64 08 07	18.74	0.40	1.10	2.58	20.16	22.20
07232	06 47 51.1	-64 08 29	17.21	0.73	1.75	2.00	18.01	21.45
07559	06 50 41.4	-64 08 44	19.46	0.46	0.68	2.54	22.19	23.32
07742	06 46 58.1	-64 08 59	18.48	0.48	0.64	2.45	21.68	22.72
07870	06 46 26.2	-64 09 14	17.59	0.45	0.87	5.53	21.90	23.44
07998	06 50 16.9	-64 09 17	18.07	0.90	1.74	2.07	18.82	22.24
08023	06 49 35.3	-64 09 18	20.59	0.38	0.69	2.18	23.27	24.42
08451	06 47 37.5	-64 09 49	20.61	0.84	0.76	2.01	22.33	23.64
08730	06 47 42.1	-64 10 15	16.86	0.50	0.87	2.20	19.47	21.01
08875	06 51 02.4	-64 10 10	20.06	0.25	0.56	2.49	22.70	23.56
09030	06 46 04.0	-64 10 34	17.05	0.55	1.61	2.71	18.69	21.83

Continued on next page

Table A.1– continued from previous page

09192	06 47 53.3	-64 10 55	17.25	0.56	1.05	4.69	21.33	23.26
09215	06 47 22.9	-64 10 44	18.89	0.47	0.97	2.40	21.15	22.90
09251	06 50 31.3	-64 10 43	19.63	0.32	1.14	3.63	22.40	24.53
09279	06 46 15.0	-64 10 40	19.55	0.39	0.48	2.13	22.51	23.19
10029	06 50 14.9	-64 11 34	18.96	0.89	1.09	2.47	20.79	22.81
10155	06 47 52.2	-64 11 51	17.85	0.52	0.81	2.31	20.39	21.80
10172	06 47 06.4	-64 11 52	17.48	0.62	2.52	2.34	17.11	22.23
10197	06 46 52.9	-64 11 50	18.07	0.67	1.65	2.09	18.92	22.15
10205	06 46 51.7	-64 11 46	21.07	0.24	0.24	4.13	25.01	25.19
10305	06 46 34.3	-64 12 01	17.49	0.63	0.90	3.36	19.89	21.49
10529	06 46 11.2	-64 12 09	19.40	0.31	0.42	2.51	23.08	23.63
10711	06 50 39.1	-64 12 18	18.81	0.85	1.45	1.67	19.52	22.31
10714	06 47 11.0	-64 12 27	19.51	0.53	0.62	2.10	22.38	23.37
10853	06 48 03.9	-64 12 41	16.76	0.65	2.06	2.53	17.19	21.31
11121	06 50 54.1	-64 12 44	20.25	0.74	2.42	2.47	20.24	25.15
11256	06 50 33.7	-64 12 57	18.29	0.20	0.72	2.78	21.78	23.00
11370	06 46 48.2	-64 13 07	18.78	0.69	0.68	2.00	21.37	22.49
11436	06 49 18.4	-64 13 15	18.37	0.53	0.87	4.29	22.51	24.04
12243	06 48 52.2	-64 14 07	20.40	0.27	0.68	1.98	22.94	24.06
12423	06 46 07.1	-64 14 17	19.17	0.45	0.65	1.87	21.80	22.85
12981	06 48 56.2	-64 15 09	17.73	0.45	0.70	3.21	21.15	22.32
13059	06 50 44.8	-64 14 58	19.27	0.98	1.07	1.82	20.95	22.91
13936	06 46 54.4	-64 16 23	16.68	0.44	2.05	1.22	16.03	20.12
14512	06 46 07.2	-64 16 59	19.96	0.63	0.48	2.03	22.37	23.06
14668	06 50 39.5	-64 17 11	20.11	0.54	0.48	2.12	22.25	22.94
15218	06 46 38.5	-64 17 57	19.30	0.39	0.87	2.75	22.18	23.72
15221	06 47 30.4	-64 18 01	17.20	0.59	1.11	2.77	19.71	21.76
15455	06 49 45.7	-64 17 54	17.46	0.48	1.07	0.67	17.74	19.72
15513	06 46 14.5	-64 18 21	17.93	0.69	2.10	2.21	18.34	22.56
15550	06 49 37.8	-64 18 38	14.95	0.53	1.43	11.32	19.45	22.21
15582	06 47 28.6	-64 18 23	19.86	0.24	0.55	2.97	22.89	23.73
15874	06 46 38.5	-64 18 48	19.23	0.32	0.71	2.43	22.48	23.68
16009	06 48 27.8	-64 18 59	19.50	0.58	1.58	3.74	21.98	25.05
16011	06 50 25.4	-64 18 56	20.00	0.31	0.70	2.08	22.93	24.10
16117	06 47 31.4	-64 19 08	17.58	0.65	0.93	2.27	19.41	21.07
16784	06 50 55.3	-64 19 60	18.65	0.47	0.53	2.71	22.26	23.07
16803	06 48 04.0	-64 20 08	17.64	0.51	0.73	2.09	20.05	21.28
16923	06 47 36.1	-64 20 15	18.69	0.57	0.69	2.52	21.01	22.16
17236	06 47 01.6	-64 20 37	20.30	0.37	0.60	2.11	22.24	23.18
17347	06 46 45.6	-64 20 48	19.65	0.71	0.82	1.87	21.28	22.72
17430	06 48 06.6	-64 20 55	19.69	0.39	0.90	1.52	21.67	23.27
17858	06 50 09.2	-64 18 37	17.01	0.42	1.12	1.97	19.16	21.24
17909	06 48 20.7	-64 21 31	19.21	0.83	1.05	1.71	21.10	23.02
18031	06 47 44.8	-64 21 40	19.06	0.43	0.96	1.66	20.92	22.66
18063	06 47 06.7	-64 21 43	18.42	0.63	2.09	1.80	18.36	22.55
18260	06 46 38.1	-64 21 53	19.26	0.69	0.69	1.96	21.79	22.94
18522	06 47 48.3	-64 22 15	19.50	0.32	0.77	2.56	22.48	23.80
18909	06 46 58.6	-64 22 41	18.64	0.55	0.90	2.42	21.41	23.00
18910	06 46 59.5	-64 22 45	17.53	0.70	2.51	3.91	17.61	22.72
19086	06 48 28.1	-64 22 57	18.43	0.51	1.12	2.67	20.81	22.90
20429	06 47 05.6	-64 24 54	18.14	0.57	0.96	4.13	20.98	22.71
20430	06 47 07.0	-64 24 44	16.41	0.64	2.42	3.93	17.04	21.94
20447	06 48 50.0	-64 24 42	19.63	0.41	0.67	3.83	24.00	25.11
20649	06 46 40.0	-64 24 55	19.94	0.34	0.65	2.48	23.09	24.15
20662	06 47 12.2	-64 25 01	17.22	0.87	1.37	1.78	18.04	20.66
20738	06 46 59.7	-64 25 07	17.06	0.67	1.86	1.87	17.57	21.25
21016	06 46 42.1	-64 25 22	17.48	0.48	1.09	1.84	19.49	21.49
21017	06 46 43.4	-64 25 26	17.92	0.45	0.76	2.73	20.97	22.27
21044	06 49 37.7	-64 25 25	18.87	0.53	0.59	2.74	22.26	23.19
21086	06 47 29.8	-64 25 31	18.67	0.46	0.85	3.49	21.73	23.23

Table A.1– continued from previous page

21093	06 49 11.0	-64 25 27	18.33	0.41	0.61	1.82	20.65	21.63
21166	06 47 00.3	-64 25 31	17.88	0.63	1.16	1.60	19.16	21.33
21187	06 49 59.1	-64 25 31	19.19	0.27	0.67	1.91	21.77	22.87
21324	06 50 35.7	-64 25 38	19.44	0.17	1.10	3.91	22.58	24.63
21357	06 48 48.2	-64 25 58	18.25	0.70	2.57	3.02	18.27	23.50
21426	06 46 57.9	-64 25 50	18.75	0.68	0.83	1.96	21.30	22.74
21465	06 47 33.0	-64 25 52	18.71	0.33	0.67	2.18	21.62	22.72
21533	06 49 04.1	-64 25 57	17.71	0.62	1.56	2.26	18.51	21.53
21872	06 50 01.9	-64 26 20	18.56	0.61	1.27	1.63	19.32	21.73
22375	06 49 31.8	-64 26 57	18.35	0.42	0.78	1.52	20.52	21.86
22457	06 48 09.6	-64 27 02	18.46	0.39	0.82	1.36	20.37	21.81
22627	06 47 07.3	-64 27 16	19.62	0.95	1.07	1.98	21.38	23.36
22752	06 48 13.8	-64 27 25	19.08	0.28	1.12	2.07	21.25	23.33
22971	06 48 24.3	-64 27 37	19.41	0.61	0.34	1.89	21.86	22.25
23417	06 47 33.8	-64 28 13	19.24	0.36	0.81	1.78	21.45	22.87
23734	06 49 18.3	-64 28 31	19.56	0.38	0.89	1.70	21.18	22.75
23758	06 46 27.9	-64 28 30	20.30	0.80	2.96	4.60	20.09	26.17
23796	06 50 31.9	-64 28 31	19.61	0.69	0.72	2.00	21.62	22.84
23823	06 49 03.3	-64 28 40	18.40	0.58	0.80	1.86	20.77	22.15
24029	06 46 33.0	-64 28 50	19.93	0.62	0.73	2.09	21.67	22.90
24043	06 46 28.0	-64 28 51	17.84	0.40	0.80	3.82	20.53	21.92
24188	06 50 20.6	-64 29 05	18.44	0.49	0.91	2.87	21.55	23.17
24246	06 47 07.5	-64 29 16	16.95	0.34	1.57	5.04	19.73	22.80
24333	06 48 40.5	-64 29 20	18.48	0.60	0.71	2.66	21.36	22.54
24388	06 47 45.9	-64 29 23	18.29	0.40	0.95	3.53	21.80	23.52
24473	06 50 57.9	-64 29 23	18.81	0.72	1.08	1.87	20.17	22.15
24606	06 46 19.4	-64 29 34	17.01	0.49	1.07	2.51	19.25	21.22
24607	06 49 34.2	-64 29 35	18.50	0.42	0.58	3.58	21.47	22.39
24732	06 47 26.1	-64 29 51	17.58	0.56	1.31	2.09	18.71	21.20
24743	06 47 47.9	-64 29 48	19.13	0.82	1.27	1.60	20.07	22.49
24778	06 47 32.1	-64 29 53	17.75	0.36	0.79	3.36	20.93	22.31
24811	06 46 26.6	-64 29 50	18.70	0.43	1.26	2.28	5.78	8.16
25304	06 47 52.6	-64 30 31	18.27	0.64	0.79	3.47	20.70	22.07
25310	06 50 56.9	-64 30 23	19.57	0.60	0.68	1.84	21.88	23.00
25500	06 47 55.6	-64 30 47	19.05	0.40	0.81	4.92	23.42	24.84

Table A.2: Faint candidate group member population around RR 210.

ID	α (2000)	δ (2000)	m$_R$ [mag]	V–R [mag]	n	r$_e$ [arcsec]	μ$_0$ [mag arcsec^{-2}]	μ$_e$ [mag arcsec^{-2}]
00129	12 07 09.0	-30 00 26	18.94	0.55	0.78	2.03	21.32	22.67
00232	12 05 47.2	-30 00 15	18.59	0.66	0.97	1.47	20.49	22.24
00371	12 05 52.4	-29 59 58	20.10	0.59	0.50	2.27	22.46	23.20
00554	12 06 46.1	-29 59 49	18.06	0.50	0.73	1.89	20.51	21.75
00568	12 06 43.5	-30 00 00	18.03	0.58	1.79	2.51	19.41	22.95
00654	12 05 50.2	-29 59 58	17.39	0.66	1.84	2.41	18.30	21.93
00889	12 06 58.9	-29 59 45	17.55	0.72	1.35	1.64	18.99	21.56
00910	12 07 41.4	-29 59 21	18.57	0.49	0.73	2.12	20.73	21.96
00967	12 07 25.3	-29 59 02	18.66	0.37	0.48	2.16	21.51	22.20
00988	12 06 58.2	-29 59 11	18.12	0.39	0.81	2.39	20.94	22.35
01257	12 07 13.0	-29 58 24	20.71	0.84	1.39	2.04	22.09	24.77
01264	12 06 59.5	-29 58 31	18.71	0.42	0.75	2.08	21.01	22.29
01475	12 06 46.2	-29 58 14	18.69	0.46	1.41	2.07	19.93	22.64
01668	12 07 16.6	-29 58 09	18.14	0.66	1.29	2.23	19.53	21.98
01701	12 05 51.4	-29 57 52	19.48	0.68	1.11	1.22	20.63	22.70
01840	12 06 59.9	-29 57 31	19.91	0.49	1.08	2.04	21.76	23.76
01941	12 05 56.8	-29 57 38	19.29	0.77	1.09	2.26	20.96	22.97
01967	12 07 21.1	-29 58 04	17.18	0.69	1.94	2.14	17.81	21.66
02053	12 05 39.7	-29 57 15	18.92	0.37	0.58	2.33	21.92	22.82
02146	12 05 52.6	-29 57 02	19.46	0.48	0.55	2.28	22.07	22.93
02265	12 07 16.4	-29 57 08	18.61	0.86	1.50	2.15	19.51	22.43
02612	12 07 33.0	-29 56 16	19.71	0.45	0.54	2.94	23.43	24.25
02724	12 06 23.1	-29 57 05	17.68	0.49	0.72	7.20	23.21	24.43
02924	12 07 47.8	-29 55 33	21.00	0.49	0.62	2.33	22.95	23.94
03105	12 05 42.5	-29 55 30	18.69	0.37	1.19	2.98	21.04	23.28
03106	12 06 34.9	-29 55 24	20.10	0.73	0.73	2.11	21.88	23.11
03409	12 07 13.7	-29 54 50	20.85	0.18	0.50	2.18	22.99	23.73
03532	12 06 15.2	-29 55 05	19.17	0.52	0.77	3.63	23.39	24.72
03533	12 06 31.3	-29 54 46	19.01	0.38	0.92	1.83	20.52	22.16
03549	12 07 47.8	-29 54 34	20.12	0.45	0.69	2.10	22.74	23.88
03693	12 06 36.7	-29 54 41	18.74	0.85	2.37	8.44	20.50	25.30
03747	12 06 38.1	-29 54 18	18.63	0.77	1.32	1.22	19.47	21.98
03791	12 06 48.7	-29 54 07	20.78	0.40	0.58	2.61	23.27	24.18
03865	12 06 01.0	-29 54 09	18.93	0.41	0.90	1.69	20.43	22.03
03871	12 07 42.0	-29 54 14	17.96	0.62	1.63	1.75	18.73	21.92
03970	12 07 28.6	-29 53 58	18.08	0.73	0.99	1.95	20.22	22.03
03974	12 07 31.9	-29 53 54	19.00	0.34	0.99	1.83	21.06	22.86
04072	12 07 44.1	-29 53 40	18.85	0.83	1.33	1.37	19.73	22.27
04421	12 07 24.4	-29 53 54	17.24	0.70	2.94	3.91	17.09	23.11
04493	12 06 54.5	-29 53 11	18.47	0.64	1.82	1.94	19.04	22.64
04504	12 06 07.0	-29 53 07	19.08	0.37	0.65	2.40	21.74	22.80
04512	12 07 09.8	-29 53 10	18.64	0.36	0.84	2.68	21.58	23.06
04614	12 07 03.4	-29 52 59	18.38	0.46	1.14	2.37	20.52	22.66
04665	12 07 34.1	-29 52 41	19.97	0.32	0.72	1.96	21.79	23.00
04682	12 07 40.9	-29 52 43	19.43	0.97	0.90	2.38	21.59	23.19
04789	12 05 57.6	-29 52 56	17.63	0.71	1.52	2.48	19.51	22.46
04807	12 06 19.5	-29 52 29	19.81	0.48	0.73	3.23	23.62	24.84
04935	12 05 38.6	-29 52 16	19.07	0.67	1.22	1.77	20.19	22.50
04951	12 06 44.1	-29 52 30	17.91	0.80	2.18	1.75	17.73	22.12
05034	12 07 38.2	-29 51 56	19.53	0.37	0.99	1.17	21.02	22.81
05135	12 05 33.6	-29 52 02	19.05	0.54	0.55	2.80	21.58	22.41
05166	12 07 25.4	-29 52 02	18.56	0.30	0.52	3.29	21.84	22.61
05265	12 05 59.4	-29 51 42	20.16	0.13	0.72	2.56	22.83	24.05
05365	12 06 44.4	-29 51 42	18.75	0.89	1.40	1.72	19.51	22.19
05778	12 07 37.5	-29 50 57	19.13	0.60	0.90	2.25	21.05	22.66
05987	12 06 03.4	-29 50 31	19.77	0.74	1.22	2.26	21.29	23.60

<div align="right">Continued on next page</div>

Table A.2 – continued from previous page

06080	12 05 52.6	-29 50 23	20.15	0.66	0.79	1.94	22.29	23.65
06111	12 06 21.3	-29 50 17	18.77	0.47	0.77	2.20	20.89	22.21
06258	12 06 49.2	-29 50 06	19.69	0.69	0.85	1.89	21.79	23.28
06339	12 07 50.1	-29 50 09	16.87	0.62	1.45	1.70	17.89	20.70
06396	12 07 31.9	-29 49 56	19.08	0.33	0.66	2.49	22.37	23.45
06463	12 06 41.8	-29 49 41	20.05	0.29	0.39	3.48	22.91	23.40
06742	12 05 53.4	-29 49 23	19.99	0.44	0.47	3.31	23.93	24.59
06839	12 07 23.5	-29 49 05	19.79	0.76	1.01	1.96	21.35	23.19
06979	12 07 20.3	-29 48 56	19.65	0.29	0.52	2.09	22.15	22.94
07113	12 05 40.0	-29 48 46	18.12	0.51	1.21	1.43	19.10	21.38
07182	12 06 04.2	-29 48 38	20.03	0.65	1.98	3.45	20.82	24.76
07203	12 05 37.3	-29 48 26	20.17	0.45	0.41	3.54	23.32	23.86
07553	12 05 35.0	-29 48 16	17.24	0.57	0.99	2.19	19.25	21.06
07570	12 05 31.5	-29 47 57	19.10	0.60	1.08	1.92	20.25	22.24
07646	12 05 50.8	-29 47 59	19.09	0.38	0.95	3.24	22.04	23.76
07893	12 07 32.6	-29 47 37	19.73	0.29	0.67	2.39	22.54	23.65
08111	12 06 44.2	-29 47 23	18.71	0.67	0.54	2.29	21.75	22.56
08116	12 06 31.1	-29 51 33	14.24	0.58	1.39	7.85	19.05	21.71
08269	12 07 47.1	-29 47 00	19.43	0.93	1.42	2.29	20.86	23.60
08507	12 06 13.8	-29 46 37	18.66	0.91	1.11	1.49	19.81	21.87
08695	12 07 49.3	-29 46 25	18.17	0.77	0.96	2.28	20.54	22.27
08727	12 07 03.7	-29 46 20	19.12	0.75	0.93	1.60	20.57	22.24
08828	12 06 22.1	-29 46 00	19.46	0.48	0.48	2.45	22.05	22.75
09013	12 07 19.2	-29 46 05	17.05	0.50	1.01	2.31	19.61	21.44
09269	12 07 46.2	-29 45 53	17.26	0.91	2.38	3.31	18.02	22.83
09327	12 05 28.2	-29 45 15	18.46	0.79	1.14	1.83	19.50	21.62
09382	12 07 09.7	-29 45 15	19.34	0.85	0.83	3.21	21.59	23.04
09531	12 06 12.4	-29 44 58	19.38	0.15	0.55	1.93	21.91	22.76
09816	12 06 29.9	-29 44 21	19.11	0.62	0.90	2.05	20.82	22.42
10073	12 07 46.1	-29 44 12	17.74	0.87	1.40	1.69	18.98	21.67
10243	12 06 50.6	-29 43 51	17.88	0.53	1.18	2.35	19.71	21.93
10247	12 05 40.0	-29 43 39	19.91	0.42	0.72	2.03	21.87	23.08
10262	12 06 03.5	-29 44 17	17.05	0.79	2.00	2.65	17.71	21.71
10313	12 06 06.7	-29 43 41	18.99	0.53	0.73	2.28	20.96	22.21
10441	12 06 41.0	-29 43 39	18.00	0.34	1.25	2.13	19.85	22.21
10601	12 07 08.0	-29 43 24	17.77	0.44	0.83	2.66	21.07	22.52
10968	12 06 38.8	-29 42 43	17.43	0.67	1.70	1.56	17.99	21.32
11044	12 06 08.3	-29 42 23	19.86	0.31	1.11	2.38	22.17	24.23
11168	12 06 30.8	-29 42 34	18.96	0.61	0.46	3.89	22.54	23.18
11372	12 07 43.3	-29 43 11	17.59	0.50	0.83	6.97	22.21	23.66
11400	12 05 54.1	-29 41 57	18.18	0.58	0.58	2.91	21.07	21.97
11412	12 06 28.6	-29 41 55	18.16	0.68	1.00	1.81	19.27	21.10
11440	12 07 42.6	-29 41 57	18.32	0.83	1.35	2.48	19.98	22.57
11532	12 05 55.9	-29 42 16	16.75	0.63	2.35	3.75	17.60	22.34
11561	12 05 45.1	-29 41 45	18.92	0.62	0.78	1.93	21.38	22.72
11710	12 05 54.3	-29 41 13	19.99	0.37	0.65	1.98	22.06	23.13
11756	12 05 44.1	-29 41 30	16.48	0.62	1.45	2.31	18.45	21.24
11810	12 05 46.9	-29 41 14	17.69	0.56	1.26	1.70	19.06	21.44
11942	12 06 17.2	-29 41 00	18.38	0.64	1.21	1.93	20.24	22.51
12116	12 06 07.7	-29 40 44	18.12	0.54	0.85	1.88	20.64	22.13
12139	12 06 14.1	-29 40 46	18.46	0.65	1.82	2.02	19.06	22.66
12167	12 05 52.2	-29 40 37	18.83	0.69	0.68	2.51	22.17	23.30
12209	12 06 16.5	-29 40 14	20.05	0.54	0.90	1.40	21.81	23.42
12231	12 07 14.5	-29 40 23	19.46	0.52	1.34	3.58	21.47	24.02
12344	12 06 29.8	-29 40 07	20.68	0.25	0.51	2.04	22.80	23.57
12388	12 05 54.3	-29 40 01	19.22	0.40	0.88	2.48	21.49	23.04
12523	12 05 45.6	-29 40 51	16.27	0.62	2.12	2.91	17.35	21.60
12543	12 05 50.3	-29 39 58	18.91	0.49	0.79	2.58	21.82	23.18
12686	12 07 21.7	-29 40 06	17.11	0.67	1.85	2.28	17.63	21.31
12828	12 05 59.2	-29 39 26	18.39	0.49	0.56	2.02	21.45	22.31

Table A.2 – continued from previous page

13000	12 05 46.3	-29 39 08	19.01	0.32	0.98	2.49	21.14	22.92
13089	12 06 15.3	-29 39 22	18.20	0.68	1.14	1.60	19.14	21.26
13169	12 06 06.0	-29 38 55	18.30	0.45	0.96	1.89	20.43	22.16
13231	12 05 34.0	-29 38 43	19.58	0.36	0.46	3.72	23.88	24.51
13285	12 06 31.4	-29 38 48	18.97	0.69	1.03	2.45	20.43	22.33
13373	12 06 55.0	-29 38 32	20.45	0.29	0.96	3.15	22.94	24.67
13417	12 06 16.0	-29 38 39	18.00	0.73	2.16	2.66	18.58	22.91
13481	12 06 46.6	-29 31 16	18.00	0.47	0.56	2.72	21.49	22.35
13493	12 06 50.3	-29 36 23	14.26	0.52	1.98	9.40	18.01	21.95
13578	12 07 03.2	-29 35 49	17.32	0.70	1.54	2.17	18.33	21.32
13651	12 05 59.0	-29 35 48	18.47	0.69	1.33	1.71	19.61	22.14
13676	12 07 28.9	-29 36 03	18.62	0.46	1.53	2.21	19.73	22.70
13744	12 06 16.1	-29 36 11	16.89	0.72	1.66	3.46	18.68	21.94
13813	12 06 29.4	-29 36 16	19.83	0.53	0.79	2.27	22.38	23.74
13833	12 06 16.4	-29 38 21	15.63	0.76	2.61	8.37	17.82	23.14
13879	12 07 48.2	-29 36 22	18.60	0.53	1.36	1.74	19.49	22.10
14043	12 06 15.2	-29 36 36	19.41	0.59	0.72	1.87	21.51	22.73
14191	12 06 59.1	-29 37 00	17.65	0.67	2.19	2.53	18.15	22.56
14298	12 06 20.4	-29 37 02	17.85	0.67	1.40	1.63	18.99	21.67
14371	12 05 30.9	-29 37 42	17.20	0.49	0.66	4.05	20.46	21.55
14386	12 06 19.4	-29 37 12	18.54	0.71	0.95	2.21	20.21	21.91
14460	12 06 30.3	-29 37 20	18.81	0.76	1.19	2.14	20.19	22.43
14705	12 06 00.9	-29 37 37	18.98	0.74	1.05	1.86	20.58	22.51
14731	12 06 35.4	-29 38 01	18.54	0.41	0.57	2.31	21.60	22.48
14880	12 05 54.4	-29 38 05	21.00	0.81	0.40	2.32	23.27	23.79
14888	12 06 17.3	-29 38 31	18.21	0.67	2.60	2.91	17.77	23.07
14950	12 05 59.7	-29 38 16	18.05	0.51	1.02	1.76	19.73	21.58
15020	12 05 35.7	-29 30 06	20.13	0.43	0.43	1.98	22.87	23.45
15115	12 05 43.4	-29 37 23	18.84	0.58	0.64	2.25	21.94	22.99
15176	12 06 24.2	-29 30 23	17.43	0.47	0.82	2.13	20.25	21.69
15704	12 07 48.5	-29 31 07	18.54	0.69	0.85	2.32	20.48	21.97
15730	12 05 56.3	-29 36 04	15.82	0.61	1.74	2.62	17.24	20.66
15863	12 06 06.3	-29 31 27	18.16	0.72	0.57	1.58	20.60	21.48
16036	12 07 03.9	-29 31 44	17.94	0.46	1.01	1.97	19.81	21.66
16130	12 06 07.4	-29 31 56	19.44	0.45	0.78	1.90	21.64	22.99
16347	12 07 39.3	-29 32 07	17.34	0.52	0.78	1.83	19.55	20.89
16463	12 07 42.2	-29 32 25	17.56	0.84	1.53	2.15	19.07	22.04
16595	12 07 23.6	-29 32 21	18.51	0.81	1.22	1.68	20.08	22.38
16960	12 06 38.8	-29 32 47	19.17	0.33	0.39	2.08	22.28	22.77
17023	12 05 54.8	-29 33 26	16.87	0.71	1.54	1.84	18.38	21.37
17074	12 05 58.5	-29 33 25	18.00	0.58	0.77	2.00	20.09	21.41
17127	12 06 09.5	-29 33 08	18.75	0.92	0.73	2.25	21.59	22.83
17346	12 07 34.9	-29 33 57	19.47	0.71	0.66	2.00	22.07	23.16
17416	12 06 34.3	-29 34 08	18.26	0.38	1.04	0.69	18.51	20.43
17464	12 05 50.5	-29 34 05	20.25	0.72	0.60	2.36	22.57	23.52
17675	12 06 09.3	-29 34 33	17.57	0.70	1.14	4.16	19.93	22.06
17787	12 05 51.0	-29 34 46	20.32	0.42	1.09	1.96	22.00	24.02
17795	12 06 09.4	-29 34 46	18.39	0.65	1.41	1.80	19.12	21.82
17798	12 06 32.2	-29 34 48	18.95	0.62	0.67	3.13	21.57	22.67
17809	12 06 14.3	-29 34 48	17.85	0.59	1.33	1.58	19.21	21.74
17860	12 07 27.5	-29 35 49	18.02	0.60	1.59	1.93	19.14	22.23
17953	12 06 25.2	-29 34 46	19.31	0.45	1.12	1.90	20.68	22.77
18009	12 06 34.8	-29 35 03	18.94	0.60	1.30	2.09	19.91	22.38
18064	12 07 28.0	-29 34 60	20.31	0.35	0.71	3.12	22.50	23.69
18245	12 06 54.4	-29 35 29	17.64	0.64	1.56	1.84	18.47	21.52
18388	12 06 44.1	-29 35 44	18.47	0.61	0.92	2.53	20.61	22.25
18428	12 07 03.6	-29 35 42	18.45	0.52	0.90	2.36	20.72	22.32
18444	12 05 41.4	-29 35 37	20.00	0.21	0.52	2.47	23.12	23.89

Table A.3: Faint candidate group member population around RR 216.

ID	α (2000)	δ (2000)	m_R [mag]	V–R [mag]	n	r_e [arcsec]	μ_0 [mag arcsec^{-2}]	μ_e [mag arcsec^{-2}]
00015	12 24 10.1	-39 59 31	18.47	0.47	0.74	1.87	20.43	21.70
00017	12 24 30.0	-39 59 28	16.20	0.59	1.03	6.54	20.37	22.25
00034	12 25 12.4	-39 59 50	19.29	0.49	0.65	1.88	21.49	22.56
00143	12 24 29.0	-39 29 21	17.19	1.03	1.17	1.64	18.83	21.02
00193	12 24 31.8	-39 29 33	18.06	0.72	1.72	1.74	18.59	21.98
00226	12 25 20.0	-39 29 36	20.03	0.60	1.27	5.74	23.21	25.62
00293	12 23 54.8	-39 29 41	18.75	0.76	0.71	3.03	21.44	22.63
00495	12 25 46.1	-39 29 54	18.81	0.28	1.21	1.95	20.20	22.47
00661	12 25 42.7	-39 30 12	19.42	0.43	1.44	2.04	20.82	23.59
01090	12 24 03.8	-39 30 35	19.07	0.58	0.69	1.91	20.96	22.10
01281	12 25 56.6	-39 30 54	18.32	0.71	1.49	1.51	18.81	21.69
01386	12 25 49.1	-39 31 02	18.75	0.82	0.85	2.65	21.16	22.64
01459	12 26 12.4	-39 31 08	17.90	0.74	1.59	1.86	18.74	21.84
01492	12 24 02.0	-39 31 06	19.16	0.46	0.87	1.41	20.91	22.46
01506	12 26 30.4	-39 31 07	19.39	0.58	0.91	2.03	21.13	22.75
01619	12 26 01.1	-39 31 21	18.57	0.92	1.45	2.57	19.97	22.76
01661	12 25 01.8	-39 31 20	18.41	0.75	1.33	1.68	19.10	21.65
01672	12 25 35.0	-39 31 20	18.57	0.65	1.04	1.78	20.21	22.11
01782	12 23 57.6	-39 31 26	19.11	0.45	1.06	1.98	20.86	22.82
01979	12 24 13.2	-39 31 49	17.97	0.57	0.48	5.05	21.21	21.90
01980	12 25 06.7	-39 31 46	16.64	0.64	1.56	1.71	17.60	20.63
02023	12 23 57.8	-39 31 46	17.62	0.51	0.98	2.91	20.51	22.30
02064	12 24 31.4	-39 31 49	19.67	0.60	0.70	2.58	21.68	22.84
02210	12 24 17.5	-39 32 00	20.52	0.87	0.34	2.06	23.46	23.85
02315	12 25 43.9	-39 32 29	17.64	0.68	3.34	4.73	16.77	23.66
02368	12 24 51.3	-39 32 23	16.60	0.49	1.00	5.50	20.89	22.70
02462	12 24 15.1	-39 32 21	17.98	0.66	1.08	1.46	19.39	21.38
02627	12 24 28.7	-39 32 33	20.60	0.47	0.72	2.17	22.68	23.88
02687	12 26 10.0	-39 32 39	18.91	0.90	1.13	1.70	19.96	22.07
02791	12 26 34.9	-39 32 46	19.51	1.02	1.15	2.02	21.24	23.39
02812	12 25 15.4	-39 32 54	17.65	0.74	1.30	1.06	18.19	20.67
03138	12 25 07.5	-39 33 11	19.06	0.71	0.69	2.40	21.23	22.38
03183	12 24 07.5	-39 33 12	18.10	0.78	1.50	1.68	18.84	21.75
03184	12 24 07.0	-39 33 16	20.34	0.52	1.24	2.39	21.72	24.06
03519	12 25 17.8	-39 33 46	17.26	0.51	1.02	5.22	21.35	23.22
03651	12 25 36.4	-39 33 53	17.90	0.79	2.05	2.09	18.29	22.38
03903	12 24 44.1	-39 34 08	18.53	0.64	0.90	1.89	20.82	22.41
04052	12 26 11.3	-39 34 47	14.57	0.60	1.07	10.78	20.12	22.09
04527	12 24 08.1	-39 34 54	17.95	0.87	1.30	2.16	19.37	21.84
04530	12 25 11.8	-39 35 07	15.84	0.44	0.88	5.92	20.28	21.85
04571	12 25 17.6	-39 35 05	17.37	0.81	2.09	3.07	18.42	22.60
04718	12 24 04.9	-39 35 16	17.12	0.73	0.67	4.53	20.97	22.08
04724	12 25 37.2	-39 35 11	17.79	0.76	1.82	1.77	18.20	21.80
04829	12 24 03.5	-39 35 15	20.16	0.50	0.58	2.55	22.47	23.38
04968	12 25 35.8	-39 35 28	18.77	0.62	1.96	2.11	18.98	22.88
05021	12 26 04.2	-39 35 31	18.26	0.76	1.51	1.40	18.84	21.77
05085	12 25 53.5	-39 35 35	19.59	0.61	0.62	2.66	21.80	22.79
05130	12 25 43.0	-39 35 39	18.77	0.51	1.24	2.08	20.69	23.03
05704	12 25 46.6	-39 36 22	18.95	0.52	0.84	1.73	21.20	22.66
06044	12 24 11.2	-39 36 44	18.38	0.70	1.11	1.76	19.73	21.78
06173	12 25 04.2	-39 36 30	16.04	0.61	2.25	2.38	16.40	20.93
06356	12 24 05.1	-39 37 16	15.69	0.76	2.60	2.95	15.80	21.10
06513	12 24 10.7	-39 37 21	19.40	0.54	0.66	1.99	21.36	22.44
06661	12 25 31.2	-39 37 37	17.53	0.77	2.16	2.09	17.55	21.89
06662	12 25 31.8	-39 37 52	17.96	0.39	1.22	3.09	20.53	22.83
06903	12 24 15.9	-39 37 50	18.16	0.54	1.33	1.77	19.61	22.14

<div align="right">Continued on next page</div>

Table A.3– continued from previous page

06905	12 24 16.3	-39 38 02	16.81	0.68	2.13	2.14	17.02	21.30
06937	12 23 54.9	-39 38 08	14.22	0.62	1.03	4.92	17.31	19.19
06976	12 24 11.6	-39 37 55	19.16	0.64	1.34	1.76	20.46	23.01
07080	12 25 16.1	-39 38 07	17.59	0.60	1.39	2.14	19.23	21.89
07630	12 24 18.3	-39 39 04	17.51	0.53	0.52	2.82	21.20	21.99
07648	12 25 19.0	-39 38 47	19.39	0.54	0.38	2.96	22.68	23.15
07705	12 25 21.3	-39 38 55	17.94	0.54	0.74	3.48	21.33	22.59
07784	12 25 15.4	-39 39 01	17.24	0.56	1.76	2.48	18.35	21.83
08792	12 24 22.5	-39 40 10	18.27	0.62	1.54	1.78	19.06	22.05
08843	12 25 53.7	-39 40 12	19.95	0.56	1.12	1.65	21.24	23.33
08963	12 24 10.7	-39 40 22	18.19	0.47	0.60	3.10	21.76	22.70
08966	12 24 21.9	-39 40 22	18.48	0.52	0.70	2.04	20.95	22.13
08992	12 23 59.9	-39 40 22	19.33	0.45	0.81	2.68	21.25	22.66
09657	12 26 13.9	-39 41 14	17.73	0.80	1.88	1.85	18.09	21.83
09665	12 25 20.9	-39 41 13	18.28	0.57	0.78	1.96	20.85	22.18
09684	12 24 39.8	-39 41 12	18.84	0.83	0.77	1.73	21.23	22.56
10148	12 25 14.3	-39 41 46	19.18	0.77	0.80	1.76	21.26	22.65
10584	12 25 42.2	-39 42 20	20.56	0.49	0.66	2.81	22.98	24.06
10605	12 25 23.9	-39 42 29	18.09	0.24	0.85	5.38	22.17	23.66
10619	12 25 27.4	-39 42 24	18.41	0.59	1.36	1.40	19.52	22.12
10886	12 26 27.3	-39 42 45	18.29	0.89	1.58	2.49	19.74	22.82
10904	12 24 54.3	-39 42 46	17.55	0.72	1.90	1.78	17.80	21.58
10920	12 26 12.7	-39 42 42	19.24	0.62	1.30	2.42	20.62	23.08
11539	12 24 52.3	-39 43 29	20.40	0.48	0.48	2.48	23.44	24.14
11612	12 25 39.4	-39 43 35	19.72	0.45	0.89	2.00	22.05	23.63
11736	12 25 55.5	-39 43 52	18.29	0.65	0.92	2.13	20.93	22.58
11798	12 24 48.9	-39 43 54	16.72	0.73	2.26	2.67	17.11	21.67
12152	12 25 32.8	-39 44 18	18.35	0.47	0.54	2.78	21.30	22.12
12209	12 25 37.0	-39 44 36	15.58	0.59	0.74	9.31	21.51	22.77
12359	12 25 26.8	-39 44 22	20.58	0.61	0.53	2.59	22.70	23.51
12412	12 24 54.4	-39 44 04	16.50	0.79	1.02	5.60	21.27	23.13
12620	12 24 41.1	-39 44 59	17.38	0.60	1.36	2.23	19.15	21.75
13025	12 25 08.0	-39 45 31	17.48	0.70	1.57	2.52	19.20	22.26
13075	12 25 37.2	-39 45 35	19.16	0.39	0.93	1.82	20.96	22.62
13275	12 25 52.6	-39 45 40	19.57	0.84	0.74	2.51	21.83	23.08
13385	12 25 08.9	-39 46 32	12.23	0.66	1.71	9.88	16.38	19.75
13646	12 25 25.5	-39 46 09	17.90	0.60	0.87	1.59	19.46	20.99
13712	12 24 18.5	-39 46 14	18.98	0.78	1.07	1.69	20.71	22.69
13937	12 24 07.3	-39 44 20	20.23	0.51	0.63	2.05	22.43	23.44
13978	12 25 22.2	-39 46 39	19.05	0.68	1.12	1.83	20.32	22.39
14011	12 25 00.3	-39 46 43	17.13	0.61	1.16	3.45	19.99	22.17
14077	12 26 33.3	-39 46 41	18.28	0.67	1.08	1.94	19.66	21.66
14194	12 25 36.6	-39 46 52	18.19	0.63	1.31	2.30	19.99	22.48
14268	12 24 09.1	-39 46 31	18.89	0.33	0.76	1.93	21.50	22.80
14445	12 26 34.2	-39 47 10	19.66	0.66	1.94	2.99	19.71	23.58
14557	12 25 21.3	-39 47 20	20.09	0.61	0.91	2.00	21.73	23.34
14618	12 23 53.7	-39 47 22	17.60	0.62	1.35	1.72	18.67	21.25
14785	12 25 59.7	-39 47 34	20.26	0.43	0.54	2.22	23.15	23.96
14882	12 24 15.6	-39 47 41	17.87	0.62	0.44	2.91	22.13	22.74
15464	12 24 34.4	-39 48 24	20.04	0.34	1.08	2.41	22.48	24.48
15509	12 24 53.3	-39 48 28	19.51	0.52	0.60	1.97	22.14	23.10
15688	12 24 17.9	-39 48 39	20.73	0.43	0.73	2.14	22.68	23.92
15689	12 24 21.4	-39 48 45	17.62	0.65	0.69	4.21	21.79	22.95
15690	12 24 21.7	-39 49 06	16.75	0.64	1.76	2.14	17.33	20.79
15819	12 24 06.9	-39 48 47	19.77	0.42	0.69	1.88	21.91	23.05
15885	12 24 24.6	-39 48 53	18.98	0.64	0.73	1.79	21.25	22.48
16231	12 23 54.8	-39 49 15	18.97	0.48	0.73	2.05	21.98	23.21
16334	12 26 21.8	-39 49 23	19.28	0.80	1.02	1.77	20.78	22.64
16468	12 26 14.6	-39 49 34	18.39	0.62	1.20	1.90	19.81	22.06
16501	12 26 26.7	-39 49 35	19.51	0.97	1.30	2.82	21.76	24.22

Table A.3– continued from previous page

16513	12 23 55.1	-39 49 32	20.86	0.81	0.95	1.35	22.41	24.13
16530	12 24 27.0	-39 49 37	19.58	0.46	0.55	1.96	22.35	23.21
16918	12 24 12.0	-39 50 04	19.76	0.84	0.67	1.85	21.95	23.05
16940	12 24 26.0	-39 50 07	18.05	0.57	1.00	2.56	20.84	22.66
17269	12 24 11.1	-39 50 28	20.01	0.30	0.76	1.85	22.47	23.78
17274	12 25 23.7	-39 50 40	15.45	0.63	1.72	3.07	17.35	20.73
17488	12 26 35.2	-39 50 49	17.79	0.69	0.93	3.33	21.21	22.88
17620	12 24 03.3	-39 50 53	17.80	0.49	0.73	1.80	20.61	21.83
17731	12 26 21.8	-39 51 04	19.67	0.45	0.41	5.83	23.93	24.46
17814	12 25 45.6	-39 51 09	19.56	0.56	0.62	1.84	21.95	22.94
18077	12 26 06.5	-39 51 35	17.90	0.39	0.40	9.11	24.14	24.66
18126	12 25 12.5	-39 51 33	19.14	0.47	0.76	2.26	21.04	22.33
18226	12 25 30.7	-39 51 41	19.76	0.39	0.69	2.37	22.46	23.61
18555	12 26 22.2	-39 52 18	16.38	0.74	3.22	3.28	15.64	22.28
18668	12 24 32.7	-39 52 12	19.66	0.81	0.66	1.95	22.01	23.09
18894	12 24 06.1	-39 52 34	18.84	0.43	0.66	6.12	23.88	24.95
19488	12 24 01.8	-39 53 12	18.96	0.40	0.71	2.14	21.80	23.00
19703	12 24 59.9	-39 53 39	19.55	0.40	0.66	1.86	22.06	23.13
19961	12 25 06.6	-39 53 57	19.88	0.59	0.67	2.38	21.94	23.04
20030	12 24 59.9	-39 54 02	18.84	0.63	0.59	2.17	21.58	22.50
20115	12 25 58.4	-39 54 08	19.28	0.63	0.90	2.03	21.12	22.72
20247	12 26 29.8	-39 54 16	18.91	0.88	0.77	2.09	21.12	22.44
20325	12 24 37.2	-39 54 28	17.42	0.43	1.12	4.66	20.71	22.80
20569	12 25 24.8	-39 54 38	20.15	0.89	1.14	1.47	20.95	23.08
20908	12 24 14.8	-39 55 03	18.18	0.55	0.69	3.84	22.27	23.42
21171	12 23 55.4	-39 55 20	18.25	0.58	0.71	2.58	20.77	21.96
21349	12 26 27.6	-39 55 33	18.86	0.76	0.93	2.19	20.79	22.45
21705	12 23 55.5	-39 55 58	19.62	0.47	0.65	1.94	21.55	22.62
21900	12 24 21.3	-39 56 14	17.94	0.64	0.97	3.36	20.01	21.77
22038	12 25 12.2	-39 56 26	18.42	0.49	0.69	2.00	20.66	21.81
22070	12 25 42.5	-39 56 31	17.86	0.63	1.31	1.65	18.93	21.42
22187	12 26 33.8	-39 56 38	17.39	0.72	1.86	1.95	17.74	21.42
22190	12 24 05.0	-39 57 18	16.64	0.64	2.77	2.34	15.91	21.58
22208	12 24 37.2	-39 56 31	19.93	0.82	0.27	1.92	22.45	22.68
22446	12 25 05.4	-39 57 01	18.65	0.46	0.67	2.61	21.42	22.53
22488	12 23 60.0	-39 57 01	17.33	0.58	1.02	2.15	19.39	21.26
22513	12 24 30.5	-39 56 60	19.86	0.68	0.37	8.88	24.89	25.34
22954	12 25 19.1	-39 57 37	19.05	0.94	1.78	1.57	19.23	22.75
23137	12 24 48.0	-39 57 50	19.12	0.97	0.73	2.16	21.50	22.73
23351	12 26 25.0	-39 58 05	20.28	0.70	0.48	2.17	23.17	23.87
23400	12 26 38.2	-39 58 07	18.82	0.92	1.37	1.58	19.31	21.92
23659	12 24 50.4	-39 58 34	17.77	0.63	1.05	4.43	20.36	22.28
23920	12 24 02.7	-39 58 50	16.56	0.51	0.94	2.47	19.24	20.92
23938	12 24 58.0	-39 58 50	20.21	0.55	1.06	1.82	21.62	23.56
23995	12 23 55.6	-39 58 58	16.37	0.58	0.84	4.21	20.31	21.79
24120	12 26 22.5	-39 59 06	16.20	0.57	0.85	2.64	19.43	20.93
24410	12 26 30.7	-39 59 23	19.83	0.89	0.67	2.35	21.86	22.97

Table A.4: Faint candidate group member population around RR 242.

ID	α (2000)	δ (2000)	m$_R$ [mag]	V–R [mag]	n	r$_e$ [arcsec]	μ$_0$ [mag arcsec^{-2}]	μ$_e$ [mag arcsec^{-2}]
00017	13 20 19.9	-43 55 57	17.03	0.69	3.05	3.58	16.44	22.72
00018	13 21 39.0	-43 55 54	17.85	0.77	2.46	1.90	16.98	21.97
00636	13 22 22.3	-43 27 10	18.63	0.43	1.30	2.30	20.89	23.36
00842	13 22 33.7	-43 26 06	20.32	0.49	0.61	1.99	22.43	23.41
00970	13 19 47.3	-43 27 32	19.54	0.64	0.71	1.84	21.59	22.79
01414	13 21 38.1	-43 26 20	16.50	0.63	1.96	1.68	16.45	20.35
02287	13 20 21.5	-43 28 23	20.46	0.47	0.60	1.89	21.98	22.93
02474	13 20 19.8	-43 27 48	16.66	0.62	2.99	2.67	15.81	21.95
02600	13 20 42.1	-43 28 40	20.55	0.62	1.04	3.16	21.95	23.85
02687	13 20 16.6	-43 27 19	14.02	0.60	0.83	13.02	20.66	22.10
02729	13 22 20.8	-43 28 49	16.08	0.68	1.66	3.01	17.94	21.20
03293	13 20 19.0	-43 29 33	18.15	0.39	1.93	2.06	18.21	22.04
05407	13 21 31.0	-43 30 51	18.21	0.67	1.09	2.00	20.04	22.05
05413	13 19 55.7	-43 30 52	17.76	0.72	0.96	1.61	19.19	20.93
05430	13 21 59.4	-43 30 48	19.89	0.54	1.84	2.93	20.63	24.27
05845	13 20 17.5	-43 31 11	20.55	0.50	1.36	5.13	22.98	25.58
05955	13 21 18.6	-43 31 15	17.90	0.59	1.51	1.53	18.13	21.05
06039	13 22 03.1	-43 31 16	18.12	0.57	0.88	1.47	20.01	21.58
06906	13 20 41.2	-43 31 56	19.37	0.48	0.81	3.50	22.54	23.95
07132	13 21 38.7	-43 32 09	17.67	0.44	0.68	3.67	21.62	22.74
08028	13 22 30.1	-43 32 41	19.15	0.65	0.84	1.52	21.31	22.79
08050	13 21 15.3	-43 32 51	17.99	0.51	0.77	2.75	20.12	21.43
08064	13 22 10.4	-43 32 56	17.85	0.64	1.21	5.45	21.79	24.06
08617	13 20 15.0	-43 33 15	20.02	0.53	0.48	1.88	22.05	22.75
08697	13 21 07.1	-43 33 16	20.48	0.53	0.67	1.99	21.87	22.98
08916	13 20 38.5	-43 33 29	18.72	0.44	0.81	3.49	21.05	22.45
09059	13 20 18.2	-43 34 17	14.91	0.58	1.01	5.75	19.61	21.46
09578	13 20 47.1	-43 34 02	17.22	0.54	0.72	4.71	20.97	22.17
10276	13 21 53.0	-43 34 30	18.54	0.71	1.69	1.47	18.56	21.89
10753	13 20 34.1	-43 34 53	17.62	0.64	0.86	2.08	19.80	21.33
10930	13 22 33.8	-43 35 01	17.11	0.64	2.53	2.21	16.49	21.64
10972	13 20 35.9	-43 35 01	20.15	0.59	0.68	3.22	23.57	24.69
11100	13 21 03.1	-43 35 12	17.29	0.68	1.13	3.84	20.67	22.77
11102	13 20 24.0	-43 35 08	20.41	0.35	0.58	2.27	23.41	24.32
11419	13 22 06.6	-43 35 28	16.56	0.84	3.08	3.64	16.13	22.47
12894	13 22 03.0	-43 36 25	20.29	0.93	0.51	3.03	22.59	23.36
13110	13 22 24.8	-43 36 33	18.11	0.55	1.20	1.75	19.47	21.73
13326	13 21 03.9	-43 36 58	16.15	0.60	1.42	8.70	20.06	22.78
13627	13 21 10.7	-43 37 07	16.69	0.62	1.73	2.86	18.00	21.41
13887	13 20 08.6	-43 37 14	19.71	0.44	0.63	3.40	22.11	23.12
14078	13 22 36.0	-43 37 22	20.51	0.51	0.91	2.24	22.06	23.68
14284	13 20 47.8	-43 37 36	17.13	0.59	1.34	1.41	17.84	20.41
15689	13 21 16.5	-43 38 53	17.73	0.74	1.38	3.02	20.38	23.02
16076	13 22 06.4	-43 39 08	19.82	0.60	0.54	2.94	22.09	22.92
16322	13 21 14.8	-43 39 19	20.63	0.24	0.59	2.47	23.50	24.43
16864	13 20 32.5	-43 39 47	17.24	0.63	0.94	2.87	20.07	21.75
18069	13 20 07.5	-43 40 36	19.40	0.63	1.27	2.24	21.17	23.58
18166	13 21 04.0	-43 40 50	19.28	0.42	1.03	1.72	21.02	22.91
18533	13 22 36.1	-43 41 06	18.58	0.56	0.89	2.37	21.37	22.95
18545	13 20 36.8	-43 40 46	18.07	0.53	1.46	5.19	21.18	24.00
18982	13 20 12.3	-43 41 40	15.86	0.71	3.15	2.83	14.87	21.35
20075	13 20 26.7	-43 42 28	16.33	0.55	1.51	5.70	19.93	22.85
20151	13 21 50.1	-43 42 15	19.64	0.47	1.42	2.06	21.52	24.25
20910	13 22 06.9	-43 42 48	19.84	0.48	0.57	2.43	22.49	23.37
20913	13 22 12.9	-43 42 47	19.38	0.90	1.46	1.86	20.31	23.14
21539	13 20 46.7	-43 43 20	18.93	0.72	1.15	1.98	20.09	22.24

Table A.4– continued from previous page

21750	13 20 03.6	-43 43 29	18.76	0.49	0.69	2.08	21.56	22.70
21838	13 20 20.4	-43 43 36	19.10	0.69	1.40	3.41	21.61	24.30
22150	13 21 32.3	-43 43 46	19.66	0.51	1.03	2.49	21.69	23.58
22454	13 21 40.5	-43 44 04	18.01	0.27	1.47	1.42	18.78	21.62
22678	13 22 27.8	-43 44 03	19.49	0.49	0.90	1.65	21.11	22.70
22809	13 20 02.3	-43 44 12	20.09	0.66	0.77	4.41	23.68	25.01
23181	13 21 29.9	-43 40 47	18.70	0.55	0.80	2.39	21.54	22.91
23290	13 21 42.2	-43 44 18	19.55	0.54	0.88	1.40	16.89	18.45
24352	13 21 14.8	-43 45 43	13.71	0.62	2.35	6.91	15.91	20.67
24968	13 20 12.8	-43 45 53	16.61	0.58	0.76	3.84	20.27	21.58
25266	13 20 34.1	-43 46 01	19.60	0.42	0.60	2.52	22.63	23.58
25510	13 22 30.5	-43 46 13	17.61	0.42	1.36	1.88	18.86	21.47
25575	13 19 44.2	-43 46 28	16.42	0.60	2.24	7.12	18.92	23.44
26321	13 20 53.5	-43 46 49	19.71	0.74	0.70	1.80	22.11	23.27
26778	13 19 54.9	-43 47 33	14.52	0.71	2.10	5.97	16.99	21.20
26874	13 21 46.9	-43 47 17	18.00	0.74	1.62	2.48	18.88	22.05
27628	13 21 28.6	-43 47 45	17.56	0.68	1.34	2.41	18.52	21.09
28535	13 20 38.0	-43 48 33	18.58	0.19	0.82	1.97	20.60	22.04
29229	13 20 06.4	-43 49 16	17.09	0.63	1.15	6.27	21.44	23.59
29391	13 22 09.8	-43 49 08	20.27	0.47	0.69	1.99	22.12	23.26
29430	13 21 23.1	-43 49 13	19.57	0.62	0.55	1.81	22.03	22.88
29780	13 20 04.3	-43 49 32	19.03	0.50	0.55	3.15	21.66	22.50
30223	13 19 47.1	-43 49 54	18.89	0.62	0.87	4.70	22.84	24.39
30287	13 20 37.4	-43 50 02	17.53	0.50	0.93	3.15	20.37	22.03
30578	13 21 48.3	-43 50 05	19.11	0.70	1.52	2.72	20.02	22.96
30790	13 19 59.6	-43 50 16	19.62	0.47	0.78	2.48	21.85	23.20
31206	13 21 11.3	-43 50 40	19.87	0.51	0.53	2.18	21.77	22.57
31496	13 22 36.4	-43 50 52	19.27	0.31	0.76	2.34	21.61	22.92
31744	13 19 59.7	-43 51 08	19.77	0.58	1.22	4.17	21.12	23.41
32672	13 21 53.9	-43 51 45	19.31	0.94	0.88	1.55	21.10	22.67
32890	13 20 43.4	-43 52 02	17.41	0.64	1.37	3.90	19.36	21.99
33526	13 22 12.0	-43 52 25	19.54	0.87	1.40	1.80	20.45	23.14
33553	13 22 10.8	-43 52 26	19.71	0.42	0.70	1.74	21.64	22.81
34453	13 21 14.8	-43 53 29	18.27	0.68	2.32	2.05	17.74	22.43
34710	13 19 45.3	-43 53 31	20.83	0.72	1.61	2.60	22.22	25.37
34877	13 22 01.6	-43 53 36	17.72	0.47	1.57	1.97	18.80	21.86
35172	13 20 00.5	-43 53 57	20.41	0.37	1.83	1.40	20.26	23.89
35824	13 21 38.1	-43 54 23	19.17	0.59	0.66	4.67	23.92	25.00
36209	13 20 33.3	-43 50 30	19.09	0.54	1.77	2.75	20.55	24.04
36679	13 20 37.5	-43 55 02	19.52	0.78	0.70	1.74	21.47	22.64
36865	13 22 28.6	-43 55 08	20.28	0.97	0.53	1.93	22.23	23.03
37278	13 20 39.7	-43 55 31	19.96	0.58	0.80	2.43	22.76	24.14
37730	13 21 39.8	-43 55 55	18.05	0.83	3.83	3.52	15.20	23.16
37952	13 22 05.7	-43 55 59	20.38	0.57	1.36	3.05	21.78	24.39
38051	13 21 31.0	-43 56 07	20.00	0.54	1.24	2.39	21.94	24.28
38663	13 21 32.4	-43 27 23	15.04	0.79	1.58	8.56	19.13	22.21

Appendix B

Catalogue of X-ray sources detected in the fields of RR 143 and RR 242

Table B.1: X-ray sources in the RR 143 field.

ID	α (2000)	δ (2000)	net counts[1]	count rate[1]	flux[1] [erg s^{-1}]	Instrument
1	06 46 40.8	-64 16 02	26.71 ±6.18	0.0104	1.013168E-13	PN
2	06 47 16.0	-64 23 17	47.95 ±8.65	0.0519	7.104581E-13	PN
3	06 47 24.0	-64 23 32	78.73 ±10.07	0.0256	2.441722E-13	PN
4	06 47 27.4	-64 04 56	86.03 ±9.97	0.0355	3.905863E-13	PN
5	06 47 34.4	-64 18 34	22.64 ±6.15	0.0053	5.150544E-14	PN
6	06 47 40.0	-64 06 53	23.01 ±6.16	0.0073	7.321936E-14	PN
7	06 47 48.7	-64 19 56	25.63 ±5.95	0.0055	6.401829E-14	PN
8	06 47 55.9	-64 07 35	17.68 ±4.68	0.0056	4.716441E-14	PN
9	06 47 56.2	-64 17 15	76.23 ±9.37	0.0138	1.559576E-13	PN
10	06 48 03.8	-64 05 44	25.18 ±6.96	0.0124	1.051518E-13	PN
11	06 48 06.1	-64 09 26	225.91 ±16.56	0.0501	5.650568E-13	PN
12	06 48 07.3	-64 25 28	140.23 ±12.61	0.0393	4.409702E-13	PN
13	06 48 12.1	-64 07 55	36.15 ±7.37	0.0089	9.970893E-14	PN
14	06 48 17.1	-64 24 21	30.10 ±6.68	0.0076	8.745382E-14	PN
15	06 48 29.4	-64 20 50	18.03 ±5.14	0.0027	1.083030E-13	MOS
16[2]	06 48 37.5	-64 16 23	1732.48 ±46.88	0.2422	2.084515E-12	PN
17	06 48 40.9	-64 15 43	238.34 ±19.60	0.0330	2.901262E-13	PN
18	06 48 42.9	-64 04 21	53.26 ±8.22	0.0179	2.009735E-13	PN
19	06 48 43.4	-64:17 01	54.07 ±11.29	0.0083	7.754885E-14	PN
20	06 48 50.1	-64 18 53	24.80 ±6.09	0.0038	4.573677E-14	PN
21[3]	06 48 50.6	-64 20 07	28.08 ±6.02	0.0039	1.758483E-13	MOS
22	06 48 51.6	-64 28 27	24.00 ±6.70	0.0082	8.467915E-14	PN
23	06 48 57.6	-64 21 18	104.25 ±11.40	0.0183	2.152999E-13	PN
24	06 49 01.9	-64 12 26	22.48 ±5.59	0.0036	3.057529E-14	PN
25	06 49 04.7	-64 10 01	50.88 ±8.68	0.0098	1.200122E-13	PN
26	06 49 11.8	-64 06 54	78.84 ±9.25	0.0211	2.692666E-13	PN
27	06 49 12.7	-64 21 30	12.97 ±3.69	0.0018	4.480486E-14	MOS
28	06 49 21.1	-64 08 12	15.06 ±4.30	0.0027	8.221321E-14	MOS
29	06 49 25.1	-64 22 43	28.51 ±6.16	0.0064	6.839662E-14	PN
30	06 49 30.7	-64 19 52	87.06 ±10.69	0.0161	1.638327E-13	PN
31	06 49 34.6	-64 22 32	19.37 ±5.18	0.0044	4.305953E-14	PN
32	06 49 46.9	-64 07 50	56.48 ±8.28	0.0167	2.240017E-13	PN
33	06 49 49.1	-64 17 52	22.52 ±5.89	0.0053	4.461954E-14	PN
34	06 49 51.9	-64:11 46	124.59 ±12.12	0.0317	4.061077E-13	PN
35	06 49 52.2	-64 13 58	23.34 ±6.67	0.0062	7.873910E-14	PN
36	06 49 56.8	-64 26 23	37.94 ±6.59	0.0141	1.800038E-13	PN
37	06 49 58.7	-64 20 09	63.02 ±8.68	0.0152	1.825993E-13	PN
38	06 49 59.6	-64 13 05	15.79 ±4.70	0.0037	3.716768E-14	PN
39	06 50 00.4	-64 18 24	29.74 ±7.14	0.0089	9.482519E-14	PN
40	06 50 06.7	-64 23 26	47.59 ±7.37	0.0148	1.280928E-13	PN

[1] In the full 0.5-10.0 keV band. Fluxes are derived for a power law spectrum with $\Gamma = 1.7$ and galactic absorption.

[2] RR 143a

[3] RR 143b

Table B.2: X-ray sources in the RR 242 field.

ID	α (2000)	δ (2000)	net counts[1]	count rate[1]	flux[1] [erg s^{-1}]	Instrument
1	13 20 00.0	-43 46 40	50.84 ±8.02	0.0102	3.082375E-13	MOS
2	13 20 12.2	-43 40 12	45.10 ±8.82	0.0082	1.227895E-13	PN
3	13 20 18.7	-43 33 56	79.76 ±10.21	0.0130	3.278396E-13	MOS
4	13 20 20.5	-43 51 24	38.20 ±8.09	0.0094	1.507757E-13	PN
5	13 20 22.6	-43 32 59	33.81 ±6.99	0.0056	2.065168E-13	MOS
6	13 20 29.8	-43 34 51	39.48 ±7.68	0.0066	7.311842E-14	PN
7	13 20 30.3	-43 41 44	30.38 ±7.96	0.0040	6.720174E-14	PN
8	13 20 40.3	-43 42 00	305.49 ±20.70	0.0323	3.203940E-13	PN
9	13 20 40.7	-43 49 20	19.66 ±5.55	0.0037	3.447273E-14	PN
10	13 20 40.9	-43 50 42	23.78 ±5.36	0.0034	1.416466E-13	MOS
11	13 20 43.0	-43 30 35	28.74 ±7.64	0.0065	8.991507E-14	PN
12	13 20 49.0	-43 52 24	116.28 ±12.17	0.0199	1.873789E-13	PN
13	13 20 50.1	-43 36 00	29.58 ±6.98	0.0037	3.102088E-14	PN
14	13 20 50.2	-43 51 20	159.05 ±13.93	0.0254	2.940479E-13	PN
15	13 20 51.1	-43 38 33	34.47 ±8.47	0.0036	4.542740E-14	PN
16	13 20 51.6	-43 40 27	33.53 ±8.53	0.0040	6.908156E-14	PN
17	13 20 56.0	-43 51 09	36.89 ±7.93	0.0056	6.668399E-14	PN
18	13 20 56.7	-43 34 11	28.52 ±7.56	0.0042	6.023459E-14	PN
19	13 21 03.4	-43 45 36	92.27 ±11.45	0.0088	1.019294E-13	PN
20	13 21 04.7	-43 37 27	53.40 ±9.48	0.0059	6.751434E-14	PN
21	13 21 05.4	-43 51 29	37.92 ±6.28	0.0050	1.852026E-13	MOS
22	13 21 07.7	-43 27 47	38.90 ±6.98	0.0121	1.949288E-13	PN
23	13 21 10.9	-43 37 08	52.11 ±8.77	0.0060	8.068702E-14	PN
24	13 21 11.0	-43 34 02	33.62 ±8.17	0.0048	4.076546E-14	PN
25[2]	13 21 13.0	-43 42 17	2945.74 ±60.14	0.2549	2.977146E-12	PN
26	13 21 20.1	-43 32 16	26.76 ±7.40	0.0053	6.022906E-14	PN
27	13 21 21.8	-43 51 11	335.21 ±13.13	0.0724	6.975664E-13	PN
28	13 21 22.4	-43 33 48	22.08 ±5.71	0.0034	3.122640E-14	PN
29	13 21 23.9	-43 38 51	53.51 ±10.72	0.0057	7.059597E-14	PN
30	13 21 24.1	-43 38 36	207.54 ±17.29	0.0221	2.534329E-13	PN
31	13 21 28.7	-43 36 55	39.17 ±8.55	0.0049	5.430766E-14	PN
32	13 21 30.6	-43 49 13	50.61 ±12.26	0.0168	5.288067E-13	MOS
33	13 21 35.3	-43 48 11	56.77 ±9.91	0.0076	9.071488E-14	PN
34	13 21 40.3	-43 39 44	34.92 ±8.37	0.0043	5.560670E-14	PN
35	13 21 49.1	-43 36 12	51.48 ±8.66	0.0084	7.141674E-14	PN
36	13 21 50.4	-43 33 56	39.79 ±8.88	0.0089	1.612898E-13	PN
37	13 21 55.8	-43 37 19	42.51 ±8.14	0.0075	6.943100E-14	PN
38	13 22 00.6	-43 44 01	29.37 ±7.90	0.0051	5.243528E-14	PN
39	13 22 04.0	-43 43 52	45.88 ±9.36	0.0096	1.016975E-13	PN
40	13 22 24.2	-43 37 50	54.34 ±9.05	0.0159	1.351174E-13	PN
41	13 22 26.1	-43 35 17	110.34 ±12.09	0.0335	4.308571E-13	PN
42	13 22 33.3	-43 40 41	21.91 ±5.48	0.0061	5.127875E-14	PN
43	13 22 33.9	-43 38 51	45.95 ±8.58	0.0148	2.298704E-13	PN

[1] In the full 0.5-10.0 keV band. Fluxes are derived for a power law spectrum with $\Gamma = 1.7$ and galactic absorption.

[2] RR 242a

Appendix C

Catalogue of radial velocities of the candidate members around the 4 pairs

Table C.1: Radial velocities of the candidate group member populations of all 4 pairs

ID	α (2000)	δ (2000)	m_R [mag]	v_{rad} [km s^{-1}]	v_{err} [km s^{-1}]	R
RR143_01908	06 50 13.3	-64 01 52	19.08	55346	156	2.06
RR143_02314	06 50 05.5	-64 02 26	19.41	33673	199	0.00
RR143_02403	06 50 44.2	-64 02 36	19.17	86278	118	2.89
RR143_02483	06 46 37.6	-64 02 42	17.65	37646	66	9.22
RR143_02668	06 49 06.7	-64 02 57	17.37	23083	53	4.23
RR143_02940	06 46 57.0	-64 02 19	18.12	49589	85	4.06
RR143_03090	06 49 01.7	-64 03 27	18.34	6	73	3.24
RR143_03578	06 46 15.0	-64 04 00	17.95	94349	74	5.96
RR143_04342	06 50 41.1	-64 04 47	19.40	45284	38	2.23
RR143_04431	06 50 55.7	-64 04 55	18.13	44478	80	5.10
RR143_04693	06 50 56.2	-64 05 14	17.65	44583	69	5.98
RR143_04874	06 48 24.7	-64 05 30	19.67	52750	92	2.78
RR143_05014	06 46 46.7	-64 05 41	18.98	64785	120	3.44
RR143_05363	06 48 41.3	-64 06 10	18.01	53066	82	6.48
RR143_05526	06 48 00.8	-64 06 14	18.52	45170	60	3.92
RR143_05757	06 46 14.0	-64 06 33	19.10	83729	50	3.05
RR143_05769	06 48 22.9	-64 06 36	18.75	61153	67	4.22
RR143_05889	06 47 57.8	-64 06 48	18.23	48	81	4.25
RR143_06038	06 46 22.1	-64 06 52	18.89	83759	77	6.46
RR143_06070	06 48 27.0	-64 07 01	17.81	52741	75	8.98
RR143_06152	06 50 12.4	-64 07 08	16.87	37348	69	8.61
RR143_06304	06 48 27.5	-64 07 17	18.43	52563	59	5.89
RR143_06459	06 46 51.5	-64 07 26	18.25	41311	121	2.58
RR143_06608	06 47 51.8	-64 07 39	19.65	155260	77	0.00
RR143_06700	06 49 30.2	-64 04 25	18.89	92432	113	3.54
RR143_06858	06 47 45.1	-64 07 59	17.58	45165	76	5.77
RR143_08730	06 47 42.1	-64 10 15	16.86	44878	75	4.69
RR143_09030	06 46 04.0	-64 10 34	17.05	20457	52	2.95
RR143_09192	06 47 53.2	-64 10 55	17.25	3296	46	3.34
RR143_09251	06 50 31.3	-64 10 43	19.63	10662	176	2.34
RR143_09369	06 50 34.7	-64 10 52	18.91	144638	90	0.00
RR143_09582	06 46 57.4	-64 11 09	19.97	141056	219	0.00
RR143_09823	06 49 05.4	-64 11 39	18.35	105210	106	4.61
RR143_10029	06 50 14.8	-64 11 34	18.96	94666	50	3.71
RR143_10155	06 47 52.2	-64 11 51	17.85	99	42	6.39
RR143_10197	06 46 52.9	-64 11 50	18.07	44365	88	5.95
RR143_10305	06 46 34.3	-64 12 01	17.49	41350	56	6.61
RR143_10365	06 49 16.0	-64 12 03	18.82	87252	144	3.39

Table C.1– continued from previous page

RR143_10711	06 50 39.1	-64 12 18	18.81	81622	98	4.36
RR143_10853	06 48 03.9	-64 12 41	16.76	44337	69	10.47
RR143_12423	06 46 07.1	-64 14 17	19.17	95753	133	0.00
RR143_12981	06 48 56.2	-64 15 09	17.73	29871	80	6.62
RR143_13059	06 50 44.8	-64 14 58	19.27	119795	179	0.00
RR143_13491	06 48 28.4	-64 15 55	18.26	202	48	2.59
RR143_13936	06 46 54.4	-64 16 23	16.68	147	79	4.73
RR143_14512	06 46 07.2	-64 16 59	19.96	103924	122	0.00
RR143_15513	06 46 14.5	-64 18 21	17.93	42979	86	9.38
RR143_16011	06 50 25.4	-64 18 56	20.00	38841	123	2.02
RR143_16117	06 47 31.4	-64 19 08	17.58	43798	81	9.70
RR143_16784	06 50 55.3	-64 19 60	18.65	39169	81	3.52
RR143_17236	06 47 01.6	-64 20 37	20.30	60052	158	2.03
RR143_17347	06 46 45.6	-64 20 48	19.65	60131	183	0.00
RR143_17858	06 50 09.2	-64 18 37	17.01	37428	117	2.46
RR143_17909	06 48 20.7	-64 21 31	19.21	97580	99	3.83
RR143_18031	06 47 44.8	-64 21 40	19.06	45117	127	4.12
RR143_18260	06 46 38.1	-64 21 53	19.26	117458	219	0.00
RR143_20429	06 47 05.6	-64 24 54	18.14	44995	81	7.88
RR143_20430	06 47 07.0	-64 24 44	16.41	44383	66	7.47
RR143_20738	06 46 59.7	-64 25 07	17.06	43162	50	5.65
RR143_21016	06 46 42.1	-64 25 22	17.48	96327	98	3.80
RR143_21093	06 49 11.0	-64 25 27	18.33	49802	128	2.58
RR143_21533	06 49 04.1	-64 25 57	17.71	45380	75	6.21
RR143_21872	06 50 01.9	-64 26 20	18.56	60147	64	10.46
RR143_22120	06 49 21.7	-64 26 18	19.66	49832	188	0.00
RR143_22375	06 49 31.8	-64 26 57	18.35	41497	85	3.12
RR143_22457	06 48 09.6	-64 27 02	18.46	45260	244	2.23
RR143_22627	06 47 07.3	-64 27 16	19.62	38178	123	2.02
RR143_22971	06 48 24.3	-64 27 37	19.41	52021	153	2.21
RR143_23417	06 47 33.8	-64 28 13	19.24	44713	152	0.00
RR143_23734	06 49 18.3	-64 28 31	19.56	66271	171	2.34
RR143_23758	06 46 27.9	-64 28 30	20.30	27143	98	2.06
RR143_23796	06 50 31.9	-64 28 31	19.61	77272	128	0.00
RR143_23823	06 49 03.3	-64 28 40	18.40	69630	38	4.08
RR143_24029	06 46 33.0	-64 28 50	19.93	3724	73	3.87
RR143_24188	06 50 20.6	-64 29 05	18.44	12231	74	3.52
RR143_24246	06 47 07.5	-64 29 16	16.91	44820	68	7.54
RR143_24333	06 48 40.5	-64 29 20	18.48	56848	22	2.44
RR143_24388	06 47 45.9	-64 29 23	18.29	93432	104	5.95
RR143_24606	06 46 19.4	-64 29 34	17.01	44547	110	0.00

Table C.1– continued from previous page

RR143_24607	06 49 34.2	-64 29 35	18.50	41082	195	0.00
RR143_24743	06 47 47.9	-64 29 48	19.13	44196	197	2.98
RR143_25304	06 47 52.6	-64 30 31	18.27	51920	101	0.00
RR143_25310	06 50 56.9	-64 30 23	19.57	93799	217	2.46
RR143_25500	06 47 55.6	-64 30 47	19.05	53175	83	5.36
RR210_09531	12 06 12.4	-29 44 58	19.38	52277	230	2.02
RR210_09816	12 06 29.9	-29 44 21	19.11	43646	62	4.89
RR210_10073	12 07 46.1	-29 44 12	17.74	74436	124	6.06
RR210_10243	12 06 50.6	-29 43 51	17.88	44233	103	3.41
RR210_10441	12 06 41.0	-29 43 39	18.00	44815	79	3.69
RR210_10601	12 07 08.0	-29 43 24	17.77	44468	81	2.67
RR210_10968	12 06 38.8	-29 42 43	17.43	43202	90	6.33
RR210_11168	12 06 30.8	-29 42 34	18.96	43230	35	5.74
RR210_11372	12 07 43.3	-29 43 11	17.59	1927	183	3.08
RR210_11400	12 05 54.1	-29 41 57	18.18	41985	61	4.30
RR210_11412	12 06 28.6	-29 41 55	18.16	43988	71	7.94
RR210_11440	12 07 42.6	-29 41 57	18.32	74979	84	3.75
RR210_11532	12 05 55.9	-29 42 16	16.75	48366	99	5.77
RR210_11561	12 05 45.1	-29 41 45	18.92	48452	225	2.70
RR210_11710	12 05 54.3	-29 41 13	19.99	28010	194	0.00
RR210_11756	12 05 44.1	-29 41 30	16.48	27687	66	6.36
RR210_11942	12 06 17.2	-29 41 00	18.38	65387	87	9.11
RR210_12139	12 06 14.1	-29 40 46	18.46	43036	46	8.28
RR210_12167	12 05 52.2	-29 40 37	18.83	102561	128	0.00
RR210_12523	12 05 45.6	-29 40 51	16.27	27558	43	5.88
RR210_12686	12 07 21.7	-29 40 06	17.11	46460	97	8.15
RR210_12828	12 05 59.2	-29 39 26	18.39	59942	101	2.67
RR210_12912	12 07 37.6	-29 39 20	18.33	59915	109	6.45
RR210_13089	12 06 15.3	-29 39 22	18.20	44293	73	8.15
RR210_13481	12 06 46.6	-29 31 16	18.00	46448	32	2.04
RR210_13493	12 06 50.3	-29 36 23	14.26	2008	45	9.08
RR210_13578	12 07 03.2	-29 35 49	17.32	46641	76	7.40
RR210_13676	12 07 28.9	-29 36 03	18.62	40007	90	3.15
RR210_13744	12 06 16.1	-29 36 11	16.89	43305	77	8.05
RR210_13879	12 07 48.2	-29 36 22	18.60	42682	85	3.92
RR210_14043	12 06 15.2	-29 36 36	19.41	43645	65	5.67
RR210_14191	12 06 59.1	-29 37 00	17.65	44273	80	7.79
RR210_14298	12 06 20.4	-29 37 02	17.85	43761	64	9.82
RR210_15704	12 07 48.5	-29 31 07	18.54	46653	50	5.15
RR210_15730	12 05 56.3	-29 36 04	15.82	14037	58	9.02

Table C.1– continued from previous page

RR210_16036	12 07 03.9	-29 31 44	17.94	64885	80	3.18
RR210_16096	12 06 37.1	-29 31 38	19.47	65648	201	2.27
RR210_16347	12 07 39.3	-29 32 07	17.34	46558	102	3.55
RR210_16463	12 07 42.2	-29 32 25	17.56	71826	126	5.63
RR210_16960	12 06 38.8	-29 32 47	19.17	72392	152	2.57
RR210_17074	12 05 58.5	-29 33 25	18.00	42826	105	2.39
RR210_17346	12 07 34.9	-29 33 57	19.47	104544	141	4.68
RR210_17416	12 06 34.3	-29 34 08	18.26	85	52	3.32
RR210_17787	12 05 51.0	-29 34 46	20.32	72360	252	2.31
RR210_17860	12 07 27.5	-29 35 49	18.02	32322	57	10.26
RR210_17953	12 06 25.2	-29 34 46	19.31	44329	134	2.17
RR210_18009	12 06 34.8	-29 35 03	18.94	42825	81	5.03
RR210_18064	12 07 28.0	-29 34 60	20.31	32137	240	2.37
RR210_18160	12 06 19.6	-29 34 21	18.24	43001	62	4.69
RR210_18245	12 06 54.4	-29 35 29	17.64	44304	75	10.54
RR210_18428	12 07 03.6	-29 35 42	18.45	44299	107	4.22
RR210_18444	12 05 41.4	-29 35 37	20.00	60398	37	2.19
RR216_01619	12 26 01.1	-39 31 21	18.57	97505	84	5.23
RR216_01672	12 25 35.0	-39 31 20	18.57	69057	73	5.92
RR216_02315	12 25 43.9	-39 32 29	17.64	54881	104	6.80
RR216_02687	12 26 10.0	-39 32 39	18.91	94704	89	2.96
RR216_02791	12 26 34.9	-39 32 46	19.51	58548	94	2.32
RR216_02812	12 25 15.4	-39 32 54	17.65	55561	105	9.70
RR216_03519	12 25 17.8	-39 33 46	17.26	3716	134	2.13
RR216_03651	12 25 36.4	-39 33 53	17.90	67373	134	6.34
RR216_04052	12 26 11.3	-39 34 47	14.57	3193	50	9.63
RR216_04724	12 25 37.2	-39 35 11	17.79	55461	75	7.05
RR216_04968	12 25 35.8	-39 35 28	18.77	55927	97	7.26
RR216_05021	12 26 04.2	-39 35 31	18.26	55900	101	9.55
RR216_05130	12 25 43.0	-39 35 39	18.77	87414	100	2.80
RR216_09657	12 26 13.9	-39 41 14	17.73	64904	92	7.72
RR216_09665	12 25 20.9	-39 41 13	18.28	48283	97	4.00
RR216_10148	12 25 14.3	-39 41 46	19.18	98846	220	3.29
RR216_10886	12 26 27.3	-39 42 45	18.29	87705	58	5.04
RR216_12152	12 25 32.8	-39 44 18	18.35	85	64	7.14
RR216_12209	12 25 37.0	-39 44 36	15.58	2697	62	5.32
RR216_12219	12 26 30.8	-39 44 26	20.10	98080	155	2.87
RR216_13075	12 25 37.2	-39 45 35	19.16	37411	151	2.52
RR216_13646	12 25 25.5	-39 46 09	17.90	32491	97	8.03

Table C.1– continued from previous page

RR242_00017	13 20 19.9	-43 55 57	17.03	44841.	94.	5.87
RR242_00018	13 21 39.0	-43 55 54	17.85	44979.	88.	4.66
RR242_00019	13 19 51.7	-43 56 07	16.90	83202.	365.	2.41
RR242_00970	13 19 47.3	-43 27 32	19.54	63214.	104.	2.03
RR242_01614	13 22 26.2	-43 27 58	18.52	117724.	88.	0.00
RR242_02287	13 20 21.5	-43 28 23	20.46	45124.	156.	2.21
RR242_02474	13 20 19.8	-43 27 48	16.66	34017.	57.	5.81
RR242_02729	13 22 20.8	-43 28 49	16.08	20908.	95.	5.18
RR242_03293	13 20 19.0	-43 29 33	18.15	16945.	170.	2.37
RR242_04964	13 20 11.6	-43 30 32	19.79	119128.	148.	0.00
RR242_05407	13 21 31.0	-43 30 51	18.21	82775.	114.	3.67
RR242_05413	13 19 55.7	-43 30 52	17.76	35402.	76.	6.22
RR242_05955	13 21 18.6	-43 31 15	17.90	15843.	155.	0.00
RR242_06039	13 22 03.1	-43 31 16	18.12	45039.	81.	4.83
RR242_06906	13 20 41.2	-43 31 56	19.37	116880.	168.	0.00
RR242_07132	13 21 38.7	-43 32 09	17.67	17231.	99.	3.06
RR242_08028	13 22 30.1	-43 32 41	19.15	35347.	252.	0.00
RR242_08050	13 21 15.3	-43 32 51	17.99	17588.	93.	2.93
RR242_08064	13 22 10.4	-43 32 56	17.85	3441.	60.	2.58
RR242_09059	13 20 18.2	-43 34 17	14.91	16958.	57.	8.66
RR242_09578	13 20 47.1	-43 34 02	17.22	15933.	80.	3.48
RR242_13110	13 22 24.8	-43 36 33	18.11	28900.	115.	3.17
RR242_13326	13 21 03.9	-43 36 58	16.15	3172.	45.	3.42
RR242_13627	13 21 10.7	-43 37 07	16.69	34022.	71.	5.92
RR242_14284	13 20 47.8	-43 37 36	17.13	15959.	137.	2.62
RR242_15689	13 21 16.5	-43 38 53	17.73	3731.	81.	7.20
RR242_16076	13 22 06.4	-43 39 08	19.82	44909.	70.	3.24
RR242_18166	13 21 04.0	-43 40 50	19.28	34002.	39.	2.10
RR242_18982	13 20 12.3	-43 41 40	15.86	15892.	91.	8.62
RR242_19745	13 20 11.5	-43 42 11	16.12	15626.	74.	9.69
RR242_20075	13 20 26.7	-43 42 28	16.33	3045.	52.	6.63
RR242_20913	13 22 12.9	-43 42 47	19.38	120355.	144.	0.00
RR242_21539	13 20 46.7	-43 43 20	18.93	66203.	74.	6.83
RR242_21750	13 20 03.6	-43 43 29	18.76	58084.	141.	2.69
RR242_22327	13 20 55.5	-43 44 20	15.06	3237.	70.	9.63
RR242_22454	13 21 40.5	-43 44 04	18.01	39347.	94.	0.00
RR242_22678	13 22 27.8	-43 44 03	19.49	33673.	199.	0.00
RR242_23181	13 21 29.9	-43 40 47	18.70	68141.	108.	2.09
RR242_23187	13 21 33.0	-43 39 43	17.37	3400.	88.	0.00
RR242_24352	13 21 14.8	-43 45 43	13.71	2697.	45.	10.05
RR242_24968	13 20 12.8	-43 45 53	16.61	15657.	103.	4.32

Table C.1– continued from previous page

RR242_25510	13 22 30.5	-43 46 13	17.61	27428.	228.	2.07
RR242_25575	13 19 44.2	-43 46 28	16.42	2655.	84.	4.26
RR242_26321	13 20 53.5	-43 46 49	19.71	101604.	286.	2.52
RR242_26778	13 19 54.9	-43 47 33	14.52	15893.	74.	10.49
RR242_27628	13 21 28.6	-43 47 45	17.56	21167.	88.	5.16
RR242_28727	13 21 22.6	-43 43 22	17.05	3017.	87.	6.80
RR242_31908	13 22 31.2	-43 51 15	19.22	114250.	340.	2.46
RR242_32890	13 20 43.4	-43 52 02	17.41	16245.	55.	6.00
RR242_33526	13 22 12.0	-43 52 25	19.54	114574.	113.	4.70
RR242_34453	13 21 14.8	-43 53 29	18.27	29.	52.	5.07
RR242_34877	13 22 01.6	-43 53 36	17.72	35756.	61.	8.68
RR242_35172	13 20 00.5	-43 53 57	20.41	34971.	206.	2.23
RR242_36267	13 20 21.8	-43 55 38	18.67	2997.	40.	3.19
RR242_36865	13 22 28.6	-43 55 08	20.28	101996.	296.	0.00

Curriculum Vitae

Mag. Ruth Grützbauch

date of birth	October 3, 1978
place of birth	Vienna, Austria
address:	Institute for Astronomy
	Türkenschanzstraße 17
	A–1180 Wien, Austria
tel.:	+43 1 4277518–67
fax :	+43 1 42779518
e-mail :	gruetzbauch@astro.univie.ac.at

Education

1984 – 1988	Elementary school in Vienna, Austria
1988 – 1996	Secondary school in Vienna, Austria
June 11, 1996	Secondary school diploma

University career

Oct. 1996 – June 2003	Master studies of astronomy at the University of Vienna
June 1999	First diploma examination
March 2001	Beginning of master thesis
June 23 2003	Second diploma examination, completion of master degree with distinction. Topic of master thesis: *Isolated groups of galaxies: gravitational interactions and properties of the group members*
October 2003	Beginning of PhD studies, PhD position at the Institute for Astronomy, University of Vienna
April 2004	*ÖGAA*-award for the best master thesis of the year 2003

International experience

Nov. – Dec. 2004	Research period at the Osservatorio Astronomico di Padova, Italy
May – June 2005	Research period at the Osservatorio Astronomico di Padova, Italy
April – July 2006	Short-term studentship at the European Southern Observatory, Santiago de Chile
Nov. – Dec. 2006	Research period at the Osservatorio Astronomico di Padova, Italy
May 2007	Working visit at the School of Physics & Astronomy at the University of Nottingham

Conference attendances

Sept. 24 – 28, 2007	Annual scientific meeting of the Astronomische Gesellschaft in Würzburg, including a poster presentation
August 14 – 18, 2006	General Assembly of the International Astronomical Union in Prague, including a poster presentation
Sept. 26 – Oct. 1, 2005	Annual scientific meeting of the Astronomische Gesellschaft in Cologne, including a poster presentation
Sept. 20 – 24, 2004	Annual scientific meeting of the Astronomische Gesellschaft in Prague, including a talk
Sept. 13 – 17, 2004	JENAM 2004 in Granada, including a poster presentation
Sept. 15 – 19, 2003	Annual scientific meeting of the Astronomische Gesellschaft in Freiburg, including a poster presentation
April 24 – 25, 2003	Scientific meeting of the Österreichische Gesellschaft für Astronomie und Astrophysik in Innsbruck, including a poster presentation
Sept. 10 – 14, 2001	JENAM 2001 in Munich, including a poster presentation

Affiliations

- Member of the *Österreichische Gesellschaft für Astronomie und Astrophysik (ÖGAA)*

- Member of the *Astronomische Gesellschaft (AG)*

- Member of the *Verein der Freunde der Zahl PI*

Additional qualifications

- Languages: German (native), English (fluent), French (basics), Spanish (basics)

- Computer literacy:

  - operating systems: Linux, Windows
  - astronomical software: IRAF, MIDAS, SExtractor, GALFIT,...

- Web design:

  - Homepage of the *Extragalactic Research Group* at the Institute for Astronomy, University of Vienna
  - *Österreichischer Astronomietag*
  - *Studienrichtungsvertretung Astronomie*

List of publications

Refereed journals

- Rampazzo, R., Marino, A., Tantalo, R., Bettoni, D., Buson, L. M., Chiosi, C., Galletta, G., Grützbauch, R., Rich, R. M. 2007: *"The Galaxy Evolution Explorer UV emission in shell galaxies: tracing galaxy rejuvenation episodes"*, **MNRAS 381**, 245

- Grützbauch, R., Trinchieri, G., Rampazzo, R., Held, E. V., Rizzi, L., Sulentic, J. W., Zeilinger, W. W. 2007: *"Small Scale Systems of Galaxies. III. X-ray detected E+S galaxy pairs in Low Density Environments"*, **AJ 133**, 220

- Grützbauch, R., Annibali, F., Bressan, A., Focardi, P., Kelm, B., Rampazzo, R., Zeilinger, W. W. 2005: *"Optical Properties of the NGC 5328 group of galaxies"*, **MNRAS 364**, 146

- Grützbauch, R., Kelm, B., Focardi, P., Zeilinger, W. W., Rampazzo, R. 2005: *"Small Scale Systems of Galaxies. II. Properties of the NGC 4756 group of galaxies"*, **AJ 129**, 1832

Conference proceedings

- Grützbauch, R., Rampazzo, R., Zeilinger, W. W., 2007: *"How do galaxy groups evolve? Testing evolutionary scenarios via the faint galaxy population of X-ray detected galaxy pairs"*, AN 328, 698

- Grützbauch, R., Rampazzo, R., Trinchieri, G., Zeilinger, W. W., 2006: *"The Eventful Life of Galaxies in Poor Galaxy Structures"*, IAUS 235, 168

- Grützbauch, R., Rampazzo, R., Trinchieri, G., Zeilinger, W. W., 2005: *"Evolution of Small Scale Systems of Galaxies: X–ray detected E+S galaxy pairs"*, Astronomische Nachrichten Vol. 326, 492

- Grützbauch, R., Zeilinger, W. W., Rampazzo, R., 2004: *"The NGC 4756 Group of Galaxies: Evolutionary Processes in Loose Galaxy Groups"*, Astronomische Nachrichten Vol. 325, Issue S1

- Grützbauch, R., Zeilinger, W. W., Focardi, P., Kelm, B., Rampazzo, R., 2003: *"Isolated Groups of Galaxies: Gravitational Interactions and Properties of the Group Members"*, Astronomische Nachrichten Vol. 324, Issue S3

- Kelm, B., Focardi, P., Grützbauch, R., Zeilinger, W. W., Rampazzo, R., 2003: *"Galaxy Systems in Low Density Environments: The NGC 4756 System"*, Proceedings of the ESO Workshop held in Venice, Italy, 24-26 October 2001, p. 54.

- Grützbauch, R., Zeilinger, W. W., Focardi, P., Kelm, B., Rampazzo, R., 2001: *"Physical Properties of Galaxies in Low Density Environments"*, AG Abstract Series Vol. 18, P138